Titre: Title:	Durable Thermochromic VO2 Films Deposited by HiPIMS
Auteur: Author:	Simon Loquai
Date:	2017
Type:	Mémoire ou thèse / Dissertation or Thesis
Référence: Citation:	Loquai, S. (2017). Durable Thermochromic VO2 Films Deposited by HiPIMS [Thèse de doctorat, École Polytechnique de Montréal]. PolyPublie. https://publications.polymtl.ca/2487/

UNIVERSITÉ DE MONTRÉAL

DURABLE THERMOCHROMIC VO_2 FILMS DEPOSITED BY HIPIMS

SIMON LOQUAI

DÉPARTEMENT DE GÉNIE PHYSIQUE

ÉCOLE POLYTECHNIQUE DE MONTRÉAL

THÈSE PRÉSENTÉE EN VUE DE L'OBTENTION

DU DIPLÔME DE PHILOSOPHIAE DOCTOR

(GÉNIE PHYSIQUE)

FÉVRIER 2017

UNIVERSITÉ DE MONTRÉAL

ÉCOLE POLYTECHNIQUE DE MONTRÉAL

Cette thèse intitulée:

DURABLE THERMOCHROMIC VO_2 FILMS DEPOSITED BY HIPIMS

présentée par : LOQUAI Simon

en vue de l'obtention du diplôme de : Philosophiae Doctor

a été dûment acceptée par le jury d'examen constitué de :

M. PETER Yves-Alain, D. Sc., président

M. MARTINU Ludvik, Ph. D., membre et directeur de recherche

Mme KLEMBERG-SAPIEHA Jolanta-Ewa, Doctorat, membre et codirectrice de recherche

M. WERTHEIMER Michael R., D. Sc. A., membre

M. HELMERSSON Ulf, Ph. D., membre externe

DEDICATION

I dedicate this thesis to Gilles and Edouard

ACKNOLEDGEMENTS

First, I would like to thank both of my advisors, Ludvik Martinu and Jolanta-Ewa Klemberg-Sapieha, who support and direct me for all those years. Under their supervision, I grow as from an engineer to a scientist.

Second, I would also like to thank Michael Wertheimer, Prof Ulf Helmersson and Prof Yves-Alain Peter for their acceptance to read my dissertation and to be my jury members. I would like to thank Margaret McKyes for the English editing on some part of this thesis.

Therefore, I would like to thank Oleg Zabeida for his expertise in plasma and vacuum systems, and Bill Baloukas for his expertise in active optical materials. Their combined expertise allows me to overcome many hurdles and motivates me during down times in this project.

The Functional Coating and Surface Engineering Laboratory (FCSEL) will be nothing without the technical assistance of both Francis Turcot and Sébastien Chénard. Your hard work and efficiency keep the system running and our research active.

I would like to personally thank Matjaz Panjan for taking me under his wing during this few months in 2013. I learned a lot with you, especially how to plan an experiment and get things done when its running.

I would like to thank the summer students that work with me during those last seven years, Aimé Labbé, Philippe Jubinville and Rodrigue Beaini.

I would like not to forget all my colleagues at the FCSEL, who are excellent scientists and eventually became good friends: Alexis Ragusish, Amaury Kilicaslan, Erika Herrera, Fabrice Pougoum, Francis Blanchard, Gabriel Taillon, Jacques Lengaigne, Jean-Phillipe Fortier, Jincheng Qian, Jiri Capek, Jiri Kohout, Julien Gagnon, Julien Schmitt, Martin Caron, Matej Hala, Médard Koshigan, Michael Laberge, Soroush Hafezian, Stephen Brown, Thomas Poirié, Thomas Schmitt, William Trottier, Yuxiao Wu, and all the former students.

Finally, I would like to thank my family and my fiancé Aurélie for supporting me during all those years.

RÉSUMÉ

Le dioxyde de vanadium, VO_2, est le matériau thermochromique le plus étudié. Il présente une transmission de la lumière infrarouge élevée à basse température et une extinction de cette dernière au-dessus de sa température critique. Ce changement de propriété est réversible et ne nécessite pas de stimulus externe. De ce fait, le VO_2 est un candidat parfait pour les applications de contrôle de transfert d'énergie. L'application la plus directe est celle des vitrages dits 'intelligents', où la couche mince thermochromique module la transmission du rayonnement solaire infrarouge en fonction de la température. Un tel dispositif contrôle la température du milieu ambiant passivement, limitant la consommation des équipements de chauffage et climatisation. Dans un objectif similaire, les matériaux thermochromiques peuvent aussi être utilisés pour créer des dissipateurs thermiques pour les satellites, appelés 'Smart Radiative Device' (SRD). Cependant, les dispositifs thermochromiques à base de VO_2 sont toujours à l'échelle du laboratoire, principalement à cause de la complexité de synthèse du VO_2. Le Vanadium est en effet un métal de transition, possédant de multiple oxydes stœchiométriques dont seul le VO_2 présente un intérêt pour ces applications. Un contrôle du niveau d'oxydation lors du dépôt est donc nécessaire, complexifiant l'industrialisation du procédé. De plus, la température de dépôt du matériau pour obtenir la phase cristalline, généralement 400°C, génère un cout prohibitif pour beaucoup d'industriels.

Lors de la dernière décade, la communauté scientifique des dépôts physiques en phase vapeur a connu une forte effervescence autour d'une nouvelle technique, la pulvérisation magnétron pulsée de haute puissance (HiPIMS en anglais). Cette dernière combine la flexibilité des procédés de pulvérisation magnétron avec la modulation du temps d'impulsion pour obtenir un plasma de haute densité. Cette technologie est prometteuse pour le dépôt de couches minces. En particulier en mode réactif, le procédé HiPIMS offre un taux de dépôt avantageux comparé au procédé conventionnel de pulvérisations; tout en améliorant les propriétés des couches déposées, telles qu'une plus haute densité, une contrainte mécanique inférieure et un abaissement de la température nécessaire pour obtenir des couches minces cristallines. Les contributions des différents effets de la décharge HiPIMS (haut flux d'ions de basse énergie et le rayonnement du plasma) à la performance des couches ne sont pas encore expliquées, malgré une bonne connaissance du comportement de la décharge HiPIMS. De ce fait, nous avons choisi d'appliquer ce procédé au dépôt de couches minces de VO_2 afin d'en améliorer les propriétés et illustrer les aventages du procédé HiPIMS pour le dépôt de ce type d'oxyde.

En premier, nous avons observé l'expansion du plasma réactif HiPIMS au-dessus d'une cible métallique de vanadium. Cette mesure se fait à l'aide d'une caméra haute vitesse et de filtres interférentiels passe-bande permettant de séparer les différentes plages énergétiques de l'émission optique du plasma. Il a été démontré que la décharge HiPIMS opérée dans un mélange argon-oxygène a des caractéristiques très similaires aux décharges dans des atmosphères d'argon et d'oxygène pour la période allumée du pulse. Cependant, dans les premières microsecondes après l'extinction du plasma, la post-décharge, une forte émission optique est observée pour les espèces de faible énergie du plasma. Ce phénomène d'émission optique est lié au refroidissement des électrons une fois que le voltage appliqué à la cathode est supprimé, suivi de la diffusion de ces électrons dans le champ magnétique jusqu'au point d'annulation du champ (piège magnétique). Ce phénomène optique nécessite un seuil d'oxygène inséré dans la chambre, nous avons supposé que les électrons refroidis interagissent avec les molécules d'oxygène sous forme d'une réaction de capture dissociative. Les ions négatifs créés par cette réaction peuvent ensuite se recombiner avec les ions positifs environnants, peuplant les niveaux radiatifs observés lors de l'imagerie haute vitesse. Les espèces recombinées possèdent aussi une énergie cinétique estimée à près de 1 eV, ce qui génère un bombardement ionique de faible énergie de la couche mince en croissance. En conclusion, cet effet présent dans les décharges pulsées offre une source d'oxygène atomique supplémentaire et explique partiellement la réactivité plus grande des décharge HiPIMS, diminuant le flux d'oxygène nécessaire pour déposer des oxydes stœchiométriques. De plus, le flux de particules fournit une partie de l'énergie nécessaire pour abaisser la température de dépôt de ces oxydes sous forme de couches cristallines.

Nous avons ensuite cherché à démontrer l'intérêt de l'abaissement de la température de dépôt de VO_2 à l'aide de substrat polymère. En utilisant l'énergie apportée par le procédé HiPIMS, des couches minces de VO_2 ont été synthétisées sur deux type de polyimides: le Kapton HN et le Kapton CS. Le Kapton HN est un standard de l'industrie aérospatiale, un polymère orange à haute résistance thermique et connu pour survivre dans le vide spatial. Au contraire, le Kapton CS est un polymère transparent de résistance thermique inférieure mais d'intérêt pour les applications de fenêtres intelligentes. Les couches minces déposées sont thermochromiques, avec des changements de propriétés optiques attendues dans l'infrarouge, une première pour du VO_2 déposé sur un substrat polymère. La stœchiométrie du matériau a été confirmée par mesure de spectroscopie photoélectronique X (XPS). Cependant, la nature des polymères utilisés rend impossible de

confirmer la structure cristalline directement; celle-ci fut mesurée par diffraction des rayons X (XRD) et spectroscopie Raman sur des substrats de silicium insérés dans la chambre lors des dépôts sur Kapton. Ces mesures présentent des spectres comparables avec la littérature. La composition des couches minces a pu être calculée à l'aide des spectroscopies de rétrodiffusion de Rutherford (RBS) et détection de recul élastique (ERD). Ces résultats concordent avec les mesures XPS, tout en soulevant la présence de diffusion du vanadium dans le substrat polymère. Cette diffusion d'atomes améliore l'adhésion des couches minces au détriment d'une perte sèche de vanadium. Une diffusion similaire a été observée sur les échantillons déposés sur des substrats de verres, avec la présence de bore au sein de la couche de VO_2.

La dernière étude cherche à contrôler la diffusion à l'aide d'une barrière à l'interface VO_2/verre. Le VO_2 se dégradant fortement en milieu humide, une seconde barrière de diffusion est envisagée à la surface des échantillons. Le matériau choisi est le nitrure de silicium, SiN_x, connu pour ses bonnes propriétés de barrière de diffusion ainsi que pour sa stabilité à haute température; de plus, ce matériau est simple à déposer par pulvérisation magnétron. Pour estimer la durabilité des couches de VO_2, des échantillons de références sont déposés à l'aide de la méthode conventionnelle de pulvérisation magnétron radiofréquence (RFMS). Avant exposition à un environnement humide, les échantillons présentent des propriétés optiques similaires et ne peuvent pas être différenciés formellement par Raman et XRD. L'utilisation d'une barrière de diffusion SiN_x est un succès, aucune dégradation majeure n'étant observée sur les couches protégées, tout comme une absence de diffusion du bore dans le VO_2. Au contraire, pour les couches où le VO_2 est exposé à l'environnement oxydant, une différence marquante entre les couches préparées par HiPIMS et RFMS est obtenue. Alors que les échantillons préparés par RFMS se dégradent très rapidement, les échantillons préparés par HiPIMS offrent une période d'incubation où la dégradation des propriétés optiques est très lente. L'analyse d'image de microscopie électronique à balayage et de la densité des couches minces par RBS-ERD montre que les couches HiPIMS incorporent moins d'hydrogène lors de la dégradation. De plus, il ne se forme pas les aiguilles poreuses en surface observées sur les couches RFMS. Nous lions cet effet à une plus grande densité des grains de la couche, qui limite la diffusion de l'oxygène lors de la dégradation et donc ralentit le phénomène de dégradation.

ABSTRACT

Vanadium dioxide, VO_2, is a well-known thermochromic material that exhibits high or low infrared transmittance when its temperature is below or above a critical temperature, respectively. Because this change in properties is reversible, VO_2 has long been a candidate for radiative energy control devices. One innovative application is the smart window, in which a thermochromic layer controls the transmission of infrared radiation from the sun as a function of the surrounding temperature. This enables self-controlled temperature regulation, which in turn limits heating and cooling requirements. Similar devices called smart radiator devices (SRDs) are being developed for passive cooling of satellites. However, all these applications remain in the development phase due to VO_2 deposition issues. Vanadium is a transition metal that exhibits multiple oxide stoichiometries, of which only VO2 is of interest. Precise control of the oxygen fraction is therefore needed for VO_2 synthesis, accompanied by a high deposition temperature, usually around or in excess of 400 °C, in order to obtain the crystalline material. These imperatives currently limit industrial applications of VO_2.

Over the past decade, high power impulse magnetron sputtering (HiPIMS) has emerged as a newcomer in the magnetron sputtering community. Because HiPIMS combines the versatility of magnetron sputtering with short high power pulses to generate highly ionized plasma, it is a promising technique for thin film material deposition. In reactive sputtering, HiPIMS provides deposition rates similar to or higher than those for conventional sputtering, along with superior film properties such as higher density and lower stress, among others. Furthermore, crystalline films can be obtained at lower deposition temperature. However, the impacts of the high ion flux, plasma radiation, and HiPIMS dynamics on the metal-oxide properties are still unclear, despite a good understanding of the HiPIMS discharge. We therefore chose to apply HiPIMS to thermochromic VO2 to demonstrate the advantages of using HiPIMS to deposit crystalline films.

First, the expansion of a reactive-HiPIMS discharge over a vanadium target was investigated using high-speed plasma imaging combined with optical bandpass filtering. The results showed that the reactive discharge operating in an argon–oxygen mixture behaved similarly in “pulse-on” time to discharges in pure argon and oxygen. However, in the post-discharge, the first microsecond after the cathode voltage was removed, strong light emission in the low-energy spectra was observed. This light emission can be explained by electrons that cool and drift toward the null magnetic field

trap. A threshold oxygen content in the mixture is needed in order to observe this phenomenon. This led us to hypothesize that the main interaction is dissociative attachment between the electrons and the molecular oxygen. The resulting negative ions recombine with positive ions, generating excited radiative species. These resulting species, which have an estimated kinetic energy approaching 1 eV, provide a low-energy bombardment of the growing films. This reaction in pulsed plasma also generates additional atomic oxygen, compared to conventional magnetron sputtering. Therefore, such post-discharge emission provides a partial explanation for the reactivity observed in the pulsed discharge, for the lower oxygen content needed to produce stoichiometric material, and for the lower temperature required to deposit crystalline films.

Following the exploration of the reactive discharge, HiPIMS, a previously demonstrated approach to lower the deposition temperature, was used to deposit thermochromic VO_2 on polymer substrates. Using the energetic HiPIMS process, VO_2 films were synthesized onto two different polyimide substrates, Kapton® HN and Kapton® CS. These two substrates present different optical properties that target different potential applications of VO_2 for energy-control devices. First, Kapton® HN, an orange-tinted polymer, is standard in the aerospace industry because it is resistant to high temperatures and space radiation. On the other hand, Kapton® CS provides a clear substrate with moderate temperature resistance, and is more suitable for earthbound applications such as smart windows. The produced films exhibited active thermochromic behavior, the first time that this has been achieved with VO_2 on a polymer substrate. The film stoichiometries were confirmed by X-ray photoelectron spectroscopy (XPS). Unfortunately, due to the nature of the polymer substrate, it was not possible to directly quantify the film crystallinity. However, Raman spectroscopy and X-ray diffraction (XRD) of the deposits on silicon strips showed spectra comparable to those in the literature. Rutherford backscattering spectrometry (RBS) and elastic recoil detection (ERD) were used to confirm the stoichiometric composition of the Kapton®-coated sample, revealing a strong need for film–substrate interface control. In fact, pronounced diffusion of vanadium and oxygen into the polymer substrate was measured. Although this diffusion could improve the film adhesion, it represents a net loss of material in terms of deposition efficiency. Similar diffusion was observed for reference films deposited onto glass substrates; namely vanadium diffusion into glass, and boron (glass dopant) diffusion into VO_2.

To prevent this type of diffusion at the VO_2–glass interface, the design was improved with the addition of a barrier coating. Because it is well known that thermochromic VO_2 is sensitive to water

degradation, an additional diffusion barrier was added as a top layer. For this purpose, we chose SiN_x, a commonly used diffusion barrier that is stable at high temperatures and can be deposited by magnetron sputtering. To assess film durability, VO_2 films were deposited using both HiPIMS and conventional RFMS. Before oxidation, the deposited devices presented similar transmission and performance in terms of infrared modulation, independently of the deposition method. Raman and XRD were unable to detect significant differences in the HiPIMS- and RFMS-deposited VO_2. As expected, SiN_x provided an adequate diffusion inhibiter. No trace of the glass dopant was found in the VO_2 layers, and both RFMS- and HiPIMS-deposited coatings provided good resistance to a steam environment. However, the unprotected VO_2 coating behaved differently. The HiPIMS-deposited layers exhibited slower kinetics, with an incubation period of slow degradation, whereas the RFMS-deposited VO_2 layer showed rapid dissolution. Based on the results of scanning electron microscopy (SEM) image analysis combined with RBS/ERD density measurement, we attributed the higher durability of the HiPIMS-deposited VO_2 coating to a higher grain density, low amount of grain boundaries, which lowered oxygen diffusion at grain boundaries and hence slowed the material degradation. On the other hand, the lower density of the RFMS-deposited layer gave rise to high roughness, with V_2O_5 needles topping the SiN_x layer. The higher diffusion of atoms into the RFMS sample was confirmed by the ERD-measured hydrogen content, showing higher hydrogen density in the vanadium layer during water oxidation in the RFMS-deposited layers.

TABLE OF CONTENTS

LIST OF TABLES

LIST OF FIGURES

LIST OF SYMBOLS AND ACRONYMS

2 D	two-dimensional
3 D	three-dimensional
a-C	amorphous carbon
A(λ)	spectral absorption
AC	alternative current
A_{ul}	Einstein's coefficient
APCVD	atmospheric pressure chemical vapour deposition
ASTM	American society for testing and materials
B	magnetic field
c	speed of light
CCD	coupled charged device
COP	conference of parties
CVD	chemical vapour deposition
DC	direct current
DCMS	direct current magnetron sputtering
e	electron elementary charge
E*	reduced energy
E_b	binding energy
E_F	Fermi energy
E_l	lower energy level
E_u	higher energy level
EEDF	electron energy distribution function

ERD-TOF	elastic recoil detection in the time-of-flight mode
$f(O_2)$	oxygen flow
f_{lu}	absorption coefficient
FSCEL	*Functional Coating and Surface Engineering Laboratory*
g	grating density
g_l	degeneracy of the lower level
GHG	greenhouse gases
g_u	degeneracy of the upper level
HiPIMS	high power impulse magnetron sputtering
IEA	international energy agency
ITP	indium tin oxide
IR	infrared
J_0	sheath current density
k	dispersion order
k_{Ar^M}	reaction rate
k	absorption coefficient
k_B	Boltzmann constant
L_A	spectrometer entry length
L_B	spectrometer exit length
LIF	laser induce fluorescence
m_e	electron mass
MIT	metal insulator transition
MPP	modulated pulsed power
N_0, N_1	complex refractive indices

N_C	charge density
n_e	electron density
n_i	ion density
n	refractive index
OECD	organisation for economic co-operation and development
OES	optical emission spectroscopy
PECVD	plasma enhanced chemical vapour deposittion
PID	proportional–integral–derivative
PLD	pulsed laser deposition
PVD	physical vapour deposition
$R(\lambda)$	spectral reflection
RBS	Rutherford backscattering spectroscopy
RFMS	radio frequency magnetron sputtering
r_p	‘p’ polarisation reflection coefficient
r_s	‘s’ polarisation reflection coefficient
SRD	smart radiative devices
SZD	structure zone diagram
s	sheath length
T	temperature
T*	reduced temperature
t*	film growth rate
$T(\lambda)$	spectral transmission
TC	thermochromic
T_s	substrate temperature

T_e	electron temperature
T_i	ion temperature
T_0	neutral temperature
T_{lum}	luminous transmittance
T_{solar}	solar transmittance
$T_{2500\ nm}$	transmission at 2500 nm
U_C	Cathode voltage
UNFCCC	United Nations Framework Convention on Climate Change
USA	The United States of America
UV	ultra-violet
v_e	electron velocity
v_i	ion velocity
v_B	Bohm velocity
V_b	substrate bias
XPS :	X-ray photon spectroscopy
XRD	X-ray diffraction
Y	sputter yield
ΔH	formation enthalpy
ΔT_{solar}	variation of solar transmittance
$\Delta T_{2500\ nm}$	infrared optical modulation at 2500 nm
ΔT_{loss}	loss of performance
ΔT_{lum}	luminous transmittance
$\Delta \tau_c$	transition hysteresis
$\Delta \tau_c^+$	transition temperature, heating cycle

$\Delta\tau_c^-$	transition temperature, cooling cycle
φ_{solar}	solar spectral irradiance
η_{lum}	spectral luminous efficiency function for the photopic vision
ϵ_t	total emissivity
$\epsilon(\lambda)$	spectral emissivity
ϵ_0	vacuum permitivity
τ_c	critical temperature
α_H	Bohr radius
α	incidence angle
ß	reflected angle
η	oxygen flow ratio
Ψ and Δ	ellispsometric data
λ_D	Debye length
λ_{ul}	wavelength
θ_0	incidence angle
θ_1	refracted angle

CHAPTER 1 INTRODUCTION

Since mankind first walked the earth, human evolution has been fuelled by energy innovations, from the discovery of fire to modern control of fossil energy sources (coal, gas, oil, and uranium). Each transformation of primary energy into mechanical and electrical energy has been followed by leaps in human technology and lifestyles. The first Industrial Revolution took place in the 19th century, with the invention of the steam engine, thereby improving the welfare of European citizens. The introduction of electricity, oil, and its derivatives marked the Second Industrial Revolution, which further improved the well-being of citizens in industrialized countries.

These types of technological revolutions create gaps between industrialized countries and the rest of the world in terms of development and energy access. In the modern era, after the Cold War, another issue arose: greenhouse gases (GHG). This problem was ignored by the world's governing bodies because technological supremacy was a necessity in the ideological war between the Western and Eastern Blocs. After the collapse of the Communist bloc, the United Nations formed the United Nations Framework Convention on Climate Change (UNFCCC) in 1992 in an effort to stabilize GHG levels and limit the impacts of human activity on the climate. Since the UNFCCC was created, yearly negotiations have been conducted among the 197 members, called the Conference Of Parties (COP). The two most famous sessions are COP-3 in Kyoto (1997) and COP-21 in Paris (2015). At each session, a non-binding agreement was signed in the aim of reducing GHG emissions by 2012 (COP-3) and 2100 (COP-21). However, these agreements are limited to the countries that actually translate the agreement into local legislation. Thus, if a major political influencer such as Canada or the United States of America (USA) does not apply the agreement, its impact is dramatically reduced.

Since the 1970s, local policies have been enacted to regulate the electric sector and electric energy consumption, and to mitigate the impact of oil shortages due to a series of oil crises in 1973, 1991, and 2008. The most successful of these policies, the California Energy Code, was implemented in 1978 by the Californian Building Standards Commission. The code introduced strict regulations for household appliances and building insulation, and is claimed to be the main reason for the low per capita electricity consumption in California compared to the rest of the USA. It is therefore frequently cited as an example to promote the enactment of stricter policies for building construction standards [1], [2]. On the other hand, in microeconomics, authors such as Levinson

and Sundarshan interpret this difference in energy consumption per capita to be due to demographic migration and climate parameters [3]–[5].

Human habits have strong impacts on day-to-day energy consumption. According to behavioural economics, these habits are based on the elasticity of household budgets, or how much the consumption of a resource changes with the resource price or availability. Therefore, decreases in household appliance consumption, such as those provoked by the California Energy Code, changed household habits: the number of appliances and gadgets per household increased. This resulted in a slow rise in global energy needs, as shown in Figure 1-1.

However, heating, ventilation, and air conditioning (HVAC) provide greater opportunities to reduce per capita energy consumption. In fact, more than 50% of energy consumption by buildings can be attributed to space heating and cooling [6]. Although the residential sector uses a balanced energy source mix (biomass, electricity, and natural gases), commercial buildings rely mainly on electricity and fossil fuels, as shown in Figure 1-2.

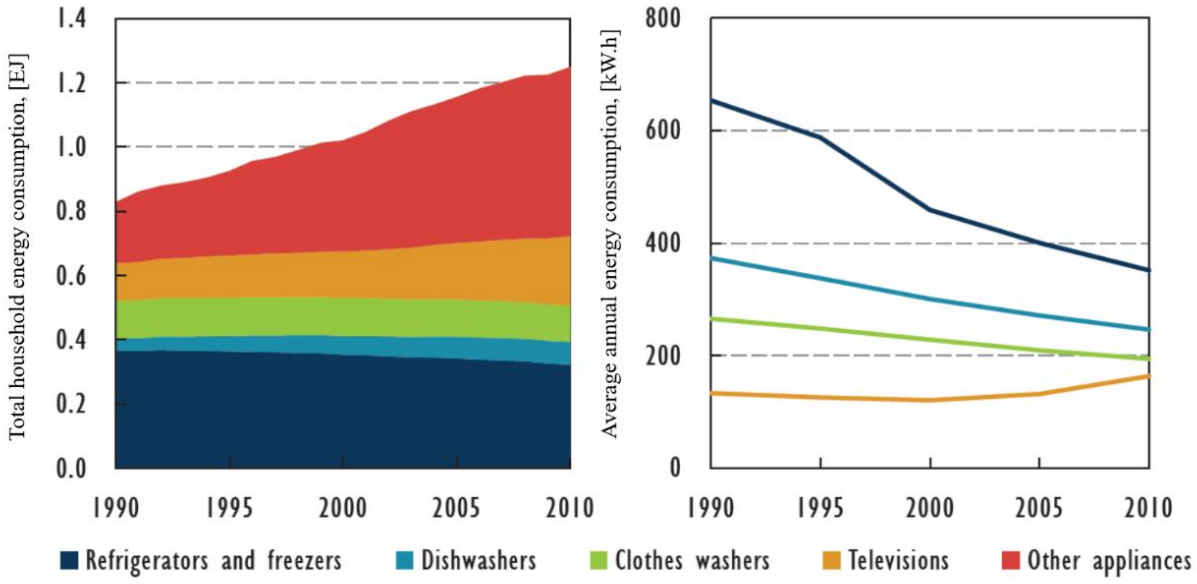

Figure 1-1 Large and small appliance energy consumption in the Organization for Economic Co-operation and Development (OECD) countries for the last two decades. Left panel presents the total consumption by appliances; right panel presents the average consumption for each unit. Reproduced from [7].

It is worth noting that travel and relocation have increased enormously in the last two decades. In North America, people commonly move from the cold northern states to the warmer southern states such as Texas or Florida for seasonal vacation or retirement. Those migrations decrease household size and transfer the primary energy source from hydroelectricity (Canada) or nuclear (northeastern USA) to coal and natural gas (southern USA). This is not an issue in Europe, which has a unified electricity grid operated by the Union for the Coordination of the Transmission of Electricity (UCTE). Focusing on reducing energy expenses for private heating and cooling and for publicly owned real estate parks [8], [9] would achieve larger cuts in global energy consumption, especially in North America.

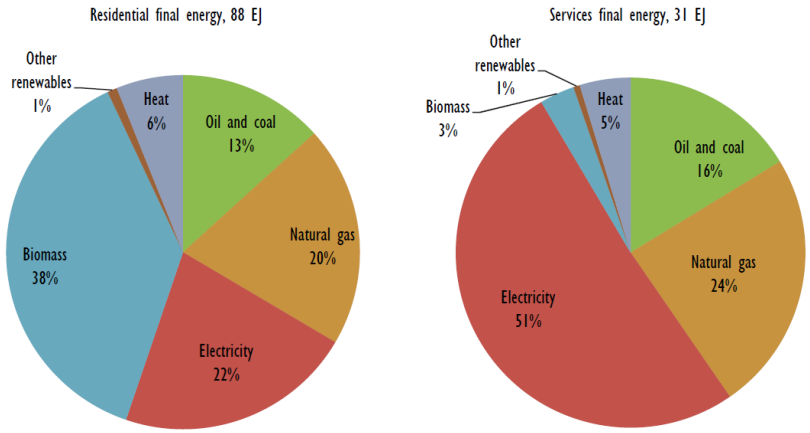

Figure 1-2 Global building final energy use fuel shares for residential and services, 2012. Final energy refers to the energy delivered to the building, not how it is used in the building. For example, natural gas denotes that the building uses a system that burns natural gas, to generate either heat or electricity. Reproduced from [6].

The improvement that has made the largest energy impact is building insulation. Since the 1970s, windows have been known to be the weakest point in insulation, with an estimated radiative and conductive heat transmission of around 6 $Wm^{-2}K^{-1}$. Nevertheless, modern architecture and lifestyles favour large glass surfaces.

The first approach to limit the heat that is transmitted by conduction through glass surfaces was to use a double or triple-pane window filled with controlled inert gas. These windows were produced

in the 1970s in response to the first Oil Crisis. The double or triple glazing provides initial gains in insulation coupled with additional sound dampening features. It does not, however, address the heat that is transmitted by radiation. Part of the thermal solar radiation and the radiation that is re-emitted from the local environment is positioned in the near infrared and short- to mid-wave infrared bands. Specific spectral control of the transmission is needed to further lower heat transmission. An example of an idealized solar blocker and the solar energy spectrum at sea-level are presented in Figure 1-3. A perfect radiation blocker would admit visible light while blocking harmful ultraviolet rays (UVs) and infrared heat.

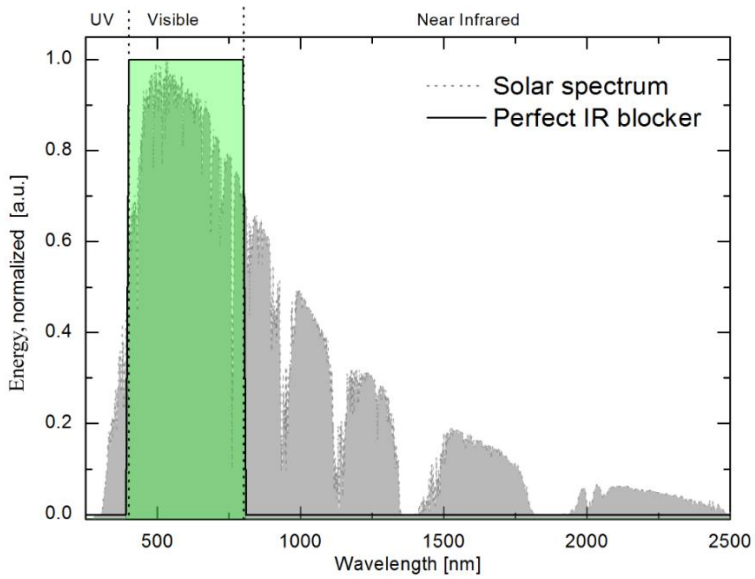

Figure 1-3 Normalized solar energy spectrum at sea level ASTM-G173-03 (grey) and optimal window energy transmittance (green).

A passive layer consisting of a thin metallic-like coating provides the best performance to block infrared light transmission. Thus, as the metal layer becomes thinner, it starts to transmit visible spectrum radiation while maintaining electrical conductivity, therefore reflecting infrared light. Many technologies have been tested, with gold, silver, indium tin oxides, or bismuth-based oxides as the reflective layers [10]. In the end, silver appears to be the optimal material, with a good balance between cost, performance, and colour neutrality. This type of passive reflective device is known as a low-emissivity (low-e) coating.

As of 2013, the low-e coating industry had reached 50% market penetration in the residential and commercial sectors [11], with an acceptable cost premium over double glazing, at less than US$45 m^{-2} [8]. Improvements in the processes and materials are ongoing, and further performance enhancements and cost reductions are expected in the coming decades.

As low-e technology matures and market acceptance is gained, the next generation of energy-saving glazing will be based on what are called “smart windows”. The active material used in these devices provides additional savings on heating, ventilation, and cooling costs, because the solar heat gain through the glazing can be controlled throughout the year. In summer, total insulation is required to limit cooling, while admittance of solar infrared light in winter lowers heating costs. These devices provide perfect performance in regions where temperatures vary widely between winter and summer, such as Canada and the northern European countries.

The idea for smart windows emerged concurrently with low-e technology during the first oil crisis. Since then, various technological solutions have been proposed for the active layer, including electrochromic and thermochromic materials, called chromogenic materials [12]. These materials exhibit changes in optical and electrical properties upon a change in electric field (electrochromic) or temperature (thermochromic), among others. Table 1-1 presents the performance of such devices as reported in the literature (experimental or modelling studies).

Table 1-1 Performance indexes for various chromogenic smartwindows. T_{lum} is the visible light transmittance, T_{sol} is the fraction of solar radiation transmittance. Index calculation methods are given in Chapter 2.

	Thermochromic VO_2 [13], [14]	Electrochromic WO_3 [15]	Low-e [15]
T_{lum}	0.40	0.69	0.74
T_{sol}	0.40	0.67	0.43
ΔT_{lum}	0.03	0.60	0
ΔT_{solar}	> 0.2	0.59	0

The main electrochromic materials are cathodic tungsten oxide (WO_3) and anodic nickel oxide (NiO) [16]. Electrochromic smart windows are currently commercially available. Modulation of infrared optical properties affects the visible light transmission linearly: $\Delta T_{solar} \approx \Delta T_{lum}$. This limits their application for privacy control. In addition, the need for electrodes to drive the electrical charge transfer raises a uniformity issue in large-scale products. Any pinhole, crack, or metallic contamination can create a short-circuit, which will disable the electrochromic effect at a large scale. Smaller devices that are less prone to short-circuiting, for example, anticounterfeiting devices, can make more effective use of electrochromic coating [17].

The material of interest in thermochromic devices is VO_2, first characterized by Morin [18]. At a critical temperature of 68 °C, VO_2 undergoes a thermochromic transition from a tetragonal to a monoclinic structure, also called a metal-to-insulator (MIT) transition. The high-temperature metallic state is highly reflective to infrared radiation, and the low-temperature insulator phase is transparent to infrared radiation. In addition, luminous transmittance shows a low change. This modulation of the transmission allows designing devices with active properties, eliminating the need for external control. Hence, it provides real "smart" control over solar transmittance. A more detailed discussion of VO_2 films and their applications is provided in the next chapter.

To date, the material and process challenges that have limited the large-scale implementation of VO_2-based glazing can be summarized as follows:

- High deposition temperature
- High transition temperature
- Low visible transmittance
- Greenish tint

Additionally, because the material is still being researched at laboratory scale, the durability of VO_2 is not well documented. However, poor resistance to oxidation is expected, because vanadium pentoxide (V_2O_5) is a thermodynamically stable oxide[19].

1.1 Objectives

Under the scope of this project, I had the opportunity to investigate two research topics: 1) high power impulse magnetron sputtering (HiPIMS) and 2) the development of high quality thermochromic VO_2 coatings using magnetron sputtering. I conducted my research at the Functional Coating and Surface Engineering Laboratory (FSCEL) under the supervision of Prof. Ludvik Martinu, Ph.D., and Prof. Jolanta-Ewa Klemberg-Sapieha, Doct.. I also had the opportunity to collaborate with Matej Hala, Ph.D., whose dissertation focused on HiPIMS-deposited amorphous oxides [20], and Jean-Philippe Fortier, M.Sc., who initiated the study of VO_2 synthesis by magnetron sputtering [21]. Their work pioneered the HiPIMS deposition of VO_2 at lower substrate temperatures than for conventional magnetron sputtering. However, certain questions remained unanswered. For instance, a better understanding of the reactive discharge over the vanadium target is needed as well as assessing the ability of HiPIMS to deposit crystalline VO_2 onto temperature-sensitive substrates.

My main objective was therefore to:

1. Advance the development of VO_2-based coatings using HiPIMS for energy control applications.

Additional specific objectives were set to focus the exploratory research:

2. Better understand the reactive HiPIMS discharge over the vanadium target and its impact on film properties.
3. Control and enhance the performance of HiPIMS-deposited VO_2 coatings on various substrates.
4. Evaluate the properties of HiPIMS-deposited VO_2 and RFMS-deposited VO_2 in terms of deposition rates, thermochromic performance, and film durability.

Initially, this thesis was strongly oriented toward smart window applications. However, the creation of the Multisectorial Industrial Research Chair in Coatings and Surface Engineering (MIC-CSE), partnered by the Canadian Space Agency, motivated the development of devices with HiPIMS-

deposited VO_2 coatings to control heat radiation for application to the aerospace industry. These devices will be introduced in the next chapters.

1.2 Publications

During the preparation of this thesis, the research work resulted in the publication of three articles in peer-reviewed journals and one publication in a journal dedicated to an international professional organization. These articles are summarized in

Table 1-2. In addition, collaborations with various researchers over the course of my thesis have resulted in two other peer-reviewed papers, as presented in Table 1-3. Oral and poster presentations were also given at numerous international conferences. The main conferences are listed in Table 1-4.

Table 1-2 List of articles related to this Ph.D. thesis.

Articles in peer-reviewed journals
S. Loquai, O. Zabeida, J.E. Klemberg-Sapieha, and L. Martinu, "Anomalous post discharge emission in reactive HiPIMS discharges", *Applied Physics Letters*, vol. 109, pp 114101, 2016
S. Loquai, B. Baloukas, O. Zabeida, J.E. Klemberg Sapieha, and L. Martinu, "HiPIMS-deposited thermochromic VO_2 films on polymeric substrates", *Solar Energy Materials & Solar Cells*, vol. 155, pp 60–69, 2016
S. Loquai, B. Baloukas, J.E. Klemberg-Sapieha and L. Martinu "HiPIMS-deposited thermochromic VO_2 films with higher environmental stability", *Solar Energy Materials & Solar Cells*, vol. 160, pp 217–224, 2017
Articles published in non-peer-reviewed journals
S. Loquai, J.-P. Fortier, M. Hala, O. Zabeida, J.E. Klemberg-Sapieha and L. Martinu, "Oxygen dynamics during reactive HiPIMS deposition of thermochromic VO_2 films", *Society of Vacuum Coaters Bulletin*, Spring 2014, pp 48–51

Table 1-3 List of articles resulting from collaborations.

Articles in peer-reviewed journals
M. Panjan, S. Loquai, O. Zabeida, J.E. Klemberg-Sapieha and L. Martinu, "Non-uniform plasma distribution in dc magnetron sputtering discharge: origin, shape and structuring of spokes", *Plasma Sources Sciences and Technology*, vol. 24, issue 6, pp 065010, 2015
B. Baloukas, S. Loquai and L. Martinu, "Low emissivity coatings incorporating thermochromic VO_2: Performance enhancement and new opportunities", *in preparation*

Table 1-4 List of contributions to international conferences.

Contributions to international conferences
S. Loquai, M. Hala, J. Capek, O. Zabeida, J.E. Klemberg-Sapieha and L. Martinu. " Diagnostic de plasmas pulsés haute-puissance, pulvérisation du chrome par HiPIMS", *Colloque de Plasma-Québec : Les plasmas à l'avant-garde de la science et de la technologie*, Montréal, Québec, Canada, 2012
S. Loquai, J.-P. Fortier, M. Hala, O. Zabeida, J.E. Klemberg-Sapieha and L. Martinu, "Oxygen dynamics during reactive HiPIMS deposition of thermochromic VO_2 films", *56th Society of Vacuum Coaters (SVC) Annual Technical Conference 2013*, Providence, Rhode Island, USA, 2013 Best Poster Award
S. Loquai, O. Zabeida, J.E. Klemberg-Sapieha and L. Martinu "Oxygen discharge dynamics during low temperature deposition of thermochromic VO_2 films by HiPIMS", *Colloque de Plasma-Québec: Évolution-Révolution*, Montréal. Québec, Canada, 2014
S. Loquai, O. Zabeida, J.E. Klemberg-Sapieha and L. Martinu "Oxygen discharge dynamics during low temperature deposition of thermochromic VO_2 films by HiPIMS", *7th Symposium on Functional Coatings and Surface Engineering (FCSE)*, Montréal, Québec, Canada, 2014
S. Loquai, J.-P. Fortier, B. Baloukas, R. Vernhes, O. Zabeida, J.E. Klemberg-Sapieha and L. Martinu, "Low Temperature Deposition of Thermochromic VO_2 Optical Coatings Using HiPIMS", *57th Society of Vacuum Coaters (SVC) Annual Technical Conference 2014*, Chicago, Illinois, USA, 2014, Sponsored Student
S. Loquai, J.-P. Fortier, B. Baloukas, R. Vernhes, O. Zabeida, J.E. Klemberg-Sapieha and L. Martinu, "Low Temperature Deposition of Thermochromic VO_2 Optical Coatings Using HiPIMS", *41st International Conference on Metallurgical Coatings and Thin Films (ICMCTF)*, San Diego, California, USA, 2014
S. Loquai, B. Baloukas, R. Vernhes, O. Zabeida, J.E. Klemberg-Sapieha and L. Martinu, "HiPIMS deposition of High Quality Thermochromic VO_2 films at low substrate temperature", *16th International Conference of Thin Films*, Dubrovnik, Croatia, 2014
B. Baloukas, S. Loquai and L. Martinu, "Low emissivity coatings incorporating thermochromic VO_2: Performance enhancement and new opportunities," *Optical Interference Coatings (OIC) 2016*, Loews Ventana Canyon, Tucson, Arizona, USA, 2016

1.3 Outline of the thesis

The thesis is divided into eight chapters, including this Introduction. The two chapters that follow present the theoretical and historical background. Chapter 2 provides a global overview of vanadium oxides and introduces the challenges of synthesizing thermochromic VO_2. Chapter 3 describes the principle of the magnetron sputtering, and more specifically, high power impulse magnetron sputtering (HiPIMS) and its applications for metal oxide coatings.

Chapter 4 describes the characteristics of the deposition chambers used for this project as well as the different types of power supplies and pulse management strategies used across studies. Finally, the material science techniques used to characterize the deposited films are presented.

This thesis is organized as a series of articles that constitute the core of the text and are reproduced in their original form as Chapters 5 to 7:

> Paper I (Chapter 5) reports an anomalous optical emission in a reactive HiPIMS discharge over the vanadium target. This phenomenon was observed using energy-resolved plasma imaging that combined band pass filters and a high-speed camera. A model is proposed to explain the energy exchange in the post-discharge phase that generates the observed optical emission.
>
> Paper II (Chapter 6) presents the deposition by HiPIMS of thermochromic VO_2 on two different kinds of polymeric substrates. The optimization of the HiPIMS discharge is first described. The properties of the resulting films are then analyzed in terms of thermochromism, composition, and microstructure.
>
> Paper III (Chapter 7) provides a critical comparison of the environmental stability of HiPIMS-deposited VO_2 compared to RFMS-deposited VO_2, both synthesized in the same apparatus. The results demonstrate superior oxidation resistance of HiPIMS-deposited coating. This resistance is sufficient to eliminate the need for a protective coating.

The final chapter, Chapter 8, presents a critical summary of the main results, followed by a general discussion and the conclusions of the thesis. Finally, perspectives for improving the HiPIMS VO_2 process and prospective applications are presented to indicate avenues for future laboratory work in this area.

CHAPTER 2 THEORETICAL BACKGROUND, VO_2

2.1 Foreword

VO_2, well known for its thermochromic properties, was introduced by Morin [18] in 1959. These thermochromic properties are due reversible metal to insulator transition, generally noted MIT, associated with a crystalline phase transition from a monoclinic phase to a tetragonal phase. This MIT can be defined by two main parameters, the critical temperature, τ_c and its temperature hysteresis $\Delta\tau_c$. At temperature under τ_c, the VO_2 monoclinic phase is an insulator while the high temperature phase, the VO_2 tetragonal rutile phase, presents metal-like properties. This phase change will produce a change in the band structure and in the infrared optical properties that can be used to control heat transfer.

In this section, we will present the different forms of vanadium oxides, then will discuss the VO_2 structure and its optical and electrical properties. In the following, we will introduce how one can tailor these properties toward specific applications, and we will close the section with an introduction to the deposition methods for VO_2 thin films.

2.2 Vanadium oxides

Vanadium is a transition metal in which the electronic structure offers an incomplete 3d shell. The presence of this half-filled d shell, common to transition metals, will result in a variety of stable oxidation valence, from V^{2+} to V^{5+}. These various oxidation valence states lead to many stoichiometric vanadium oxides, namely VO, V_2O_3, V_2O_4 (VO_2) and V_2O_5. V_2O_5 and the V^{5+} oxidation states are known to be the most stable form for vanadium [22], but other non-stable stoichiometry can be synthesized under specific oxidation conditions.

Single oxidation stoichiometry is hard to obtain; often, a local defect in the structure with a lack of oxygen will occur. In the presence of such oxygen deficiency, a mixture of different oxidation states in the vanadium oxides are obtained. In the case of V^{4+} and V^{3+} ions, oxides with a stoichiometry of V_nO_{2n-1} (V_6O_{11}, V_7O_{13}, V_8O_{15}, etc.) form the Magnéli series. V^{4+} mixed with V^{5+}

forms the $V_{2n}O_{5n-2}$ oxides, named Weysely series [23]. This large number of metastable oxide phases gives rise to a complex phase diagram, presented in Figure 2-1. One can observe a solid solution of V and O until 56% of O added. At 56% a mix of V_2O_3 and solution forms. Above 60%, only V oxides are obtained in various mixtures.

In our case, we want to deposit specifically VO_2, the oxygen range is relatively small, underlining the importance of a precise control of the process to obtain a desirable stoichiometric phase. The thermodynamically stable temperature to form the VO_2 phase, 1542ºC, is not attainable in conventional thin film deposition systems. VO_2 is also not chemically stable at room temperature, and degrades over time via incremental oxidation toward V_2O_5. These issues will be addressed later in this document.

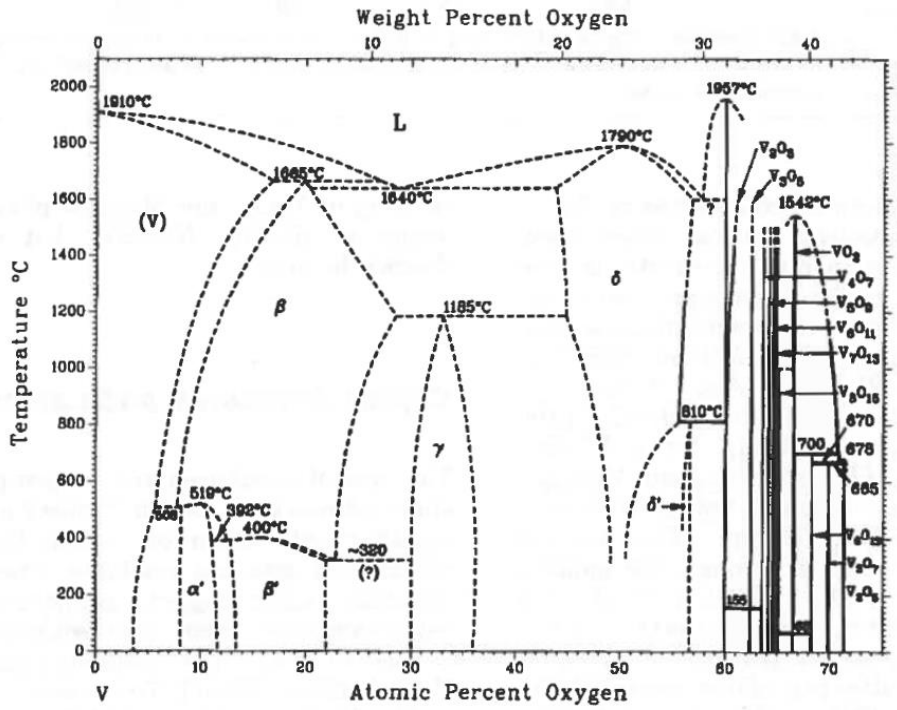

Figure 2-1 The O-V phase diagram (reproduced from [19] with permission of Springer).

Most of the stoichiometric vanadium oxide phases are thermochromic, and the bulk τ_c for a few of them are shown in Table 2-1 One can observe that only VO_2 offers a critical transition temperature close to room temperature. For applications in smart windows or smart radiation device, SRD, VO_2

is then the material of choice. Whereas other vanadium oxide phases are not of interest to us, their MITs are currently investigated to control the ferromagnetism of Ni [24], [25]. In the rest of this section, we will focus on the VO_2 phases only.

Table 2-1 Known critical transition temperature and formation enthalpy of vanadium oxides.

Material	V_6O_{13}	V_2O_3	VO_2	V_2O_5
τ_C °C [5]	-123	-104	68	257
ΔH, KJ.mol^{-1} [26]		-1219	-717	-1550

In Figure 2-2 we present the two different crystalline structures of interest in this work, the VO_2 M1 phase. On the left, the low temperature phase presents a monoclinic lattice with a $P2_1/c$ group, while on the right, the high temperature tetragonal structure presents a rutile $P4_2/mmm$ structure. While not trivial, a direct translation of the monoclinic cell onto the tetragonal cell is possible with the monoclinic cell including 2 tetragonal cells along its c rutile axes [27].

Table 2-2 Cell parameters of monoclinic and tetragonal VO_2 phases.

	Monoclinic M1-VO_2 [28]	Tetragonal R-VO_2 [29]
a	5.743 Å	4.5546 Å
b	4.517 Å	4.5546 Å
c	5.375 Å	2.8514 Å
β	122.1°	90°

VO_2 presents other polymorphic phases, namely VO_2 (A), VO_2 (B), VO_2 (M2), VO_2 (BCC) VO_2 (D) and VO_2 (N) [27], [30], [31]. Most of those polymorphs are obtained through liquid reaction synthesis and thus contain contaminant atoms and molecules. This leads to a loss of symmetry in the low temperature cell, and then an inhibition of the in-plane displacement of the vanadium ions [27]. Thus, such systems do not have thermochromic properties.

In the rest of the document, the two crystal phases will be denoted M1-VO_2 and R-VO_2, for the low and high temperature forms of the thermochromic VO_2.

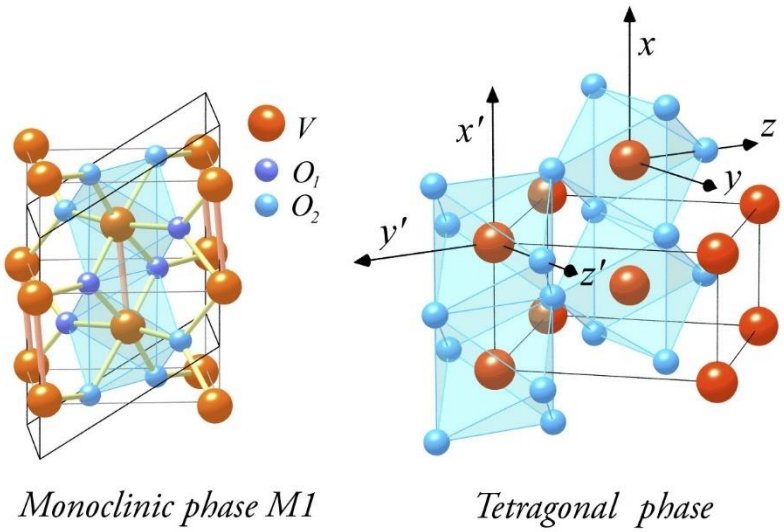

Figure 2-2 Structure diagram of thermochromic VO_2 crystal cells. The left panel shows the low temperature insulator monoclinic cell while the right panel shows the high temperature conductive tetragonal cell (adapted from [27]).

2.3 VO_2 phase transition

To consider the phase transition mechanism, a profound insight into the VO_2 band structure in its low and high temperature phases is needed. The band structure of VO_2 was first proposed by Goodenough [32] and is reported in Figure 2-3. Based on the crystalline geometry of each cell, he derived the degeneracy of the V 3d band. In the case of the tetragonal cell, the V^{4+} ions are positioned in octahedral sites, with a general cubic symmetry in a and b axis, and an orthorhombic symmetry along its c axis. The cubic symmetry presents two degenerate electron energy states in a and b orientation, while the orthorhombic component along the c axis is not degenerated. Three bands are then created, a high-energy σ band (not shown), and two symmetric bands that overlap the band gap, $3d_{\pi}$ and $3d_{\|}$.

When the phase transition occurs, two aspects of the band structure are modified: the position of the $3d_{\pi}$ band and a splitting of the $3d_{\|}$ bands. Both are due to the displacement of V^{4+} cation that

shortens the V-O bond, thus raising the position of the $3d_{\pi}$ band relatively to the Fermi energy. As the displacement is antiparallel, a transitional symmetry along the c axis is created, and it splits the $3d_{||}$ band and destabilizes the π band. Thus, all electrons are transferred to the lowest energy $3d_{||}$ band and the material becomes a semiconductor. It is to note that due to the oxide form of the structure, three optical gaps are observed in VO_2. An intra-band gap of 1.1 eV between both parallel bands and a 0.65 eV inter-band gap between the lowest parallel band and the π band in the low temperature state, while a 2.5 eV band gap is still present in the metallic phase.

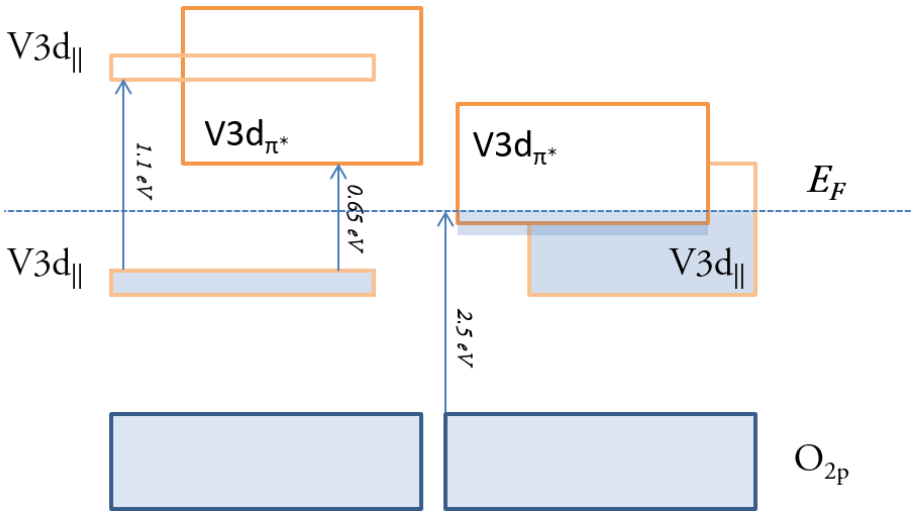

Figure 2-3 Illustration of the VO_2 band structure. The left portion presents the low temperature monoclinic insulator state, with a split $V3d_{||}$ that creates an indirect band gap of 0.65 eV, and a direct band gap of 0.65 eV; the right portion presents the tetragonal conductive state, where the non-degenerate $V3d_{||}$ band overlaps the $V3d_{\pi^*}$ band to form a metal-like conductive state (adapted from [17]).

The crystallographic change is linked to a change of the electronic function in the form of a metal-to-insulator phase transition (MIT), as introduced for VO_2 by Mott in 1979 [33]. Theories of the MIT transition and their developments into understanding of the VO_2 phase change are not within the scope of this thesis but the concepts will be introduced in the next paragraphs.

Research on the MIT phase change is a broad domain that includes different driving mechanisms for the phase change, like pressure, temperature or electromagnetic fields.

While there are various excitation mechanisms that can produce a phase transition, MIT materials are classified into two groups; structural or electronic. For the structural MIT materials, change of the lattice under external stimuli will lead to a splitting of the electronic conduction band and therefore to the insulator phase. In the electronic category, no changes to the lattice or no lattice at all is needed.

The first model of the MIT mechanism was that of Mott, considering a perfect lattice with one free electron per atom and a pure Coulomb interaction. In such a case, screening of the ionic core can be obtained for a small enough inter-atom spacing that leads to a metallic state, expressed by the Mott criterion:

$$(N_c)^{1/3} \times \alpha_H > C \qquad eq\ 2.1$$

where N_c is the charge density, α_H is the atom Bohr radius and C is a constant. One can approach the VO_2 phase transition with this criterion, as movement of V atoms diminishes the inter-proton distance, but it does not explain the phase change mechanism.

Based on earlier studies [34]–[37], VO_2 can be considered a Mott-Hubbard insulator as proposed by Pouget *et al.*, or as a strongly correlated electron material. To confirm, nuclear magnetic resonance spectroscopy was used to estimate the population of different VO_2 electron bands as a function of temperature and stress. However, they did not explain the electron transfer from one band to the other as the material is subject to the MIT transformation.

There is still a debate on whether the transition is structural- or electronic-driven. The transition is initiated either by strain, temperature, electron injection or photon absorption, and all those points of view have impacted the focus over multiple VO_2 applications. Depending on the excitation mechanism and the associated characterization techniques used, different conclusions can be drawn:

- Pressure-driven observations conclude that the transition is purely structural [38], others found that a strong strain leads to an electronic-driven transition [39].
- Observing time-resolved dynamics of the electrons and the crystalline cell, Miller [40], later Siwick [41], proposed that a photon-driven transition generates an electronic driving force. This force induces dynamic structural change in the material.
- Electron injection at low electric fields suggests a pure electron-coupled transition [42].

- Numerical modelling, by first-principle calculations proposed that the transition is both a correlate electron Mott transition and a structural Pierels transition [43].

With those diverse points on the MIT mechanism presented, we will now focus on the macroscopic scale for energy-control and energy-saving applications.

The important change of the VO_2 electronic band structure can be inferred from changes in the optoelectronic properties at the macroscopic scale. As a matter of fact, the insertion of electrons into the conduction band will drastically change how the material interacts with light and how it conducts electronically.

In the case of the optical properties, the appearance of free electrons in the material is indicated by an increase of the infrared absorptions as can be seen in Figure 2-4 by Fortier *et al.* [44]. One can observe that most of the change in the thermochromic VO_2 optical properties occurs in the near-infrared region (780-2500 nm), while a small change of the refractive index occurs in the visible.

The main features of the optical properties noted in Figure 2-4 are two local extrema in the visible: a maximum of the refractive index around 430 nm at low temperature, and at 1000 nm at high temperature, as reported by Mlyuka [45] and Kakichida [46], [47]. While all references observed the same position for those features, there is a spread in the values of the extrema. For example, Fortier's values were 3.0/1.5, whereas Kakichida reported 3.6/1.5, and Mlyuka gave 2.8/1.8. All those samples were prepared by magnetron sputtering, but obviously not on the same substrates and apparatus; therefore, this shows a dependence of thermochromic VO_2 deposition upon experimental parameters.

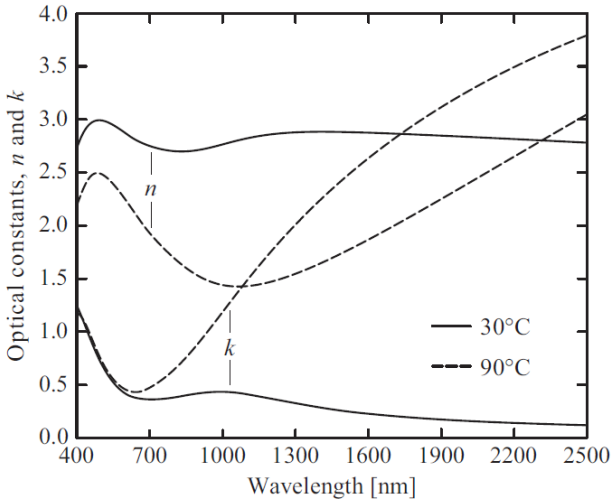

Figure 2-4 Optical parameters n and k at low and high temperature states of thermochromic VO_2 (reproduced from [44] with permission from Elsevier).

The MIT impact on the optical properties (*n* and *k)* mirrors the transformation of electronic properties, while its effect on the device application is far from trivial. The increase of n and k in the near-infrared region produces a combination of absorption and reflection, while the small decrease of n has a small impact on the visible transmission. In Figure 2-5, the spectral transmission for a typical thermochromic VO_2 layer and the solar spectrum at sea-level are presented. The film thickness was chosen so as to maximize the solar infrared change at 2500 nm with a minimal change in the visible solar spectrum. One should be reminded that such design will not only control the energy intakes from the solar irradiation, but also the radiative flux emitted by the local environment in the 10–100 μm range. In the visible, thermochromic VO_2 displays a broad absorption with a band-edge around 435 nm, transmission being maximum close to 715 nm, resulting in an undesirable greenish tint.

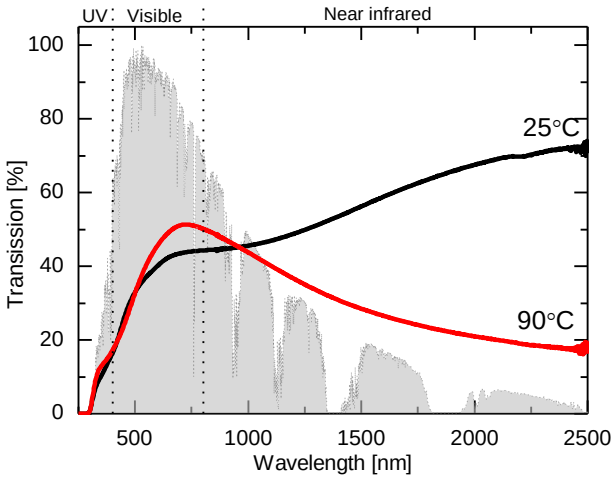

Figure 2-5 Variation of the transmission spectra for a VO_2 thin film at low and high temperature phases. The grey shade represents the solar irradiance as defined by the ASTM G173-03 [48].

2.4 VO_2 coating index of performances

In the previous section, we introduced VO_2, its metal-to-insulator transition and the effect on macroscopic optoelectronic properties. Now, we introduce the different performance metrics used to describe thermochromic devices, followed by the effect of thin film structure on the thermochromic performance. Then, we present film modification that can be used to tailor thermochromic VO_2 layers toward specific applications.

To better describe and compare the performance of optical devices and energy control systems, quantitative values are needed. Calculations are made on the basis of optical properties, considering the emitter, the solar spectrum, and the detector sensitivity to create indices that have values between 0 and 1. Below, we report three: solar luminous transmittance, T_{lum}, solar transmittance T_{solar}, and emissivity ϵ_t.

T_{lum} describes the amount of visible light transmitted through a device from its optical spectral transmission, $T(\lambda)$, which is weighted with the eye's sensitivity, η_{lum} defined as the spectral luminous efficiency for photopic vision [49], and integrated over the solar irradiance at sea-level, φ_{solar} as defined in the ASTM G173-03 [48]. This is expressed as:

$$T_{lum} = \frac{\int_{350}^{750} T(\lambda) \times \eta_{lum}(\lambda) \times \phi_{solar}(\lambda) d\lambda}{\int_{350}^{750} \eta_{lum}(\lambda) \times \phi_{solar}(\lambda) d\lambda} \qquad eq\ 2.2$$

T_{solar} expresses the fraction of solar radiation that passes through a device. The solar irradiance at sea-level is in this case solely used to weight $T(\lambda)$ over a broad spectral range from 250 to 2500 nm. This is derived from:

$$T_{solar} = \frac{\int_{250}^{2500} T(\lambda) \times \phi_{solar}(\lambda) d\lambda}{\int_{250}^{2500} \phi_{solar}(\lambda) d\lambda} \qquad eq\ 2.3$$

If we multiply T_{solar} by the total solar irradiance defined as 0.87 kW/m^2, the device's radiative heat transmittance is obtained. This is one of the main metrics used by the glazing industry.

For the visible to near-infrared performance, SRD applications, the equivalent emissivity ϵ_t can be calculated weighting the measured spectral emissivity $\epsilon(\lambda)$ with the black body emissive power at the temperature T, $P(\lambda,T)$ (W.m^{-2}). It can be calculated by:

$$\varepsilon_t = \frac{\int_{\lambda_1}^{\lambda_2} \varepsilon(\lambda) \times P(\lambda, T) d\lambda}{\int_{\lambda_1}^{\lambda_2} P(\lambda, T) d\lambda} \qquad eq\ 2.4$$

As we use an active material, such metrics will change with the phase transition. Active effect is then calculated by subtracting high- from low-temperature values. These are denoted ΔT_{lum}, ΔT_{solar}, and $\Delta\epsilon$. In smart window applications, one wants to maximize ΔT_{solar} and T_{lum} while minimizing ΔT_{lum} to have the maximum control over the radiative energy transmitted through the glazing and a sufficiently high luminosity inside the building. As single VO_2 layers do not excel in terms of ΔT_{solar}, the variation of transmission at 2500 nm, $\Delta T_{2500\ nm}$, is often used instead.

2.5 Polycrystalline VO_2

Before presenting how we can control the VO_2 MIT properties, a small introduction on the polycrystalline nature of VO_2 thin film will be given. This theory was mainly developed by the group of Klimov [50]–[52]. They tried to develop a mathematical model linking the shape of the thermochromic phase transition, critical temperature τ_c, and temperature hysteresis $\Delta\tau_c$, to the grain size and property distributions.

When synthesizing a given material, single-crystal growth is an exception due to a high cost and a low growth rate of such a manufacturing process. Crystalline materials are therefore mainly polycrystalline, defined by the crystallites (also called grains) separated by grain boundaries. Depending upon growth conditions, crystallites can present different orientations, sizes, and a non-uniform impurity content or stoichiometry.

In the case of polycrystalline thermochromic VO_2, the distribution of grain size and local stoichiometry strongly affect the MIT phase transition. Each grain will present a local transition temperature τ_c defined by its oxygen deficiency (deviation from the VO_2 exact stoichiometry).

The phase transformation induces a change in the lattice volume, which is limited by the grain boundaries in polycrystalline films. Therefore, the transition temperature increases to overcome the additional energy barrier, noted $\Delta\tau_c^+$. The same effect occurs in cooling, the cooling change to the transition temperature to the M1-VO_2 phase being $\Delta\tau_c^-$. The hysteresis is $\Delta\tau_c = \Delta\tau_c^+ - \Delta\tau_c^-$ for each grain. When the grain-size increases, the fraction of the grain boundaries decreases, as well as $\Delta\tau_c^+$, $\Delta\tau_c^-$, and $\Delta\tau_c$.

In the case of perfectly identically sized stoichiometric grains, τ_c would be equal to the bulk critical temperature, 68 °C with a $\Delta\tau_c$ function of grain size. However, in the case of polycrystalline thin films, the grains present a distribution of their size and local stoichiometry. Therefore, to obtain the macroscale thermochromic properties, integration over the distribution of size and local composition is needed.

2.6 Process functionalization of VO_2

This section presents how the deposition parameters can provide control or constraints over the VO_2 thermochromic properties.

The first process step of the film growth occurs on the substrate. In the case of a crystalline substrate with similar structure as high temperature VO_2, a local epitaxy occurs. Epitaxy-like growth promotes larger grains and affects the thermodynamic equilibrium of the MIT phase transition. The most used substrate is rutile TiO_2 (001) and (110) [53], [54], and (0001) hexagonal Al_2O_3 [55]–[57], $SrTiO_3$[58] or $LaAlO_3$ [59].

In the case of TiO_2, a strong dependence of the phase transition on the orientation of TiO_2 is observed. The (001) plane offers an epitaxial growth with the VO_2 tetragonal c axis perpendicular

to the surface. It constrains the monoclinic VO_2 structure in a closer arrangement to the rutile phase of the substrate, a = 4.58 Å compared to the 4.55 Å of R-VO_2 (JCPDS No 88–1175). This strain on the low temperature cell lowers the disorder of the material and stabilizes the R-VO_2 phase, thus lowering the transition temperature and phase transition hysteresis, as shown in Figure 2-6. On the other hand, a film grown with its c axis parallel to the (110) surface orientation has the structural M1-VO_2 cell stretched by the 2.94 Å atom spacing of this plane. The large mismatch widens the transition hysteresis and increases the transition temperature because the grains are strongly elongated [34].

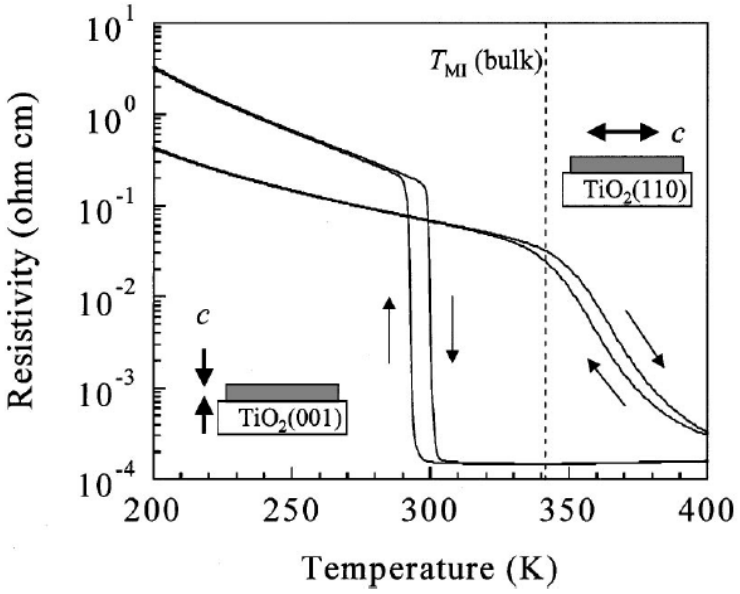

Figure 2-6 Effect of the underlying TiO_2 crystal film orientation on the VO_2 phase transition in resistivity (reproduced from [53] with the permission of AIP Publishing).

Sapphire (Al_2O_3) or sapphire-like substrates ($LaAlO_3$, $SrTiO_3$, etc.) can withstand a high deposition temperature, are widely available, and present a hexagonal structure. They are preferred substrates for depositing high quality VO_2 in a pulsed laser deposition system (PLD), presented latter-on. The (001) M1-VO_2 crystallographic planes overlap the (0001) hexagonal ones, with a M1-VO_2 cell containing 4 (0001) units, as shown in Figure 2-7. The deposited VO_2 is strongly textured in the (020) direction with a minimal deformation of the crystal structure c-axes compared to TiO_2. Also,

epitaxial growth on a hexagonal surface locates a V atom on the top of each Al site, without constraining lateral movement during the phase transition.

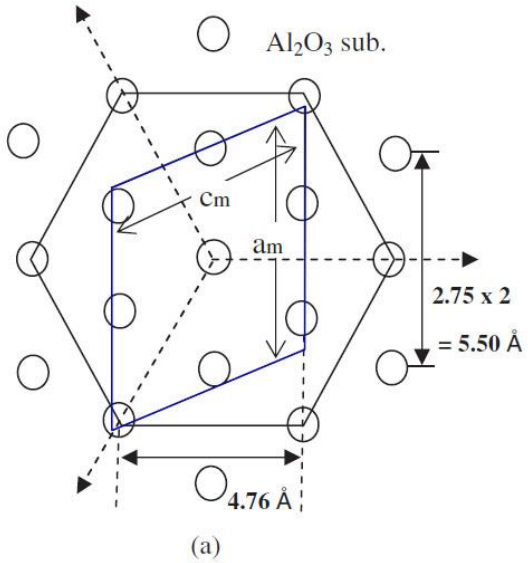

Figure 2-7 Schematics of the 0001 plane of the Al_2O_3 hexagonal crystal structure (open circle) and the thermochromic VO_2 M1 monoclinic 010 cell (Blue). cm and am are the VO_2 crystallographic structure cell as shown in Table 2-2 (adapted from [56]).

We just showed that an adequate crystalline surface underneath the VO_2 films improve the material crystallinity and its MIT properties. Deposition temperature is a critical process parameter. Depending on the deposition method chosen, a temperature threshold is observed to obtain a thermochromic crystalline VO_2. For PLD, the threshold temperature is around 400 ºC [60], and is reported between 450 ºC [61] to 550 º C [62] for film recrystallization. In the case of the magnetron sputtering, additional energy is provided by ions bombardment, so that deposition temperature can be lowered to 300 ºC as in the case with HiPIMS [44], [63], [64] or RF bias assisted RFMS [65]. Figure 2-8 presents the effect of temperature on the MIT transition as a function of substrate temperature for PLD deposited VO_2 film (a) and magnetron sputtering and HiPIMS VO_2 films deposited on glass with no seed layer (b).

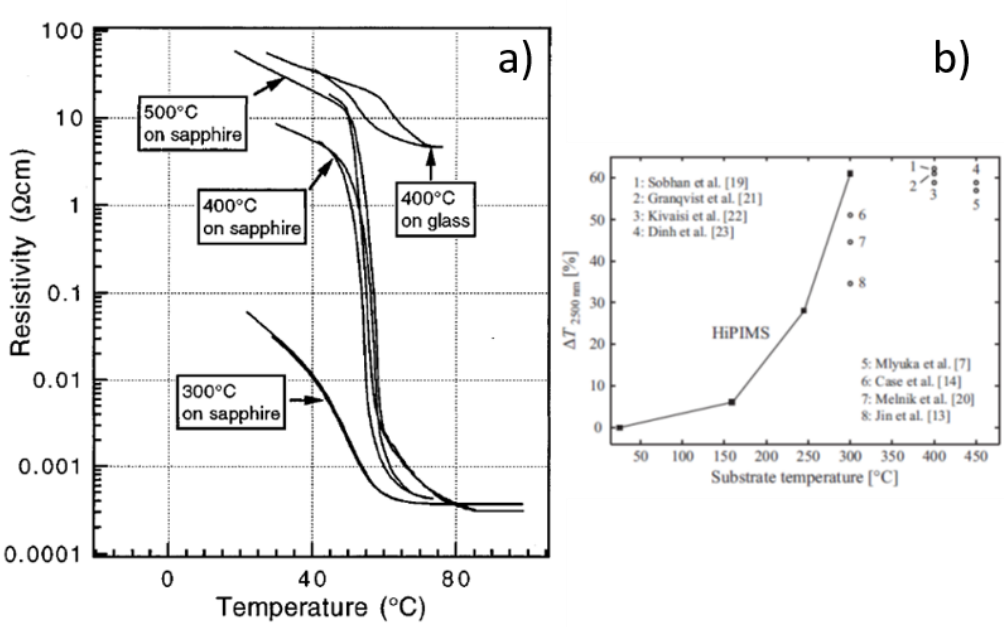

Figure 2-8 Effect of substrate temperature on the performance of VO_2 thins film deposited on a crystalline Al_2O_3 substrate (a) (adapted from [60], copyright 1997 American Vacuum Society), and glass substrate (b) (adapted from [44] with permission from Elsevier).

To change the transition temperature τ_c, a change of the V-O bond strength is needed. This can be obtained through the substitution of V by an atom with a larger nucleus, or substitution of O with a lower mass atom. The preferred substitution atom for V is W. It is reported to lower the transition temperature by 9 °C to 36 °C/at %W added. As with the transition mechanism, two divergent explanations are provided: 1) W acts as an electron donor in the Mott transition like MIT; 2) the stress induced in the crystal cell lowers the energy needed for the structural transition [66].

The transition of W-doped VO_2 films deposited by PLD is given in Figure 2-9.a for the resistivity of doped films, and in Figure 2-9.b for the transmittance. One can see that, in addition to lowering of the critical transition temperature, doping also decreases the transition strength and broadens the hysteresis.

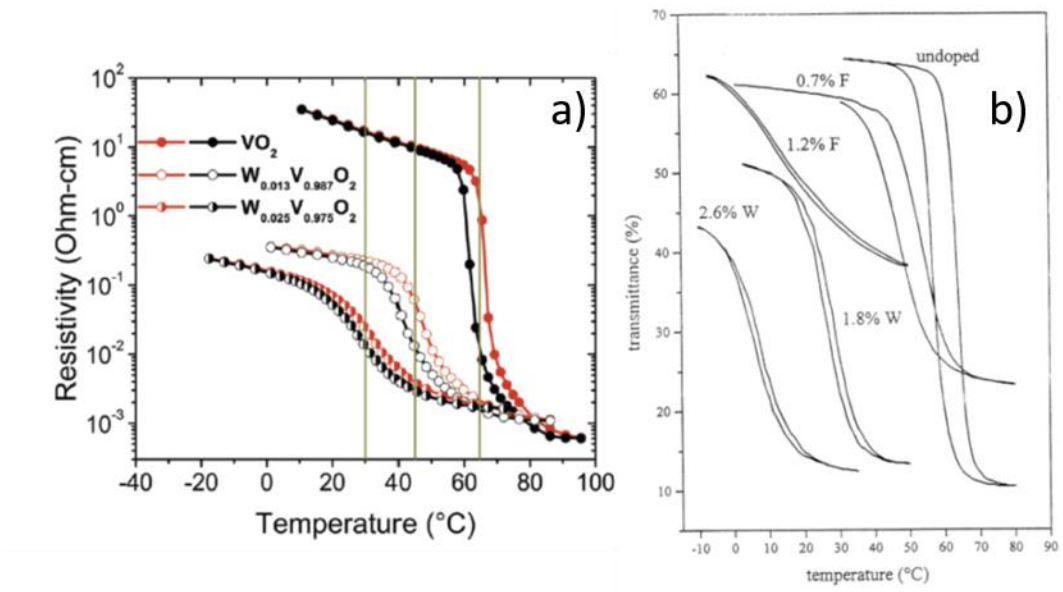

Figure 2-9 Effect of doping on the phase transition of VO_2 thin films in the case of W-doping on the resistivity (a) (adapted from [59] with the permission of AIP Publishing), or co-doping W and F on $\Delta T_{2500\,nm}$ (b) (adapted from [67] with permission from Elsevier).

Further transition metal atoms have been used to substitute the V ions, such as Mo (-10 °C/at % [68]), Re (-10 °C/at % [69]) or Nb [69]. Addition of an anion with an oxidation level limited to +3 such as Al only degrades the properties of the VO_2 [70].

A more electronegative anion in substitution to oxygen, namely fluorine, gives rise to a reduction of τ_c by 15.7 °C/at % [71], or co-doped with W, -20 °C/at % [67], [72]. Additionally, F doping changes the semiconductor states with an increase of the absorption band-gap and a decrease of the visible absorption. This modification of the VO_2 band edge has been reported of up to 35 nm at 2.5%at. fluorine inserted [72].

2.7 Functionalization of VO_2 devices

In the previous section, we introduced various ways to optimize the VO_2 layer MIT via material engineering. When designing multi-layer devices, additional effects such as interference and interface engineering can leverage the performance of the VO_2 thermochromic layer. A more general introduction on interface engineering and interference filters can be found in M. Ohring and A. MacLeod handbooks, respectively [73], [74].

Interface engineering can tailor the crystalline structure of the VO_2 on low-cost substrates such as borosilicate or float glasses. Addition of a seed layer such as TiO_2 [36], [39], [53], [75] or ZnO can [76] promote a (001) or (020) texture of the VO_2 film.

In the case of low-cost glass substrate an additional issue arises. Low ionization state glass dopants such as Na or K can diffuse onto the growing VO_2 film. By substituting a V ion in the lattice, the MIT phase transition is inhibited. A barrier coating such as SiN_x [77] or any underlayer used for other purposes presented previously will prevent such diffusion.

Such a barrier coating can also be used to protect VO_2 against subsequent oxidation in subsequent process steps, or degradation of the device during its service life. Commonly proposed materials are Al_2O_3 [78], [79], CeO_2 [80] or ZnO:Al [80], but any top coating presenting a protection against water and oxygen diffusion could offer such protection.

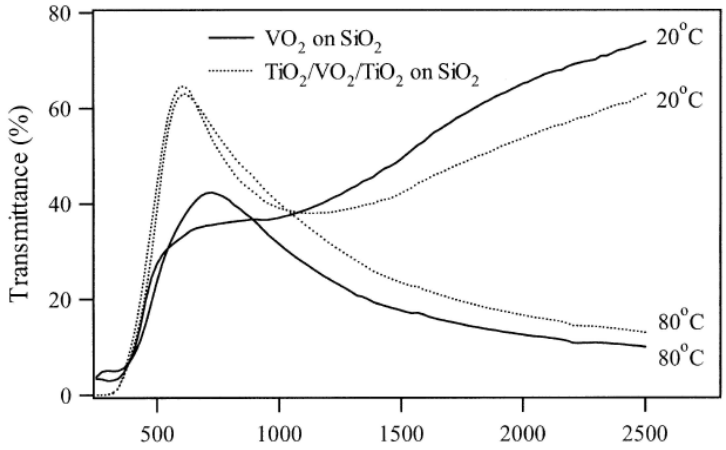

Figure 2-10 Spectral transmission of a VO_2 film sandwiched between two TiO_2 layers on SiO_2, with an increased visible transmittance over a similar single layer of VO_2 deposited on the same substrate (adapted from [81] with permission of Springer).

While interface engineering can promote better crystallinity and protect against diffusion and over-oxidation of the layer, such films can also be effectively used to improve the optical performance of the coatings by an anti-reflective effect [82].

For example, TiO_2 is an excellent candidate for an interference layer. With an optical index of 2.1 to 2.4 at 550 nm [83], lower than the VO_2 index of 2.8-3.1 at 550 nm [44]–[47], it can act as the low index of a three-layer interference filter [82]. Therefore, it reduces reflection at the interfaces and improves T_{lum} [45], [81], [84], [85]. It also enhances contrast between the low and high temperature states in infrared application [30,40,77]. Such effects are illustrated in Figure 2-10 by a three-layer structure $TiO_2/VO_2/TiO_2$ that increases the maximum visible transmission from 40% to 60%, a relative gain of more than 50%.

The addition of a low emissivity layer, such as ITO [86] or a conventional Ag low-e [87] can also be used to improve the performance in the near-infrared spectrum. It can provide performance improvement in smart window applications, with T_{Lum} and ΔT_{Solar} ,60% and 6%, respectively.

For applications in the mid-infrared to far-infrared, specifically in the 3 to 1000 µm range, VO_2 offers an interesting variable emissivity. At low temperature, it exhibits low absorbance and reflection, while the high temperature phase reflects infrared light like a poor metal. These effects can be used to protect detectors against strong irradiation [88], [89] or to control satellite temperature [90]–[92]. In the case of smart radiators, the medium emissivity of thermochromic VO_2 material (ε= 0.34-0.41 [93]) is used in contrast with a metallic reflector (typical ε <0.10). In such way, at low temperature the total emissivity is low as the metal presents high reflectance and VO_2 is transparent for the radiation. At higher temperature, as the thermochromic material is subject to its transition, its absorption increases and masks the under layers; therefore, the device emissivity will be the one of the top VO_2 layer, higher than that of a metal reflector.

Spectral emissivity variation of such a device, modelled after [94], is presented in Figure 2-11. One can observe a strong absorption peak close to 10 µm due to the use of SiO_2 as the interference layer. Compared to a single VO_2 layer, the addition of SiO_2 increases emissivity variation from

0.22 to 0.53. Experimental devices of such configuration were reported with Δε of 0.49 for a SiO_2 interlayer [94], or up to 0.55 in the case of a HfO_2 interlayer [95].

In this specific application, perovskite based materials are also widely investigated. The most promising candidate is $LaMnO_3$ doped with either Sr and Ca that is reported to exhibit $\Delta\varepsilon$ of up to 0.40 [96].

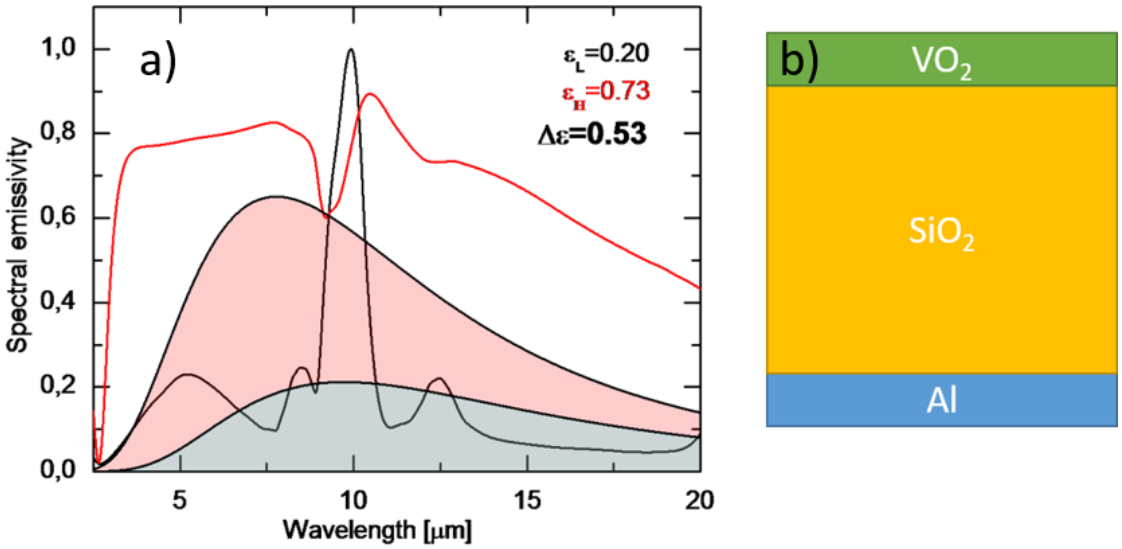

Figure 2-11 Spectral emissivity of an optimized $VO_2/SiO_2/Al$ thermochromic stack at low (black) and high temperature (red) (a) and a schematic of the modelled device (b). Calculated using an approach from [97].

VO_2 coatings can also be incorporated in thermal sensors or infrared detectors (bolometers). In this case, calibrated change of VO_2 resistivity is used to derive the energy received by the sensor. Such applications do not need to exhibit a sharp transition; on the contrary, they can benefit from enlarged hysteresis. An example of such devices is shown in Figure 2-12, where three different W-doped VO_2 layers are stacked to obtain a resistivity variation of three orders of magnitude over a 60 °C range.

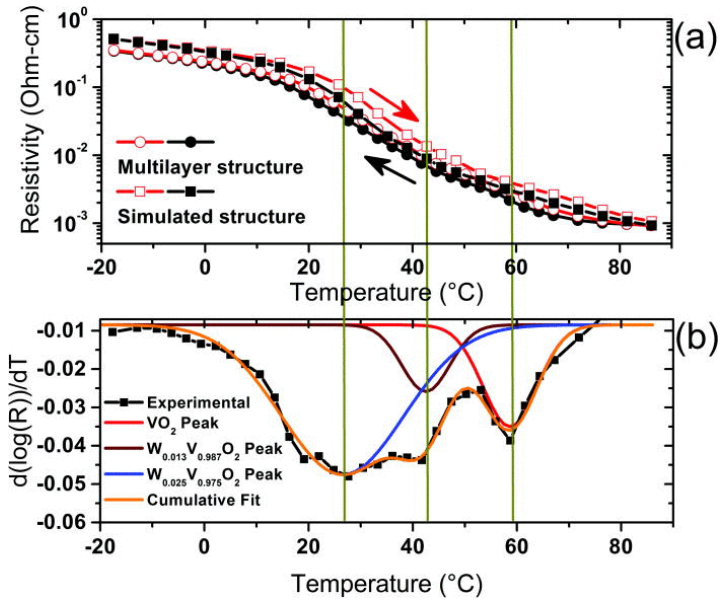

Figure 2-12 (a) Electrical resistivity of multi-stacked W-doped VO_2 layers, heating (open circles) and cooling cycles (closed circles) with a linear model (1) (open squares for heating cycle and closed squares for cooling cycle). (b) Derivative plot of the temperature-dependent resistivity fitted with Gaussian to obtain the individual transition temperature of each layer (reproduced from [59] with the permission of AIP Publishing).

A similar approach has been proposed to increase T_{lum} of VO_2 based devices in the visible. It involves dilution of the active material in a matrix such as TiO_2 [68], [98], [99] or SiO_2 [100], sometimes called nano-thermochomics, or structuring the surface to trap reflected light at the surface [14], similar to the texturing used on Si-based solar cells.

In conclusion of this section, tailoring the metal-insulator-transition of VO_2 devices is clearly a vast domain. While most of the known dopants and inter-layers have been studied, additional performance such as scratch resistance or oxidation control was seldom addressed. Optical and mechanical properties of potential materials for a resistant coating from industrially proven process (PVD and PECVD) are presented in Figure 2-13. Additional work is needed to ensure compatibility with VO_2, and their impact on the device performances.

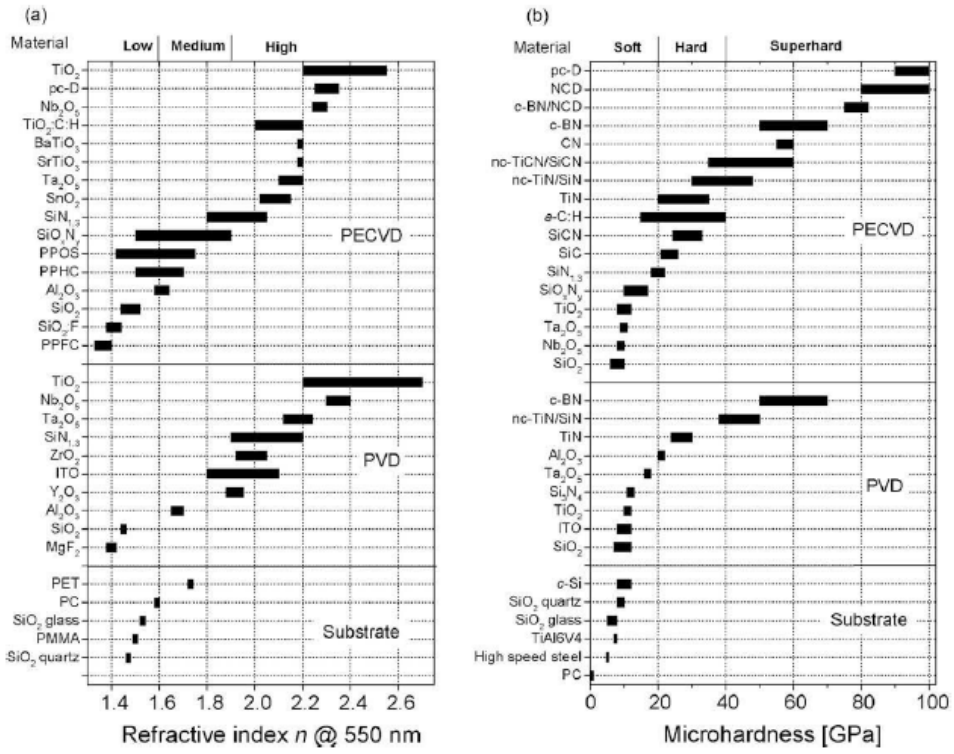

Figure 2-13 Refractive indices (a) and micro-hardness (b) of various functional coatings and substrates (reprinted from [101] with permission from Elsevier).

2.8 VO_2 Film Synthesis

Above, we have presented how one can tailor the VO_2 MIT properties toward applications in smart windows or smart radiation devices. In this section, we will introduce the main processes used to synthesize thermochromic VO_2 films, and we present a quick summary of advantages and disadvantage for each of them.

VO_2 deposition processes can be divided in two families: a) direct synthesis of VO_2 in thermochromic crystalline form, and b) the indirect one that necessitates post-treatment, vacuum annealing, or post-oxidation to transform the deposited film into VO_2. Thus, we will only focus our attention on the four processes that are mainly investigated, namely Pulse Laser Deposition (PLD), Chemical Vapour Deposition (CVD), magnetron sputtering from category (a) and Sol-Gel from category (b).

Introduced in the early 1980s, PLD and reactive PLD (R-PLD) use a short pulse from high energy excimer laser focused onto a metallic target. At sufficient laser fluence, an equilibrium plasma is formed at the interface, named plasma plume. Atoms from the target are vaporized and diffuse toward the substrate holder to condense; schematics of a typical deposition chamber with a short description of the plume dynamics is given in Figure 2-14.

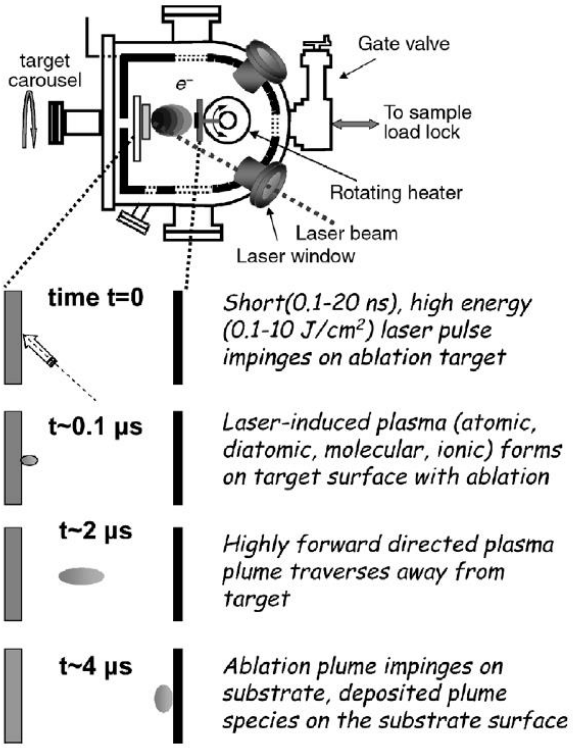

Figure 2-14 Schematic of a PLD chamber, and dynamics of the plasma plume during the PLD process (adapted from [102]).

The deposition rate of the PLD process is directly proportional to the repetition rate of the laser, and a minimal change of the laser plume is observed in reactive deposition. As such this process provides one of the best controls on deposition rate and film composition for small substrates.

On the other hand, no additional energy is provided to the growing film and therefore high substrate temperatures are needed to obtain crystalline materials. Also, the complexity of high-energy laser beam scanning limits large-scale implementation of PLD. An exhaustive review [102], reports

large-scale production of PLD films with thickness uniformity of 7% over 150 mm substrates. This is large-scale for a PLD process, but still laboratory-sized and unsuited for industrial applications toward “smart windows” or SRD.

Nevertheless, this is a reference process for a case study of VO_2 either through doping or substrate effect. The previously presented substrate effect of TiO_2 [53], effect of substrate temperature [60], and transition mechanism [41] were all based on the PLD studies.

The processes offering a higher scaleability and higher deposition rates are based on CVD. In CVD, precursor vapours are fed into a chamber; then either through heating, plasma or a combination of both, energy is provided in order to dissociate the precursors. Once fragmented, the precursors become highly reacting molecular or atomic radicals. Depending on the pressure and on the diffusion rate, radicals react in the gas phase to form powders or at the substrate surface to form a film [103], [104]. This chemical based process allows the use of multiple chambers configurations, examples of which are schematically shown in Figure 2-15. CVD is the only atmospheric pressure process to deposit VO_2 by Atmospheric Pressure Chemical Vapour Deposition (APCVD) [105], [106].

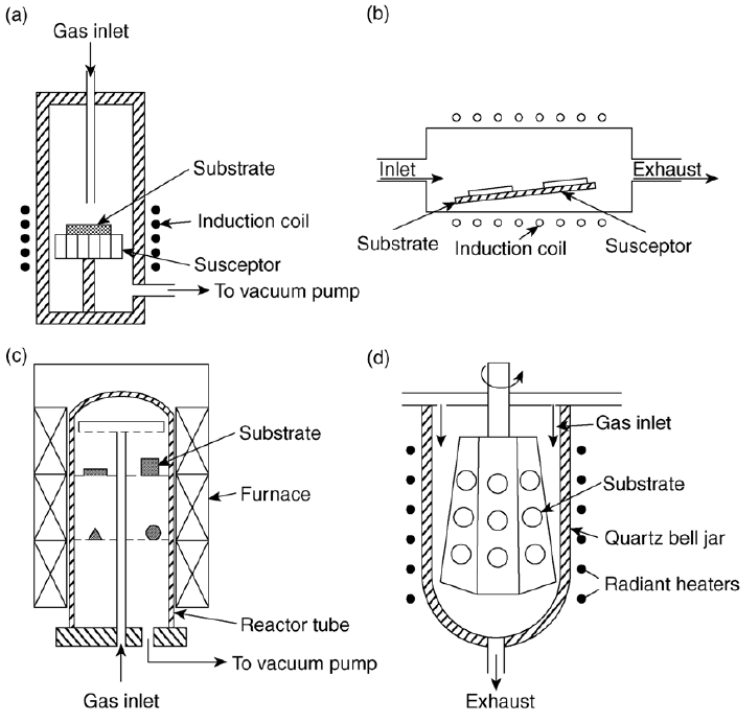

Figure 2-15 Schematic views of typical CVD process chambers. Cold wall reactors (a, b), hot wall reactor (c) and barrel reactor (d) (reprinted from [107] with permission from Elsevier).

Precursors are molecules specifically formulated to be in vapour form and provide easy extraction of the reaction by-product. For metal, two precursor families are available, halides and organometallics. Additional gas such as H_2 or Ar may be incorporated to stabilize the deposition and optimize halogen removal.

Either in thermal-CVD or assisted with additional plasma energy, the commonly used precursors are halides like vanadium oxychloride ($VOCl_3$), vanadium tetrachloride (VCl_4), or organometallics such as vanadyl tri-isopropoxide ($VO(OC_3H_7)_3$), vanadyl tri-isobuxide ($VO(C_4H_9O)_3$) and vanadium acetylacetonate ($V\text{-}C_5H_8O_2$) [108]. Most of them contain additional elements besides V and O such as C, H and Cl. Such elements can remain in the final film, partially degrading its TC performance.

While CVD processes can be classified as direct techniques [109], very frequently additional annealing under neutral atmosphere is needed to reduce the most stable V_2O_5 phase to VO_2 [110].

When using a multi-step process, other less expensive alternatives are currently explored. The most studied low-cost processes are the sol-gel methods. Here, V_2O_5 is put into solution using various processes and stirred until adequate viscosity is obtained. Then the sol is spin-coated onto the substrate, dried to form the gel, and annealed to solidify the film. The annealing step also reduces V to its 4+ oxidation state.

Two main challenges accompanying sol-gel methods are dissolution of V_2O_5 and the annealing steps. V_2O_5 can be efficiently dissolved from powder using three processes. The first one uses an acidic solution of H_2O_2 at 30 volume % at controlled temperature [111]; this reaction is strongly exothermic. The second one uses organic solvents mix, for example, isobutanol and benzyl alcohol at a medium temperature of 110 °C [61], above the flash point of both solvents. Finally, molten V_2O_5 at 800 °C (melting temperature: 690 °C) is poured into water at room temperature and stirred until the solution is homogeneous [112]. The high reactivity of such methods is complex to implement in a strictly regulated academic laboratory, but can be managed at an industrial scale. Another way is to employ vanadium siloxanes, but in this case a high concentration of contaminants will be present in the final film.

The next critical step is annealing. For example, in the previously presented methods of sol preparation, the annealing temperature ranges from 440 °C [61] to 750 °C [111] which hampers the deposition of VO_2 thin films onto polymer substrates or even low melting point glass.

To avoid high-annealing temperature, one can choose to embed already crystalline nanoparticles into a matrix. Such particles can be prepared either by APCVD [105], [106], solution chemistry or other cluster processes [113]. The matrix can then be chosen to offer a much lower solidification temperature, especially if a polymeric matrix is used.

Such a method is proposed by Lu *et al*. [114], who used chemical precipitation to generate nano-sized powders before embedding them in a polysiloxane matrix. The reacting agents for VO_2 powder precipitation were vanadyl sulphate hydrate – $VOSO_4$:H_2O – and ammonium bicarbonate – $(NH_4)\ HCO_3$. Afterwards, the powder was recrystallized at 800 °C in a controlled atmosphere before milling to reduce the particle sizes. The resulting specular spectral transmission at room and high temperature are presented in Figure 2-16. One can observe that an increased fraction of VO_2 particles improves the $\Delta T_{2500\ nm}$. However, the visible transmission is strongly reduced above 4% of VO_2 in the matrix. Nevertheless, the performance is far from optimal with $\Delta T_{2500\ nm} < 30\%$.

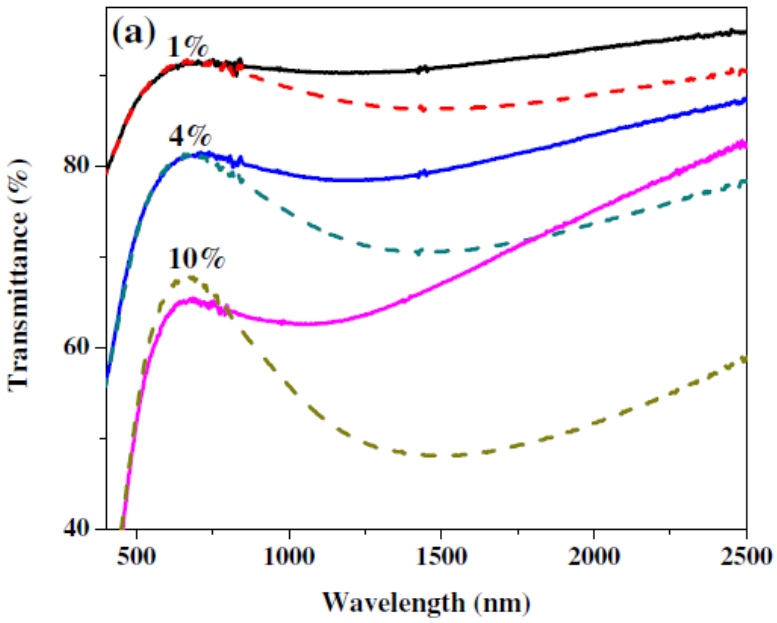

Figure 2-16 Specular spectral transmittance of 80 µm VO_2 doped polysiloxane films at different weight contents of VO_2 (reproduced from [114] with permission from Elsevier).

Chemical processes for VO_2 can provide large area coating, but present traditional issues of wet organic chemistry: the abundant use of solvents, organometallics and halides such as $VOCl_3$. All vanadium precursors present significant toxicity and flammability; therefore, good control of the effluent is needed. It is also to note that reactions using V precursors or even the milling of V containing powders are strongly exothermic, increasing the explosion risk when working with a large batch of materials.

All those concerns may make implementation of chemical processes complicated for the industry in "green" economy. Recently it was rediscovered that annealing in a SO_2 atmosphere at T> 600 °C reduces the V_2O_5 into VO_2 [115]. This reaction is a by-product of catalytic reaction of SO_3 with V_2O_5 to produce sulfuric acid [116], [117].

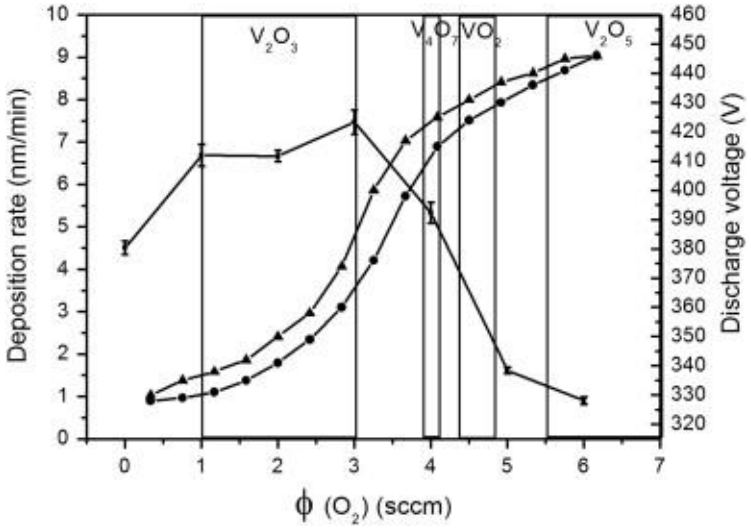

Figure 2-17 Deposition rate, discharge voltage and deposited phases of vanadium oxides by direct current magnetron sputtering at a constant power of 200 W. One can observe a hysteresis in the discharge voltage due to the choice of direct current magnetron sputtering, DCMS (reproduced from [118] with permission from Elsevier)

The processes that demonstrate the best scaleability of thermochromic VO_2 are based on the magnetron sputtering (MS). This is a standard approach to obtain high-value coatings in the glass

and polymer industries, and therefore it is of interest to the thermochromic VO_2 deposition. Next chapter will offer a more complete presentation of MS processes, and their application to deposit VO_2. MS is a plasma-based physical vapour deposition process. Plasma ions are accelerated toward a solid target to volatilize it. The sputtered atoms condense on a substrate in a line of sight manner. In comparison to diode sputtering, MS entraps the plasma within its magnetic field, at the target vicinity, thus increasing the plasma density, sputtering- and deposition rates. Magnetrons exist in different shapes (circular, planar, cylindrical) and sizes depending on the intended applications. Cylindrical magnetrons of up to 4 m length are common for fabrication of low-e coatings on glass.

At the laboratory scale, MS of vanadium oxide has been used since the end of the 1940s [119], and VO_2 since the end of the 70s [120]. Since then, magnetron sputtering has been widely applied to VO_2 depositions; most of the studies previously cited in this chapter used MS. In particular, Kakiuchida worked on the VO_2 optical properties [46], [47], [121], Mlyuka and Granqvist developed “smart windows” [122]. This indicates that MS-VO_2 is relatively mature to move to an industrial scale. However, significant work is still ongoing to overcome the issues of film durability and deposition temperature. Traditionally, sputtered VO_2 needs to be covered to protect against further oxidation [78], [80], and additional ways to increase the energy of the impinging particles in order to decrease the deposition temperature, namely biasing [55], [65], [123], or use of a more energetic method such as HiPIMS [44], [63]. Each of those issues is treated in the following chapters. HiPIMS and biasing are presented in the next chapter and in Chapter 5 and 6. Finally, protection against oxidation is the subject of Chapter 7.

CHAPTER 3 THEORETICAL BACKGROUND, PLASMA AND MAGNETRON SPUTTERING

3.1 Foreword

Magnetron sputtering is a physical vapor vacuum deposition technique that uses ions generated by a plasma to volatilize a target, a metal or a ceramic, in order to deposit a thin film coating on a substrate placed in a line of sight of the sputtering target.

In this chapter, we will first describe what is a plasma and how it generates ions. Then we will present the interaction of the energetic ions on the target surface and eventually on the growing surface. The specificity of the magnetron sputtering and of the HiPIMS process and applications will conclude this chapter.

3.2 General plasma properties

In the case of diode sputtering or MS, the sputtering particles are ions originating from a plasma. In this section, we will present how such ions are created and some of the processes inside the plasma relevant to MS discharge and process chamber design.

As a system energy increases, it induces phase transitions, such as the vaporization from the liquid phase to the gas phase. If the temperature is sufficiently high, a significant fraction of the lesser-bound electrons of gaseous atoms and molecules can be released, creating therefore molecular and atomic positive ions. In such state, electrons and ions – positive or negative – are free to move within the gaseous phase, forming the plasma state. Plasma is sometimes described as the fourth state of matter (after solid, liquid and gas). In laboratory scale plasma, the average temperature of the system is quite low, since only a fraction of the gaseous species is ionized. On the contrary, high temperature plasmas, where nearly all the particles are ionized, are common in nature, such

as the core of the stars or solar flares. This type of plasma is also obtained in modern nuclear fusion reactors.

When observed in a macroscopic scale, the plasma must respect two rules:

1. The plasma presents a collective behaviour; In effect, the charged particles interact among themselves by collisions but also by means of a long-range electric field and often by magnetic field self-generated by the moving charged particles.
2. The plasma is on average neutral; the overall density of electrons and negative ions balance the density of positive ions. In a microscopic scale, electric non-equilibrium can happen but the collective behaviour will limit such non-uniformity.

For a simple illustration of those two basic concepts of the plasma, we can hypothesize that locally in an infinite plasma non-uniformity appears such as an electron deficit. This results in a local positive charge which generates a long-range electrostatic force. Such force attracts the negative-charged particles, increasing the negative particle flux toward the disturbed region and recovering charge neutrality. At electrical neutrality, the charge gradient and the Coulomb force will vanish. This shows the collective behaviour of the charged particle toward plasma neutrality, called the quasi-neutrality.

While the plasma is neutral on the macroscopic scale, it is known that on the small scale a charge non-equilibrium can be observed in the plasma. The scale of such length is called the Debye length, λ_D, and can be expressed by the following equation:

$$\lambda_D = \sqrt{\frac{\varepsilon_0 k_B T_e}{e^2 n_e}} \qquad eq\ 3.1$$

where k_B being the Boltzmann constant, ε_0 the vacuum permittivity, e the electron charge, n_e the electron density and T_e the plasma density. This equation assumes that the electrons are the most energetic particles of the plasma, the case in all low-temperature low-pressure plasmas.

In most cases, the laboratory plasma, used for example for etching, surface modification, and thin film synthesis, works at low pressure: in the range of 2 to 300 mTorr (0.25-40 Pa). An external electric field provides energy to the system by accelerating the charged particles: electron and ions. but the low pressure and mass difference limits the loss of energy by collision between the electron and the heavier gas particles. On the contrary, ions easily lose energy colliding with the neutral gas

and thermalize their energy. This can lead to the fact that the different particles of the plasma have a different average energy. This average energy, named the particle temperature is therefore vastly larger for the electrons, with T_e in the range of 1-3 eV (10-30 thousand K) while the neutral and ion energy is close to room temperature, $T_i \approx T_0 \approx 0.025$ eV (290 K). Such plasma is called *non-thermal plasma*. For the rest of this thesis, plasma will be assumed to be *non-thermal*.

We just discuss the properties of the bulk plasma. But in a laboratory plasma, always interacts with it surrounding creating a boundary zone. Figure 3-1 depicts the low-pressure glow discharge with its quasi-neutral bulk plasma and the plasma wall interfaces, called the plasma sheath.

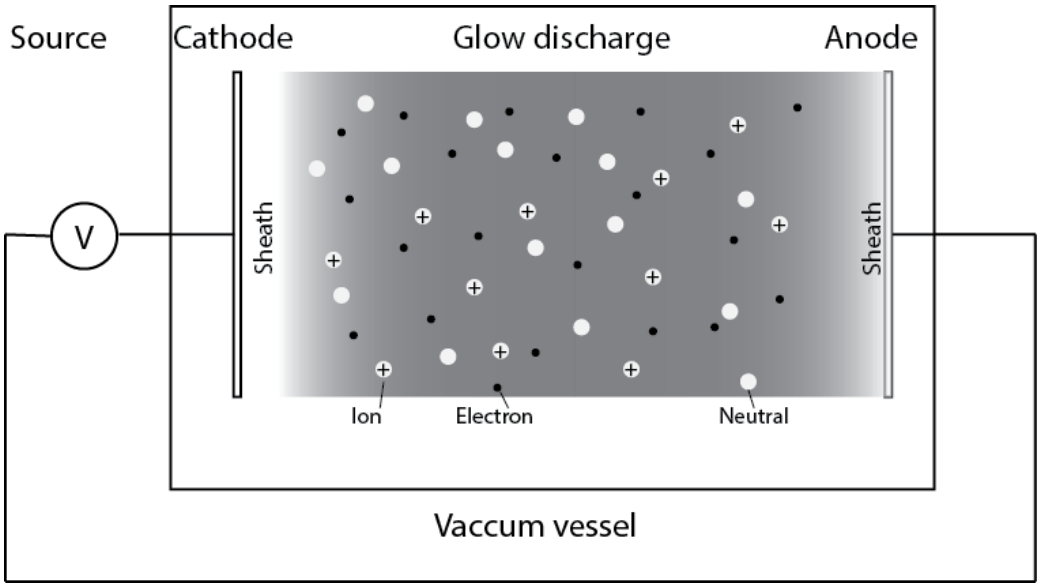

Figure 3-1 Schematics of a vacuum glow discharge with the electrons, ions and neutrals in the quasi-neutral bulk plasma.

The sheaths are areas of space charge due to the dynamics of the particles. If we look at the velocities of the charged particles, the thermal velocity of the electrons, v_e is of significantly larger magnitude than the one of the low temperature ions, v_i. This is due to two factors: first the large dissimilarity in thermal energy, i.e. $k_B T_e >> k_B T_i$ and the 3–4 orders of magnitude difference in mass with $m_i >> m_e$. Since those velocities are calculated with the following equations:

$$v_e = \sqrt{\frac{k_B T_e}{m_e}}, \qquad eq\ 3.2$$

and

$$v_i = \sqrt{\frac{k_B T_i}{m_i}}\ . \qquad eq\ 3.3$$

At the plasma edge the electrons leave the plasma at a higher rate due to their higher speed. When the surrounding surface is an insulator or cannot dissipate the charges to the ground, it will quickly gain a negative charge. This accumulation of charge creates a potential that repels negative charges and attracts positive ions. An equilibrium potential between the surface and the plasma is obtained when there is no net charge traversing the sheath, the positive ion flux equilibrating the negative flux. Such potential of an isolated surface immersed into a plasma is called the floating potential.

If a surface is not isolated, charge can dissipate by flowing into the external circuit, such as the case of the electrodes or grounded chamber walls. A potential gradient is formed between the plasma and the fixed-potential surface. As with the floating potential, in order to limit the electron current flux, the surface potential needs to be lower than the one of the plasma. Therefore, the plasma potential is slightly positive (5 to 15 V [124], [125]) and the floating potential is usually a few volts lower.

In low pressure plasma, one of the electrodes (cathode) is placed at a negative voltage to provide energy to the electrons. The driving potential of the cathode is in the range of a few hundred to thousands of volts, one can assume that the potential drop across the cathode sheath is equal to the cathode voltage (i.e. we can neglect the few volts of the plasma potential). With such large negative potential, the electrons are nearly totally depleted from the plasma sheath and the current through the sheath is dominated by the ions. Such a sheath is called the Child-Langmuir sheath and need to respect two rules: the ion energy conservation and flux energy conservation law:

$$J_0 = e n_i(x) v_i(x), and \qquad eq\ 3.4$$

$$\frac{1}{2} m_i v_i^2(x) = -e\mathrm{V(x)} \qquad eq\ 3.5$$

where e is the electron charge, n_i, v_i and m_i are the density, velocity and mass of the ions, V is the potential and J_0 is the constant current through the sheath. Such a condition is called a space-charge limited sheath. After solving for the density, the current through the sheath can be expressed for a planar cathode with the Child's law [126]:

$$J_0 = \frac{4\epsilon_0}{9}\sqrt{\frac{2e}{m_i}}\frac{U_C^{3/2}}{s^2} \qquad eq\ 3.6$$

where ϵ_0 is the vacuum permittivity, U_c is the sheath plasma drop and s is the sheath thickness. Knowing that at the plasma sheath boundary, the plasma is neutral (i.e. n_e=n_i, if we suppose an ionization level of the ions of 1, and assuming the ions entering the sheath satisfy the Bohm criterion (demonstration can be found in [124]), the Bohm speed of the ions, v_B, is expressed as:

$$v_B = \sqrt{\frac{k_B T_e}{m_i}} \qquad eq\ 3.7$$

We can combine Equations 3.1, 3.4, 3.6 and 3.7 substituting v_B to v_i and n_e to n_i, to obtain the sheath thickness s:

$$s = \frac{\sqrt{2}}{3}\lambda_D\left(\frac{2U_c}{T_e}\right)^{3/4} \qquad eq\ 3.8$$

One can see that if eU_c is between 100 to 1000 times larger than T_e, the sheath thickness is between a few tens and a few hundreds of Debye lengths in a conventional low pressure plasma discharge. On the other hand, if the plasma potential is low, the sheath of a grounded surface is of a few λ_D. Such distance is in the order of millimetres and as there is no electrons in the cathode sheath, they cannot excite the particle in this region and therefore this area will be dark. The sheath length is critical for the design and operation of plasma processes and diagnostics as it determines the minimal dimension needed to sustain a plasma.

3.3 Ion-Surface interaction

In this section, we will discuss how the plasma interacts with its surroundings by the ions accelerated through its sheath, but before this we discuss how the ion current maintains the plasma.

To sustain a glow discharge, new electron-ion pairs are needed to compensate for the loss at the plasma edges. In electrically driven plasma, this energy is provided to the electrons by the cathode and its sheath. In the sheath, ions are accelerated toward the cathode, and upon impact with the target they generate ejection of electrons via an effect called secondary electron emission. Those electrons are accelerated by the negative cathode potential toward the plasma with an energy up to the full cathode bias. Such highly energetic electrons can generate multiple ionization collisions inside the plasma volume compensating for the charge loss.

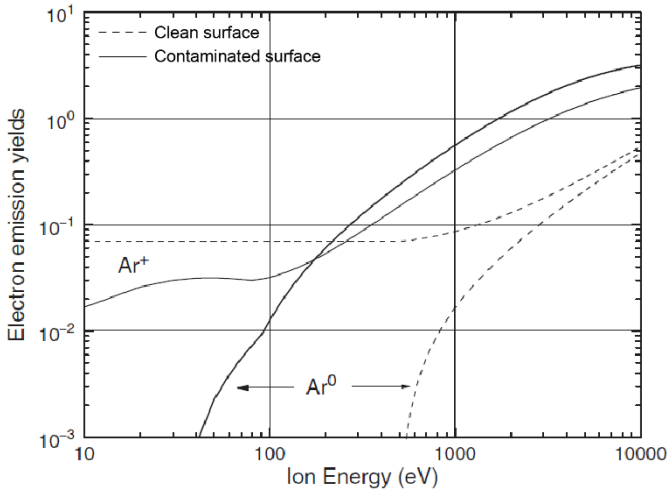

Figure 3-2 Secondary electron emission coefficients for Ar and Ar^+ on clean and contaminated metal surfaces from the model proposed by Phelps in [128]. The experimental data used to build the model present a small impact of the metal atomic number (adapted from [20]).

Secondary electron emission yield for Ar particles impinging on a metallic target is presented in Figure 3-2. Based on calculations, Phelps [127] proposed that the contamination of the surface is the main driving mechanism for secondary electron yield. One can observe that the secondary emission yield of Ar^+ ions is quasi-constant in the lower cathode voltage range (energy under

700 eV) and it exponentially increases with the ion energy above 700 eV. When the surface is contaminated, the coefficient is lower for energy up to 200 eV while it is an order of magnitude higher for ion energy exceeding 600 eV. This fact to explain why reactive magnetron sputtering works at a higher current density compared to a process in a metallic mode.

In MS the ions interact with all exposed surfaces, including the target and the growing films. As describe above the first effect of an energetic particle bombarding a surface is the ejection of a secondary electron. Several other processes induced by the energetic ions are illustrated in Figure 3-3. At low kinetic energy (E_i < 100 eV), the bombardment generates surface effects only, such as enhanced atom mobility, enhanced chemical reactions, desorption of weakly bound species, etc… At higher energy, the ions can start to move atoms in the sub-surface region, either by implantation or through the recoil implantation of a surface atom. When atoms start to move, an altered region is formed. If the energy is sufficient, multiple atoms can be moved through cascade effect. In a suitable crystallographic orientation, the energetic particle can be channelled between the crystalline planes and implanted far from the surface. Atom displacement and implantation can cause defects in substrate or growing films in the form of lattice defects and trapping. Finally, one of the effects of energetic particles important in this work is the sputtering of surface particles.

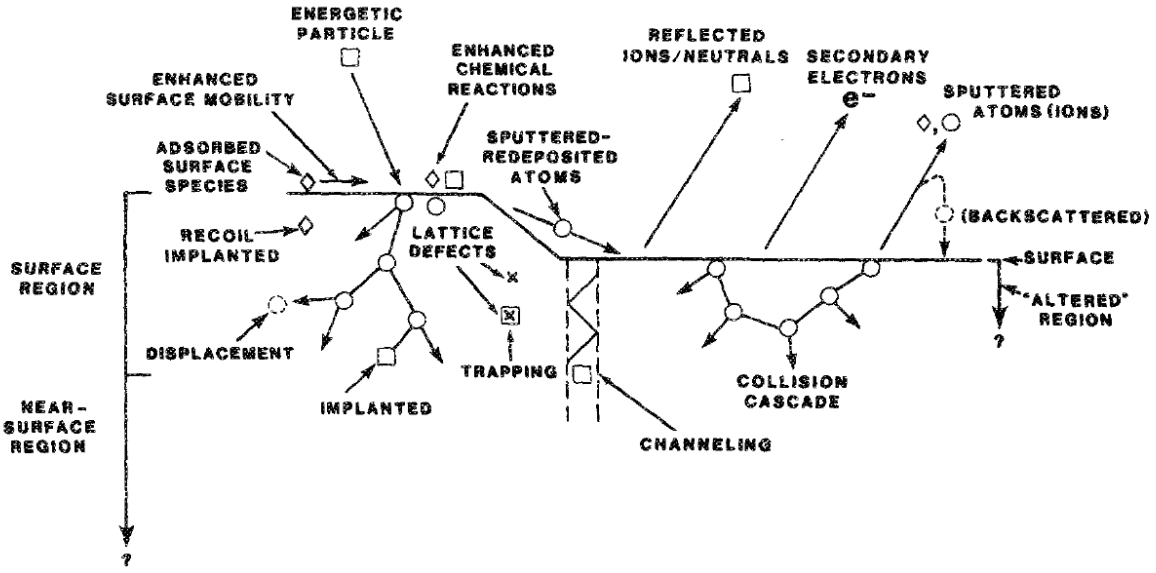

Figure 3-3 Schematics of the various plasma energetic particle surface interactions (reproduced from [129] Copyright 1989 American Vacuum Society).

Like all other plasma-surface interactions, sputtering efficiency is controlled by the energy and mass of the impinging particle as well as the surface material. An example of such a relation is given in Figure 3-4 where the sputtering yield (number of atoms sputtered per incoming particle), of V by Ar ions is plotted as a function of ion energy. One can see that at ion energy less than 70 eV nearly no sputtering is observed, while above 1000 eV the sputtering yield is close to 1. Regarding the surface itself, two main parameters are the atomic mass and the binding energy. Eckstein in [14] computed the surface binding energy for different metals under ion bombardment, and we show some values from this report in Table 3-1. One can see that V presents an abnormally high surface binding energy for its atomic mass. It explains its significantly lower sputtering rate compared to Ti and Cr that have a similar atomic mass. Finally, sputtering also strongly depends on the state of surface contamination; for example, it was shown that a small presence of oxygen or nitrogen atoms on the surface will diminish by a factor of 3 the sputtering rate of Ti or V with 11 keV Ar^+ ions [130], [131].

Therefore, by a careful choice of the ions energy and mass, one can tailor the effect of the plasma ion beam on a surface. A low energetic Ar^+ beam on the vanadium surface will clean it of its contaminants while at energy above 200 eV, a sufficient amount of material is sputtered to deposit films.

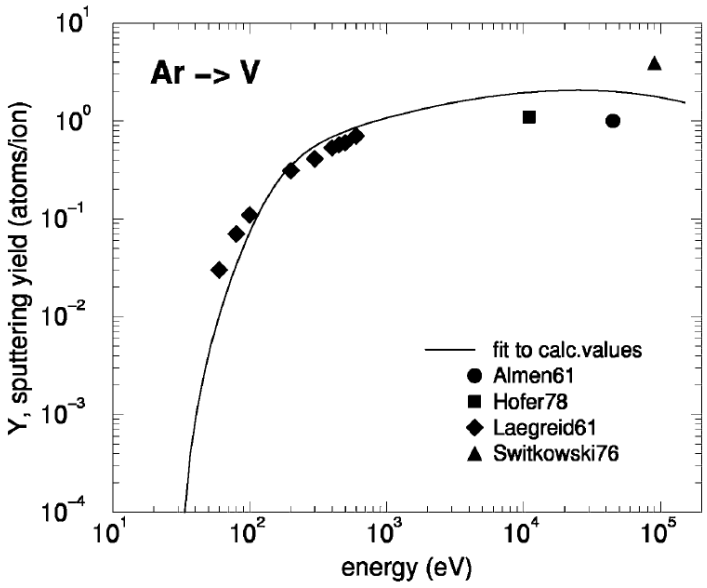

Figure 3-4 Sputtering Yield of Ar^+ ions on a clean vanadium surface as a function of the ion energy (reproduced from [132]).

Table 3-1 Atomic Mass and binding energy of various interesting metals for sputtering, from [132].

Target Material	Al	Ti	V	Cr	Co	Ni	Nb	Ag	Ta	W
Atomic mass	27	47.9	50.9	52	58.9	58.7	92.9	107.9	180.9	183.8
Surface binding energy eV	3.36	4.89	5.33	4.12	4.43	4.46	7.59	2.97	8.10	8.68
Sputtering Yield by Ar^+ at 1000 eV	1.24	1.15	1.23	1.75	1.87	1.75	1.06	3.54	0.99	0.93

3.4 Thin film growth

The growth of polycrystalline films occurs in 4 steps: (i) nucleation, (ii) island growth, (iii) island coalescence, and (iv) growth of the polycrystalline structure [133]. The physical processes that create a film are bound to the physico-chemical environment of the impinging particles, named ad-atoms.

(i) Nucleation is the first step of growing a crystal, where two ad-atoms form a new particle cluster. The first nucleation occurs over the whole surface of the substrate and is called heterogeneous

(ii) Island growth occurs when different nucleus sites compete to capture the ad-atoms to grow. Depending on the material deposited, 3D islands are possible if the surface energy favours island over a layer-by-layer growth.

(iii) Smaller islands can be captured by larger ones or simply coalesce to form large domains on the substrate but the film is not completely covering the substrate.

(iv) When it is not energy favourable to keep free domains over the substrate, the islands will connect, a phenomenon also called percolation [134]. When the film is continuous, the 3D growth starts.

This model describes well the physical aspect of the initial growing of a film. In the sputtering community, where thickness of the thin films is above a few nm, a more descriptive approach is taken. One example approach is the structure zone diagram, SZD, first introduced by Movchan [135] and then improved by Thornton and Messier [136], [137]. It represents the morphology of the films as a function of two parameters, namely the reduced temperature T^*, ratio between the deposition temperature and melting point, and the reduced energy E^*, average energy per deposited atom. The most recent SZD for ion assisted deposition, proposed by Anders in 2010 [138] is reprinted in Figure 3-5. The improvement over the previous diagrams is the inclusion of the arriving particle potential energy in T^*, and the ion kinetic energy in E^*. The detailed calculation can be found in reference [138].

The specific microstructures are named zones: at low energy, the film grows in zone 1 mode, with a porous columnar structure. When the energy available for the ad-atoms increases, the film

densifies with a mechanical stress changing from tensile to compressive; this structure is called transition or zone T. At higher energy (*T**), the growing grains form packed columns with preferred orientation, called zone 2. The last region, zone 3, is formed at high temperatures; here, volume recrystallization occurs and a large grain structure is obtained, like the ones observed in bulk metals. One can see that at high energy, ions will increase the film density in zone 1 and in zone 2 it can provoke reduction of the grain size, called grain refining. However, a high ion energy flux can significantly reduce the deposition rate, noted as *t** (vertical axis).

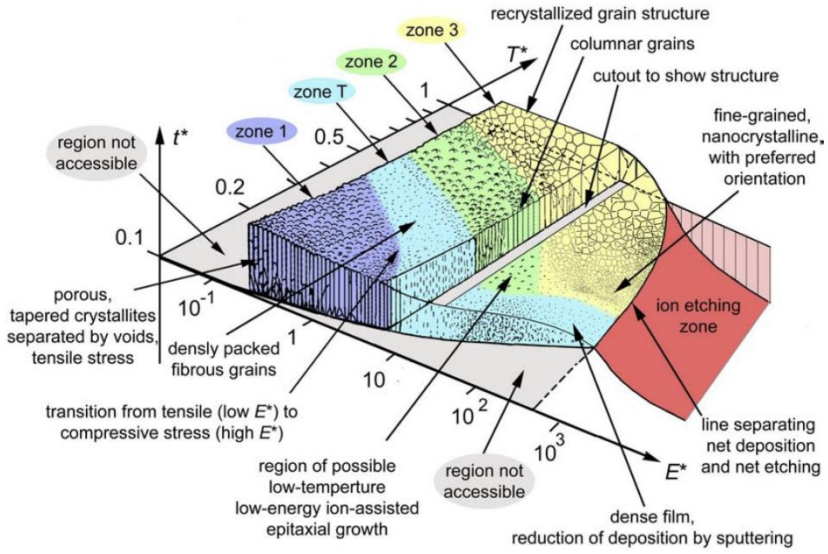

Figure 3-5 Structure Zone Diagram with generalized growth temperature and normalized energy, *T** represents the reduced temperature and *E** represents the energy per deposited atoms (reproduced from [138] with permission from Elsevier).

With phenomenological models, such this SZD, one can see that the deposition temperature can be lowered by increasing the average energy per deposited atom, *E**, to grow a crystalline film. In a sputtering process, this can be achieved by biasing the substrate. *E** can be quantified with two parameters, namely the number of ions per deposited atom and the average energy of impinging ions. *E** enables the comparison of different processes and a better interpretation of the SZD structure. Figure 3-6 presents a diagram for the densification of various materials deposited by CVD and PVD. In terms of energy per deposited atom, between 1 and 100 eV a are needed to

obtain a modified microstructure. Significant volume modification occurs at high average ion energy above 40 eV, as the bulk displacement energy is exceeded [132]. An increase of the ion-flux is therefore needed to avoid damage to the growing crystal and film amorphization.

An additional microstructure effect arises from the bombardment of the growing crystalline film. The sputtering rate of such material is dependent on the crystalline orientation. The growth of a prefered orientation under high-energy bombardment has been well demonstrated; for example ZnO or TiN present <100> orientation for ion beam energy above 400 eV [133], [139].

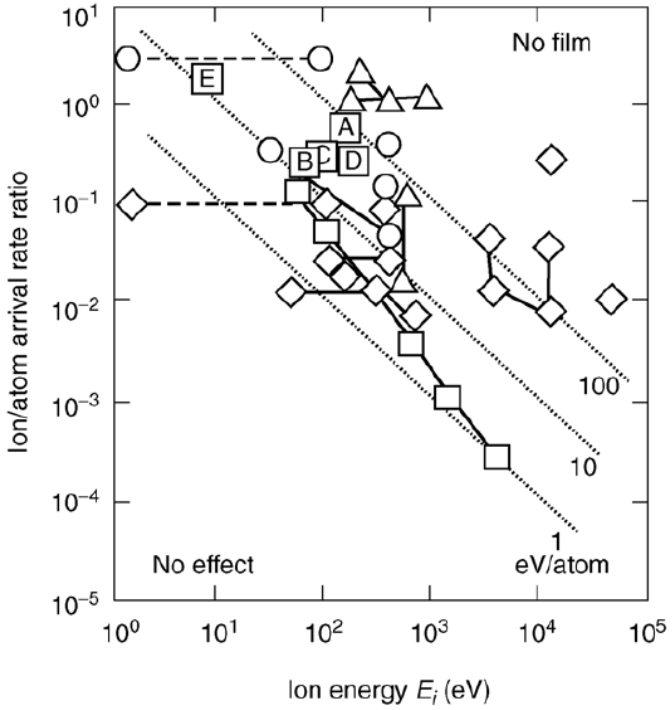

Figure 3-6 Plot of the ions/neutral flux ratio versus the average ion energy for the growth of structurally modified films with a high density for Si_3N_4:H (A), SiO_2:H (B), a-C:H (C), and TiO_2 (D, E) obtained from microwave and radiofrequency PECVD. Other materials deposited by PVD are reported: SiO_2 (circles), dielectrics (triangle), metals (square), semiconductors (lozenges). It shows that an below average energy per deposited atom of 1 eV/atom, no effect of the bombardment is obtained, while above 100 eV/atom, film growth is compromised up to the point of total sputtering of the growing film (reprinted from [101] with permission from Elsevier).

3.5 Magnetron sputtering and HiPIMS

Now that we have introduced the general notions of plasma discharge and the effect of plasma ions on film growth, we will introduce the specificity of magnetron sputtering and introduce its recent advance in the form of High Power Impulse Magnetron Sputtering.

In magnetron sputtering, magnets are placed behind the target material to control expansion of the plasma inside the process chamber. Such magnets generate a magnetic field that traps the electrons in the vicinity of the target, therefore increasing locally the plasma density, ion density and therefore enabling operations at lower pressure and voltage than conventional diode sputtering.

This confinement of the electrons can be evaluated by the ratio between the relative position of null-magnetic zone from the target and magnetron size. When this number is higher than 1, the confinement is strong and the magnetron is called balanced. If this is under 0.5, the confinement is weaker and the magnetron is called unbalanced. An example of the magnetic field distribution of such an unbalanced magnetron (ratio 0.35) is presented in Figure 3-7. This magnetron is used in our laboratory for VO_2 deposition, [44] and Chapter 5 and Chapter 6.

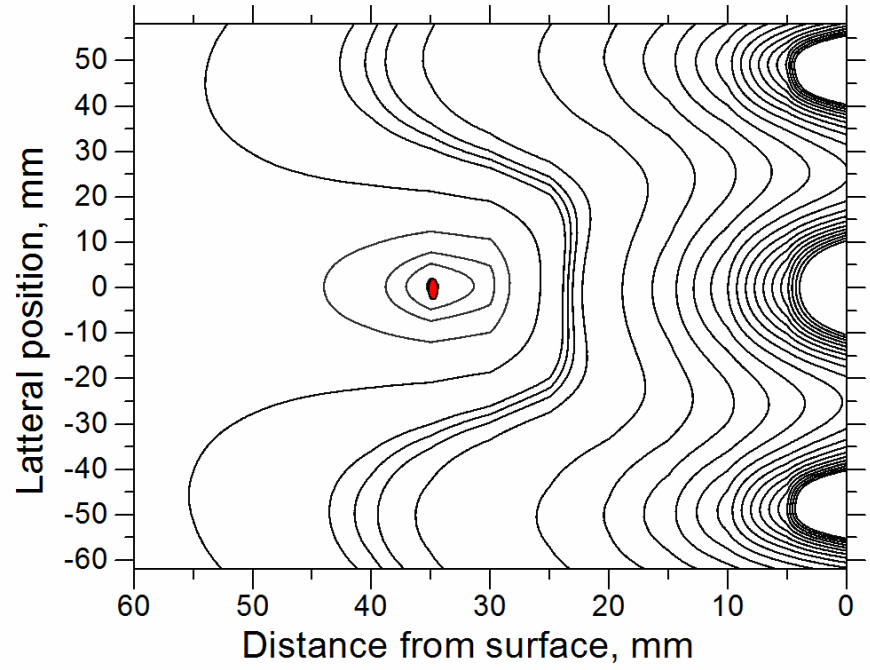

Figure 3-7 Magnetic field map of the extremely unbalanced magnetron. The magnets are placed on the left, at the 0 position and the central red zone is the null-magnetic zone.

Magnetron discharges are primarily used for sputtering of the target, but ions from the plasma can also be used to provide energy to the growing film. Change of magnetic field and confinement of the electrons also changes the distribution of ions inside the chamber, due to the plasma quasi-neutrality. Unbalanced magnetrons provide an increased ion density in the vicinity of the substrate, enhancing the ion flux toward the substrate [140]. Another way to improve the ion flux is to increase the plasma density by addition of a complementary energy sources such as an RF coil to generate a secondary plasma [141]. Both methods are quite convenient in laboratory-scale study, but present drawbacks in industrial applications. Unbalanced magnetrons have lower deposition rates, and the addition of an RF antenna is problematic in a system sputtering a dielectric because the antenna will be coated during the deposition process. In order to not compromise the deposition rate and to avoid a complicated additional electrode, increasing the plasma density and hence the ion flux independently of the average ion energy is needed.

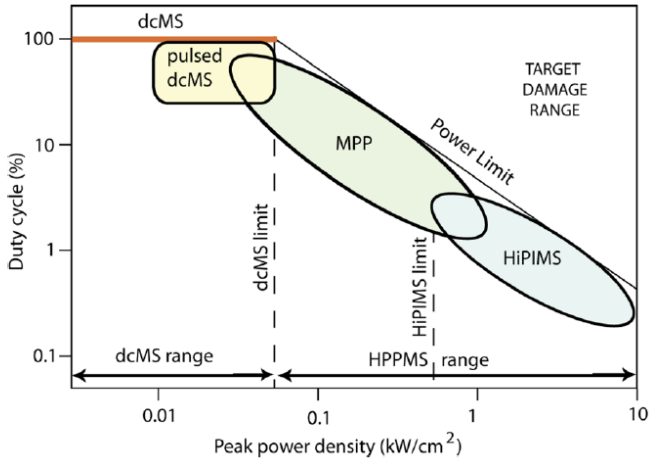

Figure 3-8 Graphical representation of the classification of magnetron sputtering process as a function of the power delivered. Due to thermal ceiling limitations of the magnetron, increase of the plasma density is obtained through an increase of the instantaneous power (reproduced from [142] copyright 2012 American Vacuum Society).

To increase plasma density generated over the target, the applied power density should be increased. Due to the cooling limitation and Curie temperature of the magnet, a maximum average power is inherent to each magnetron system. Therefore, pulsing is needed. Gudmundsson proposed

a classification of the different magnetron processes in term of pulse management [142]. He classifies them in three regimes: 1) DCMS-like, where peak power is comparable to one obtained by DCMS; 2) Modulated Pulse Power, where dynamic shapes are used to slightly increase the peak power; 3) HiPIMS, where power peak densities are above 1 kW/cm^{-2}.

HiPIMS is defined in the scientific community as pulsed magnetron sputtering, with a low repetition frequency (usually 50-1000 Hz), a low duty cycle (0.5 to 5%) and therefore an instant power density which is 2–3 orders of magnitude higher than average.

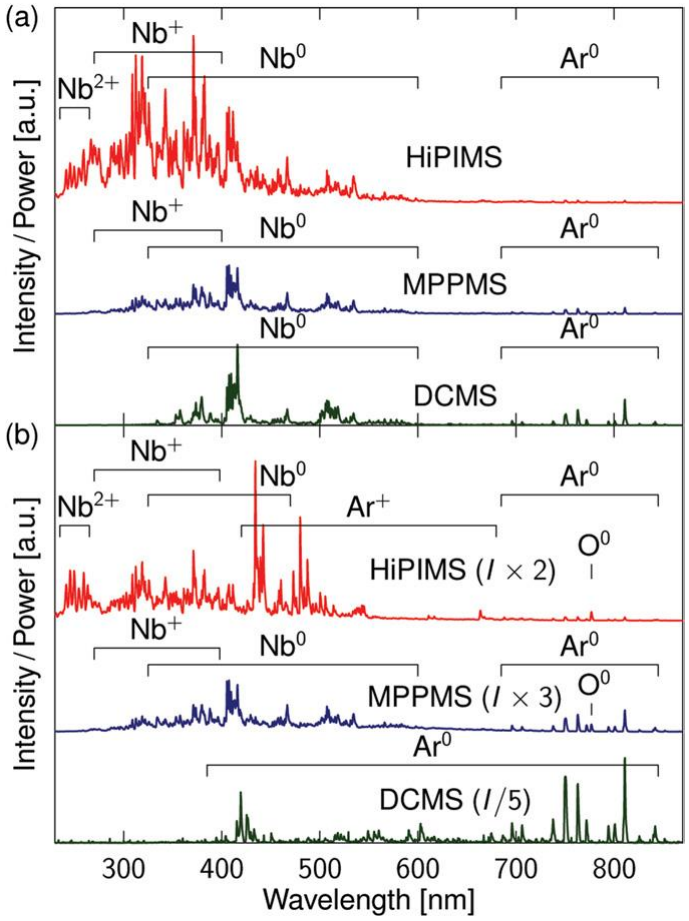

Figure 3-9 Optical emission intensities from discharges operated by HiPIMS, MPPMS and DCMS above a Nb target in pure Ar (a) and in O_2/Ar mixture (b), normalized with an average power of P = 320W. The intensities were multiplyed to clarify (reproduced from [143] © IOP Publishing. Reproduced with permission. All rights reserved).

This large instantaneous power density gives rise to an increase of the plasma density during the pulse with an electron density above 10^{18} m^{-3} [144]. Such high density causes a large fraction of the sputtered flux to be ionized [145], [146]; up to 80% measured with ion-current probe has been reported [147].

A significant fraction of electrons has an energy above 10 eV in this plasma. This source of multiply charged ions, from Ar and metals alike, were reported using optical emission spectroscopy for Cr^{2+} [148], Cr^{2+} Ti^{2+} [149] and Ti^{4+} [150]. An example of such measurement at the presence of Nb^{2+} ions is shown in Figure 3-9**.**

In HiPIMS the energy of the sputtered particles is larger than the one in DCMS; measurements with mass spectrometry suggest that more than 50% of titanium ions have an energy larger than 20 eV [151]. The same effect was observed for materials such as chromium [152], [153]. This high energy ion flux can be effectively used to tune the deposition conditions according to Figure 3-5 and Figure 3-6. However, the rapid pulse dynamics of the process produces a complex plasma behaviour and additional instabilities in the plasma. This can be illustrated by anomalous transport of electrons in the plane perpendicular to the magnetic field [154], or supra-thermal electrons in the first μs of the pulse [155]. One can see in Figure 3-10 that the electron energy distribution presents a dual distribution at the start of the HiPIMS pulse, a low energy part below 5 eV, and a very high energy tail that goes extends 30 eV in the first ten μs.

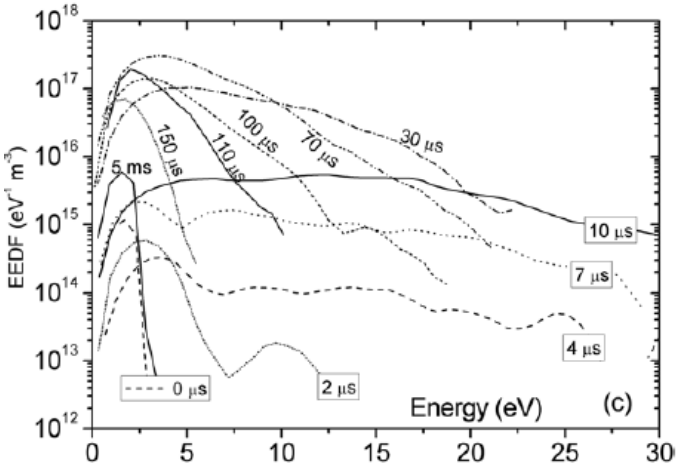

Figure 3-10 Distribution of the electron energy in the HiPIMS at various times during the 100 μs pulse, showing the high-energy electrons produced in the first 10 μs. These measurements were

performed at 0.5 Pa with a peak power density of 500 $W.cm^{-2}$ over a Ti target in pure Ar atmosphere (reproduced from [155] © IOP Publishing. Reproduced with permission. All rights reserved).

The abnormal transport of charged particles, observed for high current density, is called cross-B field transport. It occurs for electrons [154] and heavier particles [156]. This generates a loss of particles toward the chamber walls, a loss of deposition rates. The charge transport instabilities are usually observable through high-speed imaging in the form of spokes [157]–[162]. There is still a debate on the origin of such spokes, from the fast variation of plasma potential [162] to the anomalous cross-B transport of electrons [160]. We also observed such phenomenon occurring in DCMS discharges [163]. In that paper, the spoke formation was identified as repetitive localized breakdown of the Ar sputtering gas. The form of the spokes was linked to the dispersion of the electron drift velocity and a high magnetic field was identified as a condition to trap the spokes close to the surface and maintain spoke formation in direct current regime. Study of the HiPIMS process offers an interesting plasma dynamics.

As mentioned before, HiPIMS results in a highly ionized fraction of the growing material. This was used to improve conformity for trench metallization [164] and to promote the film adhesion by introducing carefully prepared interfaces. However, this same high ionization of sputtered material generates a significant flux back to the target that lower deposition rate in a HiPIMS process for pure metals [165].

Nowadays, however, HiPIMS enjoys more interest from applications using the reactive mode, due to a similar or enhanced deposition rate compared to the conventional DCMS and RFMS, combined with improved film properties [166], [167]. Enhanced process control is one of the main advantages of reactive HiPIMS. It has been reported for a large number of target materials such as Al, Nb, Ta or Si that HiPIMS enables one to obtain a stable discharge, and a hysteresis-free process [143], [168], [169].

Another particularity of reactive HiPIMS originates from ion bombardment of the growing film by negative ions. Significant negative ion density has been reported in reactive HiPIMS discharge at pressure under 0.5 Pa. As one can see in Figure 3-11, the dominant negative species O^- signal is two orders of magnitude lower than the signal of Ar^+ ions as measured by mass spectrometry and Langmuir probes [170], [171]. The first study [170] uses measurements of the average density and energy of the negative ions to identify three energy groups. The largest one at low energy is

generated outside the HiPIMS pulse. The second and thirds groups are generated during the pulse, with energy equivalent to the cathode applied voltage and half of the cathode voltage due to collisions respectively.

Using the transfer from the second to the third group by collisions, they also evaluate the collisional cross-section of high-energy O^- ions to be 2.2 10^{-19} m^{-2}. Such cross section is large enough to scatter high-energy O^- ions at pressure above 2 Pa. This suppress the effect of high-energy O^- bombardment on the growing film.

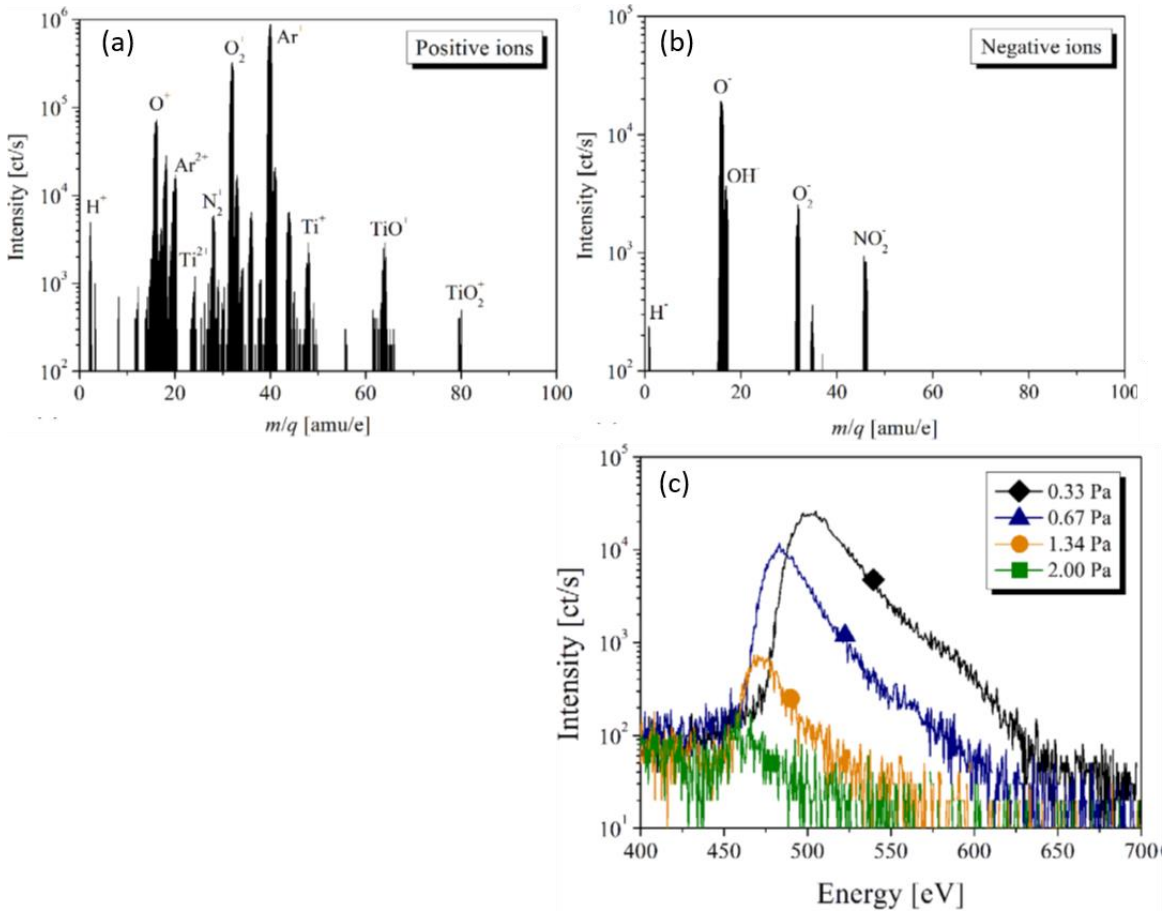

Figure 3-11 Mass spectra at 2 eV of positive (a) and negative (b) ions generated in reactive HiPIMS over a Ti target in an 80:20 Ar/O_2 mixture at 0.33 Pa. (c) Density of the high energy ions as a function of pressure in the same conditions (adapted from [170]).

The second study [171] discusses the formation of the first group, low-energy negative ions. Measuring the plasma electronegativity, they observe an exponential increase in the 3 ms of the post discharge due to electron capture by atomic and molecular oxygen. They attribute these negative ions to a large flux toward the non-biased surfaces [171]. This flux assists the on-pulse low-energy positive ion flux toward the surface to provide additional energy to the growing films when the latter is not biased.

In Chapter 5 we will discuss an unusual light-flash we observed in the reactive HiPIMS post discharge that involves these negative ions and may serve as an indirect proof of their abundance.

The high positive ion flux can also be used to control the film growth in reactive sputtering. As presented in the structure zone model (Figure 3-5), the transition of film structure from zone 1 to zone T of the SZD is achieved with the surface bombardment by energetic ions. In addition, the HiPIMS films offer a higher index of refraction, and a lower mechanical stress that is reflected by a better scratch resistance as illustrated in Figure 3-12 [46]. It has been suggested that mobility the lower stress buildup is due to the higher ad-atom mobility in HiPIMS process [172], [173].

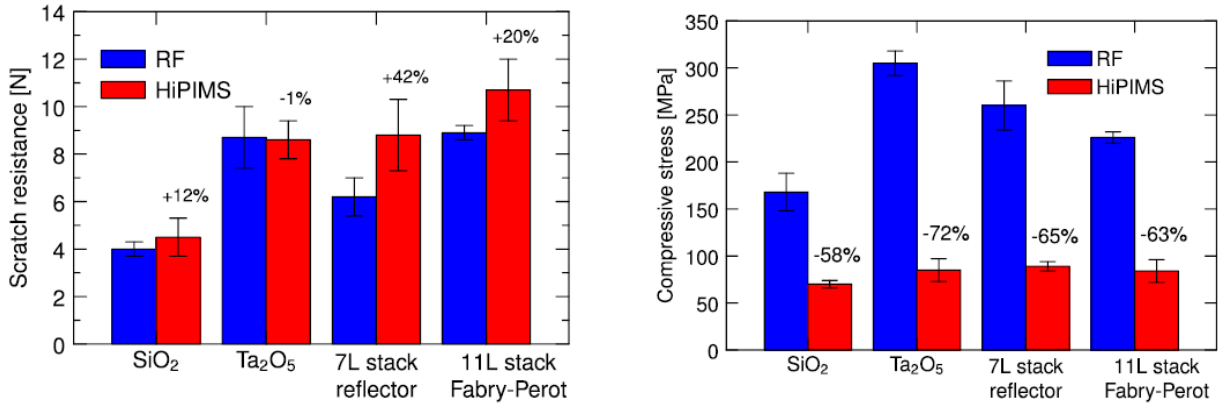

Figure 3-12 Scratch resistance (a) and compressive stress (b) of SiO_2/Ta_2O_5 stacks and single layers' film deposited on glass by HiPIMS (red) and RFMS (Blue) (reproduced from [169] with the permission of AIP Publishing).

The large ion flux is also reported to provide sufficient energy to obtain crystalline films in the zone 2 mode. For example, at room temperature, the crystalline phase of TiO_2 can be changed from anatase to rutile structure as a function of the instantaneous HiPIMS discharge power [174]. Also, a lower oxygen fraction in the mixture is needed to obtain stoechiometric TiO_2 compared to DCMS

[175]. Crystalline zirconia deposited by HiPIMS possesses a higher band-gap and lower leakage current in comparison to RFMS deposited material [176]. Similar observations were reported for protective coating such as TiN [177–180].

Further discussion of the impact of HiPIMS on crystalline film will be made in the following chapters.

CHAPTER 4 EXPERIMENTAL METHODOLOGY

In the present chapter, the experimental methodology applied in the context of this thesis will be presented. I will introduce descriptions of the power supplies and of the deposition chambers used in this work. The second part will describe in detail the optical and material characterization techniques used to evaluate the VO_2 coating properties.

4.1 Deposition systems

4.1.1 Power Supplies

As presented in the previous chapter, HiPIMS is a promising technique to synthetize metal oxides such as the thermochromic VO_2. The term HiPIMS covers numerous process conditions which are compliant with the definition, since the peak power density is two orders of magnitude larger than the average power density. Two main families of power supplies are mainly: (i) unipolar single-pulse power supplies, and (ii) modular pulse power supplies. The main difference between the two families comes from the waveform delivered to the cathode, schematics of such pulses being given in Figure 4-1. In the case of the unipolar single pulse, a single square voltage impulse is applied to the cathode with a fixed repetition rate (a). On the other hand, modular pulse power supplies can generate complex shapes, either a burst of unipolar single voltage square shape pulses, or even bipolar or multi-frequency modulated pulse shapes (b, c). Those features can help to maintain a stable discharge in a reactive environment with strongly reactive materials such as Si, Ta [169], [181], or Al [172]. However, the presence of many frequencies in complex shape pulses can be transmitted to the plasma. This effect adds additional dynamic oscillations within the plasma, which increases the complexity of the discharge diagnostic.

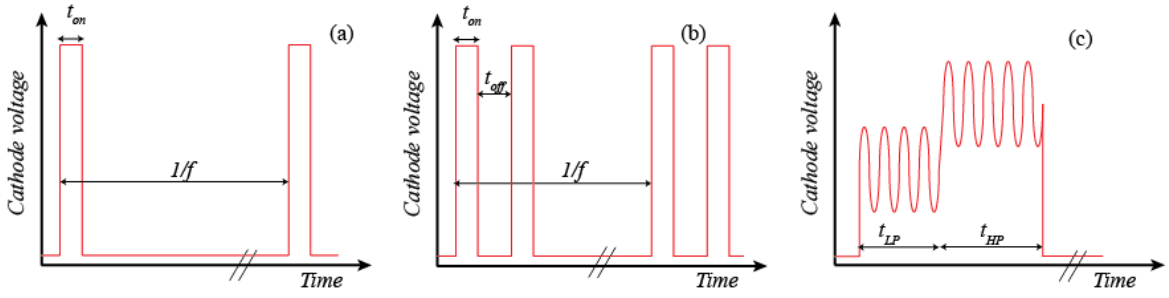

Figure 4-1 Schematic representation of the cathode voltage pulse form delivered by unipolar pulser (a), burst-modulation pulser (b), and multi-frequency modulated pulser (c).

A HiPIMS power supply can be described using a four-block diagram; it consists of a pulse generator, a charging unit, a pulsing unit and a pulse conditioner, as represented in Figure 4-2. The pulse generator is a low power electronic stage, isolated from the three other blocks, that generate the pulse and provides input/output and safety control of the unit such as current limitations, power limitations and interlock. Some units have an integrated control panel such as the HUTTINGER HMP2/1, but most of them need to be controlled through a virtual panel on a computer, for example the Ionautics/Solvix HiP3 5K or the Melec SIPP2000USB.

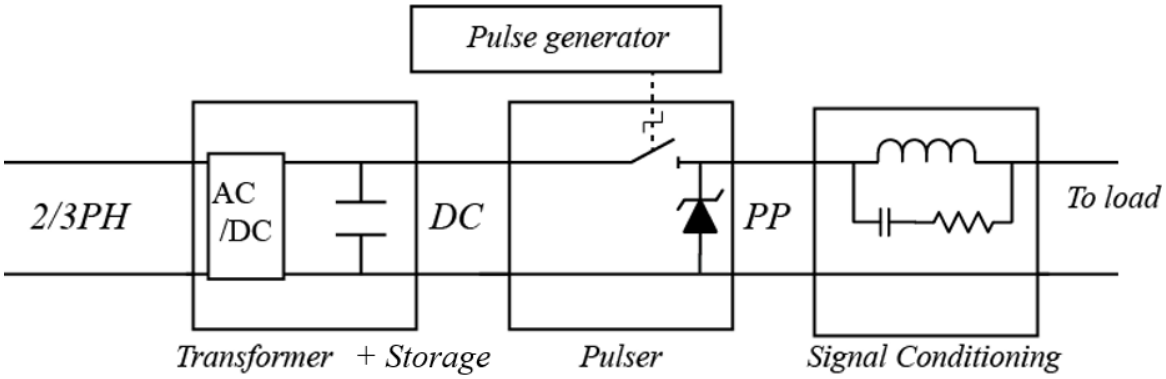

Figure 4-2 Schematic of the HiPIMS power supply (adapted from HUTTINGER HP1/2 manual).

The other three blocks form the power stage of the pulser. First, the transformer converts the input power either from three phases or two phases into DC and raises it to the nominal charge voltage of the capacitor bank. 1 to 20 µF is sufficient to provide the energy for short pulses at low repetition cycle. Then, the next unit is the pulsing unit itself. The main technology used to control the pulse is well known in the form of a thyristor controlled through the pulse generation signal with a Zener diode to form a crowbar circuit (freewheeling diode) to protect the system from voltage spikes. This stage is the most crucial one of the power supply, since it will determine the voltage, power, frequency and pulse time limits of the system.

It is to note that, in the first patent published by Kouznetsov [182], the pulse generation was provided by the grid oscillation. It uses the positive half of the cycle to charge the capacitor bank through a diode, and the negative one to trigger the thyristor conduction. On the other hand, other companies such as Zpulser use another approach; here the pulse-width modulation generates a low power modulated signal before raising it to the required voltage through a low-pass transformer.

The last part of the HiPIMS power stage is the signal-conditioning unit, like the matching unit of a radio-frequency power supply. In this case, a purely inductive circuit is used to limit the rise of the current and thus enables long pulse mode and filter high frequency jitters. This is also the stage that affects the current-waveform when presented with an equivalent load system. The technical data of HiPIMS power supplies that were used for this thesis are presented in Table 4-1.

4.1.2 Deposition Chambers

During this thesis, two different deposition chambers were used with a combination of power supplies, see papers [44], [148], [183]: this includes a small 18 l chamber with a 10 cm (4 inches) unbalanced magnetron, and a chamber equipped with four 7.5 cm (3 inches) balanced magnetrons supplied by Kurt J. Lesker Company. They are schematically illustrated in Figure 4-3 and Figure 4-4. The choice to deposit films in two different systems was made in order to prove that the performance of VO_2 HiPIMS deposited films was not configuration-specific.

Table 4-1 Technical data of the three HiPIMS pulsers used for this thesis

	HUTTINGER Electronic HMP2/1	**Solvix HiP3 5K**	**Melec SIPP2000USB**
Max Voltage, V	2000	1000	1000
Max Current, A	1000	600	500
Pulse length, µs	5–200	10–500	20+
Pulse modulation	No	Yes	Yes
Time between pulse, µs	N/A	10+	20+
Repetition frequency, Hz	50–200	50–1000	<2000
Matching			
Impedance, µH	1.2 to 20		
Capacitance, µF	3		
Resistance, Ohm	0.75		

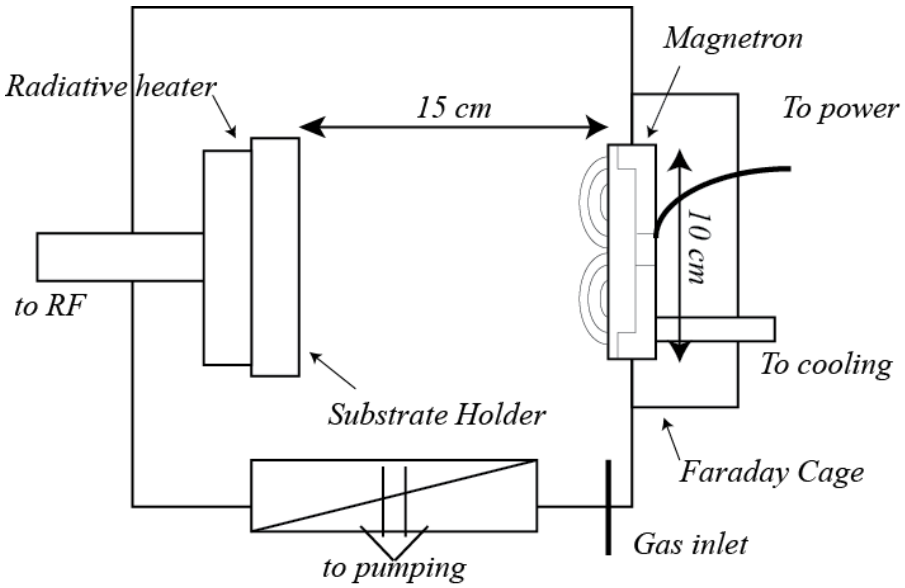

Figure 4-3 Schematic of a small chamber equipped with a 10 cm diameter unbalanced magnetron. This system was used in the context of the work described in Chapter 5 and Chapter 6. For more clarity, shutters and viewing ports are not represented.

The first chamber used for the deposition of VO_2 by HiPIMS as developed by M. Hala and J-P Fortier [44] is represented in Figure 4-3. This is a small high-vacuum (base pressure 1.10^{-6} mTorr, 1.33 10^{-7} Pa) chamber equipped with a radiation-heated copper substrate holder and a 10 cm directly cooled magnetron. Since the target is directly cooled, the magnetron can accept large power density, up to 15 $W.cm^{-1}$ on average. The substrate faces the magnetron at a distance equal to 1.5 of the magnetron diameter (15 cm), giving a high deposition rate. Additional energy can be provided to the growing film by way of biasing the substrate. During this study, only radio-frequency biasing was used.

The second system is represented in Figure 4-4. It is a commercially available research system (CMS-18) provided by Kurt J. Lesker. The chamber consists of an 18 in (45.8 cm) diameter stainless steel vessel, pumped down to ultra-high-vacuum (10^{-8} mTorr, 1,33 10^{-9} Pa) by way of mechanical and turbo-molecular pumps. The sputtering unit uses a bottom-up configuration, with four 7.5 cm magnetrons. The magnetrons have standard copper-head cooling and a balanced magnetic field. The maximum power density is limited to 10 $W.cm^{-1}$ resulting in a maximum of 450 W. They face a circular 20 cm diameter stainless steel substrate holder placed at a distance of

30 cm. The sample holder can be biased, rotated, and heated up to 800 °C per manufacturer's specification. Due to the larger distance/target magnetron ratio and the balanced magnetic field, the ion flux and deposition rates are expected to be lower in this system compared to the previous one.

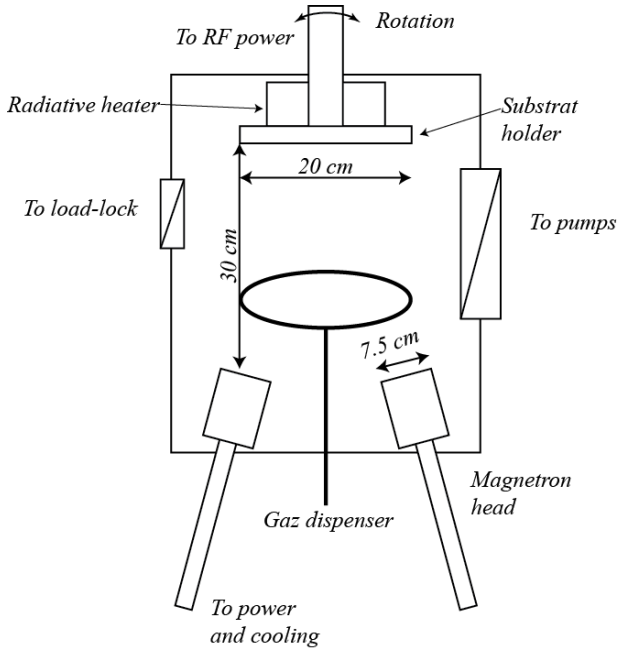

Figure 4-4 Schematic illustration of the four-magnetron CMS-18 system. Two magnetron heads of this system were used for the deposition of samples for Chapter 7 with silicon and vanadium targets. For simplicity, the load-lock and the shutters are not represented.

4.2 Optical emission spectroscopy

During this thesis, multiple plasma-diagnostic approaches have been employed to investigate the HiPIMS discharge in metallic and reactive modes. A short summary of such methods can be found in [101]. In this section, I will present the most commonly used plasma-diagnostic, Optical Emission Spectroscopy (OES), and one of its derivatives, high-speed plasma imaging.

OES is one of the most frequent plasma diagnostic tools due to its ease of implementation, non-intrusive nature and low cost of a basic setup. It is a powerful tool to quickly analyze and monitor physical and chemical processes in the plasma discharge. When backed with suitable modelling

and calibration, OES can extract quantitative information on the plasma dynamics. It can provide a good estimate of plasma composition, plasma density and electron energy, as well as the molecular vibrational temperature.

While a powerful tool, OES has its own limitation due to the nature of the collected light signal. In a plasma medium, light emission is limited by the radiative transitions of excited species, and self-absorption can modify the collected light intensity, increasing the complexity to analyse the data.

4.2.1 Principle of atomic line emission

In a low-pressure plasma, most the light is generated by spontaneous de-excitation of bound electrons in atoms or ions. Such de-excitation is characterized by a transition of the electron between a high-energy level to a lower energy level, the energy difference being emitted in the form of a photon. The wavelength observed, λ_{ul} can be estimated through the Planck equation:

$$\lambda_{ul} = \frac{hc}{E_u - E_l}, \qquad eq\ 4.1$$

where E_u is the higher energy level, E_l the lower energy level, c the speed of light and h the Planck's constant. Quantum mechanics predict and defines an energy level diagram unique for each atom. Therefore, a distinctive set of emission lines will identify each atomic species.

The strength of each of those lines is probabilistically determined by the electron configuration of the atoms and one can evaluate A_{ul}, Einstein's coefficient, of the transition at wavelength λ_{ul} using the following equation:

$$A_{ul} = \left(\frac{g_l}{g_u}\right)\frac{\varepsilon_0 c m_e \lambda_{ul}^2}{2\pi e^2} f_{lu}, \qquad eq\ 4.2$$

simplified as

$$A_{ul} = \left(\frac{g_l}{g_u}\right)\frac{10^{-4} f_{lu}}{1.5\ \lambda_{ul}^2}, \qquad eq\ 4.3$$

where f_{lu} is the absorption coefficient from the lower level to the upper level; g_l and g_u the degeneracy of the lower and upper level.

It is worth mentioning that A_{kl} is inversely proportional to the lifetime of the excited level. In the case of energetic radiative levels, a typical lifetime is between 10^{-7} to 10^{-8} s. This time is much shorter than the time between two impacts in a low-pressure plasma, where atom/atom and electron/atom collision occurs in the 10^{-4} s to 10^{-6} s range. Therefore, we can assume that most of the de-excitations are radiative and that, in time-resolved measurements, light emission is a representation of the plasma excited species states up to 10^{-7} s resolution. In Figure 4-5, we reproduce the Ar energy level diagram originating from our collaboration with Dr Panjan [163]. The selection rules of the radiative transition prohibits a transition from an upper level to a lower level of the same J index. Therefore, metastable levels appear in the lower energy level of Ar specifically the 5s and 3s lower levels, which cannot be probed via optical emission spectroscopy.

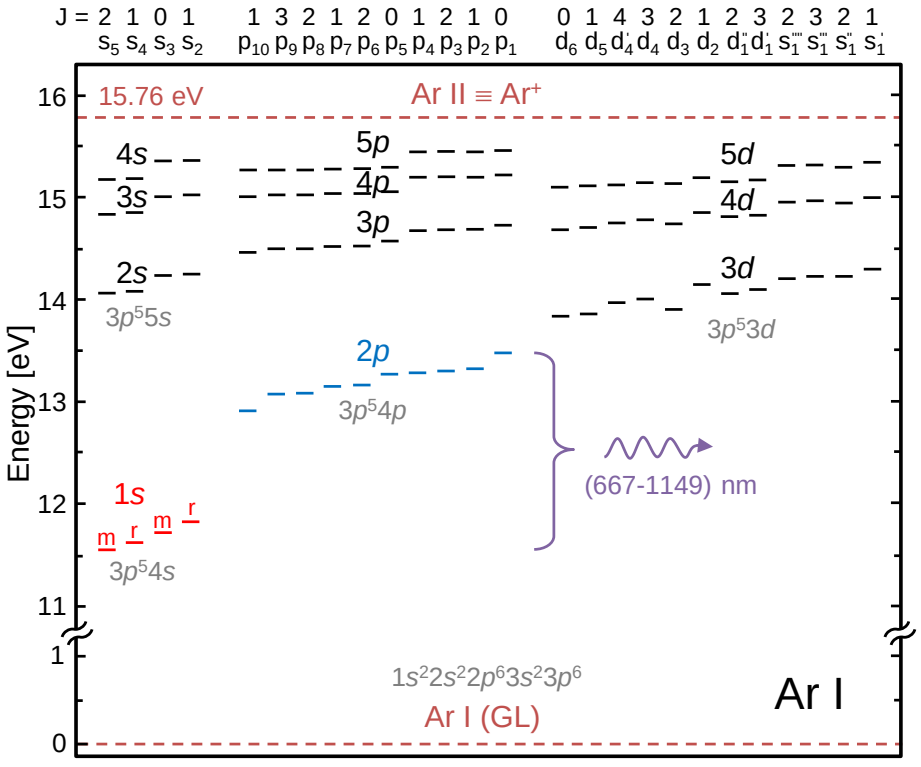

Figure 4-5 Diagram of neutral Ar energy of the excited states with Paschen notation. 1s metastable and resonant levels are denoted by (m) and (r), respectively (reproduced from [163])

Additional optical methods exist to probe the density of such non-radiative states, such as absorption [184]–[187] or Laser Induced Fluorescence (LIF)[188]–[190]. The absorption technique loses the flexibility of the OES since it necessitates a light beam as a probe, and different laser wavelengths need to be used for each transition. On the other hand, LIF uses a combination of both, by exciting species to a specific excitation level and recording the subsequent optical de-excitation. Therefore, both are very sensitive to the background light emission, especially in plasma discharges and cannot be used to detect a number of critical atomic species such as H, O, and F with a simple setup [190].

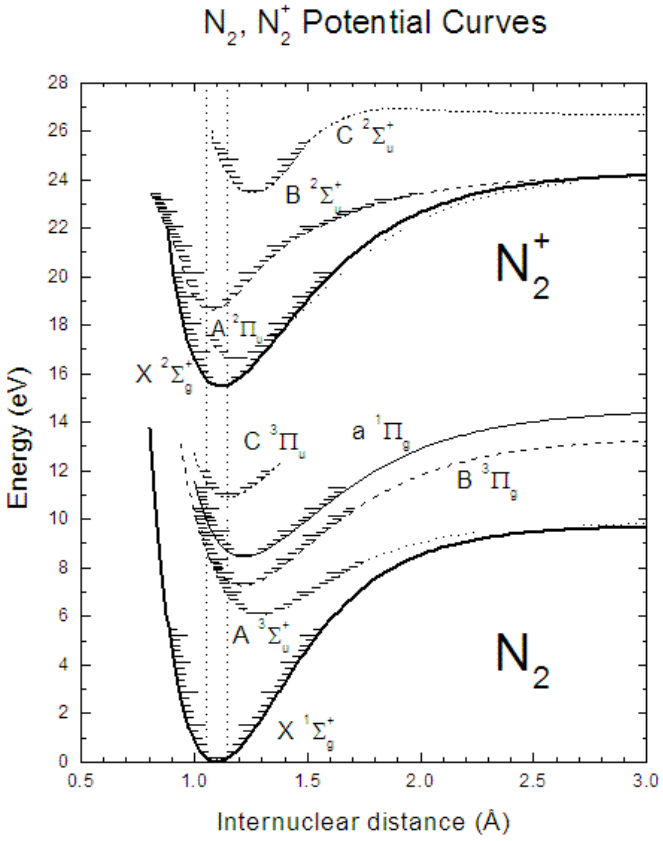

Figure 4-6 Energy level diagram of neutral and ionized dinitrogen (reproduced from [191]).

All of the tools presented in this section can also be applied to molecular species. The additional complexity in monitoring such species emerges from the electronic structure, as represented in Figure 4-6 for N_2. Due to the nature of a molecule, interatomic distance varies the accessible electron energy, generating many energy levels, and therefore many emission lines. However, the emission lines are linked to the rotational and vibrational energy levels of the ions, creating emission bands. Extensive modelling can therefore extract the energy states of the neutral molecules which give rise to a larger interest in LIF and absorption spectroscopy for molecular gas discharges.

4.2.2 Experimental apparatus

OES analysis of plasma is versatile and easy to operate. It necessitates minimal equipment to operate basic analysis. First, the emitted light needs to be collected from the plasma chamber. This can be done through a view port or by inserting an optical probe connected to an optical fibre inside the chamber. The latter one offers the possibility to have a moving support, therefore a spatially resolved measurement of the emitted light from the plasma is possible. Additional precautions are needed in a deposition plasma to avoid deposition onto the optical fibre. During this thesis, we used a fused-quartz cover on top of the optical probe and an observation perpendicular to the sputtered flux.

Once the light is collected, collimated light is diffracted in a monochromator to obtain a wavelength dispersion and send it to the detector. These two components define the performance of the OES experiment. Spectral resolution of a spectrometer strongly depends on the monochromator and will not be discussed here. Nevertheless, the simplest spectrometer uses a diffraction grating directly attached to a CCD detector (Charge Coupled Device). Such system, as the portable Ocean Optics USB 2000, are easy to use, portable, and cost effective. They offer a low-resolution plasma analysis without time resolution.

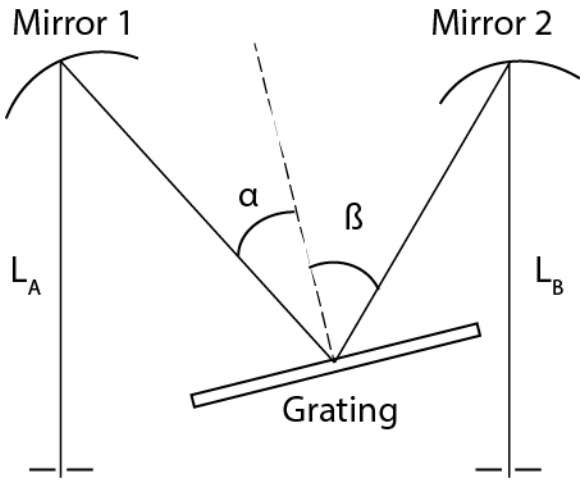

Figure 4-7 Schematics of Czerny-Turner spectrometer configuration (adapted from [192]).

For more precise measurements, separate monochromator and detector systems are used. The most commonly used monochromator is the Czerny-Turner configuration, presented in Figure 4-7. The incoming light from an entry slit at a distance L_A is projected by the first concave mirror onto a diffraction grating at an angle α. The diffracted light at an angle ß is then sent through the exit slit at a distance L_B by a second concave mirror. The angles α and ß are linked by the fixed position of the mirror as:

$$D = \alpha + ß \qquad eq\ 4.4$$

They are also related to the dispersion order k and the grating density g by the following equation:

$$\sin(\alpha) + \sin(ß) = 10^{-6} k g \lambda \qquad eq\ 4.5$$

One can obtain the linear dispersion of the grating through:

$$\frac{d\lambda}{dx} = \frac{\cos(ß)\ 10^6}{\mathrm{kg} L_B}. \qquad eq\ 4.6$$

One can observe in equation 4.6 that the linear dispersion of the grating is proportional to cos (*ß*) and inversely proportional to g and L_B. Therefore, the spectral resolution of the monochromator improves with *α,* the arm's length and grating number. Using an higher order of diffraction can increase such dispersion with a sacrifice on the intensity collected. Unfortunately, as there is a limitation in the rotation of the turret, an increase of spectral resolution proportionally decreases the wavelength range.

Nowadays, grating aberrations are holographically corrected. Such grating also offers a plane of focus instead of a focal point, therefore the use of a CCD detector enables a faster measurement over a broad spectral range. During this thesis, an Acton Spectra Pro using holographic grating was operated with a high-gating speed camera to measure time resolved spectra and emission lines. Additional information on the optical performances of monochromators can be found in [192].

Table 4-2 Spectrometers characteristics

	Ocean Optics USB-2000	**Acton Spectra Pro**
Wavelength range	200–850nm	200-1050 nm
Grating	600 mm^{-1}	120, UV-1200, UV-2400 mm^{-1}
Arm length	N-A	75 cm
Spectral resolution	1.5 nm	Up to 0.017 nm @440 nm (2400 mm^{-1})
Detector	CCD 2048 Pixels	Amplified CCD, 1024*1024 Pixels
Detector contrast	10 bit (1024/1)	16 bit (65535/1)
Time resolution	N-A	5 ns to few ms
Synchronization	N-A	150 ps to a few ms

4.3 Film characterization technique

4.3.1 Spectrophotometry

One of the most frequently used techniques to characterize optical transmission, reflection and absorption spectra of thin film is spectrophotometry.

For this work, a Perkin Elmer Lambda 1050 was used. The light source is a dual lamp system equipped with a halogen and a deuterium lamp covering wavelength range from 175 to 3200 nm. This dual beam spectrophotometer is equipped with three detectors (PMT, InGaAs, PbS). The reference beam compensates the lamps and optical path fluctuation and it increases the signal-to-noise ratio in the full spectrum.

A custom-made heat cell was adapted to fit in the sample compartment. A sample holder for B270 or polymeric samples of 5 by 5 cm was machined from aluminium and equipped with a resistive heating cartridge and a thermocouple. An Instek PID-controller was used to set the temperature of the coated surface from room temperature to 100 °C with a precision of 0.1 °C, and accuracy of 2 °C for temperature under 35 °C and 0.5 °C above this temperature.

In the context of this study, spectrophotometry was used to collect two set of data. First direct spectroscopic measurements were performed from 250 to 2500 nm at two temperatures, namely at room temperature and at 90 °C; i.e. below and above the VO_2 critical temperature. Another set of data was measured at a fixed wavelength of 2500 nm as a function of temperature during heating and cooling. As there was no active cooling of the sample, ramp rates were fixed to 1 °C/min.

It has been proven that the optical parameters n and k can be obtained through modelling from the transmission, absorption, and reflection [193]. In the current work, we chose to use a more powerful tool, spectroscopic ellipsometry to compute these parameters.

4.3.2 Spectroscopic ellipsometry

Spectroscopic ellipsometry is a complex and powerful tool to determine the optical properties of a material. This non-destructive measurement technique is based on the change of polarization of light upon reflection at an interface. As ellipsometry also relies on phase and not only intensity changes, it is much more sensitive to extremely thin films in comparison to spectrophotometry; in fact, only a few angstrom of a material is sufficient to induce observable changes in ellipsometry.

In the case of polarized light, the electric field can be divided into two components, one which is perpendicular to the plane of propagation, expressed as the *s* polarization and one which is parallel to the plane of propagation, the *p* polarization. At an interface between two different media, the *s* and *p* polarizations will be reflected differently per Fresnel reflection coefficient r_s and r_p given by:

$$r_s = \frac{N_0 \cos(\theta_0) - N_1 \cos(\theta_1)}{N_0 \cos(\theta_0) + N_1 \cos(\theta_1)} \quad \text{and} \quad r_p = \frac{N_0 \cos(\theta_1) - N_1 \cos(\theta_0)}{N_1 \cos(\theta_0) + N_0 \cos(\theta_1)} \qquad eq\ 4.7$$

where N_0 and N_1 are the complex refractive indices, $N = n - ik$, of the first and second medium; n is the refractive index and k is the extinction coefficient. In addition, θ_0 is the angle of incidence of the incoming beam and θ_1 is the angle of the refracted beam, the latter being easily obtained using the Snell-Descartes equation.

The ellipsometric parameters, Ψ and Δ, are then derived from these reflection coefficients using the following equation:

$$-\frac{r_p}{r_s} = \tan(\Psi)\, e^{i\Delta} \qquad eq\ 4.8$$

As such, Ψ is a representation of the change in intensity between both polarizations and Δ is a representation of the phase change between the two polarizations, in the presence of a thin transparent film, measurements at variable angles provide additional data to enhance the sensitivity during modelling.

Aside from some rare cases, ellipsometry is an indirect characterization method and consequently an optical model is required. In such a model, each individual layer of the sample must be defined, e.g.: the substrate and overlying film as well as their respective thicknesses. Each layer is typically modelled using oscillators, derived from physical models, which, through an optimization process, will define the dispersion functions of the material. Using these oscillators ensures that one will obtain a physically viable solution assuming that the input values are judiciously entered and the obtained solution validated (Kramers-Kronig consistency). Prior knowledge of the material can help one to choose a suitable dispersion function. The most frequently used oscillators are: Tauc-Lorentz to model the absorption band edge in the near-UV (interband electronic transitions), Drude for the metallic behaviour of a material (intraband electronic transitions), and Gaussian for modelling infrared absorption bands or very often to fine-tune the modelled absorption in the UV.

In addition, film morphology such as surface roughness can be modelled using the Bruggeman effective medium approximation. Once a suitable model is built, an optimization algorithm is used to fit the model's parameters and obtain the lowest mean square error (MSE), in other words, minimize the difference between the experimental data and modelled data. Figure 4-8 illustrates the optimization algorithm which is used. One should remember that such an optimization process is very sensitive to the starting point, as multiple solutions are often possible and the algorithm may converge to a local minimum.

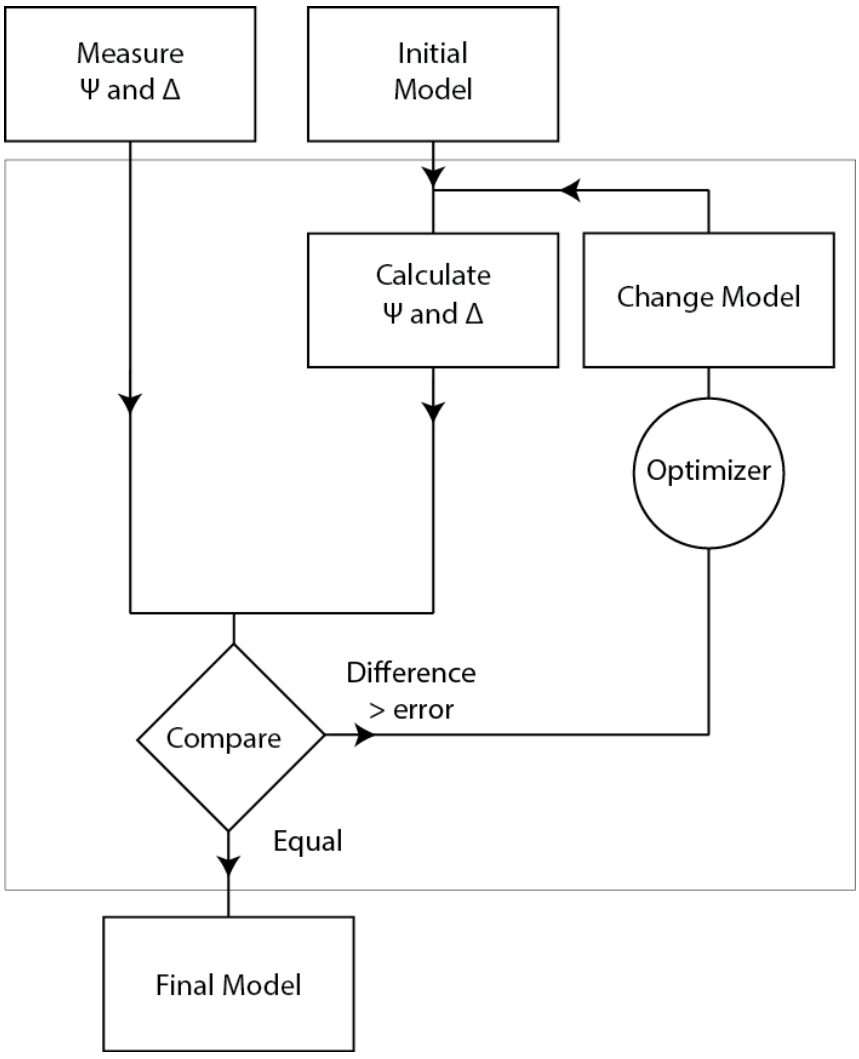

Figure 4-8 Optimization algorithm for ellipsometry measurements.

In specific cases, information can be directly extracted from the ellipsometric parameters. For instance, when measurements are performed on a sufficiently thick absorbing film so that the underlying interface is no longer “visible”, a direct inversion of equations 4.7 and 4.8 gives the optical properties of the material, if the interface is almost “perfect”, i.e. in the absence of a surface oxide in the case of metals and low surface roughness.

In the context of my thesis, a RC2 ellipsometer from J.A. Woollam Co., Inc. was used. This ellipsometer is equipped with dual rotating compensators to enhance the polarization sensitivity and allow measurement of the complete Mueller matrix. The detector is a CCD-based-array which measures between 200 and 1700 nm. The system is configured in a goniometer geometry which allows one to measure the complementary transmission of the sample and affix various accessories such as a heat cell.

Ellipsometry can be used as to monitor fine change of material such as the continuous change of properties of VO_2 while heating. This is illustrated in Figure 4-9, where we reproduce the optical properties derived from temperature-resolved spectroscopic ellipsometry on the right. On the left one can see that the phase transition of the material can also be followed by the two peaks in the film thickness due to the change of morphology of the grains. Another example, during the deposition of a thin metal layer on a dielectric surface, the polarization state of the reflected light shows an extinction of *p*-polarized light due to the plasmonic resonance of the metal islands; upon coalescence of the growing islands and formation of a conductive metallic layer, the extinction of the *p*-polarized light is seen to disappear and as a result, one can obtain the percolation threshold [134].

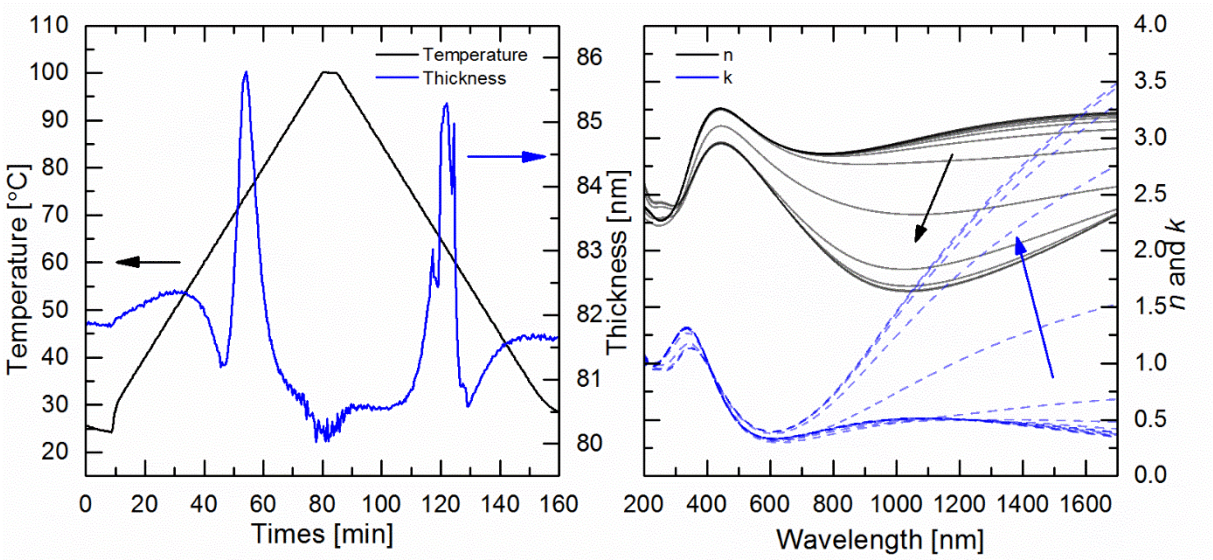

Figure 4-9 Optical thickness (left) and optical indices of our HiPIMS VO_2 sample, derived from temperature-resolved ellipsometry. The two peaks on the thickness are representative of the change of volume during phase transition. For clarity, the optical indeces are plotted for every 5 °C.

The models were developed and optimized in the *CompleteEASE* software package, also from J.A. Woolam Co., which uses the Levemberg-Marquardt optimization algorithm. More details on ellipsometry and its modelling can be found in the book of Fujiwara [194].

4.3.3 Rutherford backscattering spectroscopy and elastic recoil detection.

Rutherford backscattering spectroscopy (RBS) and elastic recoil detection (ERD) are two Ion Beam Analysis (IBA) techniques that allow one to determine quantitative composition of a sample with depth resolution. Both methods use the interaction of a high-energy ion beam, typically a few MeV, with atomic nuclei. When interacting with a nucleus, high energy ions are subject to elastic and inelastic collisions. The resulting deflected ions energy will present dependence on the mass of the impacted nucleus and incidence angle, a signature of the film composition.

Travelling through the sample, the ions are subjected to a drag force from the surrounding electron clouds. This drag force generates a shift in the recorded energy, that is proportional to the distance

travelled inside the material. The sensitivity to mass and depth of IBA is limited by the energy sensitivity of the detector. Also, additional collisions and deflection of the beam can occur with high penetration depth, degrading the composition resolution.

In the case of RBS, a low mass $^{4}He^{+}$ ion beam at 2 MeV is used and backscattering at a low angle with the surface is recorded. The recoil is purely elastic in RBS and atoms with mass inferior to the carbon cannot be detected (specifically hydrogen). In order to be sensitive to hydrogen, ERD is used. In most of the case, a higher mass ion beam, e.g.: Cu^{9+}, is accelerated to 50 MeV can be used with a detector placed in a backward position from the sample. For our experiments an alternative ERD procedure was also used with 1.7 keV $^{4}He^{+}$ beam in RBS configuration and an absorbing foil, PET, used to prevent all elements except H from striking the detector [195].

Experimental data, such as the ones presented in Figure 4-10, need to be modelled to extract the film composition and density. One should build a model based on prior knowledge of the suspected composition and thickness and refine it through numerical optimization. However, nuclear interactions and the use of experimental datasets render the modelling quite complex [196], [197] Therefore, for this project the measurements and analyses were performed by the Laboratoire de Faisceaux d'Ions, Université de Montréal.

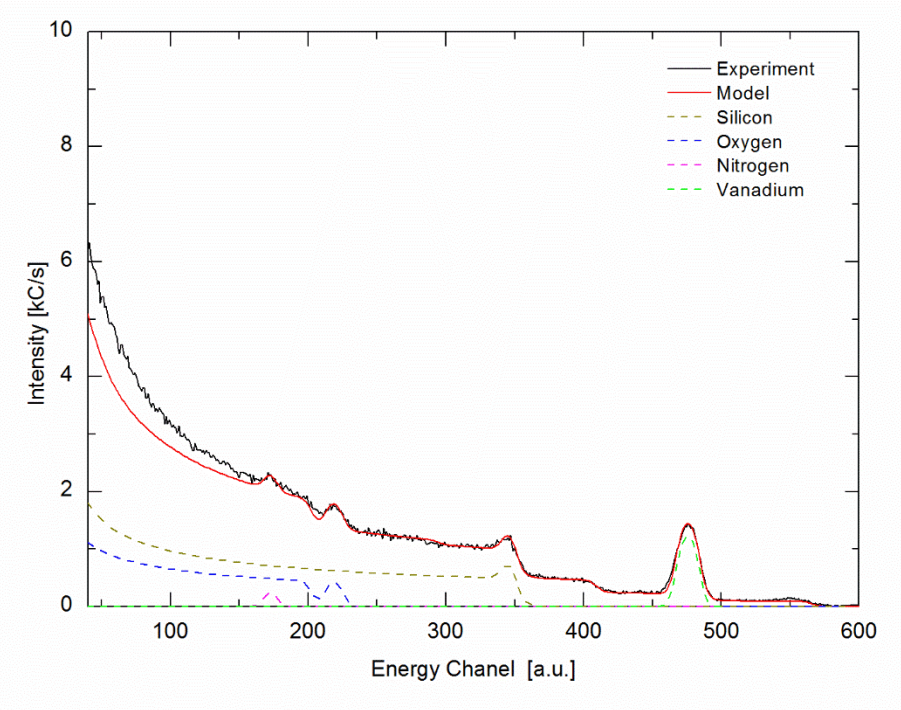

Figure 4-10 Recorded RBS spectrum and models for a 40 nm VO_2 layer deposited over a 35 nm Si_3N_4 barrier layer on B270 glass. Data analysed with the CORETO software [196] Data were recorded for the completion of Chapter 7.

CHAPTER 5 ARTICLE 1: FLASH POST-DISCHARGE EMISSION IN A REACTIVE HIPIMS PROCESS

Authors: S. Loquai, O. Zabeida, J.E. Klemberg-Sapieha, and L. Martinu

Article Published in: *Applied Physics Letters,* Volume 109, Issue 11, 114101-, September 2016

Abstract:

In the present work, time-, space- and species-resolved optical emission spectroscopy has been applied to investigate post-pulse behavior of the reactive High Power Impulse Magnetron Sputtering (HiPIMS) process with a partially poisoned target. Following each pulse, at a high O_2/Ar ratio, a well-defined post-discharge emission zone detaches from the target during the first few microseconds of the electron cool-down; this zone exhibits high emission intensity in the near-surface region, and it moves toward the substrate holder. We link this behavior to a localized high density of metastable molecular oxygen, and to the electron attachment dissociation of oxygen.

5.1 Introduction

During the past decade, High Power Impulse Magnetron Sputtering (HiPIMS) plasma, and HiPIMS processes in general, have been an extensively studied topic within the plasma processing community. Introduced in the late nineties by Kouznetsov *et al*. [164], HiPIMS has been demonstrated as a promising method for step coverage metallization, very effective tool to deposit mechanically resilient coatings [198], [199], and a suitable method for the fabrication of low-stress ultra-dense optical coatings [200]. More recently, for the particular case of VO_2, it has been shown that HiPIMS allows one to deposit high-performance thermochromic coatings at a lower temperature than other techniques [44] and on polymer substrates [201]. In addition, strong interest in HiPIMS plasma dynamics, in particular in the gas phase effects, led to a phenomenological description of the HiPIMS process in terms of the recycling trap model [165], explanation of the origin of fast ions arriving at the substrate [202], observation of a fast dynamic evolution of particles close to the magnetron in self-organizing spokes [157], [158], [162], [163], and to a description of the role of gas species in the reactive HiPIMS mode [203], [204]. In the present work we concentrate our attention on the post-pulse discharge dynamics in the reactive HiPIMS, in particular we investigate the light flash appearing after the voltage pulse in the zone close to the magnetron but detached from it. This possibly affects film growth on the substrate.

5.2 Experimental Methodology

The HiPIMS discharge experiments were performed in a stainless steel vacuum system (20 liters volume) turbomolecularly pumped to a base pressure of 10^{-6} Torr. The total gas pressure during operation was kept at 10 mTorr. Argon (99.999% purity) and oxygen (99.995% purity) were admitted to the chamber at a total flow rate of 58 sccm, while the flow ratio $\eta = O_2/(Ar+O_2)$ was varied between 0 and 7%. An unbalanced magnetron head supported a 10 cm diameter vanadium target (99.5 % purity). The magnetron was powered from a HiPIMS power supply (HMP/2, Huettinger) providing a cathode voltage of 900 V and a discharge current of up to 250 A, while using a 45 μs long pulse duration and a repetition rate of 200 Hz. The total average power peaks at 850 W, at $\eta = 6\%$. It should be noted that $\eta = 6\%$ corresponds to optimized deposition conditions yielding the best performance of thermochromic single-phase stable VO_2 films [44]. A continuous

wave radiofrequency (13.56 MHz) power (about 20 W) was applied at the substrate holder in order to facilitate HiPIMS plasma ignition and favor ion bombardment.

The dynamics of the individual pulses was investigated using a fast imaging camera (PI-MAXII, Princeton Instruments) equipped with a 24 mm Nikkor F:4 lens. The exposure time was set at 500 ns with a time delay increment of 1 μs. The camera is only able to take sequential pictures with a 250 ms image extraction time; therefore, each image presented here arises from a different pulse in the same discharge sequence. This experimental methodology was described in detail previously [148]. Custom-made interference filters were placed in front of the camera in order to probe specific spectral regions, 400-450 nm (A) and 750-900 nm (B) [183]. Light emission from the 400 to 450 nm region (filter A) is dominated by ionized argon and vanadium; above 750 nm (filter B), the main emissions are due to the 4s level of neutral argon and the 3s level of atomic oxygen.

5.3 Results and discussion

The dynamics of the observed effect is illustrated in Figure 5-1: it provides an example of the target current and voltage waveforms in the metallic mode ($\eta = 4\%$) and in the poisoned-mode ($\eta = 6\%$), and the variation of the light intensity in the region located at a distance of 4 cm from the target in the poisoned mode. After the first few microseconds of the ignition stage, the light intensity follows the rise of the cathode current during the "on" period, and then it forms a spike just after the cathode voltage is turned off. As one can note, a small shoulder appears in the cathode current peak, an artefact from the power supply that becomes more pronounced at high currents.

Subsequently, this emission decays in about 5 μs following the end of the cathode voltage pulse.

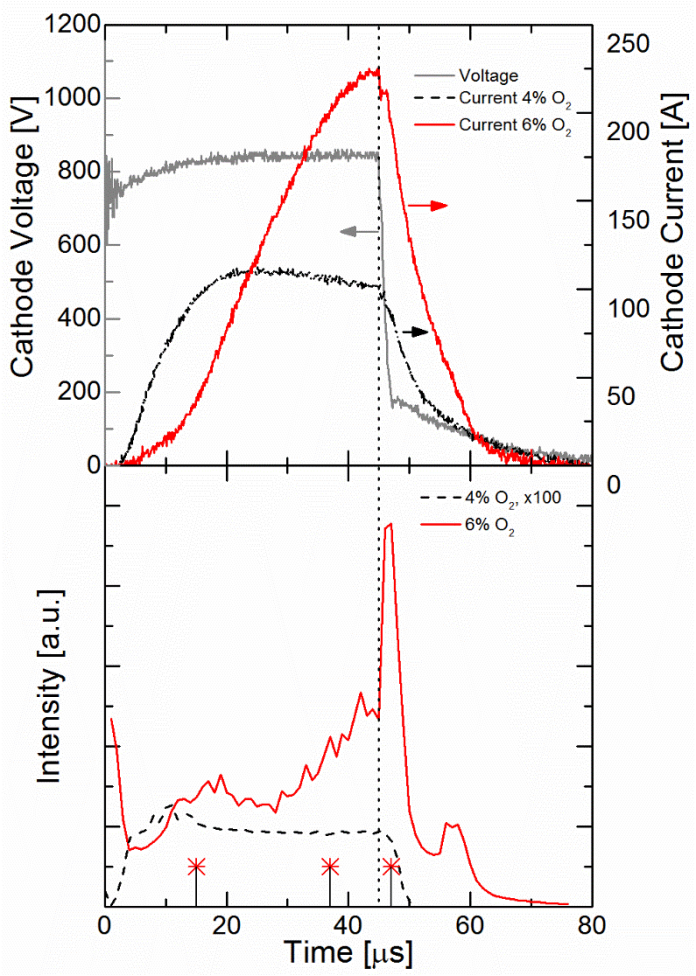

Figure 5-1 (a) Voltage and current waveforms in the HiPIMS discharge operated with the vanadium target, current is presented in the metallic mode at η = 4% (black) and in the poisoned mode at η = 6% (red); and (b) light emission collected from the area around the zero magnetic field zone of the magnetron as a function of time in the metallic mode (x100, black) and in the poisoned mode (red). Red cross in the optical emission indicates the times of the snapshots in Figure 5-2, i.e., at 15, 37 and 47 μs after ignition.

Figure 5-2 shows selected images from the discharge evolution recorded at three different times following the pulse onset: (i) at the beginning of the current rise (15 μs after ignition), (ii) nearly at maximum cathode current during the pulse (37 μs after ignition), and (iii) shortly after the end of the pulse (i.e., at the beginning of the post-discharge interval, or 2 μs after the voltage drop).

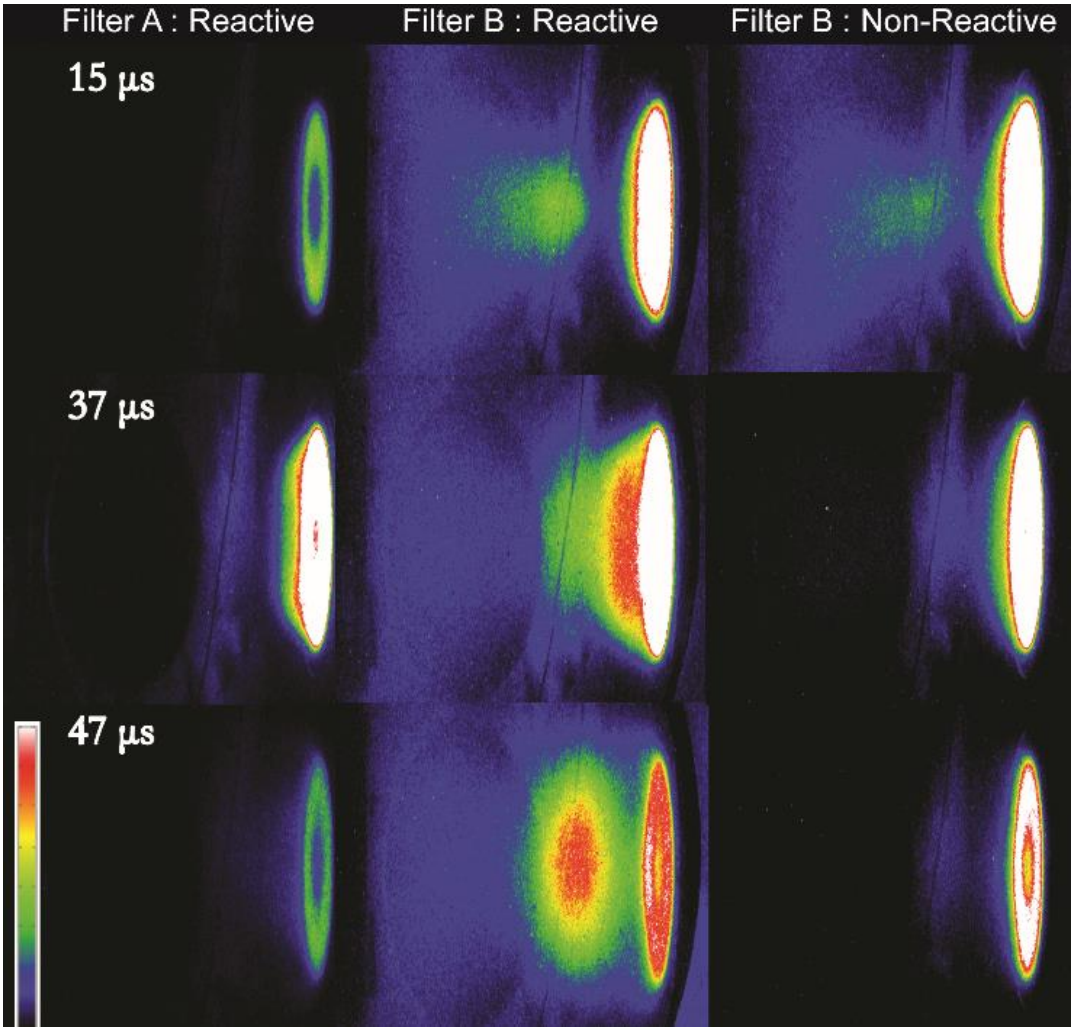

Figure 5-2 Fast camera images with optical filters of the discharge development at 15 µs, 37 µs and 47 µs after the start of the 45 µs pulse above the vanadium target. Filter A allows one to observe metallic species and ionised argon (Ar^+) (left panel), while with filter B, one can see argon neutrals and atomic oxygen in a discharge with $\eta = 6\%$ (center) and non-reactive sputtering mode (right). The vertical line appearing on some images is due to light reflection from the chamber wall.

At the beginning of the pulse (during the first several µs) gaseous species are excited, and they are visible as a small pocket of light originating from argon (15 µs delay time with filter B in Figure 5-2) in both reactive (center-column) and non-reactive (right-column) discharges. Following this period, the plasma is concentrated near the target, with higher emission intensity in the reactive mode compared to the non-reactive mode. This effect can be explained by the presence of oxygen:

target poisoning generates a higher current of 220 A in the oxygen rich discharge compared to 108 A in the metallic mode, with the cathode voltage being kept constant at 900 V.

After the pulse termination, we observe a clear difference between reactive and non-reactive discharges: a "flash" of emission from the zone close to the cathode, yet separated from it, is visible in the former case (second column in Figure 5-2). No such phenomenon is observed in argon-only discharge (third column). It is also important to note that the spectrum of this flash is quite different from the one arising from the pre-cathode zone during the pulse. While the latter one is dominated by the emission from vanadium species and Ar ions [205], the emission during the post-discharge mostly originates from neutral species, argon and oxygen atoms as presented in Figure 5-3, and it is therefore blocked by filter A (first column in Figure 5-2).

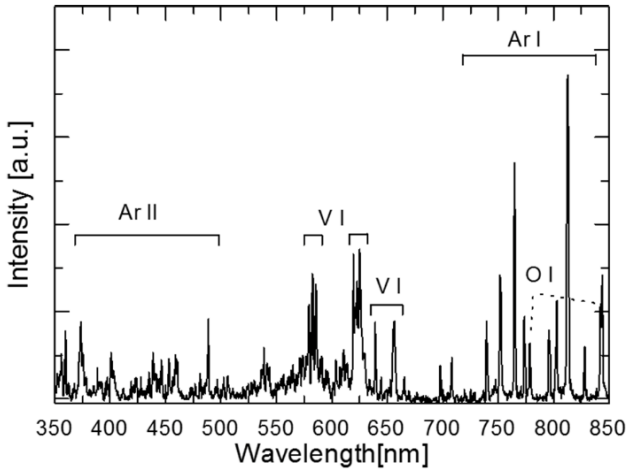

Figure 5-3 Optical emission spectrum taken at 4 cm above the cathode 46 µs after the pulse start of the HiPIMS discharge.

A minimum amount of oxygen in the gas mixture is necessary to produce the post-discharge flash, namely enough to reach the poisoned mode which in our case corresponds to 4% < η < 6%. In the following, we specifically investigate the post-discharge behavior of the reactive HiPIMS at two different concentrations of oxygen in the Ar+O_2 mixture, namely at η = 4% and η = 6%, to observe the difference between the poisoned and not poisoned target discharge dynamic such as presented on Figure 5-4.

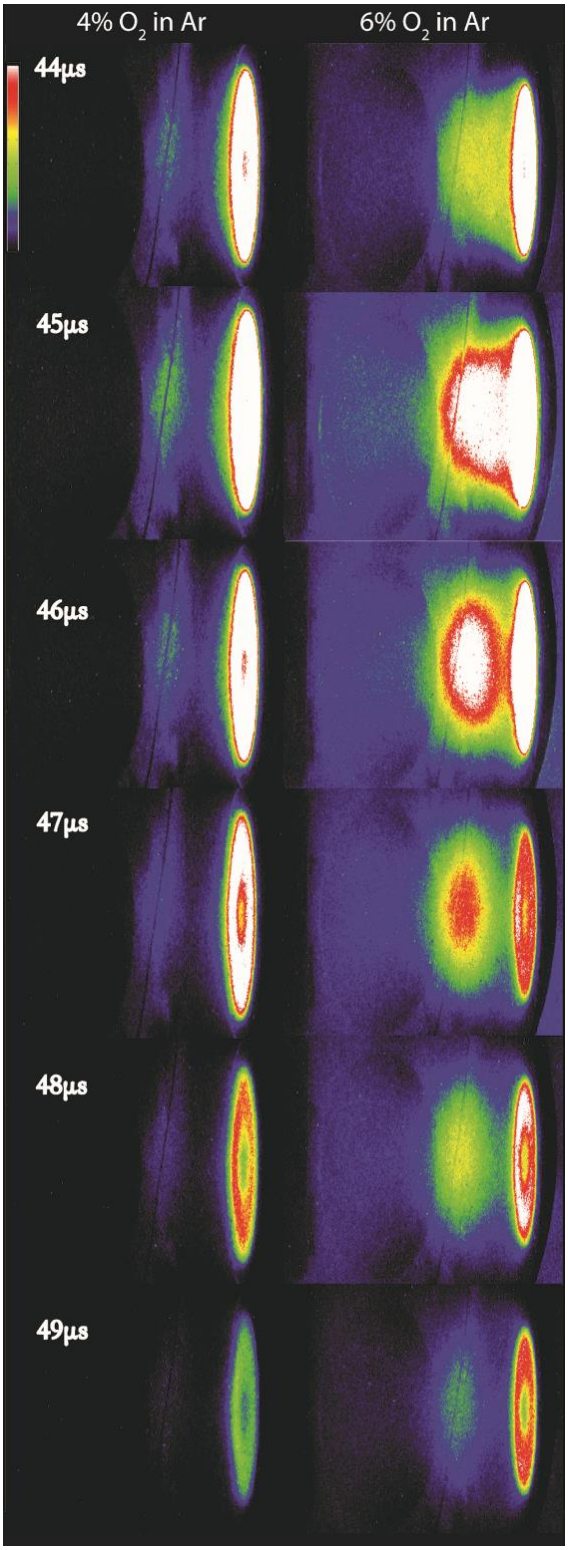

Figure 5-4 Fast camera imaging with optical filter B (λ>750 nm) in η = 4% (left) and η = 6% (right) HiPIMS discharges over the vanadium target during the post discharge.

Plasma emission imaging for η = 6% (Figure 5-4 right) clearly displays an increase of the optical emission intensity of the diffused plasma localized in a space just above the target immediately after the voltage is turned off at 45 µs. Subsequently, we observe a detachment of a spherically shaped emission zone from the main plasma, followed by its collapse during the plasma extinction. In comparison, when the oxygen concentration in the discharge is lower (Figure 5-4 left, η = 4%**)** the post discharge behavior is comparable with the non-reactive plasma regime, i.e., characterized by a fast decay of the emitted light within few µs with light confinement around the magnetron racetrack.

Here we propose a mechanism of formation of this post discharge flash-effect event. Our initial assumptions are based on (i) localization of the light source, (ii) time scale, and (iii) necessity of a threshold concentration of oxygen to produce the flash effect. Accordingly, the process can be divided in three steps:

1. Entrapment of low-energy electrons in a low magnetic field (zero B) zone of the unbalanced magnetron;
2. Radiative collisions of these electrons with argon and oxygen metastables created during the discharge phase. Atomic oxygen and O^- ions are created at this stage;
3. Radiative recombination of O^- ions with Ar^+, V^+ and O^+ ions.

In the following, we discuss these steps in more detail.

First of all, we observed that the center of the flash zone is localized in a region 4 cm away from the target. This position coincides with the null magnetic field zone of the unbalanced magnetron used in this study. The flash of light emission takes place during the first several microseconds of the post-discharge as documented in Figure 5-1 and Figure 5-4**.** This timescale implies that the only mobile particles are electrons. In fact, the ions and neutrals with a thermal energy move at a speed of 0.3 mm·µs^{-1} (300 km·s^{-1}) at 300 K; we therefore suppose that ions and neutrals from the dense plasma zone near the target cannot be displaced fast enough to cause the observed phenomenon. For reflected neutrals or negative oxygen ions formed at the target surface, the speed is too high, namely, 6.5 cm·µs^{-1} (65,000 km·s^{-1}) at 400 eV, and 15 cm·µs^{-1} (150,000 km·s^{-1}) at 900 eV. In addition, there is no reason that space distribution of these species forms a spherical shape seen in Figure 5-2 and Figure 5-4. Same is true for the radiative collisions between gas metastables and neutrals: the timing and the shape cannot be caused by these interactions.

We conclude that electron collisions are at the origin of observed phenomena. Indeed, when the cathode voltage drops from -900 V to -200 V (during the first microseconds after the pulse end) a lower number of fast electrons is produced, resulting in a fast decrease of the electron temperature and density [206], [207]. The slower electrons are subject to the resulting electric and magnetic field gradients in which they drift toward the center of this magnetic trap. This entrapment of electrons near the zero B zone may explain the spherical shape. Our measurements of the magnetic field confirm that the position of the center of this sphere corresponds to the zero B point.

The optical emission in the spectral region of 750-900 nm is dominant during the after-glow (Figure 5-3). The most intense lines correspond to transitions from the 4p to the 4s levels in argon, and from the 3p to the 3s levels in oxygen. Those Ar 4p and O 3p levels can be populated by direct electron collisions with ground-state atoms or by different transitions from the already excited metastable states. The first mechanism is very unlikely to be present in post-discharge, given a rapid decrease of the electron temperature.

Argon and molecular oxygen form metastables that possess lifetimes longer than the pulse duration [208]. The density of oxygen metastables has been measured and found to be proportional to the oxygen partial pressure [171], while the density of argon metastables depends on the pulse length, with a lower density for a short pulse length [185]. Those metastables provide a lower energy threshold for different radiative electron-impact reactions. In order to assess the probability of these reactions, we calculate the electron impact excitation and attachment rate coefficients for selected electron-particle interactions from literature data [209] for electron temperatures ranging from 0.1 to 3.0 eV, and the results are presented in Figure 5-5**.**

For argon species**,** at low electron temperature when T_e<0.5 eV, the reaction rate ratio of k_{Ar^M}/k_{Ar} is larger than 10^{12} implying that direct impact excitation of ground state argon becomes less probable than excitation from metastables ($nAr^M/nAr < 0.001$ [210]). The radiative de-excitation of these atoms contributes to the flash light signal. One should note however that this process does not depend on oxygen concentration and it should be present in non-reactive discharge as well. According to Figures 2 and 4, we conclude that the contribution of this process is not significant.

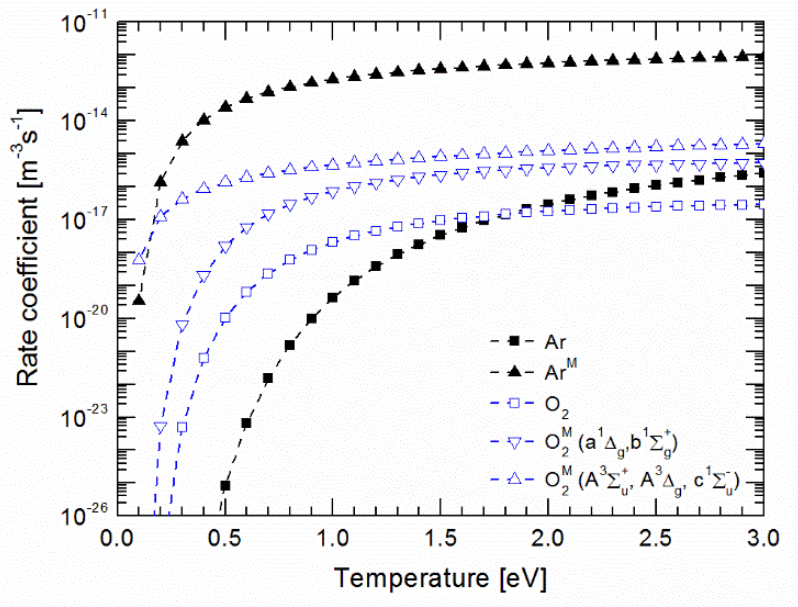

Figure 5-5 Selected rate coefficients for electron excitation of argon (full symbols) by electron impact and molecular oxygen due to electron attachment (open symbols). Data were calculated according to the equations in [209].

For the oxygen molecular species, the rate coefficients for the creation of negative oxygen by electron attachment to molecular oxygen, in the ground and metastable states (plotted in Figure 5-5 as open triangles) dominate over electron-impact excitation and ionization for electron temperatures under 1.5 eV. Especially, dissociative attachment:

$$e^- + O_2^M = O^- + O^*$$

to $(a^1\Delta_g, b^1\Sigma_g^+)$ metastable states generates a large density of negative oxygen and non-radiative O 3p [210], proportional to the low energy electron density, enhanced locally in the magnetron trap, as well as atomic oxygen metastable coming from the dissociation of $(A^3\Sigma_g^+, A^3\Delta_g, c^1\Sigma_u^-)$ molecular oxygen metastable. Such metastable atoms are known to exhibit their density peak at the end of the pulse [203].

Subsequently, the recombination of negative oxygen ions and positive ions $(O^- + I^+ = O + I^*, I = Ar, O\ or\ V)$ gives rise to excited argon and vanadium in the 4p state or excited oxygen in the 5p state with a rate coefficient of $4*10^{-14}$ $m^{-3}.s^{-1}$ independent of the electron temperature [209].

In such way, the short flash at the end of the pulse appears to be a manifestation of atomic oxygen production during the period when the voltage pulse is off.

5.4 Conclusion

In summary, we observed a post discharge flash radiation emission after the end of the HiPIMS pulses in a reactive $Ar+O_2$ gas mixture. We suggest that this singularity is related to the drift of low energy electrons during the post discharge period towards the magnetic trap where the electrons interact with argon and molecular oxygen metastables. The latter process generates negative oxygen ions which then recombine with positive argon and oxygen ions to generate light emission in the 750-850 nm wavelength range. This flash post-discharge effect leading to the production of additional atomic oxygen can explain the lower amount of oxygen needed to produce transparent metal oxide coating with the reactive HiPIMS process [4]. We surmise that the additional energy of about 1 eV obtained by oxygen atoms resulting from Reaction (1) and brought to the surface of the growing film is beneficial and, in addition to other factors, allows one to reduce the substrate temperature needed to deposit high quality thermochromic VO_2 films [44] on temperature-sensitive substrates [201].

Acknowledgments

The authors wish to thank Mr. S. Chenard and Mr. F. Turcot for their expert technical assistance. This research has been supported in part by the Natural Sciences and Engineering Research Council of Canada (NSERC Project number IRC 433808 – 11) through the Multisectorial Industrial Research Chair in Coatings and Surface Engineering (MIC-CSE), and it has benefited from a partial support from the Fonds de recherche québécois sur la nature et les technologies (FRQNT) and its grant to the Quebec Advanced Materials Strategic Research Cluster (RQMP).

CHAPTER 6 ARTICLE 2: HIPIMS-DEPOSITED THERMOCHROMIC VO_2 FILMS ON POLYMERIC SUBSTRATES

Authors: S. Loquai, B. Baloukas, O. Zabeida, J.E. Klemberg-Sapieha, L. Martinu

Article published in: *Solar Energy Materials & Solar Cells*, vol 155, p 60-69, Oct. 2016

Abstract:

Thermochromic vanadium dioxide, VO_2, is a semi-conductor of major interest for energy control applications. Generally, fabrication of high-quality VO_2 films requires a high deposition temperature over 400°C thus limiting its large scale implementation as well as its compatibility with temperature-sensitive substrates. In this work, we demonstrate the deposition of thermochromic VO_2 thin films on flexible polymer substrates using High Power Impulse Magnetron Sputtering (HiPIMS); this process is known for its high degree of ionization, high plasma density and hence high ion flux towards the substrate that allows one to deposit crystalline films at lower temperatures in comparison with conventional sputtering techniques. We first describe the optimization approach of the HiPIMS process followed by the optical performance study of the resulting VO_2 films on Kapton polyimide substrates. The films deposited at temperatures as low as 275ºC are then analyzed by means of temperature-resolved spectrophotometry, XPS, ERD, RBS, Raman spectroscopy and spectroscopic ellipsometry. Optimized films show an infrared modulation $\Delta T_{2500\ nm}$ of up to 50% with a transition temperature τ_c close to the bulk temperature of 68°C.

6.1 Introduction

Traditional glass windows, with their low thermal insulation properties, represent an energetically weak point of a building. This leads to undesirable energy gains and losses which need to be compensated by additional cooling or heating. In fact, in developed countries, temperature control in buildings by temperature management is estimated to account for more than 30% of the primary energy consumption [211]. Only in the US, the portion of this sector in total consumption has increased from 34% in 1980 to 41% in 2010 [212]. The currently commercialized and popular solution is the installation of low emissivity (low-e) windows that offer passive heat transfer insulation leading to a decrease in the energy budget due to heating and cooling. However, in regions with distinct seasons, particularly in continental climates, the possibility of using dynamic (active) glazings for heat transfer control is expected to further reduce energy consumption. For a recent review on fenestration applications, see [213].

A particularly attractive option is the use thermochromic (TC) materials. Defined by a capacity to change their optical properties as a function of temperature, TC materials can be used to provide variable infrared transmittance. First reported by Morin in 1959 [18], these materials were highly explored in the late 80's [214], with a regain of interest in the late 2010's. Of all the possible choices, vanadium dioxide, VO_2, has always been the main material considered for high performance TC systems in smart window applications for the simple reason that it possesses an intrinsic transition temperature, τ_c, of 68°C which is closer to room temperature than other inorganic TC materials. In its low temperature state ($T < \tau_c$) VO_2 displays a semi-conductor monoclinic crystaline phase with a high infrared (IR) transmission, and in its high temperature state ($T > \tau_c$), a metallic rutile crystalline phase with a lower IR transmission. Consequently, the induced transmission variation in the 1-20 μm spectral range is of interest for heat control applications. For example, transmission variations of up to 61% at a wavelength of 2.5 μm have been reported [44].

While of great interest, the commercial application of VO_2 films still faces multiple challenges which are being addressed by different researchers. First of all, the 68°C transition temperature needs to be reduced closer to room temperature – this can be achieved by doping with W and other

metals [215]. Similarly, the relatively low luminous transmittance, around 40% for conventional 60-80 nm VO_2 thick films, and the unpleasant greenish tint can both be addressed by doping [216], or by the addition of antireflection layers [13]. Finally, high performance VO_2 films requires high deposition temperatures above 400°C [19] that are not compatible with temperature-sensitive substrates. The latter problem represents the main motivation of the present study.

It has recently been demonstrated that high-quality VO_2 films can be deposited at temperatures as low as 300°C by using High Power Impulse Magnetron Sputtering (HiPIMS) [44], [63]. Furthermore, the HiPIMS process results in high ionization of the sputtered material [164], [198] that offers an opportunity to fine tune the ion bombardment energy and flux towards the substrate, thus leading to a better control of the film growth and of the resulting microstructure[133]. For example, it has been shown that by using HiPIMS dense and crystalline films of TiO_2 can be obtained at temperatures as low as room temperature [83], and that the use of HiPIMS in its reactive mode can lead to a reduction of hysteresis effects [143].

In the present work, we demonstrate the possibility to deposit high performance TC VO_2 films onto plastic substrates using HiPIMS. Specifically, we apply this approach to two types of flexible Kapton polyimides, namely the traditional yellow-colored Kapton HN as well as a new transparent and colorless Kapton CS. We first describe the optimization strategy of the HiPIMS process with respect to the optical performance criteria of the resulting films. The quality of the TC VO_2 layers is then examined by complementary chemical and structural analysis techniques, and we confirm that the films are highly crystalline and stoichiometric. The results suggest that roll-to-roll deposition of VO_2 films is indeed possible, thus opening new application opportunities such as lamination with glass for retro-fitted smart windows.

6.2 Experimental methodology

6.2.1 Substrates and deposition process

Two types of polyimide substrates were used throughout this study, namely a 50.8 µm thick yellow-colored Kapton HN and a 25.4 µm thick clear Kapton CS polyimide foil. Kapton HN is commercially available from E.I. du Pont de Nemours and Company (DuPont for short). Its ultimate temperature is 450ºC, and it is suitable for operation at temperatures in the 250-350ºC range. The Kapton CS substrate is a prototype colorless polyimide film manufactured by the same company. Due to its larger elastic modulus, we chose a 25.4 µm thick foil in order to obtain a similar rigidity as the Kapton HN. The ultimate temperature for Kapton CS is estimated at 350ºC, thus slightly limiting the deposition to a lower temperature range. Additionally, glass and silicon substrates were added during deposition in order to allow for a comparison of the deposition rates and of the film properties.

The VO_2 films were deposited in a turbomolecularly pumped magnetron sputtering system [6] equipped with a 4-inch-diameter pure vanadium target (99.5%). The cathode was powered by a SIPP2000 HiPIMS power supply made by Melec GmbH. The current and voltage waveforms were monitored with a Tektronix DPO3014 digital oscilloscope using high current and high voltage probes. The substrates were placed on a copper plate at a distance of 15 cm from the target, and the substrate temperature (T_s), controlled by a radiative heater from the back side, was adjusted between room temperature (RT) and 400°C. T_s was measured prior to plasma ignition using a thermocouple in contact with the substrate's surface. We estimate the T_s measurement precision to be about ±5°C for all of our depositions. Indeed, the plasma process may provide additional heating by the way of ion bombardment, fast neutrals' impacts and radiation from both the plasma and the target. While we did not quantify this increase of temperature, it should be similar to more conventional sputtering techniques at comparable average powers as reported by Cormier [217]and Lundin [218]. Also note that the sensitivity of the substrates to temperature acted as probes as their physical properties would have been severely affected by a significant temperature increase.

The VO_2 film fabrication was optimized in three stages: a) by depositing VO_2 onto conventional borosilicate glass (B270), b) by the application of the pre-optimized process parameters to coat polyimide substrates, and c) by applying a TiO_2 seed layer on top of the polyimide; indeed, it is known from the literature that rutile TiO_2, in correspondence with rutile VO_2, has a similar lattice parameter which promotes the growth of crystalline VO_2 [53], [68]. The films themselves were deposited in four steps: (i) the substrate was heated until it reached the desired stable temperature, (ii) the vanadium cathode was exposed to a HiPIMS discharge in pure argon and pre-cleaned for 5 minutes, (iii) oxygen was then introduced into the chamber and the discharge was left to stabilize for 10 minutes in order to obtain a steady reactive sputtering regime. During this stage, a radio-frequency power supply connected to the substrate holder was turned on in order to pretreat and clean the substrates. (iv) Finally, the target shutter was opened for deposition.

After optimization, the process parameters applied for all depositions were as follows: an argon working pressure of 9.7 mTorr (1.30 Pa), a pulse length of 45 μs, a pulse frequency of 200 Hz, and a pulse peak voltage of 900 V. The average discharge power was approximately 350 W, which is comparable to the one used in traditional RF and DC magnetron sputtering processes. Under these conditions, the deposition rates measured on the Si substrate was 0.32 Å/s. The final film thickness values were between 40 and 80 nm.

The radiofrequency (RF) power applied to the substrate holder produced a plasma which provided a stabilizing effect on the HiPIMS discharge as well as additional energy to the growing films by ion bombardment during the time-off period. The self-induced negative bias V_b was set at -200 V between the individual HiPIMS pulses. This value dropped to -30 V during each pulse. The process parameters for the deposition of VO_2 films and TiO_2 seed layers are summarized in Table 6-1 and Table 6-2

Table 6-1 Deposition parameters for thermochromic VO_2 films and TiO_2 seed layers.

	VO_2	**TiO_2**
Target diameter [cm]	10.2	7.6
Pressure [mTorr](Pa)	9.7 (1.3)	4.0 (0.67)
O_2 to Ar ratio [%]	3.9 to 5.6	20
Average target power [W]	300-380	350
Average target power density [W/cm^2]	4.0-4.8	2
Target voltage [V]	900	412
Frequency [Hz]	200	DC
Pulse length [μs]	45	n/a
Film thickness [nm]	40-80	10

6.2.2 Film characterization

Normal incidence spectral transmittance (*T*) of the samples deposited on polyimide and on glass substrates was measured at different temperatures using a Perkin Elmer Lambda 1050 spectrophotometer for wavelengths between 250 nm and 2500 nm. A custom-made heat cell was used to gradually heat the samples from 25ºC to 90ºC at a controlled rate of 1 degree per minute. Using the recorded spectral transmittance vs. temperature curve, the transition temperature could be assessed by using the inflection point of the measured temperature dependence (minimum of the first-derivative) for the heating phase ($\Delta\tau_c^+$) and the cooling phase ($\Delta\tau_c^-$). The transition critical temperature was then determined by simply averaging $\Delta\tau_c^+$ and $\Delta\tau_c^-$ as $\tau_C = \frac{\Delta\tau_{C^+} + \Delta\tau_{C^-}}{2}$.

The optical constants (*n* and *k*) of the films and substrates were determined from spectroscopic ellipsometry measurements using the RC2 ellipsometer from J.A. Woollam Co., Inc. The ellipsometric data (Ψ and Δ) for wavelengths between 400 and 1700 nm were acquired at three different angles of incidence (45°, 55°, 65°) while using a focusing probe to limit the beam area and thus reduce the possible impacts of the polymer substrates' unevenness and bending. To obtain the dependence of *n* and *k* as a function of temperature between 25°C and 100°C, the samples were placed in a heat cell mounted on the RC2 ellipsometer, and the measurements acquired at an angle of incidence of 70°. Modeling of the films was performed using the *CompleteEASE* (J.A. Woollam Co., Inc.) software package. The low temperature state of the VO_2 films themselves was modeled using Tauc–Lorentz and Gaussian oscillators for the UV absorption, a Gaussian oscillator in the near-IR, and a top surface roughness layer modeled by a Bruggeman effective medium approximation. To account for VO_2's metallic-like behavior in its high temperature state, a Drude oscillator was also added. The obtained optical constants were then used as input data to model the film transmission, reflection and absorption using the *OpenFilters* software[219], and to extract film thickness.

The chemical composition of the VO_2 films was evaluated by means of X-Ray Photoelectron Spectroscopy (XPS) with an ESCALAB 3 MKII system from VG Scientific using an Mg Kα source at 15 keV. The first set of measurements was performed on as-deposited samples, while the second set of measurements was carried out following 30 s of argon ion beam sputter-cleaning using an energy of 400 eV. The XPS spectra were then analyzed using reference data from Silversmith *et al.* [220].

The elemental compositional depth profiles of VO_2 films deposited on different substrates were measured by Elastic Recoil Detection in the Time-of-flight mode (ERD-TOF) using the 6 MV Tandem accelerator at the Université de Montréal with a 50 MeV beam of Cu^{9+} ions at a scattering angle of 30°. The elemental composition was then extracted using in-house software.

Finally, the crystalline structure of the VO_2 films was assessed by X-ray diffraction (XRD) and Raman spectroscopy analyses. The XRD measurements were performed in the θ-2θ mode from 20° to 60° and at a grazing angle of 1° using a Bruker D8-Discover diffractometer equipped with a Linkseye CCD accumulation-detector. The diffraction patterns were evaluated using the *DIFFRACT.EVA* software package from Bruker. Complementary Raman measurements were performed with a Renishaw INVIA system using an excitation wavelength of 514 nm.

Table 6-2 List of studied samples and the respective VO_2 deposition temperatures. * denotes the expected thickness.

Substrates	**Deposition time [min]**	**Thickness [nm]**	**Deposition temperatures [°C]**
Kapton HN	40	~80*	200-450
Kapton CS	40	~80*	200-350
Kapton CS + TiO_2	40	~80*	200-350
Glass	20	45	350
Silicon + TiO_2	40	80	350

6.3 Results and Discussion

6.3.1 HiPIMS deposition and process optimization

In the first part of this work, we optimized the HiPIMS deposition conditions, particularly the oxygen flow by investigating the effect of oxygen on the voltage-current waveforms, the average power, and on the TC performance of films deposited on glass.

It was observed that the discharge over the vanadium target can generate two types of current waveforms depending on the oxygen flow, $f(O_2)$. At low $f(O_2)$, from 0 to 2 sccm, the discharge current remains synchronized with the applied cathode voltage, and it follows a "square root function" shape (not shown here) with a saturated peak-to-peak current of 80 A. On the contrary, for $f(O_2)$ equal to or above 2 sccm, initiation of the discharge current is delayed with respect to the voltage, and it increases exponentially in an impulse-like manner without reaching a steady state during the 45 µs of the pulse duration (see Figure 6-1). Peak-to-peak values increased with $f(O_2)$ to saturate when $f(O_2)$ was above 2.5 sccm at 350 A, the power supply's limit. It can also be observed that the power supply was not able to maintain the cathode voltage at the 900 V level for the whole pulse duration. This change of shape of the current waveform is similar to the one reported by Aiempanakit *et al.* who sputtered aluminum and titanium in a reactive atmosphere [166].

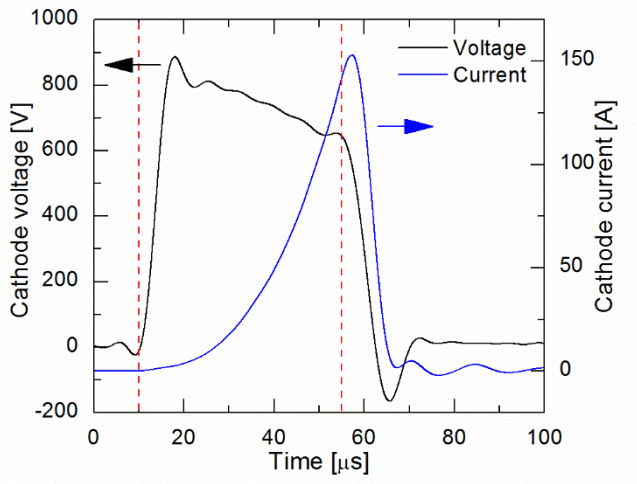

Figure 6-1 Current and voltage waveforms of the HiPIMS discharge over a vanadium target using a pulse length of 45 μs and a peak cathode voltage of 900 V in a reactive atmosphere of 4% of oxygen (2.25 sccm) in argon at a total pressure of 10 mTorr. The dotted red lines indicate the beginning and the end of the voltage pulse.

Following the waveform characterization, we explored the influence of $f(O_2)$ on the discharge power and on the main film characteristics, the results of which are presented in Figure 6-2. One can first observe that at 0 sccm < $f(O_2)$ < 2 sccm the average power slowly increases, followed by a rapid increase for 2.0 sccm < $f(O_2)$ < 2.5 sccm. We assign this sharp increase to a transition from the metallic to the poisoned sputtering regime of the vanadium target (see the gray zone in Figure 2.a). For an $f(O_2)$ > 2.5 sccm, excessive arcing led to pulse inhibition by the arc suppression system of the power supply, giving rise to a rapid decrease in the average power. Due to the large change of the current waveform shape, which becomes more narrow and intense at increased $f(O_2)$, the average target power stays rather stable between 300 W and 380 W, while the peak power increases from 60 kW to 120 kW.

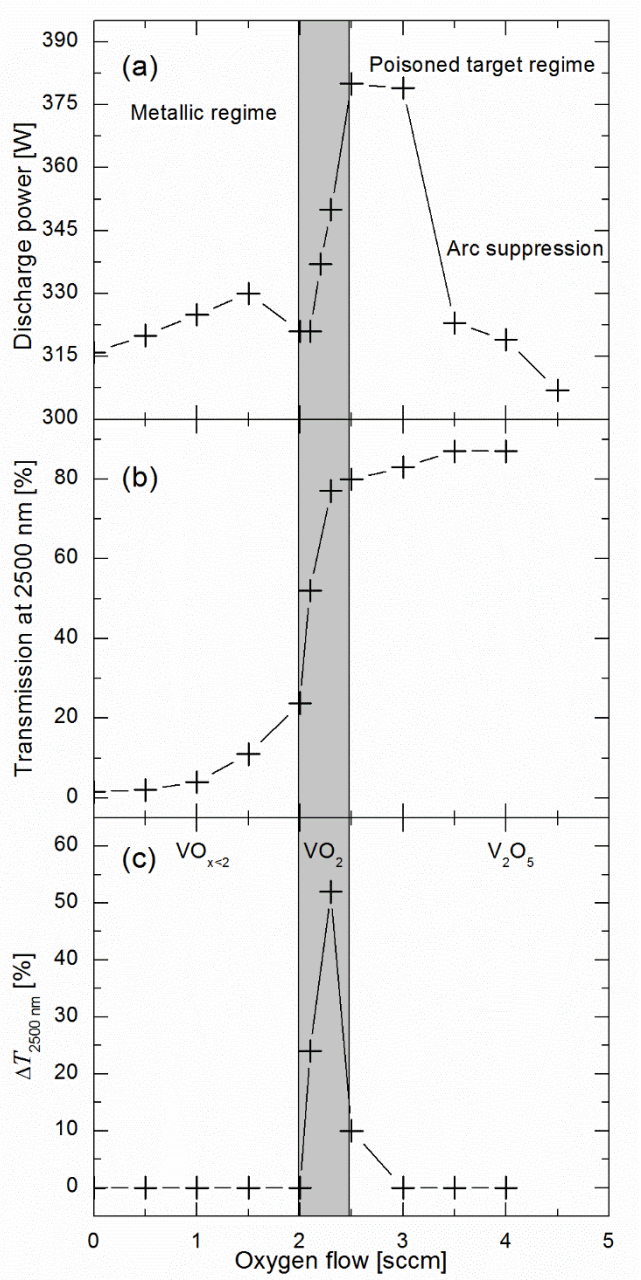

Figure 6-2 Effect of the oxygen flow on: (a) the average discharge power, (b) the optical transmission at 2500 nm, and (c) the optical modulation, $\Delta T_{2500\ nm}$, at 2500 nm. The HiPIMS discharge was operated over a vanadium target using a pulse length of 45 µs, a repetition rate of 200 Hz, a peak cathode voltage of 900 V, and an argon flow of 54 sccm. The grey area represents the transition zone between the metallic and the poisoned sputtering regimes, and corresponds to the window of working conditions used in the present work.

During this initial part of the study, reference samples were deposited on glass at 350ºC for $f(O_2)$ varying from 0 sccm to 4 sccm. The optical transmission at 2500 nm, $T_{2500\ nm,}$ is reported in Figure 6-2.b. It can be observed that $T_{2500\ nm}$ slowly increases for 0 sccm < $f(O_2)$ < 2 sccm, and it then rapidly increases to above 80% between 2.0 and 2.5 sccm. Above 2.5 sccm, the transmission slowly continues to increase to finally reach a steady-state at an $f(O_2)$ = 3.5 sccm.

Figure 6-2.c displays the transmission variation between the low and high temperature states at 2500 nm ($\Delta T_{2500\ nm} = T_{2500\ nm}(T < \tau_c) - T_{2500\ nm}(T > \tau_c)$). We observe that only films deposited for $f(O_2)$ between 2.0 sccm and 2.5 sccm are thermochromic, and that all films outside this relatively narrow window are non-active.

The above-presented results may be explained by the fact that the vanadium oxide films evolve from a sub-oxidized VO_x state ($x < 2$) for the metallic regime between 0 sccm and 2 sccm of $f(O_2)$, to a TC VO_2 in the active region (2.0 sccm < $f(O_2)$ < 2.5 sccm), and finally to the V_2O_5 phase for even higher oxygen flows. V_2O_5 is in fact the most stable form of vanadium oxide and it possesses a lower extinction coefficient in the near-IR as observed and further discussed below ($k_{2500\ nm}$ = 0.26 for VO_2 *vs.* less than 0.01 for V_2O_5 [221]). This evolution of stoichiometry with oxygen is comparable with the one typically reported for DC-sputtered [118] and pulsed laser-deposited films [222]. This shows that the parameter window for which high-quality VO_2 films are obtained is very narrow, especially when using magnetron sputtering (this paper and, e.g., [118]), and for pulsed laser deposition [222]. The data presented in Figure 6-2 can thus be used to assign each zone to the type of deposited oxide. In the rest of this work, the VO_2 films were prepared using the process window of oxygen flow between 2.0 sccm and 2.5 sccm (grey zone in Figure 6-2).

6.3.2 Thermochromic properties of the VO_2 films on polymer substrates

Based on the results described in the previous section we fixed $f(O_2)$ in the range of 2 sccm to 2.5 sccm and performed a series of depositions of VO_2 films on different substrates. We systematically evaluated the TC performance of the films in terms of the normal-incidence optical transmission at room temperature and at 90°C, with the main emphasis on the effect of T_s. Figure 3 summarizes the results for VO_2 films deposited on glass, Kapton HN, and on Kapton CS with a TiO_2 seed layer, the latter one prepared at 350°C as well as at 275°C. The spectrum in Figure 3.d pertains to the lowest temperature at which films deposited on Kapton CS with a TiO_2 seed layer displayed a significant TC behavior. Note that the interference fringes for wavelengths above 1500 nm originate from the thin nature of the substrates.

The transmission in the visible region is typical of what one would expect for a 40 nm thick VO_2 film on all substrates despite the fact that the deposition time was two times longer for the films deposited on polymer substrates (see Table 6-2); we will discuss this phenomenon in more detail in the next section. The observed lower wavelength absorption cut-off depends on the type of the substrate (see transmission curves of the bare substrates in Figure 6-3); particularly, Kapton HN absorbs for wavelengths below 500 nm (Figure 6-3.b) which explains its characteristic orange tint. On the contrary, the colorless Kapton CS transmits down to a wavelength of about 350 nm (Figure 6-3.c and Figure 6-3.d).

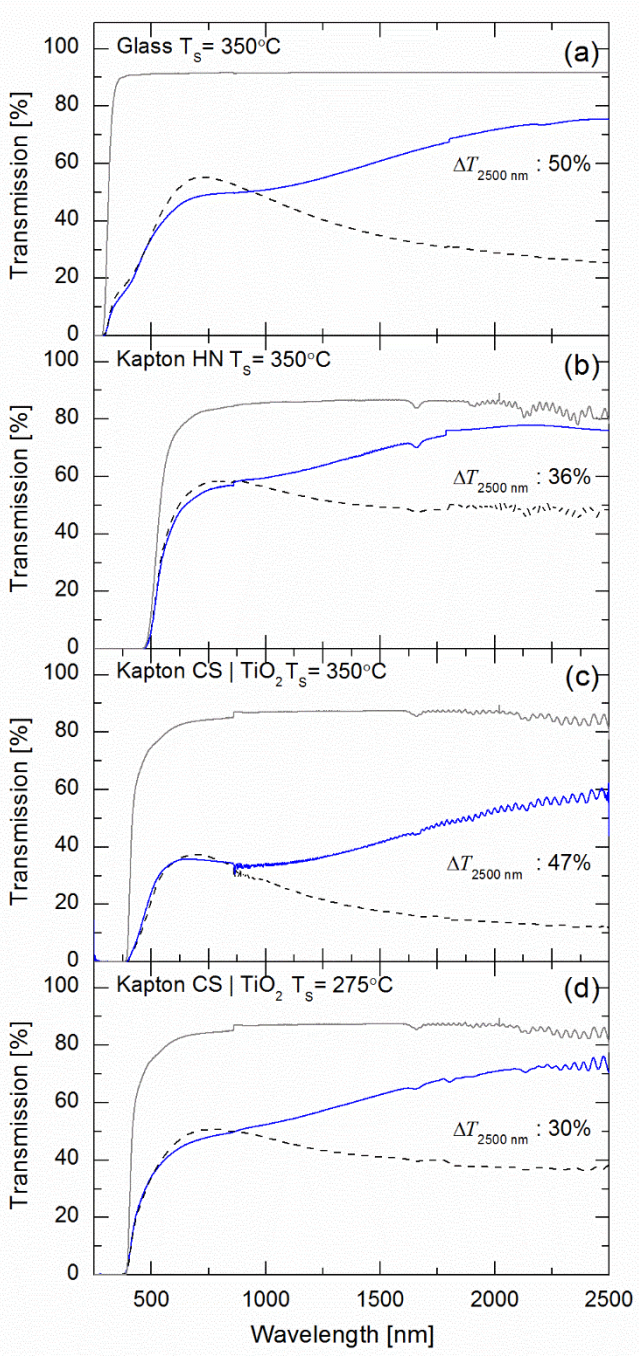

Figure 6-3 Normal incidence optical transmission at room temperature (full blue line) and at 90°C (dashed line) of VO_2 films on glass (a), Kapton HN (b), and on Kapton CS with a TiO_2 seed layer (c and d). The films were deposited at 350°C for a, b, and c, and at 275°C for d. For reference purposes, the transmission curves of a bare substrate have also been added in grey. Corresponding thickness values of the films are shown in Table 6-2.

The maximum transmission in the visible part of the spectrum is about 50% for films deposited on B270 glass. In comparison, films on Kapton HN show a slightly higher value of 55% which could be explained, in part, by the lower refractive index contrast between the VO_2 film and the substrate resulting in lower losses due to reflection (*n* of Kapton HN @ 550 nm = 1.85). Interestingly, one may also note a fairly low visible transmittance of 35% for Kapton CS with a film deposited at 350°C (Figure 6-3.c). This may in fact suggest that the substrate has possibly partially degraded since the deposition occurred close to its maximum operation temperature of 350°C in addition to being kept at this temperature for approximately 1 hour prior to deposition. Correspondingly, lowering the deposition temperature to 275°C better preserves the substrate's physical characteristics and the visible transmittance is seen to increase (see Figure 6-3.d).

The variations in transmission in the visible region between the low and high temperature states are, as expected, relatively small when compared to the near-IR. Slightly smaller changes are observed for the coated polymer, most probably due to the differences in the optical properties of the substrate which affect the substrate/VO_2 interface (see below), due to a higher absorption in the substrate itself (see reference curves in Figure 6-3.b and Figure 6-3.c) as well as due to changes in the VO_2 optical properties; this will be further discussed in Section 6.3.3.

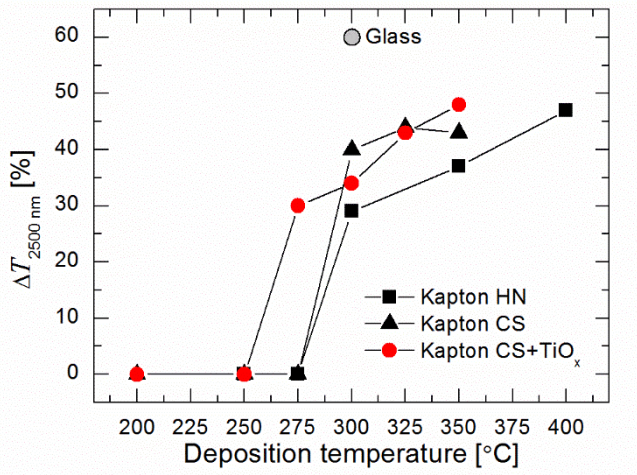

Figure 6-4 Optical transmission modulation at 2500 nm ($\Delta T_{2500\ nm}$) between room temperature and 90°C as a function of the substrate temperature for VO_2 films deposited on Kapton HN, Kapton CS and Kapton CS with a TiO_2 seed layer. The performance of a 75 nm VO_2 film deposited on B270 glass taken from [44] is shown for reference purposes.

The films' infrared optical modulation at 2500 nm, $\Delta T_{2500\,nm}$, between the low and high temperature states, as shown in Figure 6-3 and Figure 6-4, is highly dependent on T_s and the substrate type. Films deposited on glass present a $\Delta T_{2500\,nm}$ value of 50%; keeping in mind that a 45 nm thick film would present a maximum value of 56% using optimal optical properties [44]. This performance is only slightly lower than what has been reported in the literature on glass or alumina. For example, Fortier [44], Sobhan [215] and Tazawa [223] all reported values of $\Delta T_{2500\,nm}$ around 60% for films on glass with thicknesses of 60 to 80 nm.

Without the use of a seed layer, the VO_2/Kapton systems exhibit $\Delta T_{2500\,nm}$ values of 36% (Kapton HN) and 42% (Kapton CS) for the same T_s of 350°C. With the addition of a TiO_2 seed layer, the performance of VO_2 on Kapton CS is further enhanced as documented by a value of 47% for a film prepared at 350°C, i.e., close to what was obtained on glass while using similar deposition parameters. It is interesting to note that the film deposited at a temperature as low as 275°C displays a significant TC activity ($\Delta T_{2500\,nm}$ = 30%). This underlines the benefit of the HiPIMS deposition approach in this work. For comparison, films deposited on Kapton substrates were reported as non-optically active when deposited by conventional magnetron sputtering [224] or pulsed laser deposition [225]at temperatures lower than 350°C.

We can summarize the effect of T_s on $\Delta T_{2500\,nm}$ by concluding that depositions on polymeric substrates display a threshold temperature of about 300°C, whereas the addition of a seed layer allows for further decrease of T_s to 275°C. The effect of the film-substrate interface will be described in the subsequent Sections 6.3.3 and 6.3.4.

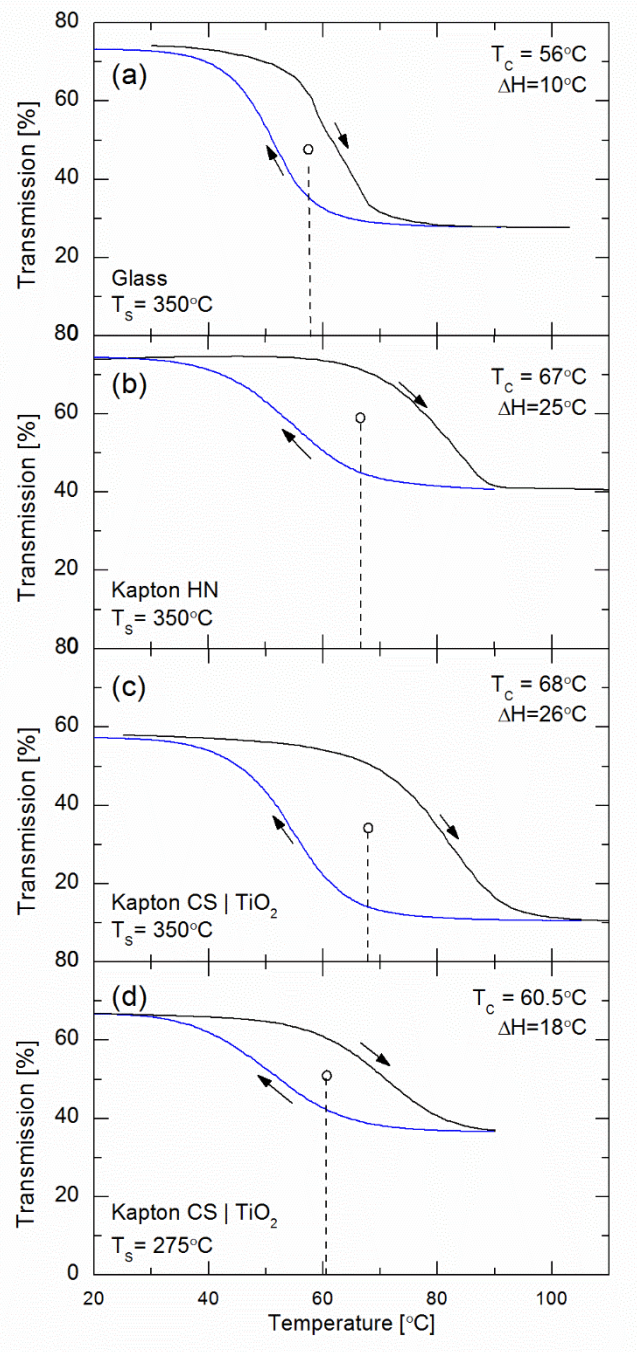

Figure 6-5 Hysteresis curves of normal incidence transmission at 2500 nm as a function of temperature for thermochromic VO_2 films deposited on B270 glass (a), on Kapton HN (b), on Kapton CS with a TiO_2 seed layer (c) at 350°C, and at 275°C (d). The open dot represents the position of the transition temperature, τc.

It is also of interest to investigate in more detail the phase transition properties of the thermochromic films by studying their transmission hysteresis curves ($T_{2500\ nm}$ *vs.* temperature) which are shown in Figure 6-5 for four different samples. The TC effect is associated with a phase transition that requires a certain amount of energy to be dissipated. It is generally accepted that the shape and form of the hysteresis bears information about the transition process which is affected by the mechanical stress and by the microstructure of the VO_2 films [50].

The films deposited on polyimide substrates at 350°C (see Figure 6-5.b and Figure 6-5.c) present a large hysteresis with a transition temperature, τ_c, close to the critical temperature of 68°C of bulk VO_2, while the film deposited at 275°C on Kapton CS with a TiO_2 seed layer (Figure 6-5.d) exhibits a lower value τ_c of 60.5°C. In comparison, the film deposited on glass (Figure 6-5.a) has an even lower τ_c of 56°C and a narrower hysteresis comparable to HiPIMS-deposited TC films previously reported [44]. We consider that the observed changes in τ_c are the result of a combination of several effects, namely the grain size, oxygen deficiency and different stress levels present in the VO_2 films. For instance, it has been reported that, for a single crystal VO_2, compressive stress can lower the transition temperature at a rate of 2°C/100 MPa [226], [227] or 7°C per 0.1% of the c-axis lattice deformation [56] . Here, we surmise that the polymer substrates possessing a lower Young's modulus and a visco-plastic behaviour may accommodate the thermal expansion coefficient mismatch between the film and the substrate by mechanical creep during the cool down period. Furthermore, a certain level of shrinkage of the substrate may occur leading to the coated substrates' tendency to roll up. This would lower the films' internal stress and consequently explain the observed bulk-like τ_c. In addition, the seed-layer coated Kapton CS, rigidified by the presence of a thin TiO_2 layer, possesses a lower τ_c value which is nevertheless higher than for the glass substrate. Finally, the hysteresis width has been shown to be linked with the grain size [51], [228]; therefore, we may assume that the films deposited on polymer substrates possess a smaller average grain size.

6.3.3 Ellipsometry measurements and the optical properties

Even if spectroscopic ellipsometry has been successfully used for the characterization of TC VO_2 films [44], [45], [223], fitting VO_2's optical properties can represent a challenge due to the presence of complex gradients inside the film. To assess the thickness of our VO_2 films on Kapton, we chose to apply a 3 step process: 1) model the properties of a VO_2 layer on a Si|TiO_2 substrate which was deposited at the same time as the Kapton sample, 2) model the Kapton substrate's optical properties, and 3) use the optical properties of VO_2 and Kapton determined in steps 1 and 2 to model the ellipsometric data of our films on Kapton.

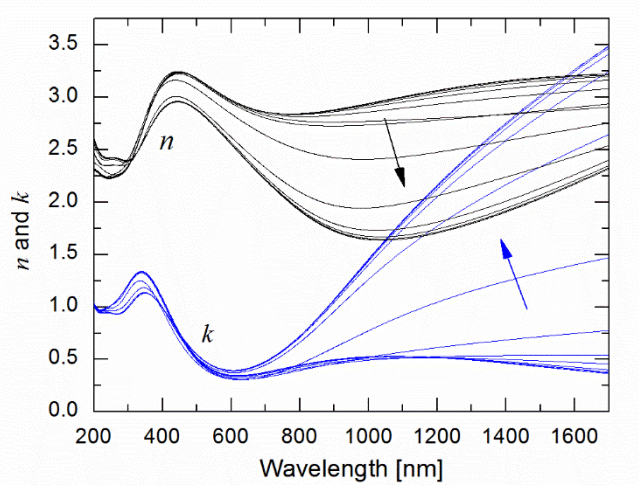

Figure 6-6 Dispersion curves at every 5°C from 20°C to 90°C of the optical constants (n and k) for an 80 nm thick VO_2 film deposited at 350ºC on a silicon substrate with a 9 nm thick TiO_2 seed layer. The arrows indicate an increasing temperature.

The obtained optical constants (*n* and *k*) as a function of temperature for a VO_2 film deposited on Si with a TiO_2 seed layer are presented in Figure 6-6. We can observe that with increasing temperature, the refractive index *n* significantly decreases in the 800-1600 nm wavelength region whereas the extinction coefficient *k* increases at the same time. This data is consistent with the values we reported on glass substrates [44] and with those published by Kakiushida *et al.* on silicon [46], [121].

The ellispometric angles, Ψ and Δ, were then measured in more detail on the films deposited on Kapton. In order to reduce interference effects resulting from the low thickness, microprobes were installed to increase accuracy (200 x 200 μm spot size) and the substrates' backside was roughened. We then proceeded to model the ellipsometric data by using a vanadium oxide film with the optical properties shown in Figure 6-6. This basic model proved to be insufficient and multiple additional model variations also proved inadequate to model both the ellipsometric data and the transmission simultaneously.

Multiple factors may explain the above-mentioned complexity, the principal one being ellipsometry's high sensitivity to the presence of inhomogeneity. While the effect of thickness non-uniformity can be reduced by using microprobes, the presence of complex growth gradients cannot. It is therefore our opinion that the highly energetic HiPIMS process is most probably at cause here by a) modifying the Kapton's properties, and b) generating a significant interphase between the substrate and the VO_2 film, an effect that will also be shown and confirmed in Section 6.3.4.

In response to the complexity of establishing an appropriate ellipsometric model, another approach was implemented in order to approximate the thickness of our films by modeling the spectral performance of an ideal Kapton HN|VO_2 sample for different thicknesses of VO_2 ranging from 10 to 80 nm (see transmission (normal incidence), reflection (8 degrees) and absorption (1 – R - T) in Figure 6-7. We can observe that the transmission, reflection and absorption of our VO_2 film on Kapton HN are almost at par with the optical performance of a 15 nm modeled-VO_2 film, especially in the near IR region of the spectrum. It is also important to note that the experimental spectra shown in Figure 6-7 contain the total transmission/reflection which corresponds to the addition of the specular and the diffuse components. Indeed, following the deposition process scattering increased from below 1% up to about 10%. Taking scattering into account is in fact essential in order to properly assess absorption. Therefore, although an approximation, Figure 6-7 allows us to confirm that the thickness, at least the equivalent amount of active VO_2, on Kapton HN is far from the expected 80 nm observed on the adjacent co-deposited Si|TiO_2 sample. This once again hints towards the presence of a broad interphase between the substrate and the VO_2 film.

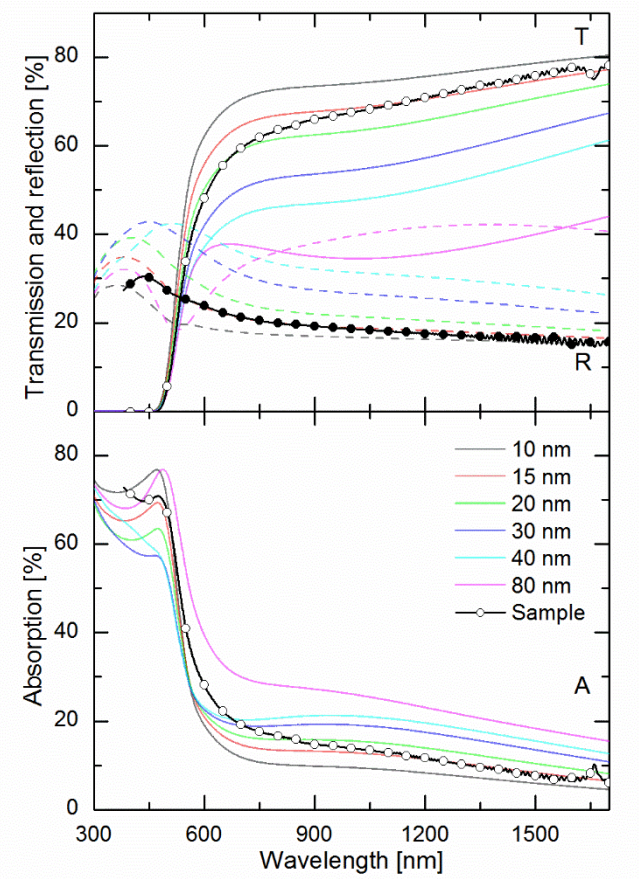

Figure 6-7 Modelled transmission (full lines)/reflection (dashed lines) [top] and absorption [bottom] of VO_2 thin films on a Kapton HN substrate. The measured values for HiPIMS-deposited film at 350°C (lines + circles) are also shown for comparison.

6.3.4 Composition and microstructure

In this final part, we performed systematic microstructural and compositional analyses of the VO_2 film systems in order to explain the observed optical and thermochromic behavior. In agreement with our earlier results [6], XRD diffractograms (not presented here) obtained for VO_2 samples deposited on glass contain peaks at 27.8°, 39.7°, 42.2°, 44.5°, 55.4° and 57.4°, corresponding the (011), (002), (210), (012), (220) and (022) planes respectively, all belonging to the monoclinic VO_2 phase (JSPDS card 44-0252). However, we did not observe these peaks for samples deposited on Kapton. In fact, the polyimide substrates give rise to a broad diffraction peak ranging from 10° to 30° due to the polymer's semi-crystalline structure [229]. This broad and intense feature overlaps with the main VO_2 diffraction peak positioned at 27.8° thus masking its relatively low intensity and prohibiting any worthy observations in this case.

A typical Raman spectrum of a VO_2 film deposited on a TiO_2-coated silicon substrate (at the same time as on the Kapton CS samples) is shown in Figure 6-8. All peaks in this spectral region, namely those positioned at 192, 223, 261, 309, 339 291, 443 and 614 cm^{-1} correspond to stoichiometric VO_2 [230]. A small V_2O_5 peak is also noticed (at 289 cm^{-1}), most probably the result of surface oxidation through interaction with the ambient humidity [78].

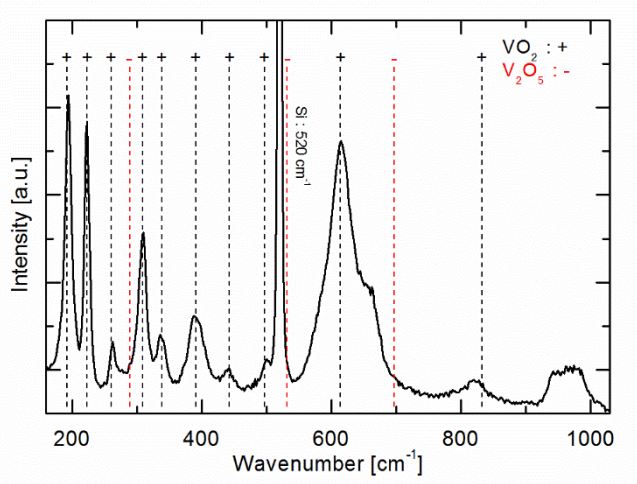

Figure 6-8 Raman spectrum of an 80 nm thick VO_2 film deposited at 350ºC on a silicon substrate with a 9 nm thick TiO_2 seed layer. The peak at 520 cm^{-1} is the silicon substrate's response.

When analyzing the Raman spectra of films on the polymer substrate, the outcome is similar to the case of the XRD measurements: Kapton polyimide presents a large fluorescence ranging from 200 cm^{-1} to 1800 cm^{-1} due to Raman scattering peaks from imide and phenoxyphenyl groups [231]. Such a high fluorescence intensity obscures the peaks related to the VO_2 film which is very thin (several tens of nm); indeed, most of the signal originates from the polymer substrate due to the high penetration depth of the Raman probe (which in our case is estimated at around 2 μm). In summary, we assume that the VO_2 films on the polymer substrate retain their crystallinity, revealed on the glass and silicon substrates, as also indicated by the TC behavior discussed in Section 6.3.2.

Table 6-3 Atomic composition obtained by XPS before and after ion cleaning.

	Glass		**Kapton HN**	
Element (at.%)	*Before*	*After*	*Before*	*After*
O	54.9	64.1	42	60.2
V	16.4	32.3	11.9	26.4
O/V ratio	3.34	1.99	3.53	2.28
C	25.1	3.6	42.8	10.3
N	1.7	0	3.4	3.0

The composition and the chemical structure of the VO_2 films were studied by XPS. The results obtained from the survey spectra from samples on glass and on Kapton HN before and after sputter cleaning are shown in

Table 6-3. The O/V ratio is seen to be relatively high for as deposited films on glass (O/V=3.34) and on Kapton (O/V=3.53), while a ratio of 2 is expected for VO_2 and 2.5 for V_2O_5. After a surface cleaning with Ar^+ ions, using very "mild" conditions (an acceleration voltage of 400 V for 30 s is estimated to remove a surface layer of a few nm), the O/V ratio drops to 1.99 on glass and to 2.28 on Kapton. This trend is also observed by analyzing the high-resolution XPS spectra where, before surface cleaning, both samples present a mix of V^{4+} and V^{5+} oxidation states (not shown here). After cleaning, the films clearly exhibit the presence of the V^{4+} phase. This is expected as some V^{5+} can form over time as VO_2 can react with oxygen and water in the atmosphere and transform into its more stable V_2O_5 when the surface is not protected, in agreement with [78].

One can also observe a more significant surface concentration of carbon (> 40 at. %) for an as-deposited film on Kapton. Such a large carbon content can be attributed, besides surface contamination due to the sample transfer through ambient air, to partial volatilization of the polymer during the substrate plasma pretreatment and the initial film growth. In such a case, carbon-containing species can redeposit [231] and intermix with the growing VO_x film, thus contributing to the formation of a broad interphase region in accordance with our optical measurements (see Section 6.3.3), and TOF-ERD results discussed in more detail below.

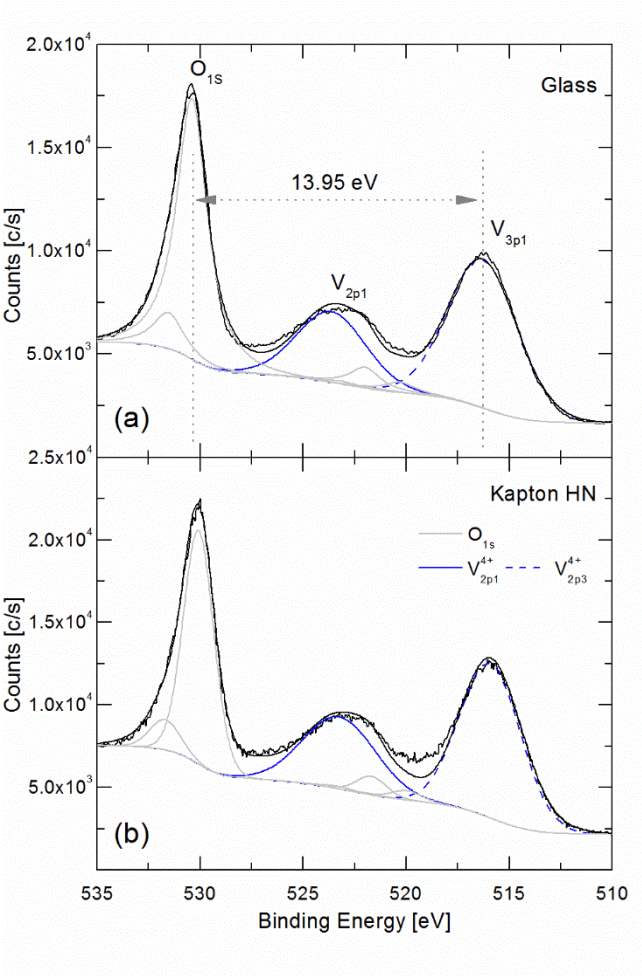

Figure 6-9 High resolution XPS spectra of the O_{1s} and V_{2p} peaks of VO_2 films deposited on glass (a) and on Kapton HN (b) at a substrate temperature of 300°C, after sputter cleaning.

High resolution core-level spectra of V_{2p} and O_{1s} peaks for films deposited at 300°C on glass and on Kapton HN are shown in Figure 6-9. The V_{2p} core-level doublet spectrum reveals peaks at the

binding energies of 516.5 eV and 524.0 eV. This corresponds to spin-orbital splitting of the $V_{2p3/2}$ and $V_{2p1/2}$ components, respectively, indicating that the valence value of vanadium is +4, in agreement with the VO_2 stoichiometry, as also observed by others [30], [232], [233].

The O_{1s} peak has been deconvoluted into two components revealing the presence of O_{1s}-VO (530.4 eV), O_{1s}-VOH and C=O (531.7 eV) bonds. In addition, the peaks at 522.0 eV and 520.3 eV derive from the X-ray $K\alpha_3$ and $K\alpha_4$ satellites of O_{1s}, while their intensity and spacing is characteristic of the Mg X-ray. The positions of the O_{1s} and $V_{2p3/2}$ peaks can, in fact, also be used to determine the oxidation state of the vanadium oxides; specifically, the energy difference between these two peaks ($O_{1s} - V_{2p3/2}$) is 13.95 eV which is consistent with the oxidation state of vanadium [232] once again confirming its valence value of +4 [233].

The elemental composition and the compositional depth profile of TC VO_2 films on Kapton and on glass have also been assessed by TOF-ERD measurements, and the results are presented in Figure 10. The regions where near-stoichiometric VO_2 is present are indicated in grey; the values of average concentration for each element throughout this gray zone are then summarized in Table 6-4.

Table 6-4 Average composition obtained from ToF-ERD measurements of the grey zone shown in Figure 6-10.

Element [at.%]	**On Glass**	**On Kapton HN**
O	56.8	51.0
V	25.5	23.6
O/V ratio	2.23	2.17
H	9.6	9.4
C	-	11.1
N	-	1.5
Si	1.3	-
B	3.7	-
Mg	1.0	-
K	0.4	-

A detailed analysis of the ERD results in Figure 6-10 shows that the total number of V atoms through the sample is 1.3×10^{17} at.cm^{-2} for glass, and 2.5×10^{17} at.cm^{-2} for Kapton HN. These values correspond to the amount of V needed to form 39 nm and 75 nm, respectively, of an "ideal" VO_2 film with a bulk density of 4.57 g/cm^3. This is in very good agreement with the film thickness values of 45 nm and 80 nm obtained from ellipsometric measurements, respectively, for VO_2 simultaneously deposited on glass and on Si.

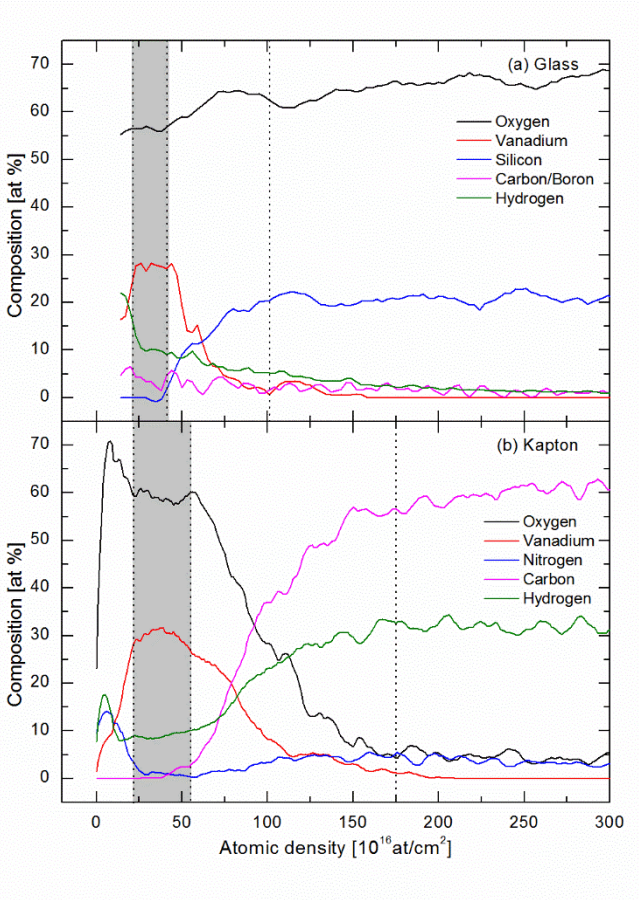

Figure 6-10 ERD-TOF compositional depth profiles of VO_2 films deposited on glass (a) and on Kapton HN (b) at a substrate temperature of 400°C. The grey area represents the thickness of the VO_2 film, i.e. the region where the O/V ratio is close to 2. The dotted line represents the penetration depth of vanadium into the substrate (depth of the interphase).

The V-containing layer is composed of different elements. Similarly to XPS, ToF-ERD analysis shows that besides V and O, the film deposited on Kapton contains carbon, and nitrogen, and it also reveals the presence of hydrogen. Presumably, the latter elements originate from the polymer that is partially volatilized during the surface pretreatment step and at the beginning of the deposition. Interactions of energetic ions and photons from the HiPIMS discharge with the surface of Kapton contributes to the formation of a physically thick interfacial region due to re-sputtering, interface mixing and accelerated diffusion in agreement with our earlier studies [234]. The results in Figure 6-10 indicate that the penetration depth, *d*, of oxygen and vanadium atoms is much deeper in the case of Kapton (d = 145×10^{16} at.cm^{-2} or 175 nm) compared to glass (d = 60×10^{16} at.cm^{-2} or

75 nm). On the one hand, the presence of such an interphase generally leads to improved film adhesion to polymers [231], [234], but, specifically in this work, the vanadium atoms confined in this region seem to be partially lost and non-contributing to the thermochromic activity of the final film.

As a result, only the top part of the film deposited directly on Kapton polyimide has the VO_2 stoichiometry and crystallinity necessary for the thermochromic activity. This finding is in accordance with the transmission and ellipsometry measurements described above. While a longer deposition time seems to resolve this problem, we believe that fabrication of a suitable diffusion barrier (e.g., SiN_x) on the polymer surface will improve efficiency of the VO_2 deposition process, and possibly further enhance the optical properties of the thermochromic layers.

6.4 Conclusions

In conclusion, we have demonstrated that high quality thermochromic VO_2 films can be deposited on polyimide substrates by HiPIMS. Using this highly energetic process, we obtained thermochromic performance, $\Delta T_{2500\ nm}$, of up to 47%, largely exceeding previously reported values for films deposited on polymers substrates. Furthermore, the addition of a TiO_2 seed layer enabled us to deposit an active VO_2 at temperatures as low as 275°C with a respectable performance of 30%. In accordance with these observations, the bulk of the films was shown to be stoichiometric. Through the use of ellipsometry in combination with spectrophotometry, we were able predict the presence of a large interphase in the case of VO_2 on polyimides. This broad interphase was also confirmed following a TOF-ERD analysis. In addition, a transition temperature close to the bulk value of 68°C was observed, indicative of a stress-free material.

The results demonstrate the potential towards large scale production of VO_2 films on polymer substrates using a roll-to-roll deposition. The resulting films could then be laminated onto glass for smart windows (by using polymers such as the colorless Kapton CS) or onto other substrates for applications requiring IR flux control capabilities including, e.g., smart radiator devices for micro and nanosatellites. As also discussed, the films' performance and properties could be further

enhanced by a judicious control of the film substrate interface to limit vanadium and oxygen diffusion into the substrate by the use of a diffusion barrier.

Acknowledgments

The authors wish to thank Mr. S. Chenard and Mr. F. Turcot for their expert technical assistance, Dr. M. Chicoine for the ions beam analyses, Dr. T. Schmitt for the XRD measurements, Dr. J. Lefebvre for her help with XPS analysis, and Dupont for providing the Kapton CS polymer foils. This research has been supported, in part, by the Natural Sciences and Engineering Research Council of Canada (NSERC) through the NSERC Multisectorial Industrial Research Chair in Coatings and Surface Engineering (MIC-CSE), and it has benefited from a partial support from the Fonds de recherche québécois sur la nature et les technologies (FRQNT) through its grant to the Quebec Advanced Materials Strategic Research Cluster (RQMP).

Additional material: Additional figure provided to the reviewer to access the non detection of XRD peaks on Kapton samples.

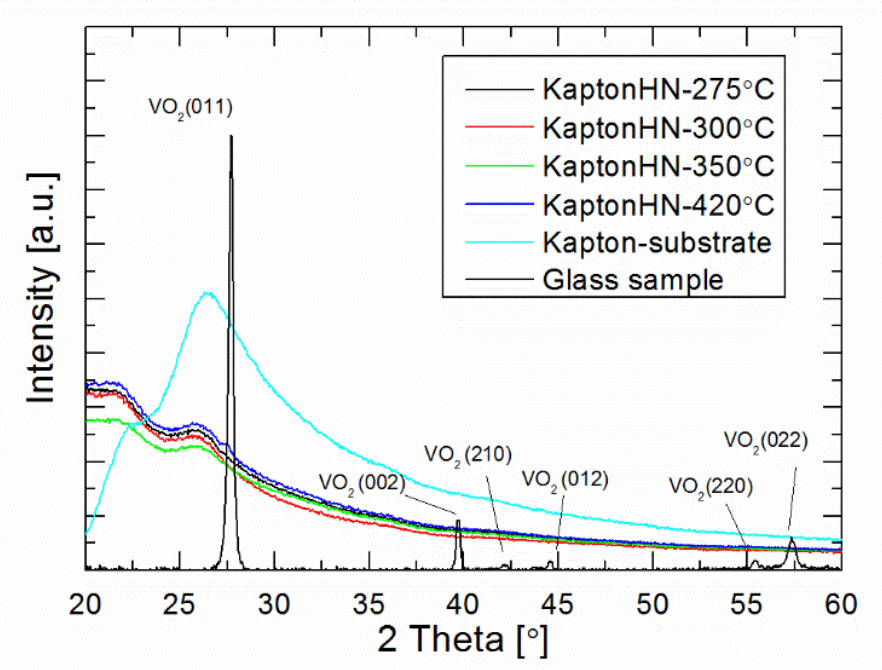

Figure 6-11 XRD pattern from a 65 nm thick VO_2 film deposited by HiPIMS on glass (black) and Kapton HN substrates at different temperatures. The light blue curve corresponds to a bare Kapton HN substrate.

CHAPTER 7 ARTICLE 3: HIPIMS-DEPOSITED THERMOCHROMIC VO_2 FILMS WITH HIGH ENVIRONMENTAL STABILITY

Authors: S. Loquai, B. Baloukas, O. Zabeida, J.E. Klemberg-Sapieha, L. Martinu

Article published in: *Solar Energy Materials & Solar Cells*, vol 160, p 217-225, Feb. 2017

Abstract:

A comparative study of the environmental stability of high power impulse magnetron sputtered (HiPIMS) and radio frequency magnetron sputtered (RFMS) thermochromic vanadium dioxide thin films in a highly oxidizing environment has been performed. We observe that RFMS-deposited VO_2 films quickly transform into V_2O_5 at 80 ºC and 100% relative humidity while HiPIMS-deposited films retain their thermochromic behaviour at least three times longer. Following a thorough analysis of the films, this increase in performance is ascribed to the films' higher density and larger average grain size. The results indicate that the HiPIMS process provides sufficient durability for VO_2 films without the need for a diffusion barrier used in typical everyday conditions. Still, when a 35 nm thick SiN_x diffusion barrier is added on top of the HiPIMS VO_2 films, the thermochromic device shows less than 5% loss in thermochromic performance following extended accelerated ageing.

7.1 Introduction

Additional control of the thermal transfer properties of architectural glass through the implementation of smart windows is one of the most important avenues presently being explored to decrease the energy consumption of buildings [84]. In this respect, vanadium dioxide (VO_2), with its thermochromic (TC) properties, is a promising material. Indeed, VO_2 presents a reversible metal-to-insulator transition at a critical temperature τ_c of 68 °C accompanied by a large modulation of its infrared (IR) transmission. Specifically, in the low temperature state ($T < \tau_c$), VO_2 is a semiconductor with a monoclinic crystalline structure which is transparent to IR whereas in the high temperature state ($T > \tau_c$), it presents a metallic-like rutile (tetragonal) crystalline phase with a low transmission in the IR due to a combination of increased absorption and reflection. For these reasons, this makes VO_2 one of the strongest candidates for smart windows [84] as well as for smart radiator devices for satellites [93], [97].

For decades now, work has mostly concentrated on modifying the fundamental characteristics of VO_2 to compensate its application drawbacks such as changing its natural greenish tint by doping [235], decreasing the τ_c closer to room temperature through doping [236], and increasing its luminous transmission through the implementation of VO_2-based interference filters [237], or by the dilution of VO_2 in the form of nanoparticles in a dielectric matrix (so-called nanothermochromics [99]).

However, there remains another important challenge associated with VO_2: its environmental instability. Indeed, vanadium oxide naturally transforms by a progressive oxidation process into the more stable V_2O_5 which, moreover, is well known to be soluble in water. Specifically, in the presence of oxygen, VO_2 will slowly transform into the intermediate oxides of V_6O_{13} and V_3O_7, before finally reaching the V_2O_5 phase [19].

The implementation of VO_2 thin films in ambient and humid water-containing environments thus leads to a relatively quick decrease in their TC performance. A typical way to protect a material from water and oxygen is obtained by the addition of an overlying diffusion barrier such as Al_2O_3, HfO_2, SiN_x, etc. In the specific case of VO_2, Saitzek *et al.* studied the effect of cerium oxide CeO_2 [80] on top of VO_2 in the context of variable infrared emissivity applications. They reported that the non-protected films displayed a dendritic growth formation on the surface following a 6-month exposure to ambient air at room temperature; however, the resulting loss in performance was not

measured. Transparent and conductive ZnO:Al coatings were also studied by Kang *et al.* [238] to enhance the performance of VO_2 in the visible and near-infrared ranges by increasing its luminous transmittance and solar transmittance variation by interference effects. Samples were subjected to a rapid thermal annealing at 450 °C in an ambient atmosphere: once again, non-protected VO_2 films oxidized in less than 400 s and possessed no TC activity. Protected coatings presented a different oxidation degradation mechanism with the formation of an overlying $Zn_2V_2O_7$ intermix-layer that, according to the authors, protects the sample from further oxidation. Finally, Ji *et al.* [78], [79] focused solely on the protection of VO_2 against degradation by the addition of a 10 nm to 150 nm thick Al_2O_3 film. The authors showed that a minimum thickness of 30 nm is sufficient to protect VO_2 against humid environments (80 °C and 100% R.H.) for up to 120 hours.

In the present work, we study the impact of high power impulse magnetron sputtering (HiPIMS [142]) on the stability of VO_2 thin films. Indeed, HiPIMS is known for its high ionization rate of sputtered particles both in metallic and reactive processes [239] while also enabling hysteresis-free reactive sputtering [143], [168]. The large flux of sputtered particles can also be used to provide additional energy to the growing film, leading to a higher density without the incorporation of gaseous species thus suppressing mechanical stress [169]. Correspondingly, HiPIMS has also been shown to result in the deposition of polycrystalline films at lower temperatures [44]. This has in fact been successfully implemented and demonstrated for the deposition of high performance thermochromic VO_2 on glass [44], [63] and polymers [201] at temperatures as low as 275 °C, a temperature significantly lower than the typically required 400–500 °C.

In order to demonstrate the beneficial impact on the environmental stability of HiPIMS-deposited VO_2 films, we compare the optical performance of films fabricated under comparable conditions by HiPIMS and by radio-frequency magnetron sputtering (RFMS). Contrary to the above-mentioned articles, we not only study the effect of exposing VO_2 to an aqueous environment in terms of its optical performance, but also systematically evaluate the resulting structural and chemical changes in the films. Finally, an additional SiN_x diffusion barrier is also added to protect against oxidation, and its impact on the degradation dynamics between unprotected and protected coatings is evaluated. Interestingly, protected RFMS samples show degradation kinetics similar to unprotected HiPIMS samples. Our results suggest that HiPIMS deposition of VO_2 offers an attractive alternative to the deposition of an additional oxidation barrier in the case of mildly oxidizing environments.

7.2 Methodology

7.2.1 Film deposition

In this study, vanadium oxide and silicon nitride films were deposited in an ultra-high vacuum multi-magnetron process chamber (CMS-18, Kurt J. Lesker Co., Ltd.). The magnetron guns were equipped with 3 inch (7.62 cm) targets of pure vanadium (99.999%) and of boron-doped silicon (0.05-0.02 Ohm.cm). The substrates were 2 mm thick 5 x 5 cm B270 glass from S.I. Howard Glass Co., Inc. During deposition, substrates were rotated to ensure good thickness uniformity (≤ 3% variation).

Both HiPIMS (HiP3, Ionautics/Solvix) and RFMS (13.56 MHz, SEREN) power supplies were used to deposit the VO_2 films, while silicon nitride films were deposited by RFMS. Experimental conditions for each type of layer were independently optimized, and the resulting deposition parameters are summarized in Table 7-1.

The substrates were first inserted into the deposition chamber through a load lock, and the system then pumped down to a base pressure of 5 x 10^{-8} Torr (6 x 10^{-6} Pa). They were then heated by infrared lamps to a surface temperature of 350 °C and plasma cleaned for 20 minutes at a RF bias of 100 V using an 80:20 Ar:O_2 mixture at 20 mTorr (2.6 Pa). Subsequently, they were covered with a 35 nm diffusion barrier of SiN_x (see Table 7-1 for deposition conditions) to suppress the possible and undesirable diffusion of dopants coming from the glass itself [77].

Vanadium oxide films were then deposited by HiPIMS or RFMS using the conditions summarized in Table 7-1. In both cases the deposition rate was about 0.6 nm/min. Finally, half of the samples were covered with a 35 nm diffusion barrier layer of SiN_x. Note that all sample architectures were deposited on three B270 substrates simultaneously to ensure sample homogeneity, and then cut into four 2.5 cm x 2.5 cm squares for a total of 12 samples in anticipation of the ageing tests.

Table 7-1 Deposition parameters for VO_2 and SiN_x films

	VO_2		**SiN_x**
Source	**HiPIMS**	**RFMS**	**RFMS**
Pressure [mTorr]	5		3
O_2 flow [sccm]	2	4	0
O_2(N_2):Ar ratio [%]	6.3	13.5	40
Average power [W]	450		350
Target voltage [V]	-600	-200	-212
Pulse frequency [Hz]	200	N/A	N/A
Pulse length [μs]	45	N/A	N/A
RF Bias [V]	-180	-180	0
Typical film thickness [nm]	35	35	35
Substrate temperature [°C]	350°C	350°C	350°C

7.2.2 Film ageing and characterization

Sample ageing was conducted in a temperature-controlled glass container kept at a constant temperature of 80 °C and saturated water vapour (~100% relative humidity). One sample was kept as a reference and the 11 other samples were then aged for different amounts of time (at 12-hour intervals). The first ageing experiment was conducted for a total of 52 hours with 4 types of samples, namely HiPIMS-deposited VO_2 samples with and without a SiN_x top layer, and RFMS-

deposited VO_2 samples with and without a SiN_x top layer. The second (longer) ageing test was then run for 144 hours (6 days) with a smaller batch of unprotected HiPIMS-deposited VO_2 samples.

The thickness and optical constants of the as-deposited films were obtained from spectroscopic ellipsometry measurements between 250 nm and 1700 nm and between 45° to 75° using a RC2 ellipsometer from J.A. Woollam Co., Inc. The ellipsometric data (Ψ and Δ) were assessed using the *CompleteEase* software package also from J.A. Woollam Co., Inc. The SiN_x was modelled with a Cody-Lorentz oscillator while the VO_2 was modelled using a combination of Tauc-Lorentz and Gaussian oscillators. A detailed description of the VO_2 model can be found in our previous articles [44], [201]. Knowledge of the optical constants obtained by ellipsometry allowed us to predict the thermochromic performance of VO_2 as a function of the film thickness using the *OpenFilters* software [219].

The crystalline structure and chemical signature of the VO_2 films were assessed by Raman spectroscopy using a Renishaw *INVIA* system equipped with holographic filters and a 514 nm excitation wavelength. Scans were performed from 180 cm^{-1} to 1050 cm^{-1} using an 1800 line/mm grating. X-ray diffraction (XRD) measurements were carried out in the θ-2θ mode from 15° to 65° at a grazing angle of 1° using a Bruker *D8-Discover* diffractometer equipped with a Linkseye CCD accumulation-detector. The diffraction patterns were then evaluated using the *DIFFRACT.EVA* software package from Bruker.

Normal incidence spectral transmittance (*T*) of the samples was measured at different temperatures using a Perkin Elmer *Lambda 1050* spectrophotometer for wavelengths between 250 nm and 2500 nm. The data was recorded at 25 °C and 90 °C, below and above vanadium dioxide's transition temperature, τ_c, using a custom-made heat cell. Time-resolved measurements of the transition speed were obtained by placing the coating directly onto a 90 ºC hot plate while measuring the transmission at 2500 nm.

The stress in the coatings was evaluated using a Tencor *FLX-2900* which measures the change in the radius of curvature of a substrate before and after the addition of a thin film. The internal stress can then be calculated using the well-known Stoney equation. VO_2 films were deposited onto 60 µm thick rectangular glass strips coated with a chromium film on their backside to increase the sample's reflectivity and thus measurement accuracy. Additionally, these substrates were also coated with SiN_x and pre-characterized before and after annealing at 350 °C under vacuum to

account for any changes in stress in the SiN_x prior to the addition of the VO_2; to ensure reliable measurements two samples were deposited at the same time. One should also note that due to the high temperature during the deposition process and possible partial oxidation of the chromium film on the backside of the substrate, the evaluated stress values may be impacted. However, the resulting shifts are expected to be consistent for all samples.

Selected films were studied by Rutherford Backscattering Spectrometry (RBS) to assess their composition and density. The measurements were performed using a 6 MV Tandem accelerator with a 2 MeV beam of helium ions at a scattering angle of 170°. The complementary hydrogen content was measured by Elastic Recoil Detection in the Time-of-flight mode (ERD-ToF) using the same 6 MV Tandem accelerator with a 50 MeV beam of Cu^{9+} ions at a scattering angle of 30°. The elemental composition was then extracted using in-house software.

Finally, scanning electron microscopy (SEM) images were obtained using a JEOL JSM-7600F field emission microscope in “gentle beam imaging mode” and in “energy-dispersive X-ray spectroscopy mode” (EDS). The samples were pre-coated with a 20 nm carbon layer to avoid surface charge build-up during the EDS measurements. The “gentle beam mode” was performed with an energy of 1 keV while the EDS measurements were obtained with a 10 keV electron beam.

7.3 Results and discussion

7.3.1 Optical properties

In the first part of this work, we compare the performance of the RFMS and HiPIMS as-deposited VO_2 films, and the results are shown in Figure 7-1a and Figure 7-1b. It can be seen that both samples possess very similar transmission characteristics in the low and high temperature states indicating that in terms of their TC performance both films behave similarly; this is exemplified by their almost identical $\Delta T_{2500\,nm}$ of 55% and 56% respectively. Such values of $\Delta T_{2500\,nm}$ are similar to what is reported in the literature for comparable deposition temperatures and what is expected for a 35 nm thick film [215], [240], [241]. However, one can note that the visible transmission is lower for the HiPIMS-deposited film. This is due to two factors: 1) its refractive index is higher which results in a higher reflectance (n - ik @ 550 nm = 3.2 - 0.48i vs. 3.0 - 0.38i for the HiPIMS and RFMS samples, respectively), and 2) the film's extinction coefficient and thickness are also slightly higher, around (2–3 nm thicker) thus resulting in a higher absorption. Both these factors explain the observed ~6% higher transmission at 550 nm for the as deposited RFMS film in its low temperature state. In addition, the higher refractive index of the HiPIMS film can also be considered as an indicator of its higher density as will be shown below.

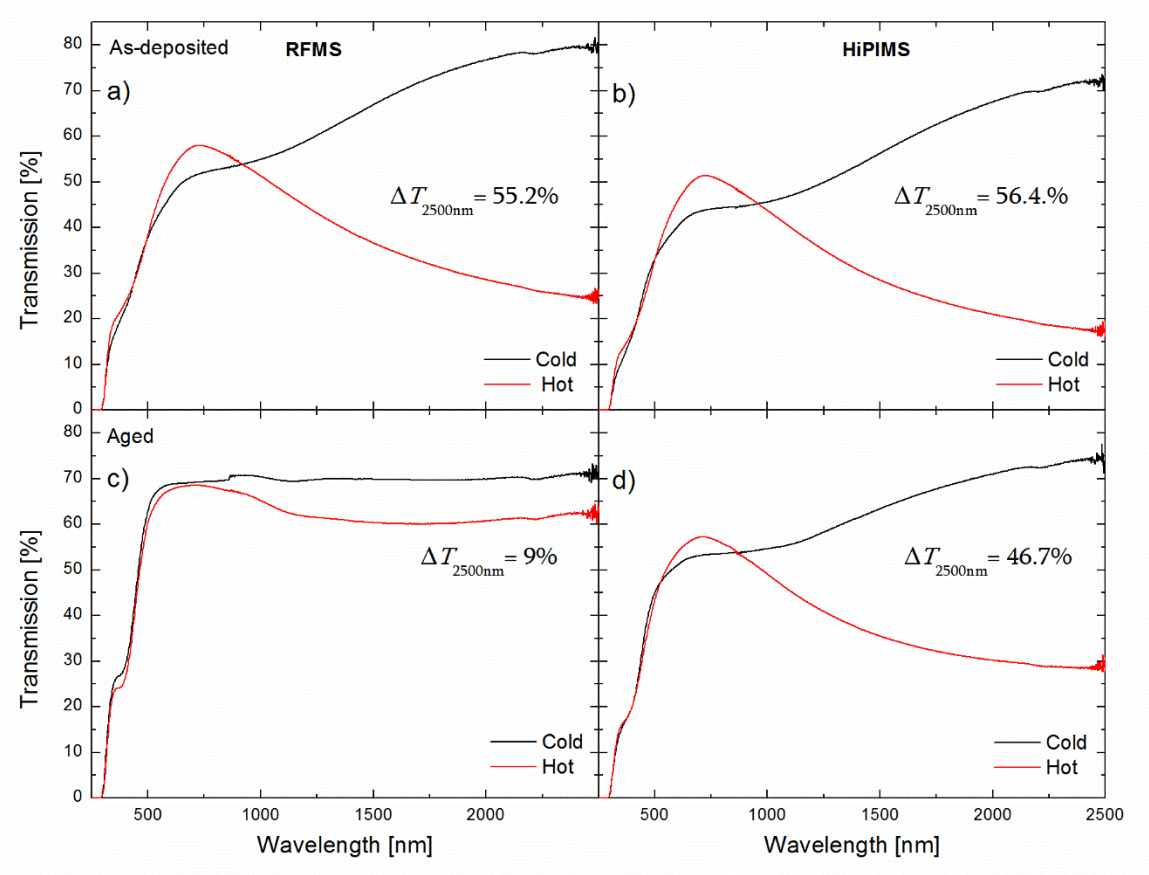

Figure 7-1 Spectral transmission below (20°C, black lines) and above (90°C, red lines) the transition temperature of VO_2 films deposited by RFMS (left panels, a and c) and HiPIMS (right panels, b and d). The top panels present the as-deposited films (a and b) whereas the bottom panels (c and d) present the 52 hour aged samples.

The transmission hysteresis curves at 2500 nm of the previous two samples were evaluated as they are highly indicative of the films' microstructure and stress levels. Indeed, a difference of τ_C from the bulk temperature of 68 °C is usually associated with the presence of compressive stress; changes of as much as 2 °C/100 MPa [226], [227], or 7 °C per 0.1% of deformation in the c-axis of the VO_2 crystal [56] have been demonstrated. In the present case, the stress was evaluated at 200 MPa (tensile) for the RFMS deposited films, and at -570 MPa (compressive) in the HiPIMS films; corresponding, according to [226], [227], to a drop of 15.4°C. These results therefore can explain, in part, the lower transition temperature for the HiPIMS-deposited film as observed in Figure 7-2.

The shape of the hysteresis curve is generally associated with the average grain size and/or the VO_x-phase distribution in the film [50], [51]. In the present case, the HiPIMS film shows a lower τ_C and a narrower hysteresis when compared to the RFMS film; τ_c of 55.5°C vs. 64.0°C and a width of 7.5°C *vs.* 11.4°C, respectively. This suggests that the HiPIMS film presents a larger average grain size and a higher compressive stress; this is expected due to the higher ion flux present during the deposition process as previously discussed [151]. In comparison, the RFMS film presents a larger hysteresis due to a smaller average grain size and a higher τ_c due to a lower compressive stress as discussed above. Both these factors provide the HiPIMS film with a higher durability. In fact, both larger grains, hence, a lower amount of grain boundaries and a higher compressive stress can hinder oxygen diffusion in the bulk of the film [242].

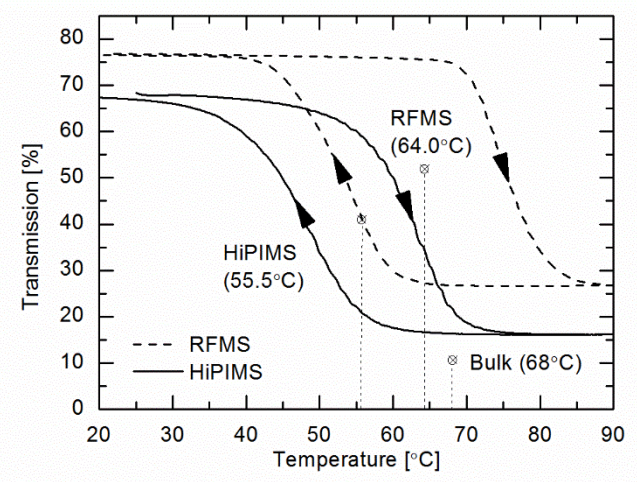

Figure 7-2 Transmission hysteresis curves for as-deposited RFMS and HiPIMS VO_2 films at 2500 nm. The transition temperatures for both films and bulk VO_2 are also indicated.

Following the optical characterization of the as-deposited films, the samples were subjected to a total of 52 hours of accelerated ageing. The bottom part of Figure 1 (1c and 1d)) shows the resulting performance for both types of layers. In the case of the RFMS sample, the visible transmission significantly increased to almost 70%, while the transmission in the near-IR slightly decreased in the low temperature state. In addition, the TC activity of the film severely decreased: $\Delta T_{2500\ nm}$

dropped to only 9% following ageing. These results are consistent with the transformation of VO_2 into V_2O_5 as observed by Ji *et al.* following a similar ageing process [78].

In the case of the HiPIMS film, we can observe a slight increase in transmission in the visible and in the near-IR ranges. This increase can be attributed to a decrease in the film thickness following partial transformation of VO_2 into V_2O_5 and its subsequent dissolution. Nevertheless, after 52 hours of ageing, the $\Delta T_{2500\ nm}$ value decreased by only 15% relative to its initial performance. When modeled using *OpenFilters* [219] and the ellipsometrically measured optical properties (*n* and *k*), this corresponds to an equivalent thickness loss of around 12 nm for the HiPIMS film. In comparison, the RFMS film lost an equivalent thickness of 30 nm during the same period.

In order to quantify the ageing process of the coatings we express ΔT_{loss} calculated using the following equation:

$$\Delta T_{loss} = \frac{\Delta T^{f}_{2500\ nm} - \Delta T^{i}_{2500\ nm}}{\Delta T^{i}_{2500\ nm}}, \qquad eq\ 7.1$$

where *i* and *f* denote the initial (as-deposited) and final (following ageing) $\Delta T_{2500\ nm}$, respectively.

Figure 7-3 shows the ΔT_{loss} as a function of ageing time for HiPIMS- and RFMS-deposited films over the first 100-hour period. It is clear that both films display very different degradation behaviours. Indeed, the RFMS-deposited samples, due to degradation, lose more than 75% of their initial performance after only 48 hours. On the contrary, the HiPIMS samples present a much slower degradation at the beginning, followed by a more rapid decay after 72 hours.

As previously discussed, the degradation mechanism of TC VO_2 films is quite complex and, as will be demonstrated below, especially in the case of the RFMS films, it leads to the formation of highly non-uniform films in multiple states of oxidation. As a consequence, optical modeling is very difficult to perform. Still, it is instructive to model the loss of performance as an equivalent thickness of VO_2 converted into V_2O_5 which is then dissolved in the liquid water.

Figure 7-3 shows the results of this optical model (black crosses) where the loss was calculated for a film thickness varying from 35 nm down to 0 nm over a period of 48 hours, corresponding to an etch rate of 0.73 nm/h of VO_2 converted to V_2O_5. The same calculation for the HiPIMS films yields

an etch rate of 0.25 nm/h. This is reflected in the loss of performance per hour of 2.3%/h for the RFMS-deposited samples as opposed to 0.3%/h for the HiPIMS samples.

Although the above approach is rather simplified, this model follows the RFMS film degradation curve quite well and shows that the HiPIMS VO_2, films present a much longer incubation time and thus much slower "dissolution". As previously mentioned, we suspect that the slower degradation rate of the HiPIMS films is related to the films' higher density, compressive stress and/or larger average grain size, all of which are the result of a higher ion bombardment during the growth process [239]. These assumptions will be discussed in more details in the following section.

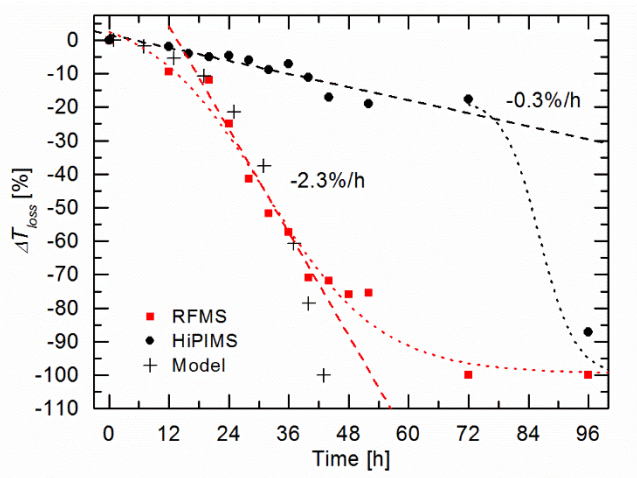

Figure 7-3 Degradation of the thermochromic properties of VO_2 films expressed in terms of ΔT_{loss}, as a function of ageing time for unprotected films deposited by RFMS (red squares) and HiPIMS (black circles). The crosses display the modelled ΔT_{loss} for a VO_2 film whose equivalent thickness is linearly decreasing from 35 nm to 0 nm in 48 hours.

7.3.2 Microstructural characteristics

To gain further insight into the degradation mechanisms of the VO_2 films, we performed Raman spectroscopy measurements. As an example, Figure 7-4 illustrates the effect of 52 hours of ageing. As-deposited films present a similar Raman spectrum for both deposition techniques with vibrational peaks at 192, 223, 261, 309, 339, 291, 443 and 614 cm^{-1}, all corresponding to stoichiometric VO_2 [230]. One can also note that the peaks are slightly blue shifted, which can be related to the presence of oxygen deficiencies in the VO_2 crystalline structure [243].

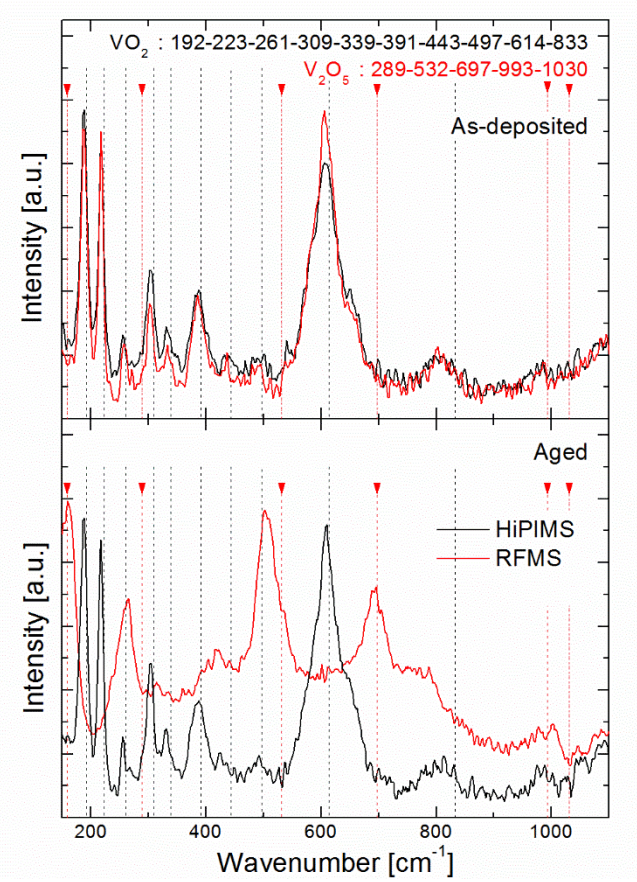

Figure 7-4 Raman spectra of as-deposited (top) and 52 hours aged (bottom) VO_2 films. Black curves represent the HiPIMS films and red curves the RFMS films. The undesirable V_2O_5 phase peaks are indicated with top arrows on red dashed lines while VO_2 phase peaks are indicated with black dashed line.

Following 52 hours of ageing, we can observe a very important change in the Raman response from the RFMS sample, in agreement with the previous optical measurements. Indeed, while the HiPIMS sample has essentially kept the same response, the RFMS sample presents peaks of both V_2O_5 [244] at 162, 697 and 993 cm^{-1} and VO_2 at 223 and 491 cm^{-1}, indicating that the film has in fact been highly oxidized. The remaining VO_2 peaks also explain the 9.0% of TC activity still present in the sample. We can also point out that after ageing, the RFMS peaks (267 vs 261 cm^{-1} and 506 vs 497 cm^{-1}) show a slight red shift; the peaks being observed at wavenumbers higher than for a stoichiometric film. This is due to an excess of oxygen in the matrix, in agreement with the results of Parker [243]; this red shift is not observed in the HiPIMS sample indicating a lower amount of oxygen intake into the crystalline structure.

XRD measurements at grazing angles were performed in order to assess the crystallinity of the films. Figure 7-5a presents the results for the as-deposited VO_2 films. Both films exhibit similar diffraction patterns with only one intense peak at 27.8º attributed to the (011) orientation of monoclinic VO_2 according to the JCPDS card 44-052; the expected 220 and 022 lattice plane diffraction peaks at 55.4° and 57.4°, previously observed without SiN_x barrier coating [44], [201], were not observable. However, the HiPIMS-deposited film also presents small features at 42.2º and 55.4º which correspond to the 210 and 012 planes, respectively. A priori, the half width at half maximum values of the 011 peak for both films are practically the same (slightly lower for the HiPIMS) indicating that the crystallite sizes should also be similar. We suspect that the change of the crystalline orientation from 220 and 022 to 210 and 012 is due to the presence of the SiN_x underlayer.

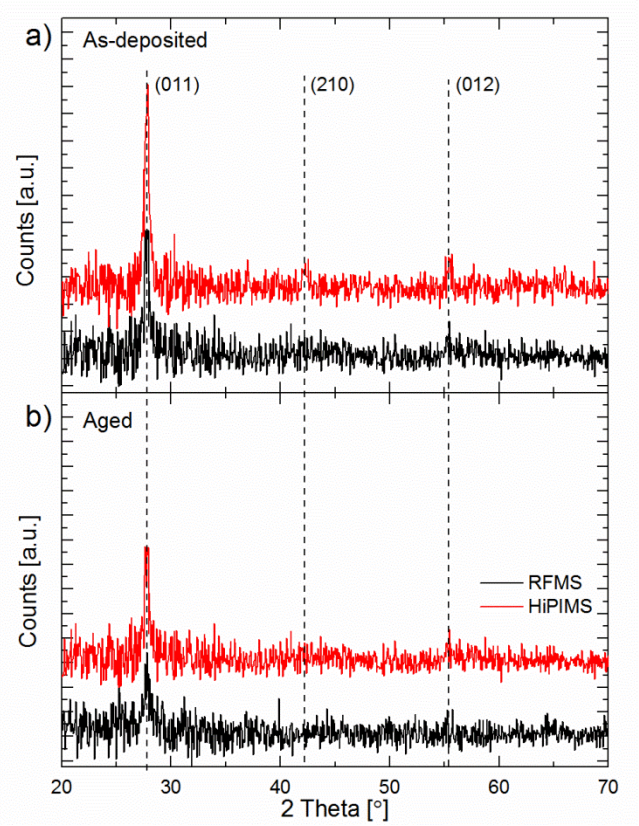

Figure 7-5 Grazing angle XRD diffraction patterns of RFMS (black) and HiPIMS (red) deposited VO_2 films: a) as-deposited films, b) aged samples.

Aged samples presented similar X-ray diffractograms (**s**ee Figure 7-5b) with no change in the crystalline structure except a decrease in the intensity of the main 011 diffraction peak. However, in accordance with our previous observations, the decrease in relative intensity of the (011) peak is of only 35% for the HiPIMS film vs. 70% for the RFMS film. This can be directly attributed to a loss of vanadium dioxide during ageing. The fact that no peaks belonging to V_2O_5 or other forms of VO_x have been detected suggests that the humid degradation of thermochromic VO_2 either forms a non-crystalline film and/or that the converted material is simply under the detection limit; the latter explanation supports the mechanism of film dissolution and reaction of the vanadium to form an acidic solution with water. The solubility of V_2O_5 in pure water of 8 g/l increases to total solubility in the presence of potassium or sodium [245] which explains the absence of any solid precipitates in the 3 l water vessel in our experiment.

To further assess and understand the differences in the degradation mechanisms between the HiPIMS- and RFMS-deposited films, we evaluated the surface morphology and composition using SEM imaging combined with EDS. Figure 7-6 presents the surfaces of the two films before and after 52 hours of ageing. One can see that the as-deposited HiPIMS film's surface is featureless (Figure 7-6a) in comparison with the RFMS film (Figure 7-6b). In addition, following ageing, one can observe a clear increase in the surface roughness of both samples. However, while the HiPIMS film remains continuous, the RFMS film has clearly been degraded and displays needle-like features. Such needles were also imaged in the chemical-sensitive mode as shown in Figure 7-7.

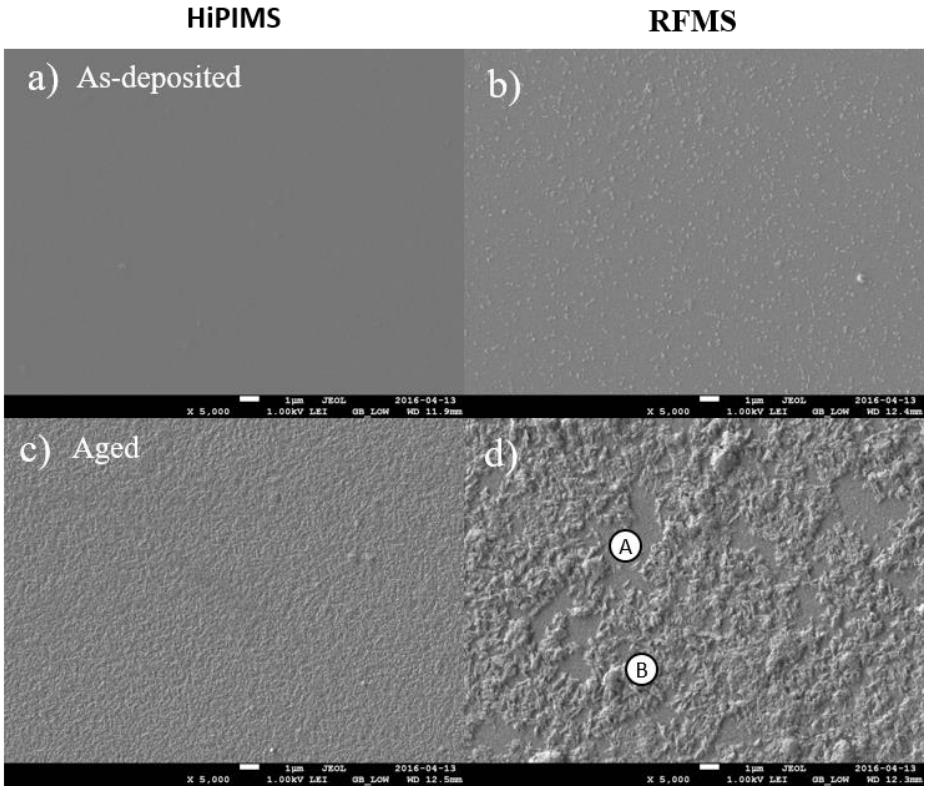

Figure 7-6 SEM images of the surfaces of HiPIMS- (a and c) and RFMS- (b and d) deposited VO_2 films before (a and b) and after (c and d) 52 hours of ageing. The A and B white circles indicate the EDS-analysed regions.

The growth of such needle-like features has previously been reported for VO_2 films prepared via hydrothermal routes [246] or in the case of unprotected VO_2 films following a 400 s exposure to

ambient air at 450 °C [80]. Using EDS, we observed different regions of the aged RFMS sample (see white circles in Figure 7-6d and Table 7-2). The smooth region A contains no residual vanadium, indicating that the converted V_2O_5 has been completely removed from the surface during the degradation process. On the other hand, region B still contains vanadium and is most probably composed of a mixture of active and non-active vanadium oxides. Imaging the surface of the 52-hour aged RFMS sample with chemically sensitive low angle backscattered electrons (LABE), see Figure 7-7, shows a strong contrast between the smooth dark-grey SiN_x layer and the light-grey needles of the remaining vanadium oxides.

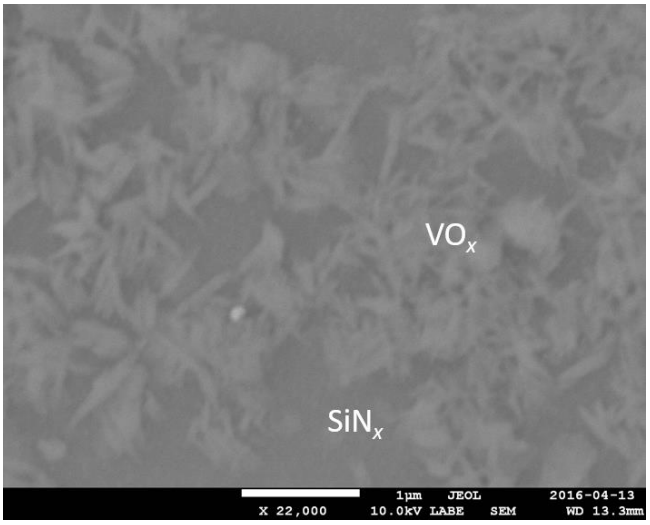

Figure 7-7 SEM image of the surface of the 52 hours aged-RFMS sample in LABE mode (chemical sensitivity). The smooth dark-grey area is the SiN_x surface, the light-grey needle is a vanadium containing oxide, and the white dot a contamination metal particle.

Note that in EDS, the L-alpha nitrogen lines are sufficiently separated from the vanadium lines, while K-alpha lines overlap with oxygen; therefore, the presence of nitrogen on the surface could not be evaluated quantitatively.

Table 7-2 EDS results for regions A and B (see Figure 7-6) of a RFMS-deposited VO_2 sample aged for 52 hours.

Element	**Region A [at.%]**	**Region B [at.%]**	**As deposited [at.%]**
Si	37	33	38
O	46	29	25
V	0	16	13
Other (Glass dopants and contaminants)	17	22	24

Finally, RBS and ERD measurements were performed to quantify the film volume elementary composition and density. With its density of 4.24 g/cm^3, the HiPIMS film is approximately 2% denser than the RFMS films (4.17 g/cm^3). For comparison, VO_2's bulk density is 4.57 g/cm^3 [247]. Complementary ERD measurements reveal that the HiPIMS-deposited VO_2 film contains a lower amount of residual hydrogen in both as-deposited and aged states (1.5% to 8% in comparison to 2.5% to 12% for the RFMS film). Interestingly, it has been shown in the literature, that vanadium oxides can contain absorbed hydrogen in their crystalline matrix [248]–[250] and that, when heated above their transition temperature, the amount of inserted hydrogen is proportional to their porosity [249]. Clearly, these results support the observations that the HiPIMS films are indeed denser than their RFMS counterparts.

In the subsequent experiment, we investigated the impact of ageing on the dynamics of the thermochromic transition. This was evaluated as the time evolution of the films transmittance at 2500 nm when placed directly onto a 90 °C surface. Note that the whole sample is in contact with the hot plate; however, there is a ~1 cm diameter hole in the center to allow for the transmission measurement. The transmittance was normalized to take into account the impact of the material loss on the maximum transmittance. The transition time from high transmittance to low transmittance is then quantified.

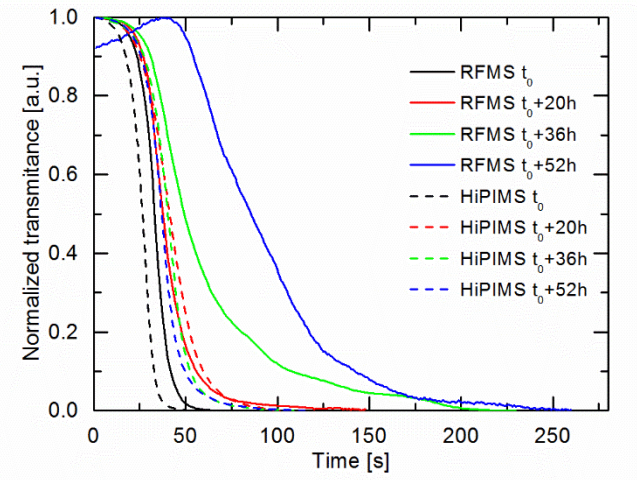

Figure 7-8 Time evolution of the normalized optical transmittance at 2500 nm for differently aged VO_2 films; t_0 represents the as deposited films. RFMS films are represented by full-lines while HiPIMS films are represented by dotted-lines.

The time-evolution of the transmittance is shown in Figure 7-8**.** One can observe that the time needed for the thermochromic transition to occur for both as-deposited films are quite similar (black curves around ~40–50 s). After ageing, the HiPIMS films (dotted-lines) maintain similar transition times while the RFMS samples (continuous lines) present an increasing time necessary to fully transform from their high to their low transmittance states; the latter's time increasing with ageing.

During these experiments, when the VO_2-coated glass is firmly pressed against a heated plate, we estimate that the time needed for the radial heat front to reach the centre of the sample to be around 20–30 s considering the thermal properties of bulk monocrystalline vanadium dioxide. The additional 10 to 20 seconds to generate the phase transition for the as-deposited films are attributed to microstructural characteristics such as grain boundaries and defects in the films. This time is, of course, much larger than a single grain's transition time which is in the fs scale [251], [252].

The similar behaviour for the as-deposited HiPIMS and RFMS samples underlines that they possess similar stoichiometries and grain microstructures, with small statistical variations. On the

other hand, we associate the increase in time with ageing duration of the RFMS films with two mechanisms.

One of these mechanisms is the result of the films' oxidation: i.e. transformation into V_2O_5 and decrease in film thickness as previously discussed. This also leads to an increase in the surface to volume ratio and grain texture which correspondingly increases interface effects. All of the effects impact the speed of the VO_2 phase transition.

The second mechanism follows the insertion of hydrogen into the film as observed by ERD measurements. Inserted hydrogen can locally change the vanadium oxidation states by the insertion of a proton in the vicinity of a V-O bond. This will slow down the displacement of the vanadium atoms during the metal-to-insulator phase transition [249], similar to the inhibition of dislocation movement in metallic alloys. In the case of our work, the hydrogen content was indeed higher in the RFMS samples.

Both effects may co-exist and will thus contribute to the degradation of the phase transition during the ageing process of HiPIMS and RFMS samples. The higher density of the HiPIMS films compared to the RFMS samples lowers the dynamics of these two mechanisms, and hence results in the higher oxidation durability of HiPIMS VO_2 coatings.

7.3.3 Effect of a SiN_x top barrier coating

In the final part of our ageing study, we tested the resistance of VO_2 to water and oxygen after the deposition of a SiN_x diffusion barrier. Figure 7-9 presents the normal incidence transmission spectrum of RFMS and HiPIMS VO_2 films in their respective as-deposited and 52 hour aged states. One can observe much less variation in the TC performance following ageing compared to the unprotected films, especially in the case of the RFMS sample. While the 2% decrease in TC performance is indeed quite low and could be attributed to the samples' slight non-uniformity, the general increase in transmission is a clear indicator of some level of degradation. We conclude that protecting VO_2 by a SiN_x barrier against oxidation is as efficient as reported for Al_2O_3 protective layers. The latter samples were shown to resist degradation for 120 hours in what was, however a milder set of oxidation conditions (60 °C with 95%RH [78]), compared to our present study (80 °C with 100%RH).

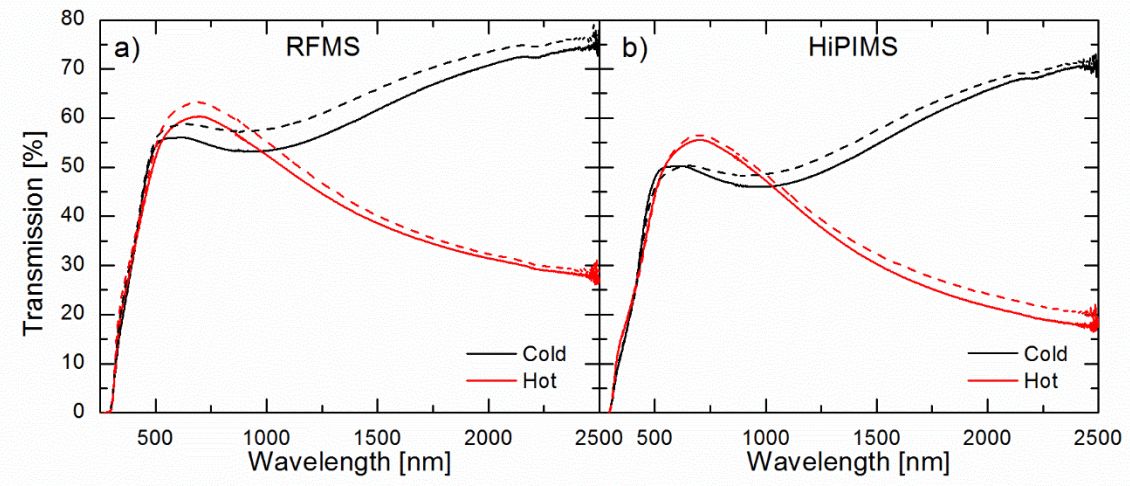

Figure 7-9 Normal incidence transmission spectra of thermochromic VO_2 films deposited by RFMS (a) and HiPIMS (b), in the low temperature (black curves) and high temperature (red curves) states. Both films contain a top 35 nm thick SiN_x barrier layer. Full lines correspond to as-deposited films and dashed lines to films subjected to 52 hours of ageing.

7.4 Conclusion

We demonstrated that high-quality HiPIMS deposited thermochromic VO_2 films on SiN_x buffered B270 glass exhibit a significantly better environmental stability than conventional RFMS-prepared VO_2 samples. This is attributed to the higher density, larger average grain size and lower hydrogen intake for the HiPIMS films. In general, HiPIMS films exhibit an operational lifetime approximately three times longer than the one obtained for RMFS samples. These results suggest that HiPIMS can be used to simplify the development of VO_2-based smart windows which are exposed to mildly oxidizing environments, rendering the use of a diffusion barrier unnecessary.

We also showed that the addition of a SiN_x top barrier coating provides an additional level of protection with very little observable degradation for RFMS and HiPIMS films. In addition to its protective properties, SiN_x and similar layers can also be used to optimize the luminous transmittance through interference-based anti-reflection.

Acknowledgments

The authors wish to thank Mr. S. Chenard and Mr. F. Turcot for their expert technical assistance, and Dr. T. Schmitt for the XRD measurements. This research has been supported, by the Natural Sciences and Engineering Research Council of Canada (NSERC) through the NSERC

Multisectorial Industrial Research Chair in Coatings and Surface Engineering (grant IRCPJ 433808-11), and it has benefited from a partial support from the Fonds de recherche québécois sur la nature et les technologies (FRQNT) through its grant to the Quebec Advanced Materials Strategic Research Cluster (RQMP).

CHAPTER 8 GENERAL DISCUSSION, CONCLUSIONS AND PERSPECTIVES

This final chapter presents a brief review of the most significant results obtained so far and highlights the main contributions to the research on HiPIMS and thermochromic technology. The extent to which the results meet the objectives presented in **Error! Reference source not found.** i s particularly discussed. After the main conclusions, avenues for further exploration and development in the research on thermochromic materials and HiPIMS are proposed.

8.1 Diagnostics of the HiPIMS discharge

The first objective of this thesis was to apply standard plasma diagnostics to investigate reactive HiPIMS discharges under conditions suitable for high-quality oxide deposition, as previously performed at the Functional Coating and Surface Engineering Laboratory (FCSEL) [44]. The first approach was to use an in-lab developed method [148], [183], [253], whereby a high-density reactive HiPIMS discharge was applied over the vanadium target to allow high-quality VO_2 deposition at lower than previously reported temperatures [44].

More precisely, in Chapter 5, to further understand the dynamics of the reactive HiPIMS process, we performed a systematic investigation of a 45 µs pulse discharge operating in an Ar/O_2 mixture at a constant pumping rate to mimic the deposition conditions of the first reported HiPIMS-deposited VO_2 [44]. Plasma imaging using custom-made optical interference filters was applied to isolate the optical emission spectra originating from different species populations. The filters allowed separating the high-energy emissions in the 400–450 nm spectral range from the low-energy spectral band at 750–900 nm. The image sequencing was complemented with optical emission spectroscopy and current waveform monitoring.

This diagnostic approach has been demonstrated to provide good insights into the different plasma dynamic phases [183], [253]: a similar discharge development was reported with 200 µs-long square-shaped voltage pulses applied to a Cr target in pure Ar, Ar/N_2, N_2 [183], and pure O_2 [253]. The emission begins when background gas is excited by high-energy electrons that are created during plasma ignition, followed by shockwave-induced expansion of the dense plasma outwards from the target. In the metallic mode, four different phases of a single HiPIMS pulse were observed: 1) an ignition phase, 2) a high-current metal-dominated phase, 3) a transition phase, and 4) a low-

current gas-dominated phase. In the study reported in Chapter 5, lower cathode voltages and higher magnetic field were used compared to [183], [253]. This method provides a slower transition to the low-current gas-dominated phase. In the Ar–O_2 mixture, the plasma in the chamber showed lower expansion during discharge “on” time: 1:2 (expansion/magnetron size) compared to 1:1 in the previously cited studies using a 5 cm magnetron. This could be due to the unbalanced magnetic field configuration, higher pressure, and lower cathode voltage (900 V vs. 2000 V).

The main results presented in Chapter 5 concern the post-discharge onset during the first 5 µs of the current decay, with sufficient oxygen in the gas mixture. Thus, with increasing oxygen content in the discharge, the current voltage waveforms transit from a metal-like stabilized discharge to an impulse-like current peak with no saturation. The total intensity of the plasma optical emission corresponds to the current waveform, whereas at sufficiently high oxygen concentration, a breakdown of the confinement is observed as the low-energy plasma extends and is located further from the target. In the subsequent post-discharge, instead of diffusing toward the chamber walls, the extended plasma optical emission increases into the null-magnetic field zone. Complementary OES measurements revealed that the oxygen neutrals presented equivalent 777 nm and 844 nm emission triplets, indicating a significant recombination process in this area [254], [255]. Figure 8-1 shows that the density of metastable oxygen measured by tunable diode laser absorption spectroscopy increased at peak discharge current and when the cathode voltage was turned off, corresponding to the timing of our optical emission measurements

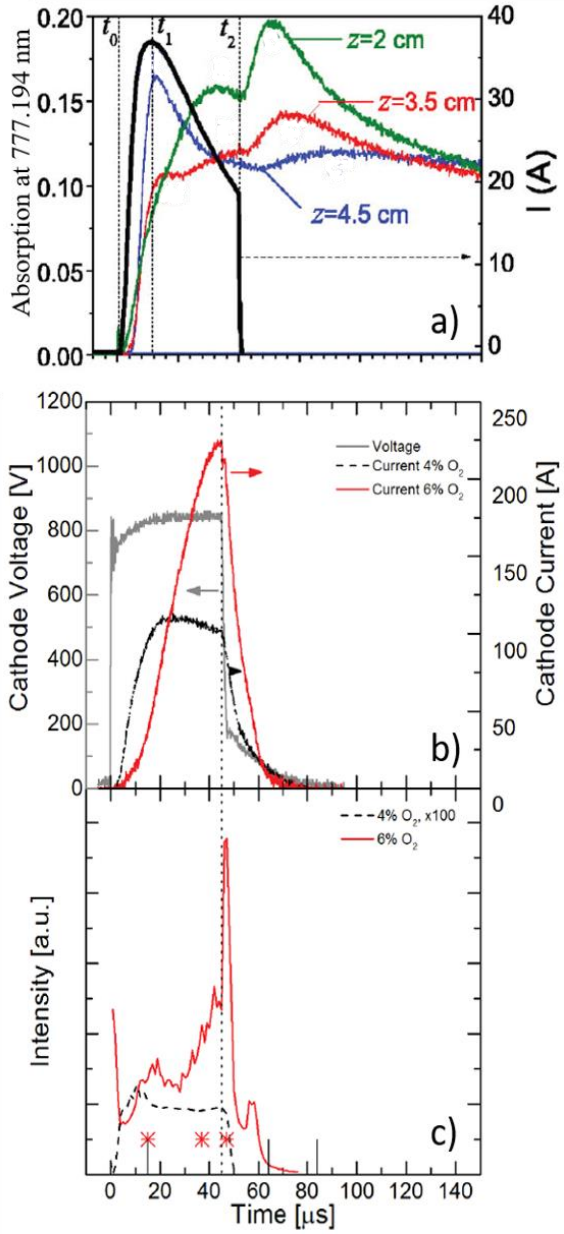

Figure 8-1 a) Laser absorption of metastable oxygen at 777.194 nm in a low-intensity (0.5 A.cm^{-2} peak) HiPIMS discharge over a titanium target at 10% oxygen content, where z represents the distance from the target (adapted from [203]); b) high-density current waveform (1.2 and 2.3 A.cm^{-2} peak) HiPIMS discharges over a vanadium target at oxygen concentrations of 4% and 6%, respectively; and c) optical emission into the null-magnetic field zone of the discharge c) as a function of time (adapted from Chapter 5).

To explain this behavior, we developed a model based on slow electron diffusion towards null-field magnetic traps, followed by interaction with molecular oxygen, ground state and metastable

species, to form negative atomic oxygen through dissociative electron capture. This model was subsequently validated in similar experiments by other groups. They observed a metastable molecular oxygen peak and low-energy electrons at the end of the HiPIMS pulse [203].

We conclude from this model that the post-discharge phenomena observed in the high-current region of the waveform in oxygen-rich reactive HiPIMS can be explained by a large fraction of energetic oxygen atoms (~1 eV). These atoms provide a low-energy substrate bombardment, similar to the low-energy negative ions reported by Bowes [171]. We proposed that this high-flux low-energy neutral adatom bombardment is one of the main reactive-HiPIMS features that promotes the formation of high-quality optical coatings such as VO_2 and others [44], [143], [200], [256].

8.2 Thermochromic VO_2 by HiPIMS

In this project, several functional coatings were deposited using magnetron sputtering with either HiPIMS, RFMS, or DCMS. More specifically, Chapter 6 investigates the use of TiO_2 for Chapter 6 and Chapter 7 investigates the use of SiN_x, both as barrier coating. In particular, the results on VO_2 development by HiPIMS and RFMS clearly demonstrate the superiority of HiPIMS for crystalline oxide applications.

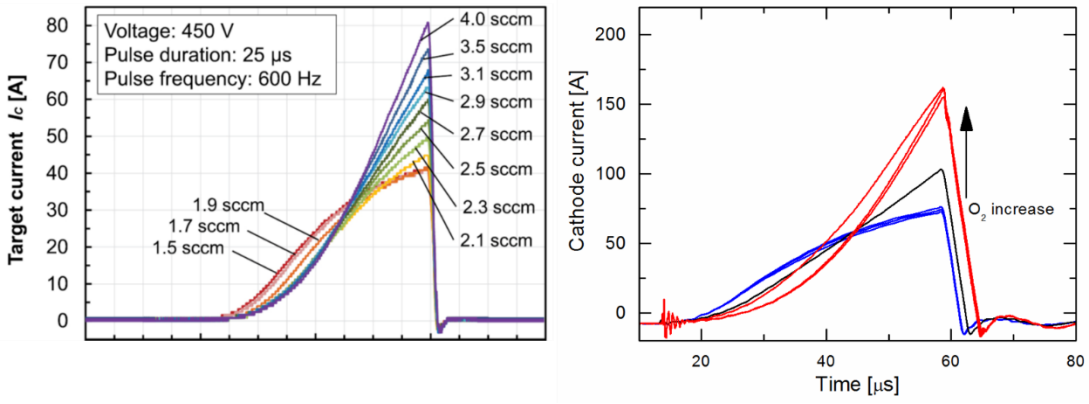

Figure 8-2 Current waveform for the HiPIMS discharge in reactive mode as a function of oxygen flow rate over a hafnium target (left, adapted from [257]) and vanadium target (right).

Table 8-1 Characteristics of the different pulses used to deposit thermochromic VO_2 and optimal oxygen flow rates.

	Huettinger HMP2/1	**Melec SiP2000**	**Ionautics/Solvix HP3**	**RFMS (Seren)**
Deposition temperature, °C	300	300–350	350	350
Magnetron diameter, cm	10	10	7.5	7.5
"On" time, µs	45			N-A
Repetition frequency, Hz	200		N-A	
Cathode voltage, V	-950	-850	-650	N-A
Peak current, A	220	220	200	N-A
Average power, W	875	875	500	500
Oxygen flow, sccm	3.4	2.2–3.4	1.9–2.2	3.8–4.4
Deposition rate, Å/min (±10%)	48	43	7.5	7.5

Initially, the development of the VO_2 deposition process using three different pulsing regimes (appropriate for the power supplies provided by Huettinger, Melec, Ionautics/Solvix) and two different magnetic field configurations (4-inch unbalanced magnetron head provided by Pilsen University; 3-inch balanced magnetron head by Kurt J.Lesker) demonstrated that good-quality thermochromic VO_2 can be deposited by HiPIMS with high reproducibility. Chapter 6 demonstrated that the process requires an optimized O_2/Ar ratio to obtain stable and reproducible thermochromic films. The required oxygen concentration in the gaseous mixture was shown to be dependent on the target area as well as the average power, with high sensitivity. In fact, oxygen flow variation deviating by less than 1% from the optimal rate impacted the thermochromic properties of the coating, obtaining a metallic coating when the flow was too low, and the most stable V_2O_5 above optimal flow.

The third article (Chapter 7) presents a comparative study of VO_2 coatings deposited by HiPIMS and RFMS. The results show that for similar average target power levels within the same deposition system, the required oxygen flow ratio (O_2/Ar) to obtain stoichiometric VO_2 coating is twice as high for RFMS compared to HiPIMS. This confirms that HiPIMS produces a more reactive discharge with higher atomic oxygen density, in both neutral and ionized states. This oxygen appears to be more easily incorporated into the coatings. The higher power and electron density involved in HiPIMS provide effective oxygen dissociation through electron impact and electron capture, as reported by Benzeggouta [258]. A similar effect was observed in the transition to the poisoned regime over a Ti target [175] and a Zn target [259].

The two chapters on HiPIMS deposition of thermochromic VO_2 present innovative results with respect to the thermochromic material. Chapter 6 demonstrates that, with a substrate bias voltage of -200 V, high-quality thermochromic VO_2 can be deposited onto polymeric substrates. Two different substrates were investigated: a transparent Kapton CS and the more conventional Kapton® HN. The film presented good thermochromic properties, with a strong interface gradient due to the low stopping power of the polymeric substrates and the high thermal diffusion. These results make a significant contribution to the development of smart windows, as transparent polymer substrates can be relatively easily roll-to-roll coated before lamination onto a glass panel.

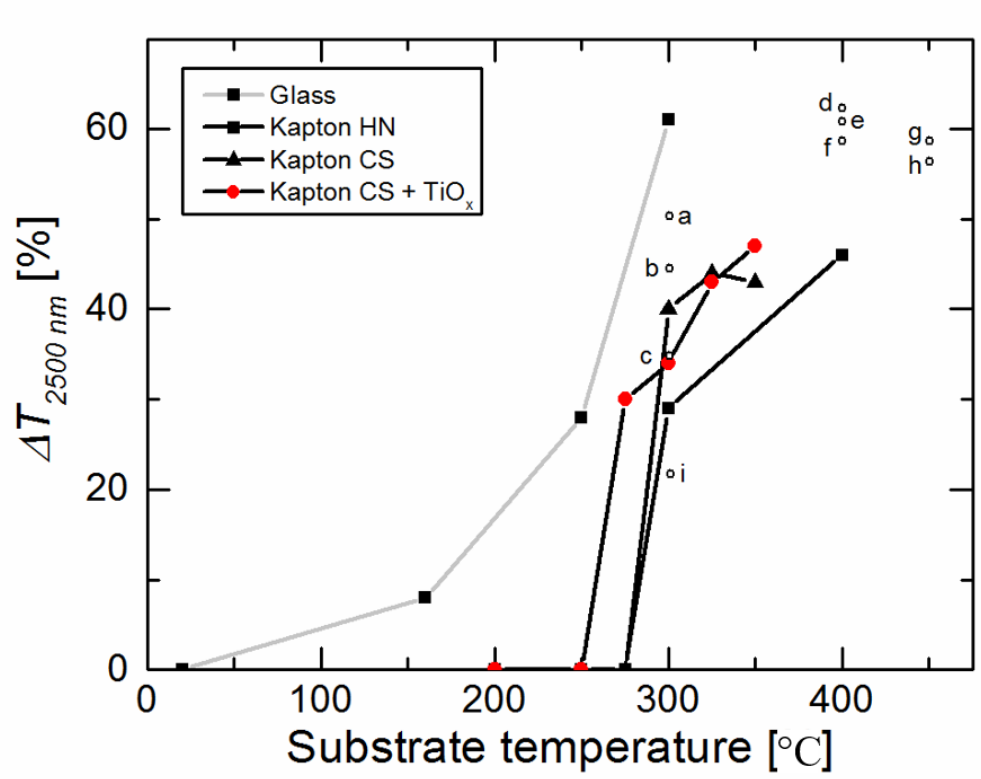

Figure 8-3 Performance of HiPIMS-deposited VO_2 coatings on different substrate materials as part of the present thesis. The $\Delta T_{2500\ nm}$ parameter is also compared with the values for VO_2 deposited on glass, as reported by researchers at the FCSEL and by other authors: a) [260], b) [261], c) [60], d) [215], e) [241] , f) [240], g) [262], h) [45], i) [63].

The final results from Chapter 7 provide insights into the effect of high-flux low-energy ion bombardment on the growth of VO_2 films during HiPIMS deposition. HiPIMS films were found to present greater density, higher compressive stress, and lower transition temperature compared to RFMS counterparts. This results in superior oxidation resistance of the VO_2 coatings in atmospheric oxidation conditions with high water content. Thus, the HiPIMS films presented lower post-degradation, evidenced by high and stable infrared modulation over lengthy exposure to the oxidizing environment: three times longer than that observed for the RFMS-deposited sample. This improved performance can be explained by the greater density and hence the lower oxygen diffusion in the film. In addition, higher concentration of the residual hydrogen incorporated in the RFMS-deposited films was observed, which could be attributed to a loss of TC performance [248], [250]. The densification effect could eliminate the need for an SiN_x barrier coating to protect the

VO_2. It is noteworthy that the SiN_x barrier coating can also be used at the substrate–VO_2 interface to prevent glass dopant diffusion in the growing VO_2 film [77].

In conclusion, HiPIMS was clearly demonstrated to be a suitable method to deposit high-quality thermochromic VO_2 film at lower temperatures than conventional RFMS. Among the technologies developed to respond to the challenges of smart window applications, HiPIMS is the first method to our knowledge that produces an optically active thermochromic layer over polymer substrate. The higher oxidation resistance obtained opens the way to promising applications for these materials, particularly in the aerospace industry, where oxidation is more aggressive due to the presence of atomic oxygen in outer space. Future experiments could be undertaken in collaboration with the Canadian Space Agency.

8.3 Perspectives and future work

This thesis reports on a research investigation and implementation of high power impulse magnetron sputtering for depositing thermochromic optical coatings. It focuses mainly on plasma diagnostics of the reactive discharge, synthesis of single-layer VO_2 films, and characterization of the thermochromic and optical properties of material in the visible to far-infrared regions as well as its oxidation resistance and long-term stability. The findings provide a solid background for further development of energy-control devices. The following sections suggest some promising directions for future research.

8.3.1 Discharge characterization

As this part of the thesis was being prepared, a hot topic emerged in the HiPIMS and plasma physics communities: plasma dynamics, such as fast spoke modes, or azimuthally propagating perturbations in the plasma discharge. The origin of this effect is currently under debate [157]–[161]. Our collaboration with a visiting researcher, Dr. Matjaz Panjan, led to an investigation of spokes using high-speed imaging in both HiPIMS and DCMS plasma regimes. The results, presented in [163], show that similar spokes were found in both DCMS and HiPIMS plasmas.

Using a systematic examination of the various discharge parameters, we assessed their influence on spoke formation. First, we hypothesized that spoke formation is due to the magnetron ExB magnetic field confinement. This is consistent with similar observations of spokes in magnetron

discharges and in Hall thrusters [263], [264]. We then linked the increase in the magnetic field strength to acceleration of the azimuthal spoke oscillation velocity. Plasma oscillation characteristics (such as spoke size) change with changes in background pressure. Increasing the pressure shortens the electron mean free path, which would explain the observed shortening of spoke length. When the collision frequency between electrons and Ar atoms is sufficient, additional spokes are formed. This additional propagation can be obtained by increasing either the pressure or the discharge current.

8.3.2 Toward solar gain control in smart windows

As this work clearly demonstrates, HiPIMS provides suitable conditions for thermochromic VO_2 thin film deposition onto either low-grade glass or polymeric substrates, providing good infrared modulation. However, certain issues related to potential industrial applications for VO_2 remain unresolved: the low luminous transmission, the greenish tint of the layer, and the lowering of the transition temperature [235].

A number of materials engineering approaches have been tested in order to remove the greenish tint from the final product, such as doping VO_2 with fluorine or gold [72], [265], and in order to lower the transition temperature, such as tungsten doping [67], [236]. Although it could be worthwhile to reproduce those experiments and verify whether HiPIMS-deposited VO_2 retains its properties when doped, other initiatives are underway at the FCSEL to resolve these issues.

The first one is to increase the luminous transmittance, thereby lowering the color intensity. This could be achieved by diluting the VO_2 in a transparent nanothermochromic matrix, which is readily obtained in the sol-gel process [98], [100]. At our laboratory, we can consider VO_2 diluted in a transparent matrix by texturing the surface, or mixing VO_2 with air. Surface patterning is currently a hot topic, with multiple applications such as surface ice accretion [266], electrochromic devices [267], [268], and low-index materials [269]. To increase the surface roughness, current avenues are nanosphere self-aligned lithography and nanoimprint lithography, both capable of achieving subvisible wavelength size that does not impact the material's appearance. Such cross-research projects have been underway for a few years and are currently maturing. They represent promising avenues for vastly improving the luminous transmittance at low cost [269], [270].

With respect to the control of solar heat gain in glazing applications, the work at FCSEL on both passive devices [134] and VO_2 is expected to provide enhanced performance compared to single-layer glazing. The addition of a silver layer combined with VO_2 decreases the thickness required to block infrared transmission at high temperatures and offers a more neutral color to the final stack. This can be observed in Figure 8-4, which shows the transmittance provided by three VO_2-based devices: using a single VO_2 layer, a VO_2 film with anti-reflective coating, and an Ag/VO_2-based device with an antireflective top coating.

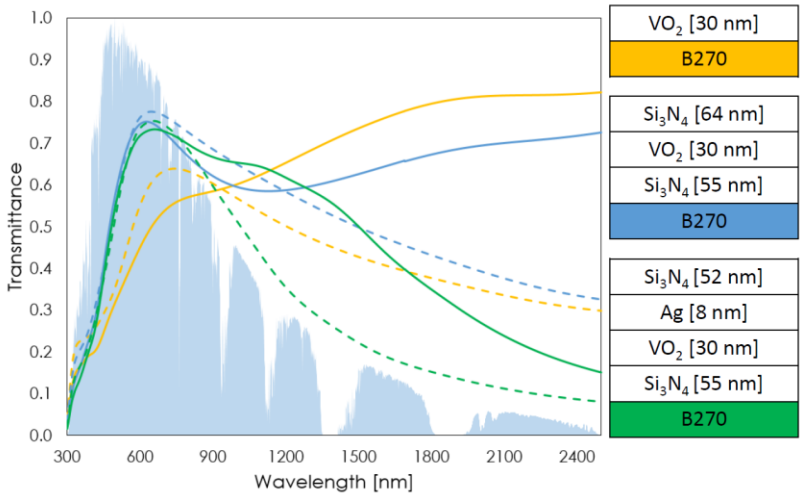

Figure 8-4 a) Specular transmission for VO_2-based infrared modulation of smart coatings. Solid lines represent the low-temperature state and dashed lines represent the high-temperature state. b) Schematics of the different configurations shown in a). Adapted from [87].

8.3.3 Passive radiator control

The advances in the development of thermochromic VO_2 coatings that stem from this thesis would be of benefit to our main industrial partners in the glazing and optical coating industries: Guardians Industries, Essilor International, Viavi, and the Canadian Space Agency. Of particular interest is the research on smart radiator devices for large area applications. The SRD consists of an active thermal radiator with a smart thin-film coating that responds passively to temperature changes. Three layers are typically used, as shown in Figure 2-11: a reflective metallic layer, a dielectric spacer, and a thermochromic layer. Because the thermochromic (TC) material is transparent to infrared radiation at low temperatures, the emissivity of the device is provided by one of the metal layers. At high temperatures, the TC material is in its metallic state, which usually provides medium

emissivity, and therefore higher emissivity than that due to the metallic layer. The dielectric spacer serves to increase the energy radiated by the device, as the TC layer emits in both directions. Thus, a suitable choice of spacer thickness generates a constructive interference that maximizes the emitted energy.

Most of the previously developed devices [90], [94], [97], [271], [272] have been produced using reactive pulsed laser deposition, a process that obtains high oxide quality but small substrate size. In Chapter 6 and 7, we demonstrated that HiPIMS allows high-quality VO_2 deposition, even when deposited directly onto flexible substrates such as Kapton®. Furthermore, we also demonstrated improved oxidation resistance over conventional RFMS-deposited VO_2. This opens promising opportunities for smart radiator devices (SRDs) for application to the aerospace industry.

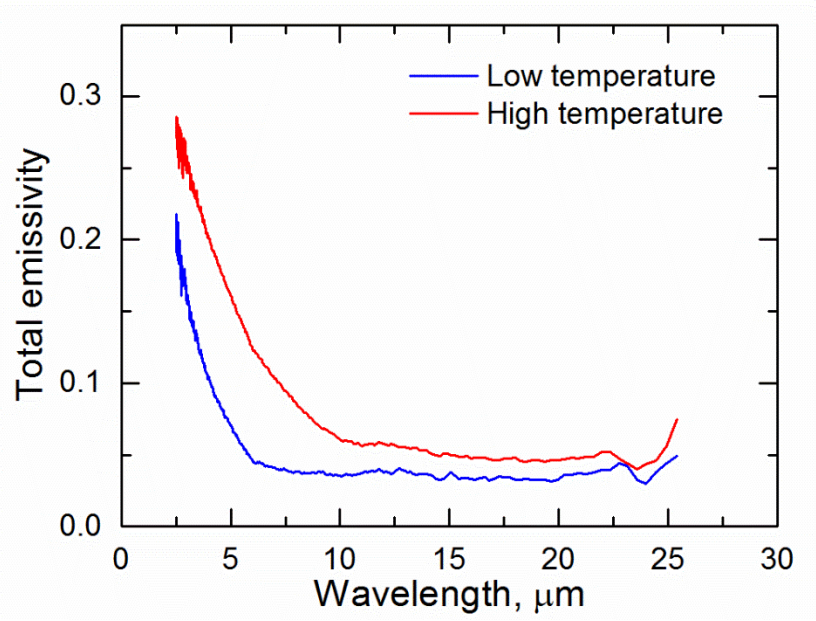

Figure 8-5 Hemispherical reflectance for a 30 nm HiPIMS-deposited VO_2 layer over an aluminum substrate with a 30 nm intermediate SiN_x layer.

Further improvements could be made to these devices by advancing the development of the spacer dielectric materials used in the three-layer device, as proposed in [94]. In such device, the SiO_2 dielectric spacer has a strong absorption band near the 5 μm wavelength, which causes deterioration of the low-emissivity properties. Ongoing work at our laboratory by Ph.D. student S.

Hafezian on the metal–dielectric interface would complement the implementation of DLC and a:C onto smart radiator systems.

8.3.4 Concluding Remarks

The HiPIMS process, through the flexibility of the magnetron sputtering and high-flux low-ion energy bombardment on the growing film, provides state-of-the-art deposition conditions for dielectrics, both oxides and nitrides. Many laboratories and manufacturing industries are investigating various applications and limitations of HiPIMS for coating deposition. The results indicate that this emerging technology promises to provide viable improvements over standard DCMS-, ACMS-, and arc-deposition systems. My hope is that the results presented in this thesis will advance the use of HiPIMS technology for VO_2 coatings in order to produce energy-saving glazing and smart radiator systems.

BIBLIOGRAPHY

[1] R. M. Bierbaum and R. B. Zoellick, *Development and Climate ChangeWorld Development Report 2010 :* Washington, DC, USA: The World Bank, 2009 [Online]. Available: http://www.sciencemag.org/cgi/doi/10.1126/science.1183876

[2] A. H. Rosenfeld and D. Poskanzer, "A Graph Is Worth a Thousand Gigawatt-Hours: How California Came to Lead the United States in Energy Efficiency (*Innovations Case Narrative* : The California Effect)," *Innov. Technol. Governance, Glob.*, vol. 4, no. 4, pp. 57–79, Oct. 2009 [Online]. Available: http://www.mitpressjournals.org/doi/abs/10.1162/itgg.2009.4.4.57. [Accessed: 13-Jun-2016]

[3] A. Sudarshan, "Deconstructing the Rosenfeld curve: Making sense of California's low electricity intensity," *Energy Econ.*, vol. 39, pp. 197–207, 2013.

[4] A. Levinson, "California energy efficiency: Lessons for the rest of the world, or not?," *J. Econ. Behav. Organ.*, vol. 107, no. PA, pp. 269–289, 2014 [Online]. Available: http://dx.doi.org/10.1016/j.jebo.2014.04.014

[5] A. Levinson, "How Much Energy Do Building Energy Codes Really Save? Evidence from California," techreport, Dec. 2014 [Online]. Available: http://www.nber.org/papers/w20797

[6] M. Van der Hoeven, Ed., *Building energy performance metrics*. Paris: International Energy Agency, 2015.

[7] M. Van der Hoeven, Ed., *Energy Efficiency Indicators : Essentials for Policy Making*. Paris, France: International Energy Agency, 2015.

[8] G. B. Parker, T. S. Mapes, and W. J. Zalis, "Highly Insulating Windows Volume Purchase Program Final Report," U.S. Department of Energy, Alexandria, 2013.

[9] C. Ka, "Low-E Storm Windows : Market Assessment and Pathways to Market Transformation," U.S. Department of Energy, Alexandria, 2013.

[10] H. J. Gläser, "History of the development and industrial production of low thermal emissivity coatings for high heat insulating glass units.," *Appl. Opt.*, vol. 47, no. 13, pp. C193–C199, 2008.

[11] B. J. Rissman, "Low-Emissivity Windows Introduction," American Energy Innovation Council, 2013.

[12] C. G. Granqvist, S. Green, G. A. Niklasson, N. R. Mlyuka, S. von Kræmer, and P. Georén, "Advances in chromogenic materials and devices," *Thin Solid Films*, vol. 518, no. 11, pp. 3046–3053, Mar. 2010 [Online]. Available: http://www.sciencedirect.com/science/article/pii/S0040609009017787. [Accessed: 17-Aug-2015]

[13] C. G. Granqvist, "Oxide-based chromogenic coatings and devices for energy efficient fenestration: Brief survey and update on thermochromics and electrochromics," *J. Vac. Sci. Technol. B*, vol. 32, no. 6, p. 60801, Nov. 2014 [Online]. Available: http://scitation.aip.org/content/avs/journal/jvstb/32/6/10.1116/1.4896489. [Accessed: 05-

Jan-2015]

[14] A. Taylor, I. Parkin, N. Noor, C. Tummeltshammer, M. S. Brown, and I. Papakonstantinou, “A bioinspired solution for spectrally selective thermochromic VO_2 coated intelligent glazing,” *Opt. Express*, vol. 21, no. 105, pp. A750--A764, 2013 [Online]. Available: http://www.ncbi.nlm.nih.gov/pubmed/24104571

[15] B. P. Jelle, “Solar radiation glazing factors for window panes, glass structures and electrochromic windows in buildings—Measurement and calculation,” *Sol. Energy Mater. Sol. Cells*, vol. 116, pp. 291–323, 2013.

[16] C. G. G. Granqvist, *Handbook of Inorganic Electrochromic Materials*. Elsevier Science, 1995 [Online]. Available: http://www.elsevier.com/wps/find/bookdescription.cws_home/525224/description#description

[17] B. Baloukas, “Thin Film-Based Optically Variable Security Devices : From Passive to Active,” Ph.D. dissertation, Université de Montréal, 2012.

[18] F. Morin, “Oxides which show a metal-to-insulator transition at the Neel temperature,” *Phys. Rev. Lett.*, vol. 3, no. 1, pp. 34–36, 1959.

[19] H. A. Wriedt, “The O-V(Oxygen-Vanadium) system,” *Bull. Alloy phase diagrams*, vol. 10, no. 3, p. 271, 1989.

[20] M. Hala, “Characterization of High Power Impulse Magnetron Sputtering Discharges,” École Polytechnique de Montréal, Université de Montréal, 2011.

[21] J.-P. Fortier, “Thermochromic VO_2 thin films deposited by mangetron sputtering for smart window applications,” Master thesis, École Polytechnique de Montréal, Université de Montréal, 2014.

[22] B. Jeon, C. Ko, A. C. T. van Duin, and S. Ramanathan, “Chemical stability and surface stoichiometry of vanadium oxide phases studied by reactive molecular dynamics simulations,” *Surf. Sci.*, vol. 606, no. 3, pp. 516–522, 2012.

[23] S. Surnev, M. . Ramsey, and F. . Netzer, “Vanadium oxide surface studies,” *Prog. Surf. Sci.*, vol. 73, no. 4, pp. 117–165, 2003.

[24] J. De La Venta, S. Wang, J. G. Ramirez, and I. K. Schuller, “Control of magnetism across metal to insulator transitions,” *Appl. Phys. Lett.*, vol. 102, no. 12, pp. 1–6, 2013 [Online]. Available: http://scitation.aip.org/content/aip/journal/apl/102/12/10.1063/1.4798293. [Accessed: 19-Apr-2016]

[25] J. de la Venta, S. Wang, T. Saerbeck, J. G. Ramírez, I. Valmianski, and I. K. Schuller, “Coercivity enhancement in V_2O_3/Ni bilayers driven by nanoscale phase coexistence,” *Appl. Phys. Lett.*, vol. 104, no. 6, p. 62410, Feb. 2014 [Online]. Available: http://scitation.aip.org/content/aip/journal/apl/104/6/10.1063/1.4865587. [Accessed: 01-May-2016]

[26] M. W. Chase, “NIST-JANAF Thermochemical Tables for Oxygen Fluorides,” *J. Phys. Chem. Ref. Data*, vol. 25, no. 2, p. 551, 1996 [Online]. Available: http://scitation.aip.org/content/aip/journal/jpcrd/25/2/10.1063/1.555992. [Accessed: 10-Aug-2016]

[27] V. Eyert, “The metal-insulator transitions of VO_2 : A band theoretical approach,” *Ann. Phys.*, vol. 11, no. 9, pp. 650–702, 2002.

[28] D. B. McWhan, M. Marezio, J. P. Remeika, and P. D. Dernier, “X-ray diffraction study of metallic VO_2,” *Phys. Rev. B*, vol. 10, no. 2, pp. 490–495, Jul. 1974 [Online]. Available: http://journals.aps.org/prb/abstract/10.1103/PhysRevB.10.490. [Accessed: 19-Apr-2016]

[29] G. Andersson, C. Parck, U. Ulfvarson, E. Stenhagen, and B. Thorell, “Studies on Vanadium Oxides. II. The Crystal Structure of Vanadium Dioxide.,” *Acta Chemica Scandinavica*, vol. 10. pp. 623–628, 1956.

[30] S. Rao Popuri, A. Artemenko, C. Labrugere, M. Miclau, A. Villesuzanne, and M. Pollet, “VO_2 (A): Reinvestigation of crystal structure, phase transition and crystal growth mechanisms,” *J. Solid State Chem.*, vol. 213, pp. 79–86, May 2014 [Online]. Available: http://www.sciencedirect.com/science/article/pii/S0022459614000504. [Accessed: 28-Jan-2016]

[31] U. Schwingenschlögl and V. Eyert, “The vanadium Magnéli phases V_nO_{2n-1},” *Ann. der Phys.*, vol. 13, no. 9, pp. 475–510, 2004.

[32] J. B. Goodenough, “The two components of the crystallographic transition in VO_2,” *J. Solid State Chem.*, vol. 3, no. 4, pp. 490–500, 1971.

[33] N. F. Mott and L. Friedman, “Metal-insulator transitions in VO_2, Ti_2O_3 and $Ti_{2-x}V_xO_3$,” *Philos. Mag.*, vol. 30, no. 2, pp. 389–402, 1974 [Online]. Available: http://dx.doi.org/10.1080/14786439808206565

[34] J. P. Pouget, H. Launois, T. M. Rice, P. Dernier, A. Gossard, G. Villeneuve, and P. Hagenmuller, “Dimerization of a linear Heisenberg chain in the insulating phases of $V_{1-x}Cr_xO_2$,” *Phys. Rev. B*, vol. 10, no. 5, pp. 1801–1815, 1974.

[35] J. P. Pouget, H. Launois, J. P. D’Haenens, P. Merenda, and T. M. Rice, “Electron Localization Induced by Uniaxial Stress in Pure VO_2,” *Phys. Rev. Lett.*, vol. 35, no. 13, pp. 873–875, 1975.

[36] H. Qiu, M. Yang, Y. Dong, H. Xu, B. Hong, Y. Gu, Y. Yang, C. Zou, Z. Luo, and C. Gao, “The tetragonal-like to rutile structural phase transition in epitaxial VO_2 /TiO_2 (001) thick films,” *New J. Phys.*, vol. 17, no. 11, p. 113016, 2015 [Online]. Available: http://stacks.iop.org/1367-2630/17/i=11/a=113016?key=crossref.c0f89112d1a3a9517061215075f363b9

[37] R. M. Wentzcovitch, W. W. Schulz, and P. B. Allen, “VO_2: Peierls or Mott-Hubbard? A view from band theory,” *Phys. Rev. Lett.*, vol. 72, no. 21, pp. 3389–3392, 1994.

[38] L. Bai, Q. Li, S. A. Corr, Y. Meng, C. Park, S. V. Sinogeikin, C. Ko, J. Wu, and G. Shen, “Pressure-induced phase transitions and metallization in VO_2,” *Phys. Rev. B*, vol. 91, no. 10, p. 104110, Mar. 2015 [Online]. Available: http://journals.aps.org/prb/abstract/10.1103/PhysRevB.91.104110. [Accessed: 22-Mar-2016]

[39] M. Yang, Y. Yang, Bin Hong, L. Wang, K. Hu, Y. Dong, H. Xu, H. Huang, J. Zhao, H. Chen, L. Song, H. Ju, J. Zhu, J. Bao, X. Li, Y. Gu, T. Yang, X. Gao, Z. Luo, and C. Gao, “Suppression of Structural Phase Transition in VO_2 by Epitaxial Strain in Vicinity of

Metal-insulator Transition.,” *Sci. Rep.*, vol. 6, p. 23119, Jan. 2016 [Online]. Available: http://www.pubmedcentral.nih.gov/articlerender.fcgi?artid=4792152&tool=pmcentrez&rendertype=abstract. [Accessed: 22-Mar-2016]

[40] M. J. Miller and J. Wang, “Coupled Effects of Deposition and Annealing Temperatures on Optical, Electrical and Mechanical Properties of Titanium Oxide Thin Films,” *Vacuum*, 2015 [Online]. Available: http://linkinghub.elsevier.com/retrieve/pii/S0042207X15300099

[41] V. R. Morrison, R. P. Chatelain, K. L. Tiwari, A. Hendaoui, A. Bruhács, M. Chaker, and B. J. Siwick, “A photoinduced metal-like phase of monoclinic VO_2 revealed by ultrafast electron diffraction.,” *Science*, vol. 346, no. 6208, pp. 445–8, Oct. 2014 [Online]. Available: http://science.sciencemag.org/content/346/6208/445.abstract. [Accessed: 22-Mar-2016]

[42] G. Stefanovich, A. Pergament, and D. Stefanovich, “Electrical switching and Mott transition in VO_2,” *J. Phys. Condens. Matter*, vol. 12, no. 41, pp. 8837–8845, 2000 [Online]. Available: http://iopscience.iop.org/0953-8984/12/41/310

[43] S. Chen, J. Liu, H. Luo, and Y. Gao, “Calculation Evidence of Staged Mott and Peierls Transitions in VO_2 Revealed by Mapping Reduced-Dimension Potential Energy Surface,” *J. Phys. Chem. Lett.*, vol. 6, no. 18, pp. 3650–3656, 2015.

[44] J.-P. Fortier, B. Baloukas, O. Zabeida, J. E. Klemberg-Sapieha, and L. Martinu, “Thermochromic VO_2 thin films deposited by HiPIMS,” *Sol. Energy Mater. Sol. Cells*, vol. 125, pp. 291–296, Jun. 2014 [Online]. Available: http://linkinghub.elsevier.com/retrieve/pii/S0927024814001263. [Accessed: 29-May-2014]

[45] N. R. Mlyuka, G. A. Niklasson, and C. G. Granqvist, “Thermochromic multilayer films of VO_2 and TiO_2 with enhanced transmittance,” *Sol. Energy Mater. Sol. Cells*, vol. 93, no. 9, pp. 1685–1687, Sep. 2009 [Online]. Available: http://linkinghub.elsevier.com/retrieve/pii/S0927024809001184. [Accessed: 07-Aug-2013]

[46] H. Kakiuchida, P. Jin, S. Nakao, and M. Tazawa, “Optical Properties of Vanadium Dioxide Film during Semiconductive–Metallic Phase Transition,” *Jpn. J. Appl. Phys.*, vol. 46, no. 2L, p. L113, 2007 [Online]. Available: http://stacks.iop.org/1347-4065/46/i=2L/a=L113

[47] H. Kakiuchida, P. Jin, and M. Tazawa, “Control of Optical Performance in Infrared Region for Vanadium Dioxide Films Layered by Amorphous Silicon,” *Int. J. Thermophys.*, vol. 31, no. 10, pp. 1964–1971, Mar. 2009 [Online]. Available: http://link.springer.com/10.1007/s10765-009-0564-8. [Accessed: 03-Sep-2014]

[48] ASTM, *Standard Tables for Reference Solar Spectral Irradiances : Direct Normal and*, vol. 3, no. Reapproved. 2013, pp. 1–21 [Online]. Available: http://enterprise.astm.org/SUBSCRIPTION/filtrexx40.cgi?+REDLINE_PAGES/G173.htm

[49] P. K. Kaiser, *CIE 086-1990 2° Spectral Luminous Efficiency Function for Photopic Vision*. 1988, p. 13.

[50] V. A. Klimov, I. O. Timofeeva, S. D. Khanin, and E. B. Shadrin, “Hysteresis Loop Construction for the Metal – Semiconductor Phase Transition in Vanadium Dioxide Films,” *Tech. Phys.*, vol. 47, no. 9, pp. 1134–1139, 2002.

[51] R. A. Aliev and V. A. Klimov, “Effect of synthesis conditions on the metal-semiconductor phase transition in vanadium dioxide thin films,” *Phys. Solid State*, vol. 46, no. 3, pp. 532–536, 2004 [Online]. Available: http://link.springer.com/10.1134/1.1687874

[52] O. B. Danilov, V. A. Klimov, O. P. Mikheeva, A. I. Sidorov, S. A. Tul’skii, E. B. Shadrin, and I. L. Yachnev, “Optical limitation of Mid-IR radiation in vanadium dioxide films,” *Tech. Phys.*, vol. 48, no. 1, pp. 73–79, 2003.

[53] Y. Muraoka and Z. Hiroi, “Metal-insulator transition of VO_2 thin films grown on TiO_2 (001) and (110) substrates,” *Appl. Phys. Lett.*, vol. 80, no. 4, pp. 583–585, 2002.

[54] Y. Cui and S. Ramanathan, “Substrate effects on metal-insulator transition characteristics of rf-sputtered epitaxial VO_2 thin films,” *J. Vac. Sci. Technol. A*, vol. 29, no. 4, pp. 41502–41507, 2011.

[55] K. West, J. Lu, and J. Yu, “Growth and characterization of vanadium dioxide thin films prepared by reactive-biased target ion beam deposition,” *J. Vac. Sci. Technol. A*, vol. 26, no. 1, p. 133, 2008 [Online]. Available: http://link.aip.org/link/JVTAD6/v26/i1/p133/s1&Agg=doi\nhttp://ieeexplore.ieee.org/xpls/abs_all.jsp?arnumber=4924479

[56] K. Okimura and J. Sakai, “Changes in Lattice Parameters of VO_2 Films Grown on c -Plane Al_2O_3 Substrates across Metal–Insulator Transition,” *Jpn. J. Appl. Phys.*, vol. 48, no. 4R, p. 45504, 2009.

[57] Y. Zhao, J. Hwan Lee, Y. Zhu, M. Nazari, C. Chen, H. Wang, A. Bernussi, M. Holtz, and Z. Fan, “Structural, electrical, and terahertz transmission properties of VO_2 thin films grown on c-, r-, and m-plane sapphire substrates,” *J. Appl. Phys.*, vol. 111, no. 5, 2012.

[58] A. Chen, Z. Bi, W. Zhang, J. Jian, Q. Jia, and H. Wang, “Textured metastable VO_2 (B) thin films on $SrTiO_3$ substrates with significantly enhanced conductivity,” *Appl. Phys. Lett.*, vol. 104, no. 7, pp. 1–5, 2014.

[59] N. Emond, A. Hendaoui, and M. Chaker, “Low resistivity $W_xV_{1-x}O_2$-based multilayer structure with high temperature coefficient of resistance for microbolometer applications,” *Appl. Phys. Lett.*, vol. 107, no. 14, 2015 [Online]. Available: http://dx.doi.org/10.1063/1.4932954

[60] P. Jin, K. Yoshimura, and S. Tanemura, “Dependence of microstructure and thermochromism on substrate temperature for sputter-deposited VO_2 epitaxial films,” *J. Vac. Sci. Technol. A Vacuum, Surfaces, Film.*, vol. 15, no. 3, p. 1113, May 1997 [Online]. Available: http://scitation.aip.org/content/avs/journal/jvsta/15/3/10.1116/1.580439. [Accessed: 03-Sep-2013]

[61] J. Wu, W. Huang, Q. Shi, J. Cai, D. Zhao, Y. Zhang, and J. Yan, “Effect of annealing temperature on thermochromic properties of vanadium dioxide thin films deposited by organic sol–gel method,” *Appl. Surf. Sci.*, vol. 268, pp. 556–560, Mar. 2013 [Online]. Available: http://www.sciencedirect.com/science/article/pii/S016943321300024X. [Accessed: 19-Aug-2015]

[62] Y. Liu, J. Liu, Y. Li, D. Wang, L. Ren, and K. Zou, “Effect of annealing temperature on the structure and properties of vanadium oxide films,” *Opt. Mater. Express*, vol. 6, no. 5, p. 1552, 2016 [Online]. Available: https://www.osapublishing.org/abstract.cfm?URI=ome-

6-5-1552

[63] A. Aijaz, Y.-X. Ji, J. Montero, G. A. . Niklasson, C. G. Granqvist, and T. Kubart, “Low-temperature synthesis of thermochromic vanadium dioxide thin films by reactive high power impulse magnetron sputtering,” *Sol. Energy Mater. Sol. Cells*, vol. 149, pp. 137–144, 2016 [Online]. Available: http://linkinghub.elsevier.com/retrieve/pii/S0927024816000131

[64] F. Fietzke and B. Zimmermann, “Plasma characterization and technological application of a hollow cathode plasma source with an axial magnetic field,” *Surf. Coatings Technol.*, vol. 205, no. 5, pp. 1491–1496, Nov. 2010 [Online]. Available: http://linkinghub.elsevier.com/retrieve/pii/S0257897210006821. [Accessed: 03-Sep-2013]

[65] H. Miyazaki and I. Yasui, “Substrate bias effect on the fabrication of thermochromic VO_2 films by reactive RF,” *J. Phys. D. Appl. Phys.*, vol. 39, pp. 2220–2223, 2006.

[66] C. Sun, L. Yan, B. Yue, H. Liu, and Y. Gao, “The modulation of metal–insulator transition temperature of vanadium dioxide: a density functional theory study,” *J. Mater. Chem. C*, vol. 2, p. 9283, 2014.

[67] W. Burkhardt, T. Christmann, B. K. Meyer, W. Niessner, D. Schalch, and A. Scharmann, “W- and F-doped VO_2 films studied by photoelectron spectrometry,” *Thin Solid Films*, vol. 345, pp. 229–235, 1999.

[68] D. Li, M. Li, J. Pan, Y. Luo, H. Wu, Y. Zhang, and G. Li, “Hydrothermal synthesis of Mo-doped VO_2/TiO_2 composite nanocrystals with enhanced thermochromic performance,” *ACS Appl. Mater. Interfaces*, vol. 6, no. 9, pp. 6555–6561, 2014.

[69] Ö. Sävborg and M. Nygren, “Magnetic, Electrical, and Thermal Studies of the $V_{1-x}Re_xO_2$ System with $0<x<0.15$,” *Phys.Stat.Sol.(a)*, vol. 48, pp. 645–652, 1977.

[70] A. Paone, R. Sanjines, P. Jeanneret, H. J. Whitlow, E. Guibert, G. Guibert, F. Bussy, J.-L. Scartezzini, and A. Schüler, “Influence of doping in thermochromic $V_{1-x}W_xO_2$ and V1−xAlxO2 thin films: Twice improved doping efficiency in $V_{1-x}W_xO_2$,” *J. Alloys Compd.*, vol. 621, pp. 206–211, Feb. 2015 [Online]. Available: http://linkinghub.elsevier.com/retrieve/pii/S0925838814023718. [Accessed: 05-Jan-2015]

[71] M. L. F. Bayard, T. G. Reynolds, M. Vlasse, H. L. McKinzie, R. J. Arnott, and A. Wold, “Preparation and properties of the oxyfluoride systems $V_2O_{5-x}F_x$ and $VO_{2-x}F_x$,” *J. Solid State Chem.*, vol. 3, no. 4, pp. 484–489, 1971.

[72] W. Burkhardt, T. Christmann, S. Franke, W. Kriegseis, D. Meister, B. K. Meyer, W. Niessner, D. Schalch, and A. Scharmann, “Tungsten and fluorine co-doping of VO_2 films,” *Thin Solid Films*, vol. 402, pp. 226–231, 2002.

[73] M. Ohring, *Materials Science of Thin Films*, 2nd ed. San Diego: Academic Press, 2002.

[74] H. A. Macleod, *Thin-Film Optical Filters*, 4th ed. CRC Press, 2010.

[75] G. J. Kovács, D. Bürger, I. Skorupa, H. Reuther, R. Heller, and H. Schmidt, “Effect of the substrate on the insulator–metal transition of vanadium dioxide films,” *J. Appl. Phys.*, vol. 109, no. 6, p. 63708, 2011 [Online]. Available: http://scitation.aip.org/content/aip/journal/jap/109/6/10.1063/1.3563588

[76] K. Kato, P. K. Song, H. Odaka, and Y. Shigesato, “Study on Thermochromic VO_2 Films

Grown on ZnO-Coated Glass Substrates for ‘Smart Windows,’” *Jpn. J. Appl. Phys.*, vol. 42, no. Part 1, No. 10, pp. 6523–6531, Oct. 2003 [Online]. Available: http://iopscience.iop.org/article/10.1143/JJAP.42.6523. [Accessed: 19-Apr-2016]

[77] H. Koo, H. You, K.-E. Ko, O.-J. Kwon, S.-H. Chang, and C. Park, “Thermochromic properties of VO_2 thin film on SiN_x buffered glass substrate,” *Appl. Surf. Sci.*, vol. 277, pp. 237–241, Jul. 2013 [Online]. Available: http://www.sciencedirect.com/science/article/pii/S0169433213007228. [Accessed: 04-Sep-2013]

[78] Y. X. Ji, S. Y. Li, G. A. Niklasson, and C. G. Granqvist, “Durability of thermochromic VO_2 thin films under heating and humidity: Effect of Al oxide top coatings,” *Thin Solid Films*, vol. 562, pp. 568–573, 2014 [Online]. Available: http://dx.doi.org/10.1016/j.tsf.2014.03.043

[79] Y.-X. Ji, G. A. Niklasson, and C. G. Granqvist, “Durability of VO_2 -based thin films at elevated temperature: Towards thermochromic fenestration,” *J. Phys. Conf. Ser.*, vol. 559, p. 12005, Nov. 2014 [Online]. Available: http://stacks.iop.org/1742-6596/559/i=1/a=012005?key=crossref.59997d7299cb0dc2d191f3477e28f9d1. [Accessed: 07-Jan-2015]

[80] S. Saitzek, F. Guinneton, L. Sauques, K. Aguir, and J.-R. Gavarri, “Thermochromic CeO_2–VO_2 bilayers: Role of ceria coating in optical switching properties,” *Opt. Mater. (Amst).*, vol. 30, no. 3, pp. 407–415, Nov. 2007 [Online]. Available: http://linkinghub.elsevier.com/retrieve/pii/S0925346706004563

[81] P. Jin, G. Xu, M. Tazawa, and K. Yoshimura, “Design, formation and characterization of a novel multifunctional window with VO_2 and TiO_2 coatings,” *Appl. Phys. A Mater. Sci. Process.*, vol. 77, no. 3–4, pp. 455–459, 2003.

[82] H. K. Raut, V. A. Ganesh, A. S. Nair, and S. Ramakrishna, “Anti-reflective coatings: A critical, in-depth review,” *Energy Environ. Sci.*, vol. 4, no. 10, p. 3779, 2011.

[83] S. Konstantinidis, J. P. Dauchot, and M. Hecq, “Titanium oxide thin films deposited by high-power impulse magnetron sputtering,” *Thin Solid Films*, vol. 515, no. 3, pp. 1182–1186, Nov. 2006 [Online]. Available: http://www.sciencedirect.com/science/article/pii/S0040609006009060. [Accessed: 03-Sep-2013]

[84] J. Zheng, S. Bao, and P. Jin, “TiO_2(R)/VO_2(M)/TiO_2(A) multilayer film as smart window: Combination of energy-saving, antifogging and self-cleaning functions,” *Nano Energy*, vol. 11, pp. 136–145, Jan. 2015 [Online]. Available: http://linkinghub.elsevier.com/retrieve/pii/S2211285514202382. [Accessed: 18-Dec-2014]

[85] Z. Chen, Y. Gao, L. Kang, J. Du, Z. Zhang, H. Luo, H. Miao, and G. Tan, “VO_2-based double-layered films for smart windows: Optical design, all-solution preparation and improved properties,” *Sol. Energy Mater. Sol. Cells*, vol. 95, no. 9, pp. 2677–2684, 2011 [Online]. Available: http://dx.doi.org/10.1016/j.solmat.2011.05.041

[86] M. J. Miller and J. Wang, “Multilayer ITO/VO_2/TiO_2 thin films for control of solar and thermal spectra,” *Sol. Energy Mater. Sol. Cells*, vol. 154, pp. 88–93, 2016.

[87] B. Baloukas, S. Loquai, and L. Martinu, “Low emissivity coating incorporating

thermochromic VO_2: performance enhancement and new oportunity," in *Optical Interference Coatings*, 2016.

[88] C. Wild, E. Wörner, and H. Obloh, "Switchable infrared filter," US8115991 B2, 2012 [Online]. Available: https://www.google.ca/patents/US8115991

[89] T. P. Fagan, J. F. Brady, T. R. Schimert, and A. J. Syllaios, "Pixel-level optically transitioning filter elements for detector devices," US8227755 B2, 2012 [Online]. Available: https://www.google.ca/patents/US8227755

[90] A. Hendaoui, M. Chaker, and E. Haddad, "Passively variable emittance device and method for making the same," US8908253 B2, 2014 [Online]. Available: https://www.google.com/patents/US8908253

[91] J. G. Keller, R. M. Moy, and J. R. Felland, "Thermal control coatings," US7691435 B2, 2010 [Online]. Available: https://www.google.ca/patents/US7691435

[92] R. V Kruzelecky, E. Haddad, B. Wong, and W. R. Jamroz, "Variable emittance thermochromic material and satellite system," 2010 [Online]. Available: https://www.google.com/patents/US7761053

[93] M. Benkahoul, M. Chaker, J. Margot, E. Haddad, R. Kruzelecky, B. Wong, W. Jamroz, and P. Poinas, "Thermochromic VO_2 film deposited on Al with tunable thermal emissivity for space applications," *Sol. Energy Mater. Sol. Cells*, vol. 95, no. 12, pp. 3504–3508, Dec. 2011 [Online]. Available: http://www.sciencedirect.com/science/article/pii/S0927024811004727. [Accessed: 17-Aug-2015]

[94] A. Hendaoui, N. Émond, M. Chaker, and É. Haddad, "Highly tunable-emittance radiator based on semiconductor-metal transition of VO_2 thin films," *Appl. Phys. Lett.*, vol. 102, no. 2013, pp. 0–4, 2013.

[95] X. Wang, Y. Cao, Y. Zhang, L. Yan, and Y. Li, "Fabrication of VO_2-based multilayer structure with variable emittance," *Appl. Surf. Sci.*, vol. 344, pp. 230–235, 2015 [Online]. Available: http://linkinghub.elsevier.com/retrieve/pii/S0169433215007114

[96] S. Tachikawa, K. Shimazaki, A. Ohnishi, H. Hirosawa, Y. Shimakawa, A. Ochi, A. Okamoto, and Y. Nakamura, "Smart radiation device based on a perovskite manganese oxide," *Eur. Sp. Agency, (Special Publ. ESA SP*, vol. 2003, no. 540, pp. 41–47, 2003.

[97] A. Hendaoui, N. Émond, S. Dorval, M. Chaker, and E. Haddad, "VO_2-based smart coatings with improved emittance-switching properties for an energy-efficient near room-temperature thermal control of spacecrafts," *Sol. Energy Mater. Sol. Cells*, vol. 117, pp. 494–498, Oct. 2013 [Online]. Available: http://linkinghub.elsevier.com/retrieve/pii/S0927024813003693. [Accessed: 03-Sep-2014]

[98] K. Laaksonen, S.-Y. Li, S. R. Puisto, N. K. J. Rostedt, T. Ala-Nissila, C. G. Granqvist, R. M. Nieminen, and G. a. Niklasson, "Nanoparticles of TiO_2 and VO_2 in dielectric media: Conditions for low optical scattering, and comparison between effective medium and four-flux theories," *Sol. Energy Mater. Sol. Cells*, vol. 130, pp. 132–137, Nov. 2014 [Online]. Available: http://linkinghub.elsevier.com/retrieve/pii/S0927024814003456. [Accessed: 07-Jan-2015]

[99] Y. Li, S. Ji, Y. Gao, H. Luo, and M. Kanehira, "Core-shell VO_2@TiO_2 nanorods that combine thermochromic and photocatalytic properties for application as energy-saving smart coatings," *Sci. Rep.*, vol. 3, pp. 1–13, 2013 [Online]. Available: http://www.nature.com/doifinder/10.1038/srep01370

[100] S.-Y. Li, G. A. Niklasson, and C. G. Granqvist, "Nanothermochromics with VO_2-based core-shell structures: Calculated luminous and solar optical properties," *J. Appl. Phys.*, vol. 109, no. 11, p. 113515, 2011 [Online]. Available: http://scitation.aip.org/content/aip/journal/jap/109/11/10.1063/1.3592350. [Accessed: 17-Aug-2015]

[101] L. Martinu, O. Zabeida, and J. E. Klemberg-Sapieha, "Plasma-Enhanced Chemical Vapor Deposition of Functional Coatings," in *Handbook of Deposition Technologies for Films and Coatings*, Third Edit., Elsevier Ltd., 2010, pp. 532–553 [Online]. Available: http://www.sciencedirect.com/science/article/pii/B9780815520313000119

[102] R. Eason, *Pulsed laser deposition of thin films : applications-led growth of functional materials*. Wiley-Interscience, 2006.

[103] M. Saeli, C. Piccirillo, I. P. Parkin, I. Ridley, and R. Binions, "Nano-composite thermochromic thin films and their application in energy-efficient glazing," *Sol. Energy Mater. Sol. Cells*, vol. 94, no. 2, pp. 141–151, Feb. 2010 [Online]. Available: http://linkinghub.elsevier.com/retrieve/pii/S0927024809002979. [Accessed: 13-Nov-2013]

[104] M. E. A. Warwick, I. Ridley, and R. Binions, "Thermochromic vanadium dioxide thin films from electric field assisted aerosol assisted chemical vapour deposition," *Surf. Coatings Technol.*, vol. 230, pp. 163–167, Sep. 2013 [Online]. Available: http://linkinghub.elsevier.com/retrieve/pii/S0257897213005926. [Accessed: 14-Aug-2013]

[105] D. Louloudakis, D. Vernardou, E. Spanakis, N. Katsarakis, and E. Koudoumas, "Thermochromic vanadium oxide coatings grown by APCVD at low temperatures," *Phys. Procedia*, vol. 46, no. Eurocvd 19, pp. 137–141, 2013 [Online]. Available: http://dx.doi.org/10.1016/j.phpro.2013.07.055

[106] T. Manning, I. Parkin, R. Clark, D. Sheel, M. Pemble, and D. Vernadou, "Intelligent window coatings: atmospheric pressure chemical vapour deposition of vanadium oxides," no. 13, pp. 744–749, 2004 [Online]. Available: http://discovery.ucl.ac.uk/130011/

[107] J.-O. Carlsson and P. M. Martin, "Chemical Vapor Deposition," in *Handbook of Deposition Technologies for Films and Coatings*, Third Edit., Elsevier Ltd., 2010, pp. 532–553 [Online]. Available: http://www.sciencedirect.com/science/article/pii/B9780815520313000119

[108] M. E. A. Warwick and R. Binions, "Chemical Vapour Deposition of Thermochromic Vanadium Dioxide Thin Films for Energy Efficient Glazing," *J. Solid State Chem.*, vol. 214, pp. 53–66, Nov. 2013 [Online]. Available: http://linkinghub.elsevier.com/retrieve/pii/S0022459613005185. [Accessed: 13-Nov-2013]

[109] C. S. Blackman, C. Piccirillo, R. Binions, and I. P. Parkin, "Atmospheric pressure chemical vapour deposition of thermochromic tungsten doped vanadium dioxide thin films for use in architectural glazing," *Thin Solid Films*, vol. 517, no. 16, pp. 4565–4570, 2009 [Online]. Available: http://dx.doi.org/10.1016/j.tsf.2008.12.050

[110] M. N. Field and I. P. Parkin, “Atmospheric pressure chemical vapour deposition of vanadium(v) oxide films on glass substrates from reactions of $VOCl_3$ and VCl_4 with water,” *J. Mater. Chem.*, vol. 10, no. 8, pp. 1863–1866, 2000 [Online]. Available: http://discovery.ucl.ac.uk/59174/

[111] N. Wang, S. Magdassi, D. Mandler, and Y. Long, “Simple sol–gel process and one-step annealing of vanadium dioxide thin films: Synthesis and thermochromic properties,” *Thin Solid Films*, vol. 534, pp. 594–598, May 2013 [Online]. Available: http://www.sciencedirect.com/science/article/pii/S0040609013001934. [Accessed: 19-Aug-2015]

[112] L. Song, Y. Zhang, W. Huang, Q. Shi, D. Li, Y. Zhang, and Y. Xu, “Preparation and thermochromic properties of Ce-doped VO_2 films,” *Mater. Res. Bull.*, vol. 48, no. 6, pp. 2268–2271, Jun. 2013 [Online]. Available: http://www.sciencedirect.com/science/article/pii/S0025540813001013. [Accessed: 19-Aug-2015]

[113] C. Clavero, J. L. Slack, and A. Anders, “Size and composition-controlled fabrication of thermochromic metal oxide nanocrystals,” *J. Phys. D. Appl. Phys.*, vol. 46, no. 36, p. 362001, 2013 [Online]. Available: http://stacks.iop.org/0022-3727/46/i=36/a=362001?key=crossref.c60fea0f3541323f659815d57aa85300

[114] Y. Lu, S. Zhou, G. Gu, and L. Wu, “Preparation of transparent, hard thermochromic polysiloxane/tungsten-doped vanadium dioxide nanocomposite coatings at ambient temperature,” *Thin Solid Films*, vol. 534, pp. 231–237, May 2013 [Online]. Available: http://linkinghub.elsevier.com/retrieve/pii/S0040609013004100. [Accessed: 04-Sep-2013]

[115] Y.-X. Ji, G. A. Niklasson, C. G. Granqvist, and M. Boman, “Thermochromic VO_2 films by thermal oxidation of vanadium in SO_2,” *Sol. Energy Mater. Sol. Cells*, vol. 144, pp. 713–716, Jan. 2016 [Online]. Available: http://linkinghub.elsevier.com/retrieve/pii/S0927024815005231. [Accessed: 09-Jun-2016]

[116] J. H. Frazer and W. J. Kirkpatrick, “A New Mechanism for the Action of the Vanadium Pentoxide-Silica-Alkali Pyro-sulfate Catalyst for the Oxidation of Sultur Dioxide,” vol. 2375, no. 7, pp. 18–19, 1940.

[117] H. Flood and O. Kleppa, “Investigations on the Equilibria in the System V_2O_4, V_2O_5, $VOSO_4$, SO_2, SO_3,” *J. Am. Chem. Soc.*, vol. 69, no. curve 3, pp. 998–1002, 1947 [Online]. Available: http://pubs.acs.org/doi/abs/10.1021/ja01197a006

[118] A. Lafort, H. Kebaili, S. Goumri-Said, O. Deparis, R. Cloots, J. De Coninck, M. Voué, F. Mirabella, F. Maseri, and S. Lucas, “Optical properties of thermochromic VO_2 thin films on stainless steel: Experimental and theoretical studies,” *Thin Solid Films*, vol. 519, no. 10, pp. 3283–3287, Mar. 2011 [Online]. Available: http://www.sciencedirect.com/science/article/pii/S0040609010017712. [Accessed: 17-Aug-2015]

[119] B. Godshalk, “Magnetic core and method for manufacturing same,” US2659698 A, 1953 [Online]. Available: https://www.google.com/patents/US2659698

[120] T. N. Kennedy and J. D. Mackenzie, “Suppression of the semiconductor-metal transition in vanadium oxides,” *J. Non. Cryst. Solids*, vol. 1, no. 4, pp. 326–330, Jun. 1969 [Online].

Available: http://linkinghub.elsevier.com/retrieve/pii/0022309369900283. [Accessed: 27-Jul-2016]

[121] H. Kakiuchida, P. Jin, and M. Tazawa, "Control of thermochromic spectrum in vanadium dioxide by amorphous silicon suboxide layer," *Sol. Energy Mater. Sol. Cells*, vol. 92, no. 10, pp. 1279–1284, Oct. 2008 [Online]. Available: http://www.sciencedirect.com/science/article/pii/S0927024808001608. [Accessed: 13-Mar-2016]

[122] C. G. Granqvist, G. A. Niklasson, and N. R. Mlyuka, "Thermochromic material and fabrication thereof," US 8889219 B2, 2014 [Online]. Available: https://www.google.com/patents/US8889219

[123] N. H. Azhan, K. Okimura, Y. Ohtsubo, S. I. Kimura, M. Zaghrioui, and J. Sakai, "Large modification in insulator-metal transition of VO2 films grown on Al_2O_3 (001) by high energy ion irradiation in biased reactive sputtering," *J. Appl. Phys.*, vol. 119, no. 5, 2016 [Online]. Available: http://dx.doi.org/10.1063/1.4941348

[124] M. A. Lieberman and A. J. Lichtenberg, *Principles of plasma discharges and materials processing*. New York: John Wiley & Sons Ltd, 1994.

[125] F. F. Chen, *Introduction to plasma physics*, 1st ed. New York: Plenum Press, 1974.

[126] C. D. Child, "Discharge from hot CAO," *Phys. Rev. (Series I)*, vol. 32, no. 5, pp. 492–511, 1911.

[127] A. V. Phelps and Z. L. Petrovic, "Cold-cathode discharges and breakdown in argon: surface and gas phase production of secondary electrons," *Plasma Sources Sci. Technol.*, vol. 8, no. 3, pp. R21–R44, 1999.

[128] R. A. Baragiola and P. Riccardi, "Electron Emission from Surfaces Induced by Slow Ions and Atoms," in *Reactive Sputter Deposition*, D. Depla and S. Mahieu, Eds. Heidelberg: Springer Series in Materials Science, 2008, pp. 43–60.

[129] D. M. Mattox, "Particle bombardment effects on thin-film deposition: A review," *J. Vac. Sci. Technol. A Vacuum, Surfaces, Film.*, vol. 7, no. 3, pp. 1105–1114, May 1989 [Online]. Available: http://scitation.aip.org/content/avs/journal/jvsta/7/3/10.1116/1.576238. [Accessed: 27-May-2016]

[130] W. O. Hofer and P. J. Martin, "On the influence of reactive gases on sputtering and secondary ion emission," *Appl. Phys.*, vol. 16, no. 3, pp. 271–278, Jul. 1978 [Online]. Available: http://link.springer.com/10.1007/BF00885122. [Accessed: 30-May-2016]

[131] W. O. Hofer, H. L. Bay, and P. J. Martin, "Sputter-erosion and impurity emission from titanium and vanadium at low-energy ion bombardment," *J. Nucl. Mater.*, vol. 76–77, pp. 156–162, Sep. 1978 [Online]. Available: http://www.sciencedirect.com/science/article/pii/0022311578901290. [Accessed: 30-May-2016]

[132] W. Eckstein, *Sputtering by Particle Bombardment*, vol. 110. Berlin, Heidelberg: Springer Berlin Heidelberg, 2007 [Online]. Available: http://www.springerlink.com/index/10.1007/978-3-540-44502-9. [Accessed: 30-May-2016]

[133] S. Mahieu, “Biaxial alignment in sputter deposited thin films,” Doctoral thesis, Gent, 2006.

[134] S. Hafezian, B. Baloukas, and L. Martinu, “Percolation threshold determination of sputtered silver films using Stokes parameters and in situ conductance measurements.,” *Appl. Opt.*, vol. 53, no. 24, pp. 5367–74, 2014 [Online]. Available: http://www.ncbi.nlm.nih.gov/pubmed/25321107

[135] B.A. Movchan and A.V. Demchishin, “Structure and properties of thick condensates of nickel, titanium, tungsten, aluminum oxides, and zirconium dioxide in vacuum,” *Phys.Met.Metallogr*, vol. 28, p. 653, 1969.

[136] J. A. Thornton, “The microstructure of sputter-deposited coatings,” *J. Vac. Sci. Technol. A Vacuum, Surfaces, Film.*, vol. 4, no. 6, pp. 3059–3065, 1986.

[137] R. Messier, A. P. Giri, and R. A. Roy, “Revised structure zone model for thin film physical structure,” *J. Vac. Sci. Technol. A Vacuum, Surfaces, Film.*, vol. 2, no. June, pp. 500–503, 1984 [Online]. Available: http://scitation.aip.org/content/avs/journal/jvsta/2/2/10.1116/1.572604. [Accessed: 08-Jul-2016]

[138] A. Anders, “A structure zone diagram including plasma-based deposition and ion etching,” *Thin Solid Films*, vol. 518, no. 15, pp. 4087–4090, May 2010 [Online]. Available: http://linkinghub.elsevier.com/retrieve/pii/S0040609009018288. [Accessed: 09-Aug-2013]

[139] A. Lejars, “Mécanisme de sélection de l’orientation préférentielle lors de la croissance de couches minces , application au dépôt d’oxyde de zinc par pulvérisation magnétron à impulsions de haute puissance,” Thèse de doctorat, Université de Lorraine, 2012.

[140] B. Window and N. Savvides, “Charged particle fluxes from planar magnetron sputtering sources,” *J. Vac. Sci. Technol. A Vacuum, Surfaces, Film.*, vol. 4, no. 2, p. 196, Mar. 1986 [Online]. Available: http://scitation.aip.org/content/avs/journal/jvsta/4/2/10.1116/1.573470. [Accessed: 19-Oct-2016]

[141] J. M. Schneider, “Crystalline alumina deposited at low temperatures by ionized magnetron sputtering,” *J. Vac. Sci. Technol. A Vacuum, Surfaces, Film.*, vol. 15, no. 3, p. 1084, 1997.

[142] J. T. Gudmundsson, N. Brenning, D. Lundin, and U. Helmersson, “High power impulse magnetron sputtering discharge,” *J. Vac. Sci. Technol. A Vacuum, Surfaces, Film.*, vol. 30, no. 3, p. 30801, 2012 [Online]. Available: http://link.aip.org/link/JVTAD6/v30/i3/p030801/s1&Agg=doi

[143] M. Hála, J. Čapek, O. Zabeida, J. E. Klemberg-Sapieha, and L. Martinu, “Hysteresis-free deposition of niobium oxide films by HiPIMS using different pulse management strategies,” *J. Phys. D. Appl. Phys.*, vol. 45, no. 5, p. 55204, Feb. 2012 [Online]. Available: http://stacks.iop.org/0022-3727/45/i=5/a=055204?key=crossref.d71f932aa7c181af8c6411cc408a8195. [Accessed: 09-Aug-2013]

[144] J. T. Gudmundsson, J. Alami, and U. Helmersson, “Spatial and temporal behavior of the plasma parameters in a pulsed magnetron discharge,” *Surf. Coatings Technol.*, vol. 161, no. 2–3, pp. 249–256, 2002 [Online]. Available:

http://linkinghub.elsevier.com/retrieve/pii/S0257897202005182

[145] A. Mishra, G. Clarke, P. Kelly, and J. W. Bradley, “High Temporal Resolution Ion Energy Distribution Functions in HIPIMS Discharges,” *Plasma Process. Polym.*, vol. 6, no. S1, pp. S610–S614, Jun. 2009 [Online]. Available: http://doi.wiley.com/10.1002/ppap.200931601. [Accessed: 03-Sep-2013]

[146] J. T. Gudmundsson, “Ionization Processes in the High Power Impulse Magnetron Sputtering Discharge (HiPIMS),” *Technology*, vol. 249, no. 2002, p. 2003, 2006 [Online]. Available: http://langmuir.raunvis.hi.is/~tumi/ps/hipims_gec06.pdf

[147] D. Lundin, M. Čada, and Z. Hubička, “Ionization of sputtered Ti, Al, and C coupled with plasma characterization in HiPIMS,” *Plasma Sources Sci. Technol.*, vol. 24, no. 3, p. 35018, 2015 [Online]. Available: http://stacks.iop.org/0963-0252/24/i=3/a=035018?key=crossref.77001a90fe258ce7b1cb11200908ad62

[148] M. Hala, N. Viau, O. Zabeida, J. E. Klemberg-Sapieha, and L. Martinu, “Dynamics of reactive high-power impulse magnetron sputtering discharge studied by time- and space-resolved optical emission spectroscopy and fast imaging,” *J. Appl. Phys.*, vol. 107, no. 4, p. 43305, 2010 [Online]. Available: http://link.aip.org/link/JAPIAU/v107/i4/p043305/s1&Agg=doi. [Accessed: 09-Aug-2013]

[149] A. Anders, J. Andersson, and A. Ehiasarian, “High power impulse magnetron sputtering: Current-voltage-time characteristics indicate the onset of sustained self-sputtering,” *J. Appl. Phys.*, vol. 102, no. 11, p. 113303, 2007 [Online]. Available: http://link.aip.org/link/JAPIAU/v102/i11/p113303/s1&Agg=doi. [Accessed: 15-Aug-2013]

[150] J. Andersson, A. P. Ehiasarian, and A. Anders, “Observation of Ti^{4+} ions in a high power impulse magnetron sputtering plasma,” *Appl. Phys. Lett.*, vol. 93, no. 7, p. 71504, 2008 [Online]. Available: http://link.aip.org/link/APPLAB/v93/i7/p071504/s1&Agg=doi. [Accessed: 03-Sep-2013]

[151] J. Bohlmark, M. Lattemann, J. T. Gudmundsson, A. P. Ehiasarian, Y. Aranda Gonzalvo, N. Brenning, and U. Helmersson, “The ion energy distributions and ion flux composition from a high power impulse magnetron sputtering discharge,” *Thin Solid Films*, vol. 515, no. 4, pp. 1522–1526, 2006.

[152] A. Hecimovic and A. P. Ehiasarian, “Time evolution of ion energies in HIPIMS of chromium plasma discharge,” *J. Phys. D. Appl. Phys.*, vol. 42, no. 13, p. 135209, Jul. 2009 [Online]. Available: http://stacks.iop.org/0022-3727/42/i=13/a=135209?key=crossref.6a99dc2cadcf7830ba18960d24e1a3d0. [Accessed: 03-Sep-2013]

[153] G. Greczynski and L. Hultman, “Time and energy resolved ion mass spectroscopy studies of the ion flux during high power pulsed magnetron sputtering of Cr in Ar and Ar/N_2 atmospheres,” *Vacuum*, vol. 84, no. 9, pp. 1159–1170, Apr. 2010 [Online]. Available: http://linkinghub.elsevier.com/retrieve/pii/S0042207X10000795. [Accessed: 03-Sep-2013]

[154] N. Brenning, R. L. Merlino, D. Lundin, M. A. Raadu, and U. Helmersson, “Faster-than-Bohm Cross-B Electron Transport in Strongly Pulsed Plasmas,” *Phys. Rev. Lett.*, vol. 103, no. 22, p. 225003, Nov. 2009 [Online]. Available:

http://link.aps.org/doi/10.1103/PhysRevLett.103.225003. [Accessed: 03-Sep-2013]

[155] P. Poolcharuansin and J. W. Bradley, “Short- and long-term plasma phenomena in a HiPIMS discharge,” *Plasma Sources Sci. Technol.*, vol. 19, no. 2, p. 25010, Apr. 2010 [Online]. Available: http://stacks.iop.org/0963-0252/19/i=2/a=025010?key=crossref.081f7539d1d102cfe630d122bcaae725. [Accessed: 18-Aug-2013]

[156] D. Lundin, P. Larsson, E. Wallin, M. Lattemann, N. Brenning, and U. Helmersson, “Cross-field ion transport during high power impulse magnetron sputtering,” *Plasma Sources Sci. Technol.*, vol. 17, no. 3, p. 35021, Aug. 2008 [Online]. Available: http://stacks.iop.org/0963-0252/17/i=3/a=035021?key=crossref.2ca07b0671dcb79b8b3592ac7ec7b457. [Accessed: 03-Sep-2013]

[157] A. Hecimovic, M. Böke, and J. Winter, “The characteristic shape of emission profiles of plasma spokes in HiPIMS: the role of secondary electrons,” *J. Phys. D. Appl. Phys.*, vol. 47, no. 10, p. 102003, Mar. 2014 [Online]. Available: http://stacks.iop.org/0022-3727/47/i=10/a=102003?key=crossref.3956d2f7e617fee2de65126eacdef7d9. [Accessed: 28-Mar-2014]

[158] S. Gallian, W. N. G. Hitchon, D. Eremin, T. Mussenbrock, and R. P. Brinkmann, “A phenomenological model for the description of rotating spokes in HiPIMS discharges,” *Plasma Sources Sci. Technol.*, vol. 22, no. 5, p. 55012, Oct. 2013 [Online]. Available: http://stacks.iop.org/0963-0252/22/i=5/a=055012?key=crossref.d649c6e08d7d75b0044c5d58bd8a0a55. [Accessed: 19-Dec-2013]

[159] A. Hecimovic, A. von Keudell, V. S. Der Gathen, and J. Winter, “Various Shapes of Plasma Spokes Observed in HiPIMS,” *IEEE Trans. Plasma Sci.*, vol. 42, no. 10, pp. 2810–2811, Oct. 2014 [Online]. Available: http://ieeexplore.ieee.org/lpdocs/epic03/wrapper.htm?arnumber=6844894

[160] A. Hecimovic, “Anomalous cross-B field transport and spokes in HiPIMS plasma,” *J. Phys. D. Appl. Phys.*, vol. 49, no. 18, p. 18LT01, 2016 [Online]. Available: http://stacks.iop.org/0022-3727/49/i=18/a=18LT01?key=crossref.db10fc30b2be0aeff261c02ec8b69eaa

[161] A. Hecimovic, V. Schulz-von der Gathen, M. Böke, A. von Keudell, and J. Winter, “Spoke transitions in HiPIMS discharges,” *Plasma Sources Sci. Technol.*, vol. 24, no. 4, p. 45005, 2015 [Online]. Available: http://stacks.iop.org/0963-0252/24/i=4/a=045005?key=crossref.0fea8691f746d14a2fe5e522125319b4

[162] A. Anders, M. Panjan, R. Franz, J. Andersson, and P. Ni, “Drifting potential humps in ionization zones: The ‘propeller blades’ of high power impulse magnetron sputtering,” *Appl. Phys. Lett.*, vol. 103, no. 14, p. 144103, 2013 [Online]. Available: http://link.aip.org/link/APPLAB/v103/i14/p144103/s1&Agg=doi. [Accessed: 19-Dec-2013]

[163] M. Panjan, S. Loquai, J. E. Klemberg-Sapieha, and L. Martinu, “Non-uniform plasma distribution in dc magnetron sputtering: origin, shape and structuring of spokes,” *Plasma Sources Sci. Technol.*, vol. 24, no. 6, p. 65010, Dec. 2015 [Online]. Available:

http://iopscience.iop.org/article/10.1088/0963-0252/24/6/065010. [Accessed: 17-Mar-2016]

[164] V. Kouznetsov, K. Macak, J. M. Schneider, K. Maca, U. Helmersson, and I. Petrov, "A novel pulsed magnetron sputter technique utilizing very high target power densities," *Surf. Coatings Technol.*, vol. 122, pp. 290–293, 1999.

[165] A. Anders, J. Čapek, M. Hála, and L. Martinu, "The 'recycling trap': a generalized explanation of discharge runaway in high-power impulse magnetron sputtering," *J. Phys. D. Appl. Phys.*, vol. 45, no. 1, p. 12003, Jan. 2012 [Online]. Available: http://stacks.iop.org/0022-3727/45/i=1/a=012003?key=crossref.b3bf7a867e76abfe82d8b694c3106308. [Accessed: 03-Sep-2013]

[166] M. Aiempanakit, T. Kubart, P. Larsson, K. Sarakinos, J. Jensen, and U. Helmersson, "Hysteresis and process stability in reactive high power impulse magnetron sputtering of metal oxides," *Thin Solid Films*, vol. 519, no. 22, pp. 7779–7784, Sep. 2011 [Online]. Available: http://linkinghub.elsevier.com/retrieve/pii/S0040609011012843. [Accessed: 09-Aug-2013]

[167] K. Sarakinos, J. Alami, and M. Wuttig, "Process characteristics and film properties upon growth of TiO_x films by high power pulsed magnetron sputtering," *J. Phys. D. Appl. Phys.*, vol. 40, no. 7, pp. 2108–2114, Apr. 2007 [Online]. Available: http://stacks.iop.org/0022-3727/40/i=7/a=037?key=crossref.1d80f28eeeecbecac6e88814a3e9f96d. [Accessed: 30-Oct-2016]

[168] E. Wallin and U. Helmersson, "Hysteresis-free reactive high power impulse magnetron sputtering," *Thin Solid Films*, vol. 516, no. 18, pp. 6398–6401, Jul. 2008 [Online]. Available: http://linkinghub.elsevier.com/retrieve/pii/S0040609007015374. [Accessed: 03-Sep-2013]

[169] M. Hala, R. Vernhes, O. Zabeida, J. E. Klemberg-Sapieha, and L. Martinu, "Reactive HiPIMS deposition of SiO_2/Ta_2O_5 optical interference filters," *J. Appl. Phys.*, vol. 116, no. 21, 2014 [Online]. Available: http://dx.doi.org/10.1063/1.4903285

[170] M. Bowes, P. Poolcharuansin, and J. W. Bradley, "Negative ion energy distributions in reactive HiPIMS," *J. Phys. D. Appl. Phys.*, vol. 46, no. 4, p. 45204, Jan. 2013 [Online]. Available: http://stacks.iop.org/0022-3727/46/i=4/a=045204?key=crossref.75a2f9e179576be8e7c5a1049ea9c282. [Accessed: 18-Sep-2013]

[171] M. Bowes and J. W. Bradley, "The behaviour of negative oxygen ions in the afterglow of a reactive HiPIMS discharge," *J. Phys. D. Appl. Phys.*, vol. 47, no. 26, p. 265202, Jul. 2014 [Online]. Available: http://stacks.iop.org/0022-3727/47/i=26/a=265202?key=crossref.e6a8eb01edb98246b4a65d24b0b7858a. [Accessed: 07-Jun-2014]

[172] J. Kohout, E. Bousser, T. Schmitt, R. Vernhes, O. Zabeida, J. Klemberg-Sapieha, and L. Martinu, "Stable reactive deposition of amorphous Al_2O_3 films with low residual stress and enhanced toughness using pulsed dc magnetron sputtering with very low duty cycle," *Vacuum*, vol. 124, pp. 96–100, 2016.

[173] J. Vlček, J. Rezek, J. Houška, T. Kozák, and J. Kohout, “Benefits of the controlled reactive high-power impulse magnetron sputtering of stoichiometric ZrO_2 films,” *Vacuum*, vol. 114, pp. 131–141, Dec. 2015 [Online]. Available: http://linkinghub.elsevier.com/retrieve/pii/S0042207X14003893. [Accessed: 23-Dec-2014]

[174] M. Aiempanakit, U. Helmersson, A. Aijaz, P. Larsson, R. Magnusson, J. Jensen, and T. Kubart, “Effect of peak power in reactive high power impulse magnetron sputtering of titanium dioxide,” *Surf. Coatings Technol.*, vol. 205, no. 20, pp. 4828–4831, Jul. 2011 [Online]. Available: http://www.sciencedirect.com/science/article/pii/S0257897211004270. [Accessed: 10-May-2016]

[175] C. Nouvellon, M. Michiels, J. P. Dauchot, C. Archambeau, F. Laffineur, E. Silberberg, S. Delvaux, R. Cloots, S. Konstantinidis, and R. Snyders, “Deposition of titanium oxide films by reactive High Power Impulse Magnetron Sputtering (HiPIMS): Influence of the peak current value on the transition from metallic to poisoned regimes,” *Surf. Coatings Technol.*, vol. 206, no. 16, pp. 3542–3549, Apr. 2012 [Online]. Available: http://linkinghub.elsevier.com/retrieve/pii/S0257897212001363. [Accessed: 11-Sep-2013]

[176] X. Zhao, J. Jin, J.-C. Cheng, J.-W. Lee, K.-H. Wu, and K.-C. Liu, “Effect of Pulsed Off-times on the Reactive HiPIMS Preparation of Zirconia Thin Films,” *Vacuum*, vol. 118, pp. 38–42, 2015 [Online]. Available: http://linkinghub.elsevier.com/retrieve/pii/S0042207X1500086X

[177] N. Bagcivan, K. Bobzin, A. Ludwig, D. Grochla, and R. H. Brugnara, “CrN/AlN nanolaminate coatings deposited via high power pulsed and middle frequency pulsed magnetron sputtering,” *Thin Solid Films*, vol. 572, pp. 153–160, 2014 [Online]. Available: http://dx.doi.org/10.1016/j.tsf.2014.06.058

[178] S. Shayestehaminzadeh, T. K. Tryggvason, F. Magnus, S. Olafsson, and J. T. Gudmundsson, “Ultra-thin poly-crystalline TiN films grown by HiPIMS on MgO(100) — In-situ resistance study of the initial stage of growth,” *Thin Solid Films*, Aug. 2013 [Online]. Available: http://linkinghub.elsevier.com/retrieve/pii/S0040609013012595. [Accessed: 28-Aug-2013]

[179] R. Machunze, A. P. Ehiasarian, F. D. Tichelaar, and G. C. a M. Janssen, “Stress and texture in HIPIMS TiN thin films,” *Thin Solid Films*, vol. 518, no. 5, pp. 1561–1565, Dec. 2009 [Online]. Available: http://linkinghub.elsevier.com/retrieve/pii/S0040609009015296. [Accessed: 03-Sep-2013]

[180] P. E. Hovsepian, A. P. Ehiasarian, and U. Ratayski, “CrAlYCN/CrCN nanoscale multilayer PVD coatings deposited by the combined High Power Impulse Magnetron Sputtering/Unbalanced Magnetron Sputtering (HIPIMS/UBM) technology,” *Surf. Coatings Technol.*, vol. 203, no. 9, pp. 1237–1243, Dec. 2009 [Online]. Available: http://shura.shu.ac.uk/1112/. [Accessed: 03-Sep-2013]

[181] M. Hála, J. Čapek, O. Zabeida, J. E. Klemberg-Sapieha, and L. Martinu, “Pulse management in high power pulsed magnetron sputtering of niobium,” *Surf. Coatings Technol.*, vol. 206, no. 19–20, pp. 4186–4193, May 2012 [Online]. Available: http://linkinghub.elsevier.com/retrieve/pii/S0257897212003040. [Accessed: 03-Sep-2013]

[182] V. Kouznetsov, “Method and apparatus for magnetically enhanced sputtering,” US6296742 B1, 2001 [Online]. Available: https://www.google.com/patents/US6296742

[183] M. Hála, O. Zabeida, B. Baloukas, J. E. Klemberg-Sapieha, and L. Martinu, “Time- and Species-Resolved Plasma Imaging as a New Diagnostic Approach for HiPIMS Discharge Characterization,” *IEEE Trans. Plasma Sci.*, vol. 38, no. 11, pp. 3035–3039, Nov. 2010 [Online]. Available: http://ieeexplore.ieee.org/lpdocs/epic03/wrapper.htm?arnumber=5565485

[184] A. Kanitz, A. Hecimovic, M. Böke, and J. Winter, “Two dimensional spatial Argon metastable dynamics in HiPIMS discharges,” *J. Phys. D. Appl. Phys.*, vol. 49, no. 12, p. 125203, 2016 [Online]. Available: http://stacks.iop.org/0022-3727/49/i=12/a=125203?key=crossref.6dbcbbbe54cb86250990389a480cb2cb

[185] C. Vitelaru, D. Lundin, G. D. Stancu, N. Brenning, J. Bretagne, and T. Minea, “Argon metastables in HiPIMS: time-resolved tunable diode-laser diagnostics,” *Plasma Sources Sci. Technol.*, vol. 21, no. 2, p. 25010, Apr. 2012 [Online]. Available: http://stacks.iop.org/0963-0252/21/i=2/a=025010?key=crossref.0b9c93c52dcacdc4fcf337078c969d00. [Accessed: 28-Oct-2014]

[186] L. Maaloul and L. Stafford, “Measurements of sputtered neutrals and ions and investigation of their roles on the plasma properties during rf magnetron sputtering of Zn and ZnO targets,” *J. Vac. Sci. Technol. A Vacuum, Surfaces, Film.*, vol. 31, no. 6, p. 61306, 2013 [Online]. Available: http://link.aip.org/link/JVTAD6/v31/i6/p061306/s1&Agg=doi. [Accessed: 19-Dec-2013]

[187] Y. Hayashi, S. Hirao, Y. Zhang, T. Gans, D. O’Connell, Z. L. Petrović, and T. Makabe, “Argon metastable state densities in inductively coupled plasma in mixtures of Ar and O 2,” *J. Phys. D. Appl. Phys.*, vol. 42, no. 14, p. 145206, Jul. 2009 [Online]. Available: http://stacks.iop.org/0022-3727/42/i=14/a=145206?key=crossref.08acf29834f3107f7304e38e045d279e. [Accessed: 26-May-2014]

[188] R. N. Zare, “My Life with LIF: A Personal Account of Developing Laser-Induced Fluorescence,” *Annu. Rev. Anal. Chem.*, vol. 5, no. 1, pp. 1–14, Jul. 2012 [Online]. Available: http://www.annualreviews.org/doi/10.1146/annurev-anchem-062011-143148. [Accessed: 06-Oct-2016]

[189] G. Inoue and M. Suzuki, “Reactions of $SiH_2(\bar{X}1A1)$ with H_2, CH_4, C_2H_4, SiH_4 and Si_2H_6 at 298 K,” *Chem. Phys. Lett.*, vol. 122, no. 4, pp. 361–364, 1985.

[190] R. Walkup, P. Avouris, R. W. Dreyfus, J. M. Jasinski, and G. S. Selwyn, “Laser detection of diatomic products of plasma sputtering and etching Detection of CF_2 radicals in a plasma etching reactor by laser-induced fluorescence spectroscopy,” *Cit. Appl. Phys. Lett. Appl. Phys. Lett. J. Vac. Sci. Technol. A Appl. Phys. Lett. Today*, vol. 45, no. 10, pp. 2779–62, 1984 [Online]. Available: http://dx.doi.org/10.1063/1.95280. [Accessed: 06-Oct-2016]

[191] A. C. Group, “N_2 and N_2^+ Energy Level Diagrams,” *accessed 10-11-2016*, 2016. [Online]. Available: http://raptor.physics.wisc.edu/

[192] J. M. Lerner and A. Thevenon, *The optics of spectroscopy*. Edison: J.Y. Optical Systems,

1988.

[193] F. Guinneton, L. Sauques, J. C. Valmalette, F. Cros, and J. R. Gavarri, “Optimized infrared switching properties in thermochromic vanadium dioxide thin films: Role of deposition process and microstructure,” *Thin Solid Films*, vol. 446, no. 2, pp. 287–295, 2004.

[194] H. Fujiwara, *Spectroscopic ellipsometry : principles and applications*. John Wiley & Sons, 2007.

[195] S. C. Gujrathi and S. Bultena, “Depth profiling of hydrogen using the high efficiency ERD-TOF technique,” *Nucl. Instruments Methods Phys. Res. Sect. B Beam Interact. with Mater. Atoms*, vol. 64, no. 1, pp. 789–795, 1992.

[196] F. Schiettekatte, “Fast Monte Carlo for ion beam analysis simulations,” *Nucl. Instruments Methods Phys. Res. Sect. B Beam Interact. with Mater. Atoms*, vol. 266, no. 8, pp. 1880–1885, 2008.

[197] M. Mayer, W. Eckstein, H. Langhuth, F. Schiettekatte, and U. von Toussaint, “Computer simulation of ion beam analysis: Possibilities and limitations,” *Nucl. Instruments Methods Phys. Res. Sect. B Beam Interact. with Mater. Atoms*, vol. 269, no. 24, pp. 3006–3013, 2011.

[198] K. Sarakinos, J. Alami, and S. Konstantinidis, “High power pulsed magnetron sputtering: A review on scientific and engineering state of the art,” *Surf. Coatings Technol.*, vol. 204, p. 1661, 2010.

[199] U. Helmersson, M. Lattemann, J. Bohlmark, A. P. Ehiasarian, and J. T. Gudmundsson, “Ionized physical vapor deposition (IPVD): A review of technology and applications,” *Thin Solid Films*, vol. 513, no. 1–2, pp. 1–24, Aug. 2006 [Online]. Available: http://linkinghub.elsevier.com/retrieve/pii/S0040609006004317. [Accessed: 03-Sep-2013]

[200] M. Hála, R. Vernhes, O. Zabeida, E. Bousser, J. E. Klemberg-Sapieha, R. Sargent, and L. Martinu, “Growth and properties of high index Ta_2O_5 optical coatings prepared by HiPIMS and other methods,” *Surf. Coatings Technol.*, vol. 241, pp. 33–37, Feb. 2014 [Online]. Available: http://linkinghub.elsevier.com/retrieve/pii/S0257897213007895. [Accessed: 05-Nov-2014]

[201] S. Loquai, B. Baloukas, O. Zabeida, J. E. Klemberg-Sapieha, and L. Martinu, “HiPIMS-deposited thermochromic VO_2 films on polymeric substrates,” *Sol. Energy Mater. Sol. Cells*, vol. 155, pp. 60–69, 2016.

[202] C. Maszl, W. Breilmann, J. Benedikt, and a von Keudell, “Origin of the energetic ions at the substrate generated during high power pulsed magnetron sputtering of titanium,” *J. Phys. D. Appl. Phys.*, vol. 47, no. 22, p. 224002, Jun. 2014 [Online]. Available: http://stacks.iop.org/0022-3727/47/i=22/a=224002?key=crossref.d320ca45604f3c9a2d1113b87dcdb10c. [Accessed: 11-Jul-2014]

[203] C. Vitelaru, D. Lundin, N. Brenning, and T. Minea, “Plasma reactivity in high-power impulse magnetron sputtering through oxygen kinetics,” *Appl. Phys. Lett.*, vol. 103, no. 10, p. 104105, 2013 [Online]. Available: http://link.aip.org/link/APPLAB/v103/i10/p104105/s1&Agg=doi. [Accessed: 13-Nov-2013]

[204] M. Bowes and J. W. Bradley, “Inert gas effects on the deposition rate of TiO_2 during reactive HiPIMS,” *Surf. Coatings Technol.*, vol. 250, p. 2, Jul. 2014 [Online]. Available: http://linkinghub.elsevier.com/retrieve/pii/S0257897214001091. [Accessed: 14-Feb-2014]

[205] N. Britun, M. Palmucci, S. Konstantinidis, and R. Snyders, “Particle visualization in high-power impulse magnetron sputtering. I. 2D density mapping,” *J. Appl. Phys.*, vol. 117, no. 16, p. 163302, 2015 [Online]. Available: http://scitation.aip.org/content/aip/journal/jap/117/16/10.1063/1.4919006

[206] M. Čada, Z. Hubička, P. Adámek, J. Klusoň, and L. Jastrabík, “Time-resolved plasma parameters in the HiPIMS discharge with Ti target in Ar/O_2 atmosphere,” *Surf. Coatings Technol.*, vol. 205, pp. S317–S321, Jul. 2011 [Online]. Available: http://linkinghub.elsevier.com/retrieve/pii/S0257897210012260. [Accessed: 12-Sep-2013]

[207] J. T. Gudmundsson, J. Alami, and U. Helmersson, “Evolution of the electron energy distribution and plasma parameters in a pulsed magnetron discharge,” *Appl. Phys. Lett.*, vol. 78, no. 22, p. 3427, 2001 [Online]. Available: http://link.aip.org/link/APPLAB/v78/i22/p3427/s1&Agg=doi. [Accessed: 03-Sep-2013]

[208] G. Piech, J. Boffard, M. Gehrke, L. Anderson, and C. Lin, “Measurement of Cross Sections for Electron Excitation out of the Metastable Levels of Argon,” *Phys. Rev. Lett.*, vol. 81, no. 2, pp. 309–312, Jul. 1998 [Online]. Available: http://link.aps.org/doi/10.1103/PhysRevLett.81.309

[209] J. T. Gudmundsson, T. Kimura, and M. A. Lieberman, “Experimental studies of O_2 /Ar plasma in a planar inductive discharge,” *Plasma Sources Sci. Technol.*, vol. 8, no. 1, pp. 22–30, Feb. 1999 [Online]. Available: http://stacks.iop.org/0963-0252/8/i=1/a=003?key=crossref.47514f9adf2b7c80d343b6ddf2104a36

[210] J. I. Steinfeld, *Molecules and Radiation: An Introduction to Modern Molecular Spectroscopy. Second Edition*, 2nd ed. Cambridge: MIT press, 1985 [Online]. Available: http://store.doverpublications.com/0486441520.html

[211] UNEP, “2011 buildings energy data book,” Washington, DC, USA, DC, USA, 2012.

[212] U. DOE, “Buildings and climate change: Challenges and opportunities,” Paris, France, France, 2007.

[213] C. G. Granqvist, “Fenestration for reducing building cooling needs: an introduction to spectral selectivity, thermochromics, and electrochromics,” in *Eco-efficient materials for mitigating building cooling needs. Design, properties and applications*, 1st ed., F. Pacheco-Torgal, J. A. Labrincha, L. F. Cabeza, and C. G. Granqvist, Eds. Woodhead Publishing, 2015.

[214] G. V. Jorgenson and J. C. Lee, “Doped vanadium oxide for optical switching films,” *Sol. Energy Mater.*, vol. 14, no. 3–5, pp. 205–214, Nov. 1986 [Online]. Available: http://www.sciencedirect.com/science/article/pii/016516338690047X. [Accessed: 07-Aug-2015]

[215] M. A. Sobhan, R. T. Kivaisi, B. Stjerna, and C. G. Granqvist, “Thermochromism of sputter deposited $W_xV_{1-x}O_2$ films,” *Sol. Energy Mater. Sol. Cells*, vol. 44, no. 4, pp. 451–455, Dec. 1996 [Online]. Available: http://www.sciencedirect.com/science/article/pii/S0927024895000518. [Accessed: 27-

Aug-2015]

[216] N. R. Mlyuka, G. A. Niklasson, and C. G. Granqvist, “Mg doping of thermochromic VO_2 films enhances the optical transmittance and decreases the metal-insulator transition temperature,” *Appl. Phys. Lett.*, vol. 95, no. 17, p. 171909, 2009 [Online]. Available: http://scitation.aip.org/content/aip/journal/apl/95/17/10.1063/1.3229949

[217] P.-A. Cormier, A. Balhamri, A.-L. Thomann, R. Dussart, N. Semmar, J. Mathias, R. Snyders, and S. Konstantinidis, “Measuring the energy flux at the substrate position during magnetron sputter deposition processes,” *J. Appl. Phys.*, vol. 113, no. 1, p. 13305, 2013 [Online]. Available: http://link.aip.org/link/JAPIAU/v113/i1/p013305/s1&Agg=doi. [Accessed: 03-Sep-2013]

[218] D. Lundin, M. Stahl, H. Kersten, and U. Helmersson, “Energy flux measurements in high power impulse magnetron sputtering,” *J. Phys. D. Appl. Phys.*, vol. 42, no. 18, p. 185202, Sep. 2009 [Online]. Available: http://stacks.iop.org/0022-3727/42/i=18/a=185202?key=crossref.4e6670c1f8e9c92c0e67ecc6b7b4a8ba. [Accessed: 03-Sep-2013]

[219] S. Larouche and L. Martinu, “OpenFilters: open-source software for the design, optimization, and synthesis of optical lters,” *Appl. Opt.*, vol. 47, no. 13, pp. 219–230, 2008.

[220] G. Silversmit, D. Depla, H. Poelman, G. B. Marin, and R. De Gryse, “Determination of the V_{2p} XPS binding energies for different vanadium oxidation states (V^{5+} to V^{0+}),” *J. Electron Spectros. Relat. Phenomena*, vol. 135, no. 2–3, pp. 167–175, Apr. 2004 [Online]. Available: http://linkinghub.elsevier.com/retrieve/pii/S0368204804002221. [Accessed: 03-Sep-2014]

[221] M. Kang, S. W. Kim, J. W. Ryu, Y. B. Xu, and R. Kato, “Optical and thermal properties of V_2O_5 thin films with crystallization,” *J. Korean Phys. Soc.*, vol. 62, no. 8, pp. 1134–1138, 2013 [Online]. Available: <Go to ISI>://WOS:000318726700010

[222] S. Lee, T. L. Meyer, S. Park, T. Egami, and H. N. Lee, “Growth control of the oxidation state in vanadium oxide thin films,” *Appl. Phys. Lett.*, vol. 105, no. 22, p. 223515, 2014 [Online]. Available: http://scitation.aip.org/content/aip/journal/apl/105/22/10.1063/1.4903348

[223] M. Tazawa, P. Jin, and S. Tanemura, “Optical constants of $V_{(1-x)}W_xO_2$ films,” *Appl. Opt.*, vol. 37, no. 10, p. 1858, 1998.

[224] M. O. Hakim, S. M. Babulanam, and C. G. Granqvist, “Electrochemical properties of thin VO_2 films on polyimide substrates,” *Thin Solid Films*, vol. 158, p. L49, 1988.

[225] M. Soltani, M. Chaker, E. Haddad, R. V. Kruzelecky, and D. Nikanpour, “Optical switching of vanadium dioxide thin films deposited by reactive pulsed laser deposition,” *J. Vac. Sci. Technol. A Vacuum, Surfaces, Film.*, vol. 22, no. 3, p. 859, 2004 [Online]. Available: http://link.aip.org/link/JVTAD6/v22/i3/p859/s1&Agg=doi. [Accessed: 19-Aug-2013]

[226] J. H. Park, J. M. Coy, T. S. Kasirga, C. Huang, Z. Fei, S. Hunter, and D. H. Cobden, “Measurement of a solid-state triple point at the metal-insulator transition in VO_2.,” *Nature*, vol. 500, no. 7463, pp. 431–4, 2013 [Online]. Available:

http://www.ncbi.nlm.nih.gov/pubmed/23969461

[227] D. Natelson, “A solid triple point,” *Nature*, vol. 500, p. 408, 2013.

[228] M. J. Miller and J. Wang, “Influence of grain size on transition temperature of thermochromic VO_2,” *J. Appl. Phys.*, vol. 117, no. 3, p. 34307, Jan. 2015 [Online]. Available: http://scitation.aip.org/content/aip/journal/jap/117/3/10.1063/1.4906122. [Accessed: 17-Aug-2015]

[229] H. S. Virk, “Physical and chemical response of 70 MeV carbon ion irradiated polyether sulphone polymer,” *Nucl. Instruments Methods Phys. Res. Sect. B Beam Interact. with Mater. Atoms*, vol. 248, no. 2, pp. 279–283, 2006.

[230] Y. Hong-Tao, F. Ke-Cheng, W. Xue-Jin, L. Chao, H. Chen-Juan, and N. Yu-Xin, “Effect of nonstoichiometry on Raman scattering of VO2 films,” *Chinese Phys.*, vol. 13, no. 1, p. 82, 2004.

[231] A. Bergeron, “Interphase in plasma-deposited silicon nitride optical films on polycarbonate: in situ ellipsometric characterization,” *Opt. Eng.*, vol. 39, no. 3, p. 825, Mar. 2000 [Online]. Available: http://opticalengineering.spiedigitallibrary.org/article.aspx?articleid=1076062. [Accessed: 17-May-2016]

[232] C. Wang, X. Liu, J. Shao, W. Xiong, W. Ma, and Y. Zheng, “Structural transition and temperature-driven conductivity switching of single crystalline VO_2 (A) nanowires,” *RSC Adv.*, vol. 4, no. 109, pp. 64021–64026, 2014 [Online]. Available: http://xlink.rsc.org/?DOI=C4RA12392A

[233] J. Mendialdua, R. Casanova, and Y. Barbaux, “XPS studies of V_2O_5, V_6O_{13}, VO_2 and V_2O_3,” *J. Electron Spectros. Relat. Phenomena*, vol. 71, no. 3, pp. 249–261, 1995 [Online]. Available: http://www.sciencedirect.com/science/article/pii/0368204894022917

[234] D. Poitras and L. Martinu, “Interphase in plasma-deposited films on plastics: effect on the spectral properties of optical filters,” *Appl. Opt.*, vol. 39, no. 7, p. 1168, Mar. 2000 [Online]. Available: http://www.osapublishing.org/viewmedia.cfm?uri=ao-39-7-1168&seq=0&html=true. [Accessed: 17-May-2016]

[235] S.-Y. Li, G. A. Niklasson, and C. G. Granqvist, “Thermochromic fenestration with VO_2-based materials: Three challenges and how they can be met,” *Thin Solid Films*, vol. 520, no. 10, pp. 3823–3828, Mar. 2012 [Online]. Available: http://linkinghub.elsevier.com/retrieve/pii/S0040609011017937. [Accessed: 20-Aug-2013]

[236] P. Jin, S. Nakao, and S. Tanemura, “Tungsten doping into vanadium dioxide thermochromic films by high-energy ion implantation and thermal annealing,” *Thin Solid Films*, vol. 324, no. 1–2, pp. 151–158, 1998.

[237] M. Jiang, S. Bao, X. Cao, Y. Li, S. Li, H. Zhou, H. Luo, and P. Jin, “Improved luminous transmittance and diminished yellow color in VO_2 energy efficient smart thin films by Zn doping,” *Ceram. Int.*, pp. 1–4, Oct. 2013 [Online]. Available: http://linkinghub.elsevier.com/retrieve/pii/S0272884213013503. [Accessed: 19-Dec-2013]

[238] L. Kang, Y. Gao, H. Luo, J. Wang, B. Zhu, Z. Zhang, J. Du, M. Kanehira, and Y. Zhang, “Thermochromic properties and low emissivity of ZnO:Al/VO_2 double-layered films with

a lowered phase transition temperature," *Sol. Energy Mater. Sol. Cells*, vol. 95, no. 12, pp. 3189–3194, 2011 [Online]. Available: http://dx.doi.org/10.1016/j.solmat.2011.06.047

[239] T. Kubart, M. Čada, D. Lundin, and Z. Hubička, "Investigation of ionized metal flux fraction in HiPIMS discharges with Ti and Ni targets," *Surf. Coatings Technol.*, vol. 238, pp. 152–157, Jan. 2014 [Online]. Available: http://linkinghub.elsevier.com/retrieve/pii/S0257897213009985. [Accessed: 11-Jul-2014]

[240] R. . Kivaisi and M. Samiji, "Optical and electrical properties of vanadium dioxide films prepared under optimized RF sputtering conditions," *Sol. Energy Mater. Sol. Cells*, vol. 57, no. 2, pp. 141–152, 1999.

[241] C. G. Granqvist, "Transparent conductors as solar energy materials: A panoramic review," *Sol. Energy Mater. Sol. Cells*, vol. 91, no. 17, pp. 1529–1598, 2007.

[242] H. Hashimoto, M. Hama, and S. I. Shirasaki, "Preferential diffusion of oxygen along grain boundaries in polycrystalline MgO," *J. Appl. Phys.*, vol. 43, no. 11, pp. 4828–4829, 1972.

[243] J. C. Parker, "Raman scattering from VO_2 single crystals: A study of the effects of surface oxidation," *Phys. Rev. B*, vol. 42, no. 5, pp. 3164–3166, 1990 [Online]. Available: http://journals.aps.org/prb/abstract/10.1103/PhysRevB.42.3164

[244] P. Clauws, J. Broeckx, and J. Vennik, "Lattice Vibrations of V_2O_5. Calculation of Normal Vibrations in a Urey-Bradley Force Field," *Phys. status solidi*, vol. 131, no. 2, pp. 459–473, 1985 [Online]. Available: http://dx.doi.org/10.1002/pssb.2221310207

[245] G. Bowers, V. Guthier, A. Hess, A. Otto, O. Roidi, Hj. Roller, and S. Sattelberger, "Vanadium and vanadium compounds," *Ullmanns Encycl. Ind. Chem.*, vol. 37, pp. 119–126, 2012.

[246] Y. Zhang, J. Zhang, X. Zhang, Y. Deng, Y. Zhong, C. Huang, X. Liu, X. Liu, and S. Mo, "Influence of different additives on the synthesis of VO_2 polymorphs," *Ceram. Int.*, vol. 39, no. 7, pp. 8363–8376, Sep. 2013 [Online]. Available: http://www.sciencedirect.com/science/article/pii/S0272884213004069. [Accessed: 03-Aug-2015]

[247] H. Wen, L. Guo, E. Barnes, J. H. Lee, D. A. Walko, R. D. Schaller, J. A. Moyer, R. Misra, Y. Li, E. M. Dufresne, D. G. Schlom, V. Gopalan, and J. W. Freeland, "Structural and electronic recovery pathways of a photoexcited ultrathin VO_2 film," *Phys. Rev. B - Condens. Matter Mater. Phys.*, vol. 88, no. 16, 2013.

[248] D. Tinet, M. H. Legay, L. Gatineau, and J. . Fripat, "Properties of Vanadium Pentoxide Hydrogne Bronzes ($H_{2x}V_2O_5$)," *J. Phys. Chem.*, vol. 90, no. 8, pp. 948–952, 1986.

[249] A. M. Chippindale, P. G. Dickens, and A. V. Powell, "Synthesis, characterization, and inelastic neutron scattering study of hydrogen insertion compounds of VO_2(rutile)," *J. Solid State Chem.*, vol. 93, no. 2, pp. 526–533, 1991 [Online]. Available: http://linkinghub.elsevier.com/retrieve/pii/002245969190327E

[250] A. M. Chippindale and P. G. Dickens, "Hydrogen insertion compounds of V_3O_7 and V_6O_{13}: structural and thermochemical aspects," *J. Mater. Chem.*, vol. 2, no. 6, pp. 601–607, 1992 [Online]. Available: http://pubs.rsc.org/en/content/articlehtml/1992/jm/jm9920200601

[251] R. Lopez, R. F. Haglund, L. C. Feldman, L. a Boatner, and T. E. Haynes, “Optical nonlinearities in VO_2 nanoparticles and thin films,” *Appl. Phys. Lett.*, vol. 85, no. 2004, pp. 5191–5193, 2004 [Online]. Available: <Go to ISI>://000225483700021

[252] A. Cavalleri, T. Dekorsy, H. H. W. Chong, J. C. Kieffer, and R. W. Schoenlein, “Evidence for a structurally-driven insulator-to-metal transition in VO_2: A view from the ultrafast timescale,” *Phys. Rev. B - Condens. Matter Mater. Phys.*, vol. 70, no. 16, pp. 1–4, 2004.

[253] M. Hála, O. Zabeida, and L. Martinu, “Dynamics of HiPIMS Discharge Operated in Oxygen,” *IEEE Trans. Plasma Sci.*, vol. 39, no. 11, pp. 2582–2583, 2011.

[254] E. J. H. Collart, J. A. G. Baggerman, and R. J. Visser, “Excitation mechanisms of oxygen atoms in a low pressure O_2 radio-frequency plasma,” *J. Appl. Phys.*, vol. 70, no. 10, p. 5278, 1991 [Online]. Available: http://scitation.aip.org/content/aip/journal/jap/70/10/10.1063/1.350237. [Accessed: 27-Sep-2016]

[255] R. E. Walkup, K. L. Saenger, and G. S. Selwyn, “Studies of atomic oxygen in O_2+CF_4 rf discharges by two-photon laser-induced fluorescence and optical emission spectroscopy,” *J. Chem. Phys.*, vol. 84, no. 5, p. 2668, 1986 [Online]. Available: http://link.aip.org/link/JCPSA6/v84/i5/p2668/s1&Agg=doi. [Accessed: 20-Jan-2014]

[256] J. Houska, D. Kolenaty, J. Rezek, and J. Vlcek, “Characterization of thermochromic VO_2 (prepared at 250°C) in a wide temperature range by spectroscopic ellipsometry,” *Appl. Surf. Sci.*, 2016.

[257] T. Shimizu, M. Villamayor, D. Lundin, and U. Helmersson, “Process stabilization by peak current regulation in reactive high-power impulse magnetron sputtering of hafnium nitride,” *J. Phys. D. Appl. Phys.*, vol. 49, no. 6, p. 65202, Feb. 2016 [Online]. Available: http://stacks.iop.org/0022-3727/49/i=6/a=065202?key=crossref.0dc98d0d02774f88d2b33b228952809c. [Accessed: 18-Oct-2016]

[258] D. Benzeggouta, M. C. Hugon, and J. Bretagne, “Study of a HPPMS discharge in Ar/O_2 mixture: II. Plasma optical emission and deposited RuO_x film properties,” *Plasma Sources Sci. Technol.*, vol. 18, no. 4, p. 45026, 2009 [Online]. Available: http://stacks.iop.org/0963-0252/18/i=4/a=045026

[259] K. Sarakinos, J. Alami, C. Klever, and M. Wuttig, “Process stabilization and enhancement of deposition rate during reactive high power pulsed magnetron sputtering of zirconium oxide,” *Surf. Coatings Technol.*, vol. 202, no. 20, pp. 5033–5035, 2008.

[260] F. C. Case, “Low temperature deposition of VO_2 thin films,” *J. Vac. Sci. Technol. A Vacuum, Surfaces, Film.*, vol. 8, no. 3, p. 1395, May 1990 [Online]. Available: http://scitation.aip.org/content/avs/journal/jvsta/8/3/10.1116/1.576888. [Accessed: 30-Sep-2016]

[261] V. Melnik, I. Khatsevych, V. Kladko, A. Kuchuk, V. Nikirin, and B. Romanyuk, “Low-temperature method for thermochromic high ordered VO_2 phase formation,” *Mater. Lett.*, vol. 68, pp. 215–217, Feb. 2012.

[262] N. N. Dinh,T.T. Thao, V.N. Thuc, N. Thi, T.Thuy, “Thermochromic properties of VO_2 films made by RF sputtering.”VNU J.Sci Math. – Phys, vol. 26, p 201-206, 2010.

[263] G. S. Janes and R. S. Lowder, “Anomalous Electron Diffusion and Ion Acceleration in a Low-Density Plasma,” *Phys. Fluids*, vol. 9, no. 6, p. 1115, 1966 [Online]. Available: http://scitation.aip.org/content/aip/journal/pof1/9/6/10.1063/1.1761810. [Accessed: 28-Sep-2016]

[264] D. Yu, C. Wang, L. Wei, C. Gao, and G. Yu, “Stabilizing of low frequency oscillation in Hall thrusters,” *Phys. Plasmas*, vol. 15, no. 11, p. 113503, 2008 [Online]. Available: http://scitation.aip.org/content/aip/journal/pop/15/11/10.1063/1.3023150. [Accessed: 28-Sep-2016]

[265] Y. Zhu, J. Na, F. He, and Y. Zhou, “The characteristics of Au:VO_2 nanocomposite thin film for photo-electricity applications,” *Phys. E Low-dimensional Syst. Nanostructures*, vol. 52, pp. 112–115, Aug. 2013 [Online]. Available: http://linkinghub.elsevier.com/retrieve/pii/S1386947713001069. [Accessed: 09-Sep-2013]

[266] M. J. Kreder, J. Alvarenga, P. Kim, and J. Aizenberg, “Design of anti-icing surfaces: smooth, textured or slippery?,” *Nat. Rev. Mater.*, vol. 1, no. 1, p. 15003, Jan. 2016 [Online]. Available: http://www.nature.com/articles/natrevmats20153. [Accessed: 30-Sep-2016]

[267] S. Papaefthimiou, G. Leftheriotis, and P. Yianoulis, “Advanced electrochromic devices based on WO_3 thin films,” *Electrochim. Acta*, vol. 46, no. 13, pp. 2145–2150, 2001.

[268] S. Papaefthimiou, G. Leftheriotis, and P. Yianoulis, “Study of WO_3 films with textured surfaces for improved electrochromic performance,” *Solid State Ionics*, vol. 139, no. 1, pp. 135–144, 2001.

[269] Z. Diao, M. Kraus, R. Brunner, J.-H. Dirks, and J. P. Spatz, “Nanostructured Stealth Surfaces for Visible and Near-Infrared Light,” *Nano Lett.*, vol. 16, no. 10, pp. 6610–6616, Oct. 2016 [Online]. Available: http://pubs.acs.org/doi/abs/10.1021/acs.nanolett.6b03308. [Accessed: 31-Oct-2016]

[270] D. Lehr, M. Helgert, M. Sundermann, C. Morhard, C. Pacholski, J. P. Spatz, and R. Brunner, “Simulating different manufactured antireflective sub-wavelength structures considering the influence of local topographic variations,” *Opt. Express*, vol. 18, no. 23, pp. 23878–23890, 2010.

[271] A. Hendaoui, N. Émond, S. Dorval, M. Chaker, and E. Haddad, “Enhancement of the positive emittance-switching performance of thermochromic VO_2 films deposited on Al substrate for an efficient passive thermal control of spacecrafts,” *Curr. Appl. Phys.*, vol. 13, no. 5, pp. 875–879, Jul. 2013 [Online]. Available: http://linkinghub.elsevier.com/retrieve/pii/S1567173913000242. [Accessed: 03-Sep-2014]

[272] J. Wu, N. Emond, A. Hendaoui, S. Delprat, M. Chaker, and K. Wu, “Broadband temperature-dependent dielectric properties of polycrystalline vanadium dioxide thin films,” in *2015 IEEE MTT-S International Microwave Workshop Series on Advanced Materials and Processes for RF and THz Applications (IMWS-AMP)*, 2015, pp. 1–3 [Online]. Available: http://ieeexplore.ieee.org/lpdocs/epic03/wrapper.htm?arnumber=7324909. [Accessed: 13-Apr-2016]